Experimental Methods and Mathematical Models to Examine Durability of Polymer Electrolyte Membrane Fuel Cell Catalysts

by

Shankar Raman Dhanushkodi

A thesis
presented to the University of Waterloo
in fulfillment of the
thesis requirement for the degree of
Doctor of Philosophy
in
Chemical Engineering

Waterloo, Ontario, Canada, 2013

Author's Declaration

I hereby declare that I am the sole author of this thesis. This is a true copy of the thesis, including any required final revisions, as accepted by my examiners.

I understand that my thesis may be made electronically available to the public.

Abstract

Proton exchange membrane fuel cells (PEMFC) are attractive energy sources for power trains in vehicles because of their low operating temperature that enables fast start-up and high power densities. Cost reduction and durability are the key issues to be solved before PEMFCs can be successfully commercialized. The major portion of fuel cell cost is associated with the catalyst layer which is typically comprised of carbon-supported Pt and ionomer. The degradation of the catalyst layer is one of the major failure modes that can cause voltage degradation and limit the service life of the fuel cell stack during operation. To develop a highly durable and better performing catalyst layer, topics such as the causes for the degradation, modes of failure, different mechanisms and effect of degradation on fuel cell performance must be studied thoroughly.

Key degradation modes of catalyst layer are carbon corrosion and Pt dissolution. These two modes change the electrode structure in the membrane electrode assembly (MEA) and result in catalyst layer thinning, CO_2 evolution, Pt deposition in the membrane and Pt agglomeration. Alteration of the electrode morphology can lead to voltage degradation.

Accelerated stress tests (ASTs) which simulate the conditions and environments to which fuel cells are subject, but which can be completed in a timely manner, are commonly used to investigate the degradation of the various components. One of the current challenges in employing these ASTs is to relate the performance loss under a given set of conditions to the various life-limiting factors and material changes. In this study, various degradation modes of the cathode catalyst layer are isolated to study their relative impact on performance loss 'Fingerprints' of identifiable performance losses due to carbon corrosion are developed for MEAs with 0.4 mg cm^{-2} cathode platinum loadings. The fingerprint is used to determine the extent of performance loss due to carbon corrosion and Pt dissolution in cases where both mechanisms operate. This method of deconvoluting the contributions to performance loss is validated by comparison to the measured performance losses when the catalyst layer is subjected to an AST in which Pt dissolution is predominant. The limitations of this method

are discussed in detail. The developed fingerprint suggests that carbon loss leading to CO_2 evolution during carbon corrosion ASTs contributes to performance loss of the cell. A mechanistic model for carbon corrosion of the cathode catalyst layer based on one appearing in the literature is developed and validated by comparison of the predicted carbon losses to those measured during various carbon corrosion ASTs. Practical use of the model is verified by comparing the predicted and experimentally observed performance losses. Analysis of the model reveals that the reversible adsorption of water and subsequent oxidation of the carbon site onto which water is adsorbed is the main cause of the current decay during ASTs.

Operation of PEM fuel cells at higher cell temperatures and lower relative humidities accelerates Pt dissolution in the catalyst layer during ASTs. In this study, the effects of temperature and relative humidity on MEA degradation are investigated by applying a newly developed AST protocol in which Pt dissolution is predominant and involves the application of a potentiostatic square-wave pulse with a repeating pattern of 3s at 0.6 V followed by 3s at 1.0 V. This protocol is applied at three different temperatures (40°C, 60°C and 80°C) to the same MEA. A diagnostic signature is developed to estimate kinetic losses by making use of the effective platinum surface area (EPSA) obtained from cyclic voltammograms. The analysis indicates that performance degradation occurs mainly due to the loss of Pt in electrical contact with the support and becomes particularly large at 80°C.

This Pt dissolution AST protocol is also investigated at three different relative humidities (100%, 50% and 0%). Electrochemical impedance spectroscopy measurements of the MEAs show an increase in both the polarization and ohmic resistances during the course of the AST. Analysis by cyclic voltammetry shows a slight increase in EPSA when the humidity increases from 50% to 100%. The proton resistivity of the ionomer measured by carrying out impedance measurements on MEAs with H_2 being fed on the anode side and N_2 on the cathode side is found to increase by the time it reaches its end-of-life state when operated under 0 % RH conditions.

Acknowledgements

I am grateful to my co-supervisor Dr. Pritzker for providing me an opportunity to work with the fuel cell research group at the University of Waterloo and for his guidance in improving my technical writing. I am thankful to my co-supervisor Dr. Fowler for his constant support and understanding that he extended throughout the course of my stay in Waterloo. I always admire his vision for our research group and the Department of Chemical Engineering. The various opportunities given by him to work with several co-ops have shaped my leadership skills and improved my patience during the last four years. I must thank my industrial supervisor, Dr. Sumit Kundu, for his invaluable suggestions and help in the progress of this PhD work. It is important to acknowledge the various technical discussions and experimental help provided by Mickey and Max. I also wish to thank the following members of the dissertation committee, Dr. Chen, Dr. Wen and Dr. Li, for their input during my PhD candidacy exam. I wish to thank my friends Manu, Imran and Dimitri for their suggestions on test bench troubleshooting. I would like to thank the assistance of co-ops Lydia, Nick, Nicolo, Kevin and Ammar, who helped in fuel cell testing; I thank Joel who helped me in scanning electron microscopy characterization. Special thanks to all my friends. I would like to thank the Natural Sciences and Engineering Research Council of Canada and Automotive Fuel Cell Corp., Burnaby, for providing financial support to this study. I would like to thank the Offices of Graduate Studies and Research, University of Waterloo, for financial support through Waterloo Institute of Nanotechnology (WIN) scholarships. I also wish to thank the Department of Chemical Engineering, especially Rose and Liz, for their constant support. Above all, I must appreciate my wife, Asha Srinivasan, for her affection, motivation, great understanding and moral support throughout my PhD study.

Table of Contents

List of Figures

List of Tables

List of Abbrevations

AC	Alternate Current
AFCC	Automotive Fuel Cell Cooperation
ANOVA	Analysis of Variance
ACL	Anode catalyst layer
AST	Accelerated stress test
BEV	Battery-electric vehicles
BOL	Beginning-of-life
CAT	Core automotive test
CCL	Cathode Catalyst Layer
CCM	Catalyst coated membrane
CL	Catalyst Layer
COH	Intermediate during carbon corrosion
CV	Cyclic Voltammetry
DOE	Department of Energy
ECSA	Electrochemical active surface area
EIS	Electrochemical impedance spectroscopy
EOL	End-of-life
EPSA	Effective platinum surface area
FCV	Fuel cell vehicles
GDE	Gas diffusion electrodes
GDL	Gas diffusion layer
GDM	Gas diffusion media
GHG	Green house gas
HEV	Hybrid-electric vehicles
HOR	Hydrogen oxidation reaction
ICE	Internal combustion engine
Ionomer	ion conducting polymer
LSV	Linear sweep voltammetry
MEA	Membrane electrode assembly
MPL	Micro-porous layer
NHE	Normal hydrogen electrode
OCV	Open-circuit voltage
ORR	Oxygen reduction reaction
PEM	Proton exchange membrane
PEMFC	Proton exchange membrane fuel cells
PHEV	Plug-in hybrid-electric vehicles

PFSA	PERFLUOROSULFONIC ACID
PTFE	POLYTETRAFLUOROETHYLENE
QC	COLUMBIC CHARGE
QD	COLUMBIC CHARGE
R&D	RESEARCH AND DEVELOPMENT
RDE	ROTATING DISK ELECTRODE
RDS	RATE-DETERMINING STEP
RH	RELATIVE HUMIDITY
RHE	REVERSIBLE HYDROGEN ELECTRODE
SEM	SCANNING ELECTRON MICROSCOPY
SHE	STANDARD HYDROGEN ELECTRODE
SI	SOLATRON INSTRUMENT
TLM	TRANSMISSION LINE MODEL
UPL	UPPER POTENTIAL LIMIT
WIN	WATERLOO INSTITUTE OF NANO
TKK	CATALYST MANUFACTURE'S NAME
V_{BOL}	CELL POTENTIAL OF BEGINNING-OF-LIFE SAMPLE
V_H	UPPER VOLTAGE
V_L	LOWER VOLTAGE

Nomenclature

a	Catalytic surface area per volume, $cm^2\ cm^{-3}$
A_g	Superficial area of the electrode,cm^2
F	Faraday constant, 96485.3 C mol^{-1}
G	Frumkin factor, unitless
i	Current density, A cm^{-2}
i_0	Exchange current density, A cm^{-2}
i_s	Catalyst specific exchange current density normalized to superfical area, A cm^{-2}
i_{H_2}	Hydrogen cross-over current, A cm^{-2}
K_1	Proportionality constant
K_2	Proportionality constant
k_1	Rate constant of reaction 1, mol cm^{-2} s^{-1}
k_2	Rate constant of reaction 2, mol cm^{-2} s^{-1}
k_i	Rate constant of reaction i, mol cm^{-2} s^{-1}
k_i^0	Pre-exponential rate constant, mol cm^{-2} s^{-1}
M	Molar mass of carbon, 12.01 g-mol^{-1}
N_c	Moles of carbon, mol cm^{-2}_{geom}
L_{Pt}	Platinum loading, mg-Pt- cm^{-2}_{geo}
N	Number of electrons transferred in an electrochemical reaction
R	Gas constant, 8.314 $Jmol^{-1}K^{-1}$
R	Reaction rate
R_v	Sum of membrane, contact and bulk electronic resistances, ohm
r_1	Reaction rate for reaction 1, mol $cm^{-2}S^{-1}$
r_2	Reaction rate for reaction 2, mol $cm^{-2}S^{-1}$
S	Specific surface area, $cm^2\ g^{-1}$
T	Temperature, K
U_1	Equilibrium potential of reaction 1, V
U_2	Equilibrium potential of reaction 2,V
U_{Pt}	MEA catalyst utilization in %
V	Difference between the metal potential and hypothetical reversible hydrogen electrode (RHE) defined for p_{H2} = 270 kPa, T= 60^0C, V

A	Transfer coefficient, unitless
α_1	Anode transfer coefficient, unitless
α_2	Cathode transfer coefficient, unitless
B	Symmetry parameter, unitless
Γ	Kinetic reaction order with respect to oxygen partial pressure, unitless
$\eta_{kinetic}$	Kinetic overpotential, V
η_{ohmic}	Ohmic overpotential, V
$\eta_{cross\text{-}over}$	Cross-over overpotential, V
$\eta_{concentration}$	Concentration overpotential, V
θ_{Vac}	Coverage of vacant/free sites, unitless
Θ_{COH}	Fractional coverage by COH sites, unitless
p_0	Partial pressure of water vapor, kPa
p_o^{ref}	Reference partial pressure of water vapor, kPa
$[active\ sites]$	Concentration of active sites, mol sites cm^{-2}
ε	Porosity, unitless
V_{Cell}	Cell Voltage, V
$V_{Cell,OCV\,i}$	Cell voltage at open-circuit voltage (OCV), V

Chapter 1
Introduction

1.1 Overview and Objective

Fuel cell research and development industries are engaged in developing highly efficient, durable, low cost and reliable fuel cell stacks [1]. The major challenges they face in commercializing PEMFCs are the durability, cost and degradation of fuel cell components. Due to its higher activity and stability than other metals and alloys in acidic environments, carbon-supported platinum is commonly used in PEMFC catalyst layers [2]. These catalyst layers contain significant amounts of platinum (Pt) in the form of very small particles (3 to 5 nm) to enhance the rates of the oxidation and reduction reactions [3]. Since this is the single most expensive component of a PEMFC, reduction of the Pt loading while maintaining excellent catalytic activity has been one of the main subjects of PEMFC research over the years.

Degradation or failure of the catalyst layer can lead to severe performance loss during fuel cell operation. Catalyst degradation or failure at the cathode and anode is commonly gauged in terms of the reduction in electrochemical surface area which can occur as a result of such processes as surface oxidation of the carbon support, agglomeration of Pt particles and deposition of Pt in the membrane during long-term cell operation. Compared to the anode, the performance of the cathode tends to degrade faster primarily because the overpotential for oxygen reduction increases continually as the cell operates. Thus, improvement of the durability of the cathode catalyst in particular would help improve the efficiency and life of the PEMFC.

Obviously, the introduction of new material systems that are robust or possess enhanced durability is important for improving catalyst design and prolonging their useful lifetimes. However, another important aspect is to conduct fundamental and applied research into catalyst degradation modes and develop diagnostic methods and mathematical tools to

evaluate the failure modes. Although many experimental studies on catalyst failure mechanisms have been reported, a limited number of empirical and numerical models for catalyst degradation are available and degradation mechanisms are still poorly understood. Such models are important not only for a proper description of fuel cell performance but also for their use in rationally designing, validating and interpreting the results of ASTs. The development and validation of degradation models for given ASTs may help researchers to understand the failure mechanisms associated with changes to the Pt catalyst and carbon support.

Carbon corrosion and Pt dissolution are the two major catalyst layer degradation modes in PEMFCs. The overall goals of this work are to: i) present strategies and protocols for use in ASTs to investigate these two degradation modes and gain a better understanding of the mechanisms involved and ii) develop empirical and simplified mechanistic models that can be routinely used for MEA design and monitoring fuel cell performance. Toward this end, this research has the following objectives:

a. To describe the contributions of the catalyst failure modes to measured performance losses in terms of carbon corrosion diagnostic indicators or ‘fingerprints’;
b. To further the understanding of carbon corrosion by developing a mechanistic model;
c. To further the understanding of Pt dissolution mechanisms at different temperatures;
d. To investigate the impact of relative humidity on Pt dissolution.

The proposed models are developed by making use of various accelerated degradation tests of fuel cells conducted under different operating conditions and potential cycling.

1.2 Scope

The scope of this work is to assess catalyst degradation using different MEAs in fuel cell hardware. Various sets of comprehensive experiments that make use of potential cycling ASTs of the membrane electrode assembly are conducted to examine Pt dissolution and carbon corrosion of the cathode. Several ASTs are developed to study the carbon corrosion mechanism in detail. Effects of temperature and RH on Pt dissolution are also studied through the use of specially designed ASTs. The contributions to fuel cell performance due to the mechanical degradation of the electrolyte membrane and degradation of gas diffusion layers are beyond the scope of this work and so are not included.

1.3 Thesis Layout

This thesis is divided into six different chapters. Chapter 2 introduces the fundamentals of fuel cell operation, hydrogen economy, current state of the literature on fuel cell catalyst degradation, electrochemical approaches to measure degradation parameters and the research needs in the area of fuel cell degradation. Chapter 3 covers information on the experimental techniques, description of different materials used in the study and the methods used to characterize the MEAs. Chapter 4 investigates the use of the carbon corrosion ASTs and the development of carbon corrosion fingerprints to characterize performance losses at cathodes in MEAs. This is followed by the development of a mechanistic model to predict carbon loss and a combination of empirical and mechanistic models to predict the performance loss. Finally, an empirical model describing the performance loss breakdown of a MEA is presented and discussed. Chapter 5 describes the development of an AST for Pt dissolution and its impact on catalyst layer degradation at different temperatures and relative humidities. The development of diagnostic signatures to estimate the kinetic losses when an MEA is subjected to Pt dissolution AST at different temperatures is also described. Finally, the thesis concludes with Chapter 6 in which the

most important conclusions and contributions of this thesis and recommendations for future work are given.

Chapter 2
Background and Literature Review

The background to the research on the degradation of the cathode catalyst layer includes the literature in the following five topics:

- fuel cell components, basis of operation, design and degradation
- basics of the catalyst layer
- carbon corrosion in the catalyst layer
- degradation of the Pt metal catalyst
- methods for analyzing cathode catalyst layer degradation

Background into fundamental aspects of PEM fuel cells such as the principle of operation, fuel cell design, commercial applications and basic modes of degradation is presented in Section 2.1. This is followed by a description of catalyst layer degradation fundamentals in Section 2.2. Section 2.3 contains a review of catalyst layer durability studies that have made use of ASTs, common testing protocols and the current understanding of carbon corrosion and degradation modes that are specific to Pt catalyst failure. This is followed by a description of common methods to analyze cathode catalyst layer degradation. Particular focus is placed on both in-situ and ex-situ techniques that enable important parameters such as electrochemical surface area, polarization and membrane resitance to be measured during ASTs. Some of the preliminary results are also presented in this chapter.

2.1 Fuel Cell Background

Advanced power systems such as fuel cells have the potential to produce high quality power with significantly fewer harmful emissions. Fuel cells enable fast start-up, are more efficient than combustion engines in today's cars and require low maintenance [4]. The basic fuel cell types, which are categorized based on the electrolyte and conducting ion, span a remarkable range of operating temperatures. The use of fuel cell in light-duty automobiles will have a significant impact on environmental problems. Due to the large consumption of energy and relatively low efficiency of light-duty vehicle fleets, the use of hydrogen fuel cells will help reduce oil consumption and CO_2 emissions and improve air quality, thereby helping to meet the environmental and energy challenges of the future [5].

2.1.1 Construction of Proton Exchange Membrane Fuel Cell

In a PEM fuel cell, chemical energy carried by hydrogen is electrochemically converted to electrical energy. It has a higher limiting efficiency than the Carnot cycle that governs combustion engines and thermal power trains [6]. The efficiency of a fuel cell is usually defined as the ratio of electrical energy produced to the calorific value of the fuel which is hydrogen in this case. Cell efficiencies typically exceed 50% at 60^0C and 100 % RH. The heart of a PEMFC is the MEA consisting of five important layers that perform specific roles: anode side gas diffusion layer (GDL), anode catalyst layer, membrane, cathode catalyst layer and cathode side GDL (Figure 2-1). The GDL may be fabricated with a ‘micro-porous layer’ of fine carbon powder at the interface between the electrode and the GDL. A scanning electrode micrograph of an MEA is given in Figure 2-2.

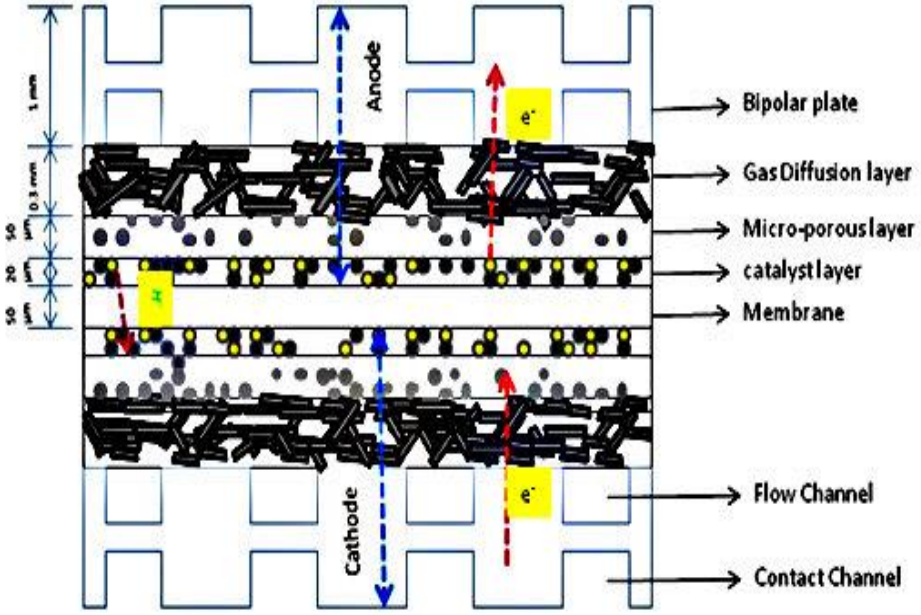

Figure 2-1: Components of proton exchange membrane fuel cell. Figure is re-plotted from the original found in ref. [7].

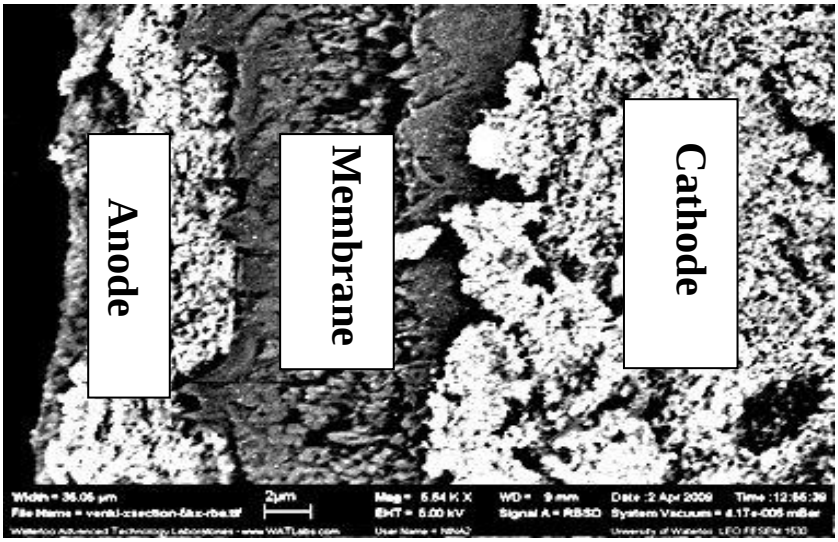

Figure 2-2: SEM image showing cross-section of commercial membrane electrode assembly consisting of a Gore catalyst coated membrane and 35 BC GDLs.

2.1.2 Functions of Proton Exchange Membrane Fuel Cell

Hydrogen enters the cell via the fuel inlet and is then distributed across the GDL to the catalyst layer (Figure 2-3). Upon contact with the anode catalyst, hydrogen adsorbs onto reaction sites, dissociates into hydrogen atoms that are split into a proton (H^+) and an electron (e^-) by anodic oxidation. Since the electron cannot cross the membrane, it leaves the fuel cell as electric current through the GDL and the bipolar plate. The proton, on the other hand, is transported across the membrane to the cathode side. On the cathode side, oxygen entering the fuel cell is distributed over the cell surface by the gas channels, diffuses to the catalyst layer, adsorbs onto reaction sites and combines with a proton and electron from the external circuit to form water on the cathodic platinum catalyst particles. The product water is then transported back through the GDL and leaves the fuel cell through the gas channels [8]. The electrochemical reactions in a proton exchange membrane fuel cell are described in reactions 2-1 and 2-2 below. The oxidation of hydrogen gas at the anode occurs by the following half-cell reaction:

$$H_2 \rightarrow 2H^+ + 2e^- \qquad E^0_{25°C} = 0V \qquad (2\text{-}1)$$

where E^0 is its half-cell potential measured against a reversible hydrogen electrode (RHE). The half-cell reaction for the reduction of O_2 gas at the cathode is given below:

$$2H^+ + 2e^- + \frac{1}{2}\,O_2 \rightarrow H_2O \qquad E^0_{25°C} = 1.229V \qquad (2\text{-}2)$$

The combined overall reaction is:

$$H_2 + \frac{1}{2}\,O_2 \rightarrow H_2O \qquad (2\text{-}3)$$

Some of the heat generated during the electrochemical reaction is transferred from the MEA to the bipolar plates by conduction and then transmitted to the ambient air through either specially designed cooling fins or cooling liquid circulating within the bipolar plates. Depending on the current density, cell voltages between 1 V and 0.5 V are typically achieved [8]. In order to increase the power and voltage generated by a fuel cell, a number of single cells are connected in series to form a so-called fuel cell stack.

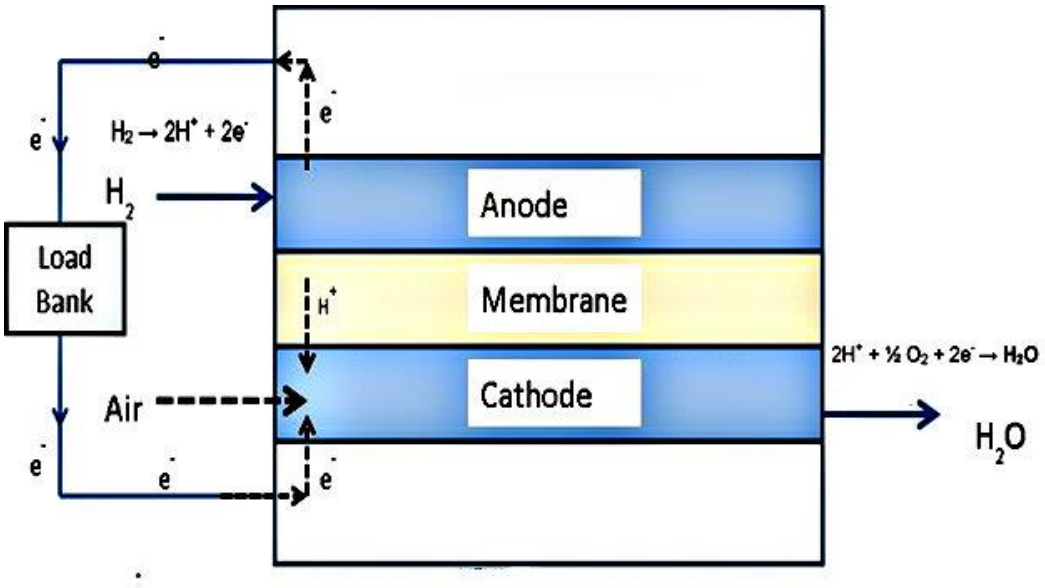

Figure 2-3: Schematic diagram showing basic components of PEM fuel cell. Figure is re-plotted from the original found in ref. [7].

2.1.3 Hydrogen Economy

Hydrogen as an energy carrier can be produced from several sources such as fossil fuels, nuclear energy and various renewable energies for multiple end-uses. This leads to the concept of the *hydrogen economy,* which encompasses the production, distribution and utilization of hydrogen in energy conversion systems, specifically to benefit the transportation sector [9]. Hydrogen is a desirable and secure long-term energy vector because it can be stored and used to generate electricity, can be produced from a diverse range of production pathways and its expanded use will lower pollution and greenhouse gas emissions from current levels. Also, the use of hydrogen allows for the implementation of intermittent renewable energy sources such as wind and solar, which require some type of energy storage [10]. For transportation purposes, hydrogen can be burned in an internal combustion engine. However, NO_x and SO_x, which are a primary cause of photochemical smog and air pollution, are generated when hydrogen is produced from fossil fuels.

Furthermore, when hydrogen is used, fuel cells operate at higher efficiencies than internal combustion engines.

2.1.3.1 Future Vehicles for Transportation

Of the various fuel cell types, PEMFCs are best suited for transportation applications due to their size, mass and operating temperature. The transportation sector contributes significantly to greenhouse gas emissions, making up 27% of Canada's CO_2 emissions. The Canadian Federal government has targeted that a 60-70 % reduction in greenhouse gas emissions from 2006 levels be reached by 2050 [5]. The potential use of electric and hybrid-electric powertrains to reduce greenhouse gas emissions is currently of interest in gasoline hybrid-electric vehicles, plug-in hybrid-electric vehicles, fuel cell vehicles and battery-electric vehicles. While plug-in electric power trains can draw some or all of their energy from the electrical grid and thereby reduce the transport sector reliance on petroleum, this potential is constrained by the reliance of the grid itself on fossil fuels. Nevertheless, the use of hydrogen and fuel cell technology has the potential to reduce the dependence on petroleum and decrease pollution and greenhouse gas emissions. Fuel cell vehicles are the main powertrain transportation technologies that can achieve this goal [11]. Battery-electric vehicles are limited with respect to their range, durability and long recharge times. Fuel cell vehicles can achieve truly zero emissions on a well-to-wheels basis (i.e. assessment of total impact of production, distribution and consumption of fuel) when fuelled with hydrogen produced from renewable energy. Even fuel cells using hydrogen produced from natural gas reduce greenhouse gas emissions by over 50% compared to current internal combustion engine vehicles. While other technologies will contribute to greenhouse gas reductions, the deepest cuts in fossil fuel consumption and greenhouse gas emissions will result from the use of fuel cell vehicles or battery-electric vehicles. As shown in Figure 2-4, most automotive companies are planning for a transition from the current internal combustion engine vehicles to fuel cell vehicles in the future.

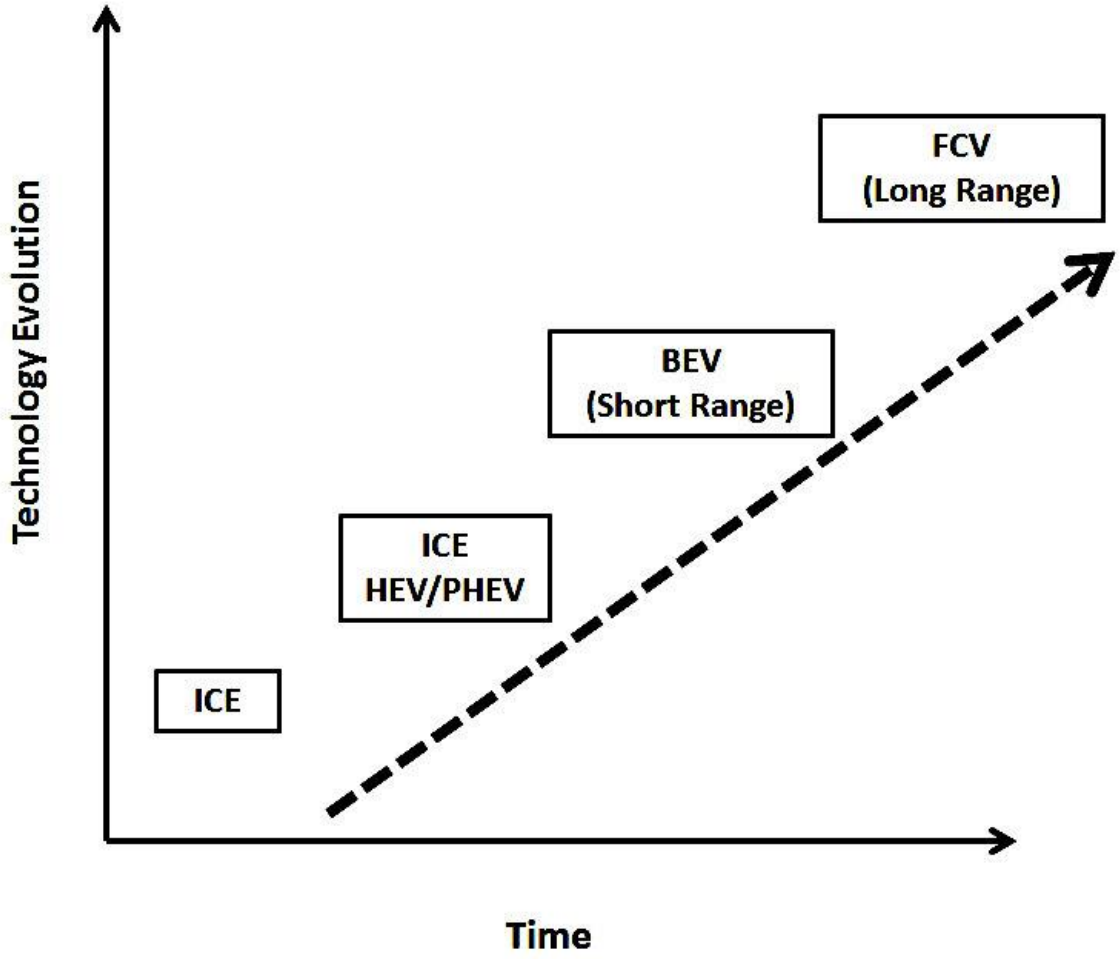

Figure 2-4: Future electrification of advanced vehicle technologies. (ICE – Internal combustion engine, HEV - Hybrid-electric vehicles, PHEV - Plug-in hybrid-electric vehicles, FCV - Fuel cell vehicles and BEV - Battery-electric vehicles). Figure is re-plotted from the original found in ref. [12].

For high volume applications, fuel cells offer the potential for the lowest life cycle costs of all zero-emission technologies and hence are expected to provide superior long-term solutions. Although an extended-range electric vehicle such as the plug-in hybrid-electric Chevrolet Volt makes use of an internal combustion engine, its operation involves very strong hybridization or electrification of the powertrain. Fuel cells can also be used in plug-in hybrid-electric vehicles as primary power generators or as ‘range extenders’ [13]. In

other words, plug-in hybrid-electric vehicles are designed to meet the near- and long-term needs of future vehicle powertrains. It is expected that hybrid-electric vehicles, plug-in hybrid-electric vehicles and extended-range electric vehicles will serve as transitional technologies while the hydrogen economy and associated technology and infrastructure are being developed and prototyped. Regardless of the fate of some of these particular technologies, hydrogen will be an important component of integrated energy systems over the long-term beyond 2020.

2.1.4 Current Challenges to Fuel Cell Commercialization

Despite numerous advantages, some barriers to wide scale market penetration of fuel cell technology exist [14]:

- Fuel cell capital costs are still high and so further improvements to catalyst utilization (or the development of non-noble metal catalysts), introduction of low cost membrane materials and the development of high volume production methods are needed.
- Fuel cell durability and reliability have not been adequately demonstrated for large-scale power generation and automotive applications.
- Infrastructure for hydrogen production, distribution and refuelling is not yet in place.

2.1.5 Fuel Cell Degradation

Components of the PEMFC, especially the MEA, are affected by numerous processes during the wide range of operating conditions. Important causes of MEA component degradation have been highlighted and explained by de Bruijn et al [15]. The degradation of the proton exchange membrane in the MEA can be classified according to whether it occurs primarily by mechanical, thermal or chemical factors. Mechanical degradation is driven primarily by mechanical stresses typically due to inadequate or uneven compression of the cell, non-uniform torque at the end plate and insufficient humidification. Thermal degradation can be defined as the deterioration of membrane components due to the high temperature operation of the cell. At high temperatures, the membrane can begin to collapse and form pin-holes and hotspots. Chemical degradation of the membrane mainly occurs due to the presence of contaminants and the formation of free radicals.

First-generation fuel cell vehicles could be driven only between 100 and 190 miles before their MEAs failed [16]. However, great improvements in fuel cell durability have been made since that time. In 2008, GM launched Project Driveway and demonstrated that FCVs could operate more than 40,000 miles before failure. Recent on-road tests by the US Department of Energy showed that FCVs could cover a distance of 431 miles on a single tank of compressed hydrogen for an average fuel economy of 68.3 miles per gallon equivalent [17]. However, severe catalyst layer degradation is still observed in the current fourth-generation vehicles [18] and remains as one of the main contributors to performance degradation in fuel cell vehicles [19]. Thus, in order to meet commercialization targets, additional improvements are required, especially at the catalyst layer, which is the most expensive component in a fuel cell. This requires a better understanding of the catalyst layer and its degradation in order to further improve the performance of the next generation fuel cell vehicles.

2.2 Catalyst Layer

The main purposes of the catalyst layers are to reduce the activation barriers for the hydrogen oxidation reaction (HOR) and the oxygen reduction reaction at the anode and cathode, respectively. The catalyst layer facilitates the electrochemical reactions by i) providing pathways for mass transport of the reactants to reaction sites, ii) providing electrochemically active sites for the interfacial reactions, iii) enhancing proton transfer between the electrode and ionomer electrolyte and iv) enhancing electronic conduction through the carbon support. This layer is formed by applying stabilized catalyst ink onto both sides of the membrane. The ink is prepared by mixing platinum catalyst, carbon support powder, binder, additives and solvent. The geometrical design of the catalyst layer is chosen by considering its ability to conduct ions and electrons, transfer the gases, remove the condensed water and retain the three-phase interface boundary between the carbon support, ionomer and metal catalyst [1]. In order to meet these criteria, perfluorosulfonic acid (PFSA) polymer and Pt-supported carbon are most commonly used in catalyst layers to enable proton and electron transport, respectively. In addition, polytetrafluoroethylene (PTFE) binder is often added to the catalyst to facilitate mass transport and control its hydrophobicity or hydrophilicity [1]. A scanning electron microscopy image of a typical catalyst layer is shown in Figure 2.5. Catalyst layers are typically between 8 and 15 μm thick with porosities between 40 and 50%.

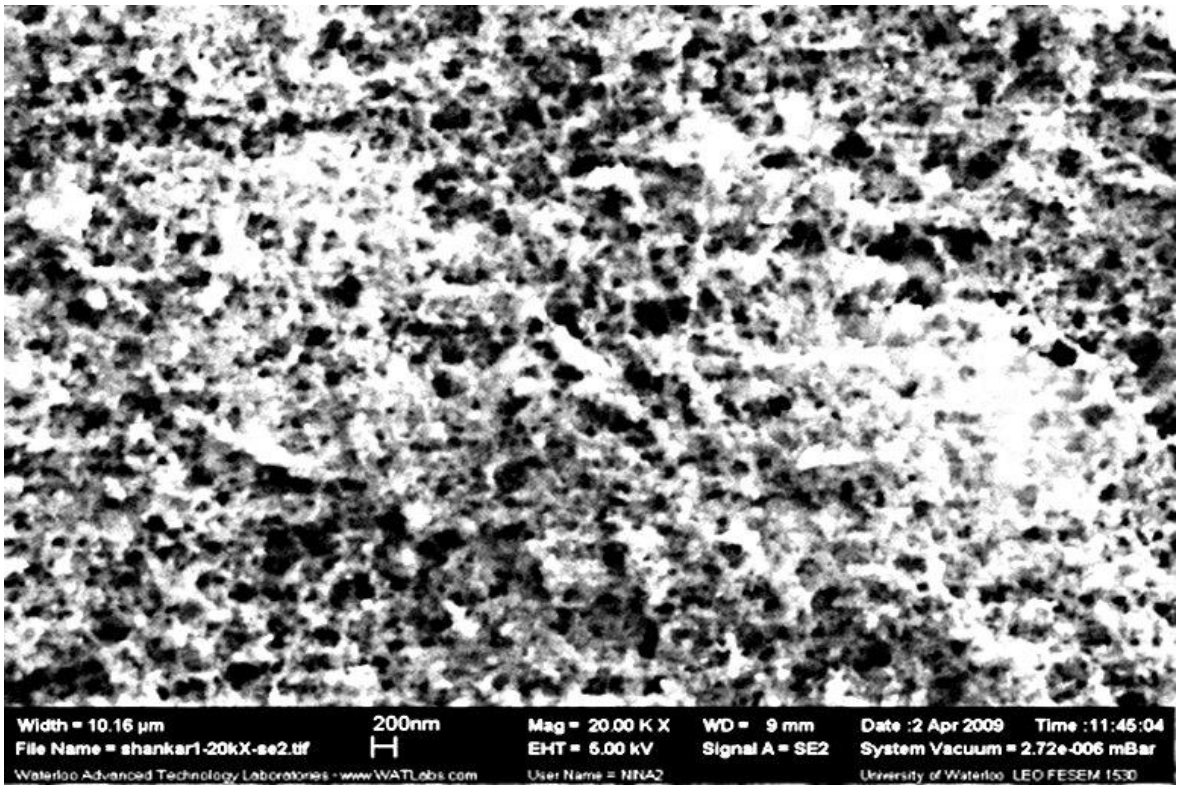

Figure 2.5: SEM image of catalyst layer: plane view of cathode layer at 20,000x magnification. The SEM image of a catalyst layer is obtained for a commercial confidential MEA.

2.2.1 Degradation of Catalyst Layer Structure

The catalyst layer degrades primarily by deterioration of the metal catalyst and carbon support that are inter-related. This problem is usually more severe in the cathode catalyst layer than in the anode catalyst layer [19]. The resulting degradation of the electrode structure and voltage degradation is reflected in the loss of electrochemically active surface area (ECSA) [20-22] which can occur by the following four mechanisms (Figure 2-6) [23]:

- detachment of Pt particles from carbon support
- Pt dissolution and re-deposition on larger Pt particles (Ostwald ripening)
- migration of smaller Pt particles on carbon support and subsequent coalescence to form larger Pt particles
- Pt dissolution and transport into ionic conductor where it is reduced by H_2

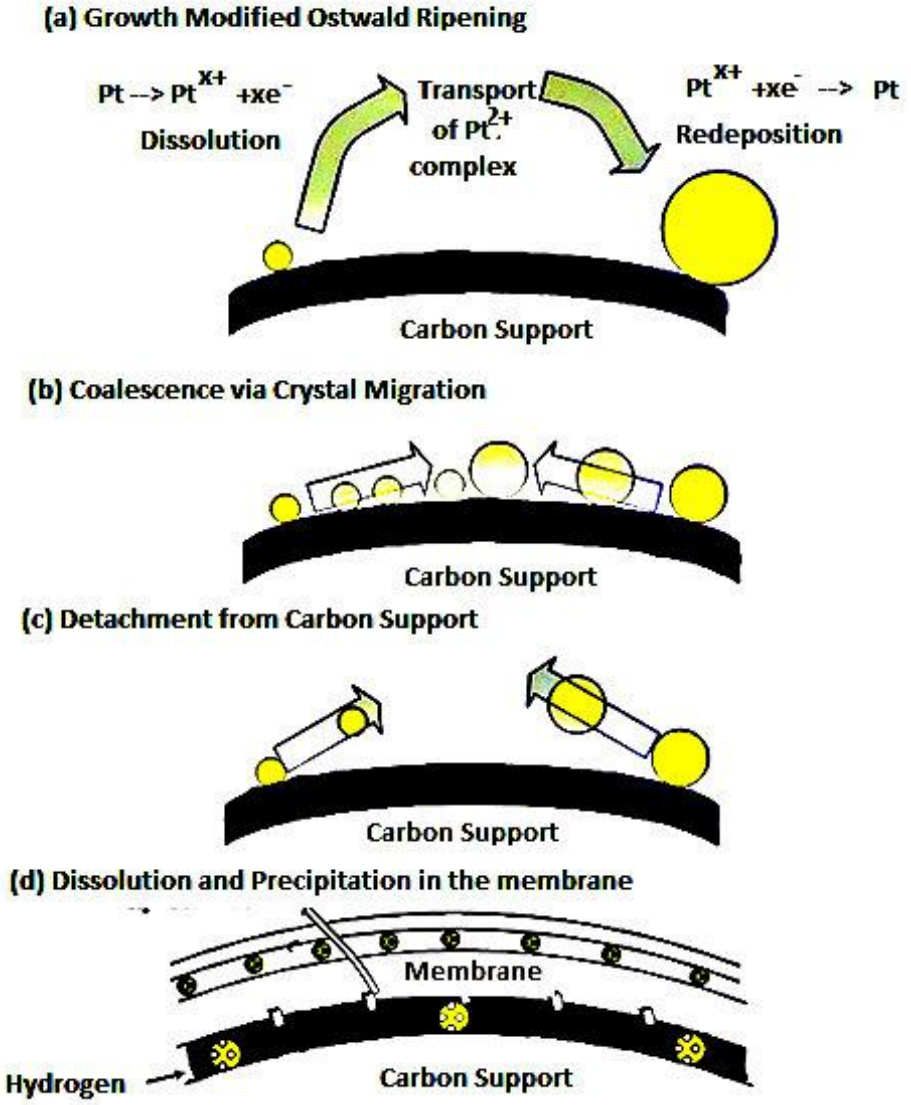

Figure 2-6: Four mechanisms for degradation of carbon-supported platinum in fuel cells (re-plotted from original source [33]): (a) electrochemical Ostwald ripening (b) particle migration and coalescence (c) detachment from carbon support (d) dissolution of platinum and its re-precipitation in membrane by H_2 reduction

2.2.1.1 Detachment of Carbon

Generally, the detachment of the carbon support occurs as a result of carbon oxidation and the water-gas reaction. Corrosion of the carbon support leads to electrical isolation and agglomeration of platinum particles, thereby decreasing the effective electrochemical area in the catalyst layer. Although it does not occur rapidly, carbon corrosion leads to a measurable decrease in carbon content in the catalyst layers during long-term operation. Furthermore, under some circumstances when the electrode potential is raised to extremely high levels, rapid degradation of both the carbon support and platinum catalyst takes place. Carbon corrosion also occurs when the cell is held at open-circuit, when the support is partially covered by hydrogen and oxygen during start/stop cycling and when fuel starvation conditions prevail.

As with other electrochemical processes, carbon corrosion kinetics depends on temperature, potential and duration of operation. Slower corrosion has been reported at potentials below 0.9 V at temperatures between 60 and 90°C in PEMFCs [24]. A variety of carbon-containing surface oxides have also been observed to form at 65°C and at potentials above 0.8 V (RHE), resulting in lower hydrophobicity [25]. The presence of Pt has been found to catalyze subsequent oxidation of surface carbon oxides to CO_2 at a potential of 0.8 V [15]. In the absence of Pt, CO_2 formation has been observed only at potentials above 1.1 V [26]. On the basis of field emission scanning electron microscopy studies, researchers have observed the presence of Pt particles in regions where carbon corrosion and blister formation occur [27]. A thermo-gravimetric analysis study on the thermal degradation of carbon and platinum in air revealed a loss of approximately 15% carbon after 1000h at a temperature of 125°C and more than 40 wt% at temperatures above 125°C [28]. It was concluded that thermal degradation of Pt-loaded carbon in air does not take place below 100 °C. The corrosion rate of carbon was enhanced when the RH of the air was high and when high surface area carbon black materials contained a fine dispersion of Pt particles. The effect of carbon corrosion is described in Table 2-1.

Table 2-1: Effects of Carbon Corrosion.

Property	Effect	Reference
CO Poisoning	- CO is observed during AST at higher cathode potentials - CO directly poisons the activity of the CL	[7]
Carbon Oxidation	- During AST, Pt can catalyze carbon and increase the rate of carbon oxidation - This process can be accelerated when Pt loading is increased - Presence of large interfacial area between Pt nanoparticles and carbon tends to increase extent of carbon oxidation	[16, 34, 35]
Physio-Chemical Changes	- Carbon loss from the CL changes support surface chemistry - CL hydrophilicity increases due to morphological change - Gas permeability and porosity decrease - Slower water transport from CL to GDL leads to 'flooding' of CL pores	[36-38]
ECSA Loss and Electrode Thinning	- Formation of CO_2 or CO during carbon oxidation decreases the amount of carbon available for Pt loading - Pt nanoparticles detach from the carbon support, decreasing the ECSA - Carbon corrosion cycles can reduce CL thickness by 33 %	[39-41]
Temperature	- Rate of carbon support degradation increases with temperature	[42, 43]
Oxygen-containing groups	- Oxygen-containing groups, e.g., carboxyl, carbonyl, hydroxyl, phenol can form on carbon surface and weaken the interaction between support and Pt -Formation of these groups accelerates sintering of Pt nanoparticles	[44, 45]
Electrical Conductivity	- CL conductivity decreases due to carbon loss and formation of oxygen-containing groups - Increase in electrode resistance and decrease in CL thickness are two important factors causing the decrease in electric contact with current collector	[19, 46, 47]

2.2.1.2 Electrochemical Ostwald Ripening

This degradation mechanism involves the dissolution and re-deposition of platinum on large particles by the process of electrochemical Oswald ripening [29]. This has a detrimental effect on PEMFC performance since it increases the average size of Pt particles and decreases the platinum surface area in the electrode. This phenomenon stems from the effect of the surface energy on the chemical potential of phases, which causes smaller particles to being inherently less stable and therefore more soluble than larger particles of the same type [45]. Ostwald ripening occurs by the following steps: (a) preferential dissolution of partly soluble smaller Pt particles in the electrolyte/ionomer [29], (b) transport of dissolved Pt to the surfaces of larger Pt particles through the electrolyte/ ionomer while electrons are transported through the carbon supports to larger particles and (c) reduction of dissolved Pt onto the surfaces of these inherently more insoluble larger particles. This results in the growth of large particles on the carbon support at the expense of smaller particles. Pt dissolved in the ionomer phase may redeposit on larger Pt particles in the cathode, which must be present on the carbon support to allow for exchange of electrons. An important characteristic of electrochemical Ostwald ripening is that particle growth is potential dependent. Indeed, Pt particle growth has been shown to be potential dependent at cell voltages above 0.8 V and lead to platinum dissolution and re-deposition [30-32].

2.2.1.3 Particle Migration and Coalescence

The Pt particle size distribution on a carbon support is a useful indicator of the contributions that crystallite migration and coalescence have on the electrochemical area loss in PEMFCs. Migration of platinum on the carbon support and its coalescence can occur during fuel cell operation without platinum having to dissolve and re-precipitate [33, 48]. This growth is expected to generate a different particle size distribution in PEMFC than does Ostwald ripening [48, 49] and cause area loss during operation at potentials

below 0.8 V where platinum does not dissolve [50]. Particle growth in PEMFC by coalescence driven by Brownian motion has been predicted to occur by some researchers [20, 22, 24, 30, 49]. However, other researchers have the opinion that coalescence may not be the prevailing mechanism since sintering does not occur significantly in catalysts at temperatures below 500°C [20, 22, 30]. Although coalescence of Pt particles causes an increase in the particle size, it leads to a size distribution with a tail at larger sizes [51]. Interpretation of the data obtained from particle size measurement is complicated by the fact that several mechanisms likely operate simultaneously and that proper sampling and size measurement can be difficult [51, 52].

2.2.1.4 Dissolution of Platinum and Precipitation in Membranes

According to this mechanism, platinum dissolved from the catalyst layer diffuses into the membrane and is reduced chemically by hydrogen permeating from the anode [49, 53, 54]. The driving force for this mechanism is likely electro-osmotic drag and/or diffusion [22, 55]. The effect of Pt precipitation on the membrane and the location of counter anions have not yet been well established. Membrane degradation products such as fluoride and sulfate anions have been detected during PEMFC operation and could possibly act as complexing ligands for Pt^{z+} [56]. The concentration of fluoride near Pt particles in an aged membrane has been found to be higher than that in a new membrane [22, 55]. The concentrations of Pt (II) and Pt (IV) species which are highly mobile in the membrane tend to increase upon ageing. This leads to the formation of platinum bands in the membrane near the interface of the membrane/cathode during cycling with H_2/N_2 and further away from the cathode when H_2/O_2(air) are used [20, 53, 57-61]. Previous studies reported the movement of this Pt band toward the anode side when the fuel cell was operated under conditions of fuel starvation [58, 59]. Band formation appears to mainly depend on the following factors: (a) partial pressure of H_2 and O_2, (b) permeability of reactants through the membrane and (c) size distribution of Pt in the carbon support [62].

2.3 Perspectives on Catalyst Durability Studies

In order to improve the durability of the catalyst layer, fuel cell operators require a fundamental understanding of the mechanisms of Pt dissolution and carbon corrosion. The following areas are identified as important and immediate research needs to produce highly durable fuel cell vehicles:

i. Development of accelerated test protocols (AST) to study catalyst support degradation
    a. Understanding fuel cell voltage degradation mechanisms at elevated potentials
    b. Improved fundamental understanding of catalyst support failure mechanisms using kinetic models
    c. An analytical or empirical tool that can monitor the voltage loss during corrosion process of fuel cell material can help to improve the system. Moreover, knowledge of the contributions to voltage loss from individual fuel cell components can be useful for developing new cell design and materials.

ii. Development of accelerated test protocols to study catalyst metal degradation
    a. Effect of cell temperature;
    b. Effect of RH;
    c. Development of highly durable MEAs that is resistant to Pt dissolution.

Details of the literature survey conducted on the above topics are presented in the following sections.

2.3.1 Accelerated Stress Testing for Cathode Catalyst Layer

Obviously, reproducible degradation rates should be obtained from ASTs. Thus, efforts must be made to design and implement well-controlled diagnostics tools and verify that reproducible results are indeed obtained. To gain a fundamental understanding of fuel cell failures, it would be desirable to conduct a steady-state test (1.7 A cm^{-2}) to measure the

electrochemical performance at given inlet conditions (ambient temperature, RH and electrical power factor) while the load and environmental conditions are held constant. However, during operation in a FCV, PEMFCs are subject to dynamic variations in load, cell potential, temperature, humidity, etc. and so dynamic tests are also needed. In addition, it would be useful to measure other properties of the electrode materials such as hydrophobicity and oxide coverage on the carbon and the platinum particles that are critical to PEMFC performance and are linked to the potential [1].

In order to reduce the cost and effort to prepare large stacks and the time required to study degradation of the cathode catalyst, protocols for accelerated stress test are needed [19, 63]. These protocols are also useful for targeting and understanding specific degradation mechanisms. ASTs are used as tools to measure the stability of fuel cell catalysts under different cycling conditions and identify catalyst dissolution and agglomeration processes. However, a systematic approach is required to isolate the carbon corrosion and Pt dissolution failure modes. Common stressors such as increased voltage, voltage cycling and load cycling tend to exacerbate catalyst layer degradation. Critical research activities supporting these advances include:

- representative AST techniques
- isolation of catalyst failure mechanisms based on AST data
- fundamental investigations of the mechanisms using ex-situ analyzes

Such efforts will help to identify the interactions between different variables (e.g., electrode potential, humidity and partial pressure of reactants) and phenomena (e.g., Pt band formation in the membrane) that affect catalyst layer degradation. Some examples of ASTs and degradation routes are shown in Table 2-2. CL failure during ASTs can be gauged by examining the (a) decrease in catalyst utilization, (b) role of contaminants from reactants and other cell hardware, (c) decrease in electrochemical activity, (d) changes in corrosion resistance of the catalyst support under extreme chemical environments and (e) decrease in the electrode thickness at the end of fuel cell operation. These parameters shown in figure 2-7 must be evaluated in samples at the beginning-of-life (BOL), during

the course of ASTs and at the end-of-life (EOL). In any type of AST, many properties and structures in the MEA may be adversely affected and lead to fuel cell performance losses. The performance losses occurring during carbon corrosion ASTs can be characterized in terms of the degradation of the current when the cell is operated at a given potential or the degradation of the cell potential when the cell is operated at a given current density. The use of ASTs should help identify the parameters important for a particular degradation mode and the appropriate strategies to mitigate it. Obviously, such information should be taken into account in the design of CLs.

Table 2-2: Examples of the degradation cycle and its mechanism.

AST	Degradation Route	Mitigation Strategy
Potential cycling	Pt particle growth at cathode[64] Pt dissolution at cathode[65]	Preparation of more stable CL[66]
Start-stop cycles	Carbon corrosion[67]	Use of carbon nanotubes (CNT) in CL[68]
Fuel starvation	Carbon corrosion[69]	Use of CNTs in CL [70] Preparation of CL with improved binder[71]

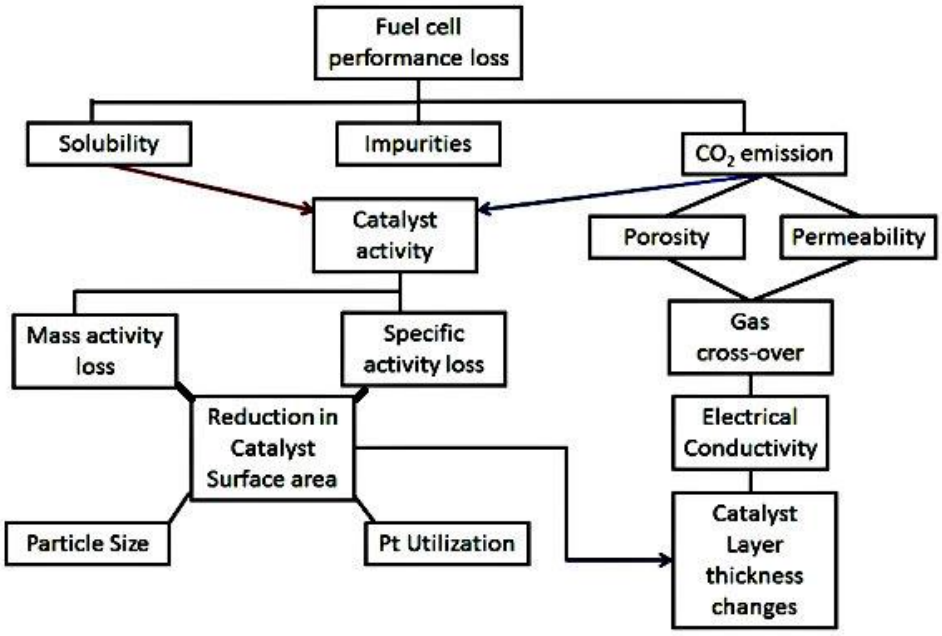

Figure 2.7: Important parameters affected by ASTs that cause voltage and fuel cell degradation. Figure is plotted based on ref. [72].

2.3.2 Carbon Corrosion in PEMFC

2.3.2.1 Carbon Corrosion and Pt Dissolution at Elevated Potentials

Carbon-supported platinum is the most common catalyst for the oxygen reduction reaction and is incorporated in the cathode catalyst layer in a PEMFC. Not surprisingly, the performance of the fuel cell is strongly influenced by the cathode catalyst layer and particularly its compositional and morphological characteristics [35]. Major functions of the cathode catalyst layer are to reduce the activation barrier for the oxygen reduction reaction (ORR), facilitate oxygen and water transport and conduct heat, protons and

electrons. Consequently, degradation of the cathode catalyst layer has major impacts on the entire cell and system. The degradation of the cathode carbon catalyst support in particular is one of the failure modes that can cause severe voltage degradation during operation. Thus, in order to further improve catalyst design, it is important to identify the key failure mechanisms of cathode degradation. A complication when assessing many automotive failure modes is that more than one mode of degradation of the catalyst layer often operates at the same time, making it difficult to identify which one has the largest impact and thus is the most important failure mode to mitigate.

Carbon corrosion can lead to catalyst 'wash out' and/or aggregation of support and catalyst particles [26, 73-75]. Carbon corrosion is believed to proceed via reactions (2-4) and (2-5) which involve carbon oxidation combined with the water-gas shift reaction [15]:

$$C + 2H_2O \rightarrow CO_2 + 4H^+ + 4e \qquad E_0 = 0.207\ V_{RHE}\ @\,25°C \qquad (2\text{-}4)$$

$$C + H_2O \rightarrow CO + 2H^+ + 2e^- \qquad E_0 = 0.518\ V_{RHE}\ @\,25°C \qquad (2\text{-}5)$$

It is most likely to occur under conditions in which highly oxidizing potentials are applied [76] or the potential changes rapidly e.g., continual cycling at high frequency. In order to study carbon corrosion, many bench scale in-situ ASTs have been developed [1]. These tests are usually aimed at identifying the specific life-limiting factors of the fuel cell materials and the degradation mechanisms on the basis of durability studies. Carbon corrosion can theoretically begin to occur at an electrode potential of 0.207 V_{RHE} [1]. At cathode potentials above 0.8 V, a variety of carbon surface oxides have been observed to form [25, 75]. In another study, carbon corrosion was found to accelerate when cathode potentials exceeded 1.2 V [1]. During normal PEMFC operation, the cathode potential is reported to vary between 0 and 1.0 V_{RHE}. However, under conditions of fuel starvation or gas switching such as during start-up and shut-down ASTs, the cathode potential is expected to exceed 1.2 V_{RHE} and lead to carbon oxidation. Hence, on the basis of these results, carbon corrosion can be observed by holding or switching the cathode potential above 1.2 V_{RHE}. This can be achieved by switching the voltage across the MEA (cell potential) between 1.0 and 1.4 V. The use of this potential window during ASTs is

generally considered to be appropriate to assess carbon corrosion [77]. In this range, the role and mechanism of carbon corrosion when different upper potentials are applied are well known [75]. Holding the MEA at a constant cell voltage (usually between 1.0 and 1.4 V) is another approach to study carbon corrosion [25, 47, 76, 78, 79]. This approach requires a longer time to observe the degradation of the catalyst, which is a disadvantage for screening and analyzing catalyst support materials. The rationale behind holding the cell potential at 1.4 V to study carbon corrosion is that this is close to the cathode potential during current reversal [80, 81] and local fuel starvation [54] conditions, which lead to severe carbon corrosion [35]. Also, if the potential exceeds 1.4 V, the rate of oxygen evolution begins to become significant. Once oxygen gas evolution is observed, then mechanical detachment of carbon black particles from the electrode can occur. Thus, the performance loss measured when the potential is held at 1.4 V can be attributed mainly to carbon corrosion alone [74, 76]. These losses due to carbon corrosion occur in the following ways:

1. sintering of Pt particles causing loss of active phase or support interaction phase
2. oxidation of carbon surface leading to catalyst layer flooding
3. breakdown of the carbon/carbon interface
4. formation of reactive species which can impair membrane durability

Diminution of the interaction between Pt particles and the carbon support surface is termed as ‘undercutting’. This is a serious problem since undercutting tends to lead to sintering of catalyst particles and loss of active area which in turn raises the kinetic overpotential of the fuel cell. Also, the catalyst layer usually becomes more hydrophilic as it corrodes due to the formation of oxygen-containing species on carbon and platinum surfaces. This increases the retention of water in the catalyst layer pores, leading to an increase of the mass transport overpotential of the cell and making the MEA more susceptible to flooding. Another important factor is the morphology of the catalyst layer which influences the connectivity within the ionically and electronically conducting phases in the porous matrices and contributes to ohmic losses during cell operation.

Pt loss during cell operation is another source of cathode layer degradation during durability experiments [1, 15, 66]. Pt loss during experiments has been estimated from the loss of Pt/C catalyst mass in acidic electrolyte systems after potential cycling [82, 83]. Dissolution of Pt particles is generally caused by many factors such as Pt dissolution and washout [15, 82-84]. The occurrence of Pt dissolution has been reported under standard operating conditions [85]. Cycling the potential across the MEA over different potential ranges can cause severe voltage loss during the Pt degradation process, while higher potentials have been found to accelerate Pt dissolution and cause higher performance loss. Wang et al. [86] reported that the concentration of dissolved Pt increased monotonically as the cell potential is raised from 0.65 to 1.1 V, but then decreased at cell potentials higher than 1.1 V due to the formation of a protective oxide film. This trend is supported by another study that showed Pt dissolution to strongly increase with electrode potential in the region between 0.6 and 1.0 V_{RHE} [49]. Therefore, the upper cell potential limit to assess Pt catalyst degradation is generally 1.0 V to avoid the possibility of carbon support corrosion. In addition, the agglomeration of Pt can also be affected by many other operating conditions such as temperature and/or RH [52, 87-89].

Platinum dissolution from the catalyst layer involves either direct anodic electrodissolution or chemical dissolution of platinum oxide formed by electrochemical oxidation. Electrochemical dissolution of Pt to Pt^{2+} is described by the reaction below [1, 86]:

$$Pt \rightarrow Pt^{2+} + 2e^{-} \qquad E_0 = 1.19 + 0.029 \log [Pt^{2+}] \qquad (2\text{-}6)$$

The formation of platinum oxide (PtO) and its subsequent chemical reaction can occur as follows:

$$Pt + H_2O \rightarrow PtO + 2H^{+} + 2e \qquad E_0 = 0.98 - 0.59\ pH \qquad (2\text{-}7)$$

$$PtO + 2H^{+} \rightarrow Pt^{2+} + H_2O \qquad \log [Pt^{2+}] = -7.06 - 2\ pH \qquad (2\text{-}8)$$

E_0 and $[Pt^{2+}]$ have units of V (RHE) and mol L^{-1}, respectively, in these expressions. ASTs employed to study the simultaneous degradation of the Pt catalyst and carbon support generally operate at cell voltages between 0.6 V and 1.4 V. Experiments that focus on

conditions where both modes of degradation occur together are important for several reasons. The presence of Pt has been found to catalyze carbon support corrosion and CO_2 formation at 0.8 V [74]. In contrast, CO_2 tends to form only at potentials above 1.1 V in the absence of Pt [47, 74-76]. However, details of the direct contribution of the Pt catalyst to carbon corrosion are still not well understood. Furthermore, failure modes in automotive applications where both mechanisms operate are also of interest. Carbon corrosion ASTs generally involves situations where the cathode half-cell potential exceeds 1.4 V_{RHE} [74] for short periods of time. During carbon corrosion AST cycles, both Pt dissolution and carbon corrosion likely contribute to the overall performance loss. In order to select the best degradation mitigation strategy, it is necessary to identify the dominant mechanism contributing to performance loss. Currently, no method is available to do so.

2.3.2.2 Kinetic Models of Catalyst Support Failure

The kinetics of carbon corrosion depends on temperature, potential and duration of operation. The corrosion behavior is expected to change depending on upper/lower potential limits of the AST, catalyst loading, support loading and particle size. In order to study carbon corrosion in PEMFC, ASTs involving lower potential limits ranging from 0.6 V to 1.0 V and an upper potential limit from 1.2 V to 1.55 V are generally chosen to mimic real-time operating conditions in automotive applications [24, 90, 91]. To study commercial catalysts and their supports for PEMFC, in addition to comprehensive experimental methods, empirical and numerical models are required to understand carbon oxidation and its reaction mechanism.

Meyers et al developed mathematical models for corrosion of carbon supports in PEMFC [92, 93]. The models describe how hydrogen cross-over can induce both oxygen evolution and carbon corrosion on the cathode of the fuel cell under fuel-starved conditions. Franco and Gerard proposed a mechanistic model describing the coupling between PEMFC MEA electrocatalysis of ORR and cathode carbon support corrosion [94]. Numerical simulations indicated that when the anode chamber was partially exposed to oxygen induced by PEM

cross-over or fuel starvation, cathode thickness and cell potential decreased. Their model-predicted carbon corrosion is favoured both platinum coarsening and investigated carbon oxidation reaction and electrocatalytic mechanisms. Gallaghar and Fuller proposed a model based on an electrochemical mechanism to predict carbon weight loss and surface oxide growth as a function of time, temperature and potential [44, 95]. It should be noted that the decay in current at the cathode can arise not only from carbon loss but also from passivation of the surface. Three mechanisms were found to contribute to current decay that is commonly observed during electrochemical oxidation: mass loss, reversible formation of a passive carbon oxide on the surface and irreversible formation of another carbon oxide. Comparison of model predictions with experimental data indicated that the current decay occurring when the cathode potential was held constant at 1.2, 1.3 and 1.4 V_{SHE} could be attributed to the formation of the reversible passive oxide. On the other hand, when the potential was cycled, the irreversible loss of the oxide intermediate that catalyzes CO_2 formation in favour of quinones was found to be the most significant cause of current decay.

Most available models either completely neglect the complex behavior observed or use empirical equations correlated with mass loss of the electrode [96]. An empirical approach is poor at predicting mass loss and surface oxide concentrations under oxidation conditions. The physicochemical model proposed by Gallagher and Fuller includes several complex intermediate steps and so may be difficult to implement for online monitoring and analysis of carbon corrosion ASTs in practical situations [95]. A simpler model capable of tracking the oxidation of the carbon during potential cycling would be preferable to accurately predict the lifespan of the fuel cell stack.

2.3.3 Pt Dissolution in PEMFCs

Pt dissolution can be studied by potential cycling of the membrane electrode assembly, which mimics conditions when power or current is extracted from the fuel cell. A change in

the power that must be delivered to a vehicle driven by a fuel cell stack occurs when a driver applies the brakes during deceleration. Since the ramp-down of the stack power occurs more slowly than that required by the vehicle system, excess power is generated by the fuel cell stack. This surplus energy can directly affect the catalyst layer in the MEA. Similarly, sudden load acceleration from an idle state can affect the cell performance. These situations of load removal and acceleration are examples of potential cycling to which a fuel stack is subjected during normal operation of a vehicle.

2.3.3.1 Effect of Temperature on Pt Dissolution

The U.S. Department of Energy (DOE) lifetime targets for PEMFCs are 5,000 h for automotive and 40,000 h for stationary applications [97]. High durability and activity of electro-catalysts are required to meet these lifetime targets. Challenges associated with catalyst durability remain in order to make fuel cells competitive with conventional internal combustion engines and power sources. Over the last ten years, more attention has been placed on developing catalyst durability protocols to evaluate MEAs in order to design and optimize catalyst layers to meet automotive sector requirements [98]. The loss of material such as the cathode catalyst layer results in morphological and physicochemical changes during ASTs. The state-of-the-art electrocatalyst layers in PEMFCs consist of nano-sized platinum particles dispersed over carbon-based supports. Problems that affect PEMFC durability are platinum dissolution and carbon corrosion in the catalyst layer. In order to reduce PEMFC costs, catalyst (Pt/C) loading levels have been reduced by more than 50-fold in the last few decades [20, 97]. Other catalyst alternatives are still not at a mature stage of development and cannot match the activities and stabilities possible with Pt-based catalysts. During life testing of MEAs, sintering of Pt particles, dissolution of platinum and corrosion of the carbon support affect Pt/C catalyst stability [52]. Growth of Pt particles and dissolution of Pt into the membrane phase that lowers the ECSA are major causes of cathode catalyst layer degradation [70]. Thus, analysis of these Pt dissolution mechanisms

and cathode catalyst layer degradation is important for further improvement in catalyst design.

ASTs such as repeated cycling of the cell voltage between 0.87 V − 1.2 V using a square-wave waveform in which the voltage is held for 30 s at each potential have been used as tools to measure the stability of the catalysts [42]. Under such AST conditions, Pt can undergo morphological changes due to both chemical and electrochemical reactions that bring about Pt migration, particle aggregation and dissolution especially at the cathode [60]. Factors such as elevated temperature influence these processes and accelerate electrode degradation [99]. Other mechanisms such as ionomer/membrane degradation and carbon corrosion are also responsible for the degradation of the MEA [42]. The effects of the upper and lower voltages, voltage waveform (square-wave, triangular wave or sinusoidal) and flow rate of input gases during potential cycling on catalyst degradation have been studied [100, 101]. Catalyst particle growth and platinum transfer into the membrane have been shown to depend on temperature, sweep potential and duration of the AST [60, 98]. Platinum dissolution during operation of fuel cell stacks is considered to occur either when the load or voltage is varying or when it is at a constant high value typical of stack "idling" conditions [85]. Subjecting MEAs to fuel cell power train drive cycles can simulate both of these conditions. The extent of dissolution is governed by a complex interplay between electrochemical dissolution of metallic platinum, formation of platinum oxide and chemical dissolution of the oxide. Pt dissolution in acid media is found to strongly increase with electrode potential in the region of 0.85 – 0.95 V_{RHE} [49]. Other input waveforms during ASTs such as square-wave cycles of the cell voltage between 1.2 V and 0.1 V [4] and slow triangular sweeps and square waves [100] have been found to degrade Pt catalysts and accelerate their dissolution rate. The dissolution rate has also been found to increase as the upper potential limit is raised from 0.8 V to 1.0 V during potential cycling of the cell. However, with further increase in the upper potential from 1.0 V to 1.2 V, carbon corrosion in addition to Pt dissolution [52] is observed. The lower potential limit also affects catalyst degradation. A decrease in the lower potential limit from 0.6 V to 0.4

V leads to Pt re-deposition and reduction of Pt oxides [102]. Thus, application of cell voltages in the range of 0.6 – 1.0 V should be appropriate for assessing Pt dissolution from catalyst layer. As would be expected, Pt dissolution has also been shown to depend strongly on temperature [103].

The arrangement and distribution of Pt within the catalyst layer are important factors for achieving high MEA performance and durability. Usually, this arrangement depends on the size of the Pt particles and their location on the support surface [104]. An important measure of the accessibility of the inlet gases to the catalyst is the electrochemical surface area (ECSA) that gives the total area of Pt available for electrochemical reactions and the unit of ECSA is $m^2\ g^{-1}$. It is determined from the area under the H_2 desorption peak appearing in cyclic voltammograms (CV) obtained while H_2 is being fed on the anode side and N_2 on the cathode side [104]. However, among this amount of Pt, only the portion connected to the ionomer and support can serve as active reaction sites for fuel cell electrochemical reactions. The dispersion of the catalyst, ionomer and carbon in the catalyst layer may not be uniform; thus, a quantitative comparison of the hydrogen desorption regions of repeated CV spectra for Pt surface area based on loading may not be accurate. The coulombic charge for hydrogen desorption also known as Q_H is generally used to calculate the active platinum surface of the electrodes. The value of ECSA is determined from the following expression:

$$\mathrm{ECSA} = \frac{Q_H}{[\mathrm{Pt}] * 0.21} \qquad (2\text{-}9)$$

where [Pt] represents the platinum loading ($mg\ cm^{-2}$) on the electrode, Q_H the charge for hydrogen desorption ($mC\ cm^{-2}$) and the charge required to oxidize a monolayer of H_2 in the Pt surface corresponds to 0.21 $mC\ cm^{-2}$ It should be noted that all of the platinum loaded on the electrode is used in this expression and so is considered to be electrochemically active. However, this assumption is valid only over a particular range of platinum loading. In situations where the loading exceeds this range, it is likely that the

access of some Pt particles to the carbon substrate and/or the electrolyte is blocked. This leads to an underestimation of the true ECSA. On the other hand, if the loading is too low, the Pt catalyst particles do not uniformly cover the electrode geometric area and the ECSA tends to be overestimated. In addition, the standard deviation associated with measurement of the ECSA depends on its derivative, which can be obtained by differentiating both sides of Eq. (2-9) with respect to [Pt] to yield:

$$\Delta ECSA = \frac{Q_H}{[Pt]*0.21} + \frac{\Delta[Pt]\,Q_H}{[Pt]^2*0.21} \qquad (2\text{-}10)$$

where ΔECSA is the error or uncertainty in the value of ECSA estimated using Eq. (2-9) due to an error or uncertainty Δ[Pt] in the measured Pt loading level in the MEA. Due to the inverse dependence of the second term on $[Pt]^2$, the error associated with estimating ECSA this way can become unacceptably large when the Pt loading is very low. For these reasons, good control of the Pt/C wt% in the CL is very important to avoid systematic errors in determining the ECSA. In addition, the experimental conditions used during the CV analysis such as the scan rate are important factors.

The surface area of the Pt atoms connected with the ionomer and support is known as effective platinum surface area (EPSA) and is smaller than the ECSA. The ratio between EPSA and ECSA is termed the catalyst utilization U_{Pt}. A decrease in the EPSA and catalyst utilization tends to increase the overpotential required to drive the electrochemical reactions in a PEM fuel cell, especially the ORR. A study of the correlation between the EPSA and overpotential is required to improve the catalyst design and durability.

2.3.3.2 Effect of RH on Pt Dissolution

Cycling of the voltage of a fuel cell can adversely affect the MEA as follows: i) increase of the cathode overpotential which lowers the overall cell voltage delivered to the external load and ii) acceleration of Pt dissolution in the catalyst layer and re-deposition of Pt by electrochemical or chemical reduction elsewhere in the catalyst layer or membrane. Wang

et al. reported a rise in the amount of Pt that had dissolved when the cathode potential was increased up to 1.1 V_{SHE} during potential cycling [86]. A detailed discussion of catalyst failure due to Pt dissolution and its mechanism during potential cycling is provided by Borup et al. [52, 64]. Other factors such as higher temperature, lower RH, high upper potential limit and fuel cross-over significantly affect the MEA. Operation of a PEMFC without external humidification (i.e., 0% RH) of the reactant gases is very desirable since this would eliminate the gas humidification system and decrease the complexity of the system integration [105]. However, external humidification is standard practice since MEAs deliver better performance when the fuel and oxidant are completely saturated due to higher proton conductivity. Proton conduction depends strongly on the water content and decreases considerably when the RH is varied [46, 106], leading to large resistive losses and poorer cell performance. Proton transport at the interface between ionomer and Pt catalyst interface in particular is severely restricted at low RH. When a fuel cell is operated at low RH, ORR kinetics is also affected due to dehydration of the ionomer surface. Uribe et al. reported that lower RH restricts ORR kinetics and performance of the cell. An increase of 40 mV in the overpotential was observed by Xu et al when the RH was reduced to 40 % from 100 % [89].

The ionomer network model proposed by Hsu and Gierke suggests that ionomer clusters are interconnected by a network of short and narrow channels and consist of both hydrophilic domains involving the sulfonic acid moiety and hydrophobic domains [107, 108]. According to this model, these clusters shrink and become less interconnected leading to slower proton transport when the Rs decreases. However, further insight into the impact of low RH operation during potential cycling on the MEA is needed. ASTs involving potential cycling under different RH conditions are useful tools to investigate the failure modes in fuel cell electrodes and improve MEA design. In fact, the significant effect of humidity on the catalyst layer and membrane/catalyst layer interface has been demonstrated in several studies on the basis of ASTs in which the potential was cycled between 0.6 V and 1.0 V with 3 s dwell times at each limit [52, 64, 109-111].

Pt dissolution from the catalyst layer under saturated conditions can occur by the oxidation to PtO, which subsequently dissolves as follows:

$$Pt + H_2O \rightarrow PtO + 2H^+ + 2e^- \quad (2\text{-}11)$$

$$PtO + 2H^+ \rightarrow Pt^{2+} + H_2O \quad (2\text{-}12)$$

Formation of an oxide layer on the Pt surface that causes the Pt surface at the cathode to disintegrate has been reported at cathode potentials above 1.2 V_{SHE} [112]. Potential cycling is also known to promote the formation of Pt oxides. Similarly, increased sorption of water in the membrane should increase the diffusivity of Pt ions and consequently increase the rate of mass loss of Pt from the cathode into the membrane [64]. At higher RH, Pt dissolution is likely to occur by reactions (2-11) and (2-12). However, when the cell operates at low RH or 0% RH conditions, Pt dissolution is expected to occur through a different pathway. In such cases, platinum oxidation is initiated by reaction with gaseous O_2 followed by a series of electrochemical reactions given below:

$$Pt + O_2 \rightarrow PtO_2 \quad (2\text{-}13)$$

$$PtO_2 + H^+ + e^- \rightarrow Pt\text{-}HO_2 \quad (2\text{-}14)$$

$$Pt\text{-}HO_2 + Pt \rightarrow Pt\text{-}OH + PtO \quad (2\text{-}15)$$

$$Pt - OH \rightarrow PtO + H^+ + e^- \quad (2\text{-}16)$$

2.4 Characterization Techniques

2.4.1 Fuel Cell Performance Curve

A plot of the cell potential versus current density obtained for a given set of operating conditions is known as a polarization curve (Figure 2-8) [113]. It can be converted to a plot of power density versus current density by multiplying the potential by the current density at each point of the curve. A steady-state polarization curve is obtained by measuring the current at each applied cell potential or the cell potential at each applied current density over time until it levels off to a constant value. A non-steady-state polarization curve can be obtained by measuring the potential (or current) as the current (or potential) is varied with time at a fixed rate. Polarization curves provide information regarding the effects of operating conditions such as composition, flow rate, temperature and RH of the reactant gases on cell performance. However, this technique cannot provide information on the performance of the individual components within the cell. Importantly, it is difficult to determine whether one degradation mechanism is more important than another on the basis of a polarization curve. The polarization curve for a hydrogen/air fuel cell exhibits three major regions, as shown in Figure 2-8. The plot and Table 2-3 indicate these regions and the associated causes of performance loss during cell operation.

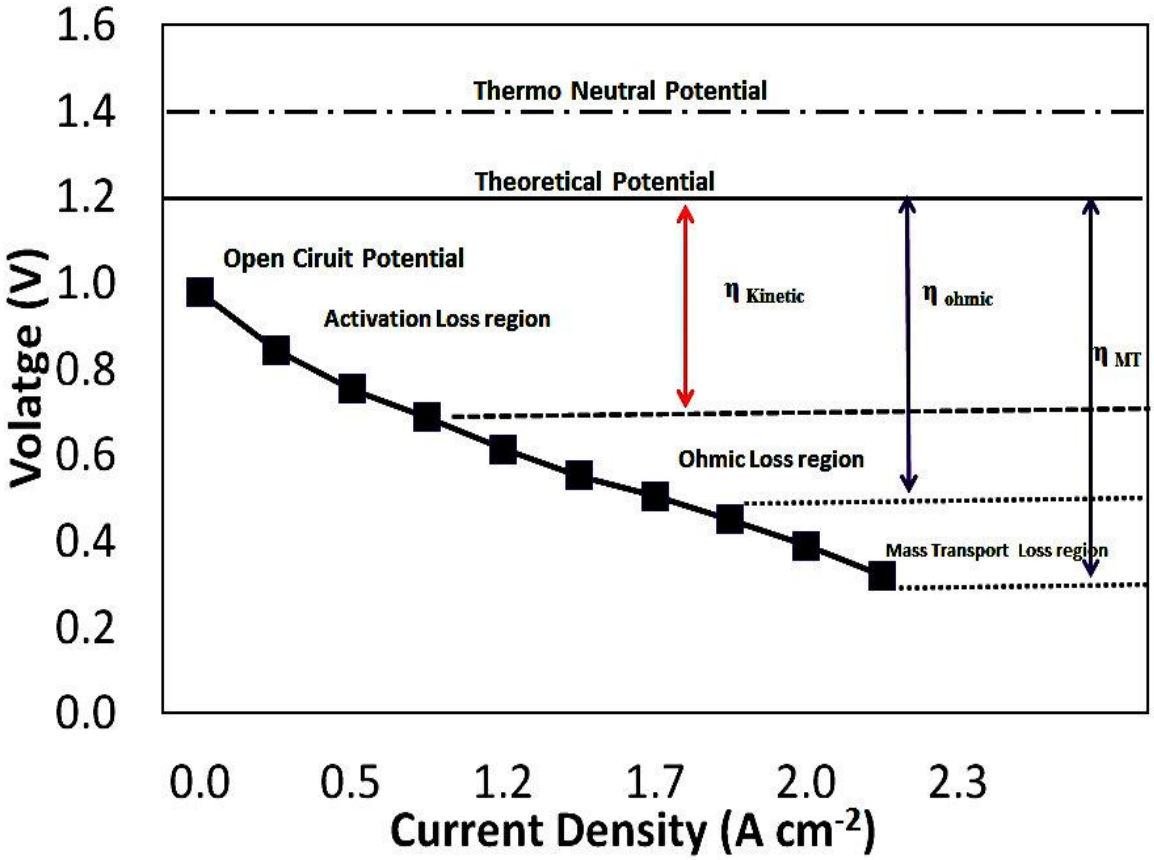

Figure 2-8: Voltage losses on a typical polarization curve of an operating fuel cell during test station qualification experiment. Polarization curve is obtained for a commercial confidential MEA using a Hydrogenics test station at Waterloo. Test conditions are given in Table 3-2.

Table 2-3: Major regions of fuel cell performance curve.

Region	Observation	Reason
Low current density	Sharp cell potential drop	Kinetic limitations of oxygen reduction reaction [114]
Intermediate current density	Voltage loss caused by ohmic resistance Linear decrease of cell potential with current density Constant activation overpotential	Resistance to flow of ions in the electrolyte and resistance to flow of electrons through electrode [115]
High current density	Drastic drop in cell performance	Limited mass transport of reactant gas through pore structure of gas diffusion and catalyst layers [116]

2.4.2 Current Interruption Method

The current interruption method is used to measure the ohmic losses in a PEM fuel cell. This method is based on the observation that ohmic effects respond quickly to variations in current, while the electrode potentials change more slowly. A current interruption experiment is conducted by recording the voltage transient upon interruption and turning off of the current after the fuel cell has been operating at a constant current (Figure 2-9).After a given interval, the current is restored. The response of the cell to this change in current can be analyzed in terms of the equivalent circuit for a fuel cell. The simplest equivalent that can be used for this purpose consists of two resistors and a capacitor. The first resistor R_r accounts for the ohmic losses, the second resistor R_a represents activation losses and the capacitor C_1 represents the double-layer capacitance [117]. When the current is interrupted, no current flows through the first resistor in the fuel cell circuit. This causes the voltage to increase sharply at first, but then to increase more slowly as the capacitor discharges. The system reaches the OCV once the capacitor is completely discharged [119]. This technique can provide information on parameters such as the exchange current density, Tafel slope, oxygen solubility and double-layer capacitance [119]. One

disadvantage of this technique is that it is limited to measurement of ohmic resistances larger than 5 mΩ, although typical commercial membranes such as NE 117 and NE 112 have ohmic resistances between 2 - 5 mΩ depending on the operating conditions. Furthermore, at room temperature in dehydrated conditions, membranes can exhibit resistances of 0.1 $\Omega\,cm^2$ or less [119]. Another disadvantage with this method is the difficulty in determining the exact point at which the voltage jumps sharply; thus a fast oscilloscope should be used to record the voltage changes.

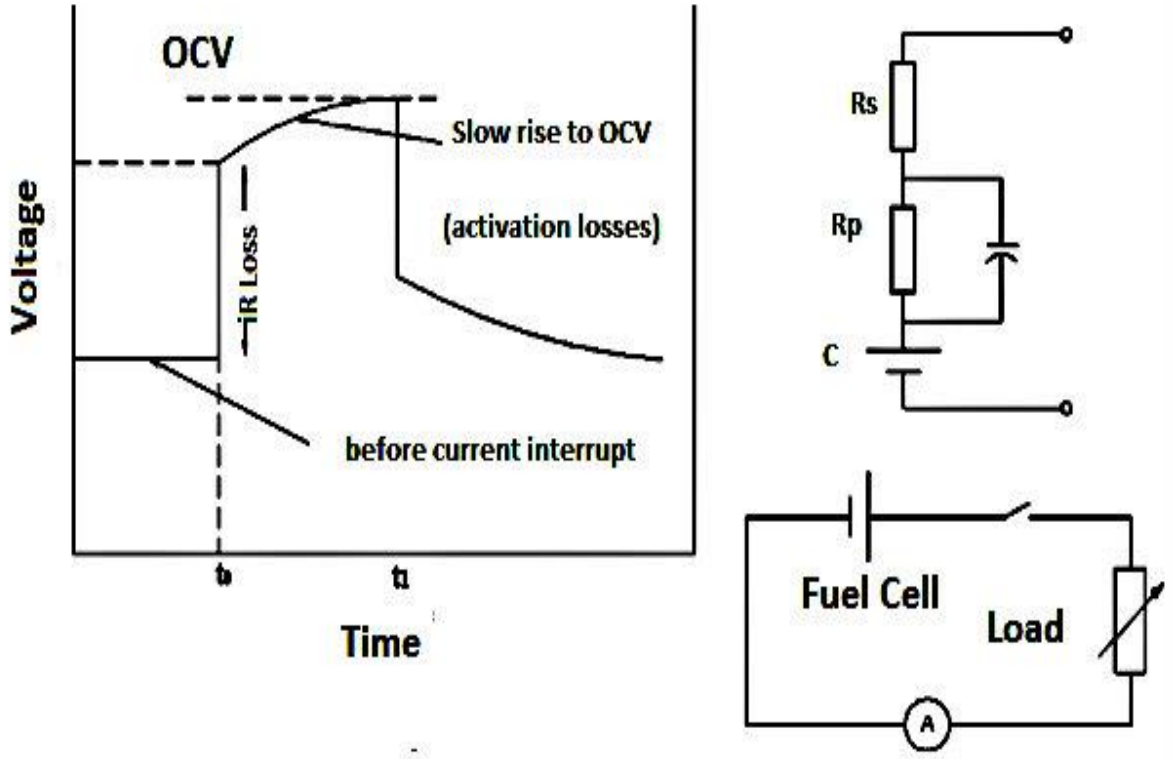

Figure 2-9: Ideal voltage transient in a PEM fuel cell after current interruption and equivalent circuit for a fuel cell [113, 117, 118].

2.4.3 Cyclic Voltammetry

To measure changes in the ECSA during ASTs, cyclic voltammetry analysis is carried out. The experiments are generally done in two-electrode systems by shunting the counter electrode (fuel cell anode in this study) to the reference electrode. Thus, the measured electrode potential of the working electrode (cathode in this study) becomes equivalent to the cell potential. The cell potential is swept back and forth at a fixed rate between upper and lower limits and the resulting current is measured. H_2 and N_2 are fed to the anode and cathode sides, respectively. N_2 rather than air or O_2 is used to prevent any further degradation of the catalyst or cathode CL during measurement of the ECSA since the purpose of the CV is to monitor the state of the MEA without altering it. A relatively slow sweep rate of 10 mV s^{-1} is selected in order to minimize the impedance losses in the porous electrodes. Figure 2-10 shows a schematic of the fuel cell system used to conduct electrochemical experiments on a fuel cell [120, 121]. Figure 2-11 shows a typical CV obtained on a Pt/C working electrode. It should be noted that the x-axis corresponds to the electrode potential of the working electrode. The various regions and current peaks typically observed in these CVs and the processes or reactions associated with them are listed in Table 2-4. The area under the H desorption peaks (three of which are distinct for Pt-black electrodes and two of which are well resolved in the case of Pt/C electrodes) gives a quantitative measure of the area associated with the electrochemically available Pt sites and is a common way of characterizing the ORR activity of Pt catalysts.

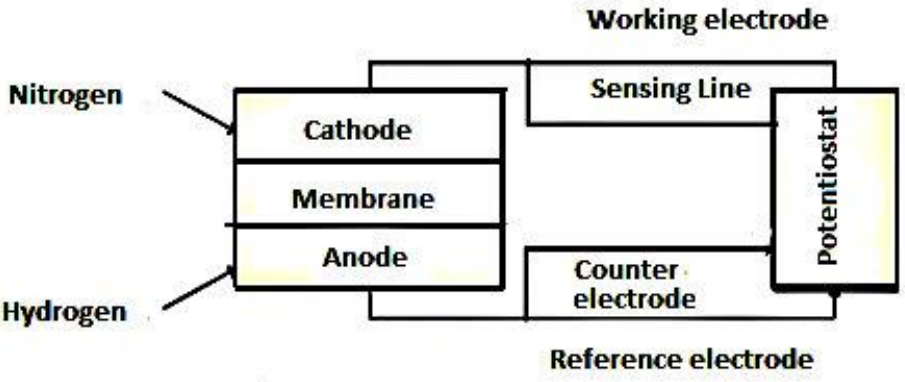

Figure 2-10: Schematic of electrochemical measurements on a fuel cell using a 3-electrode set-up.

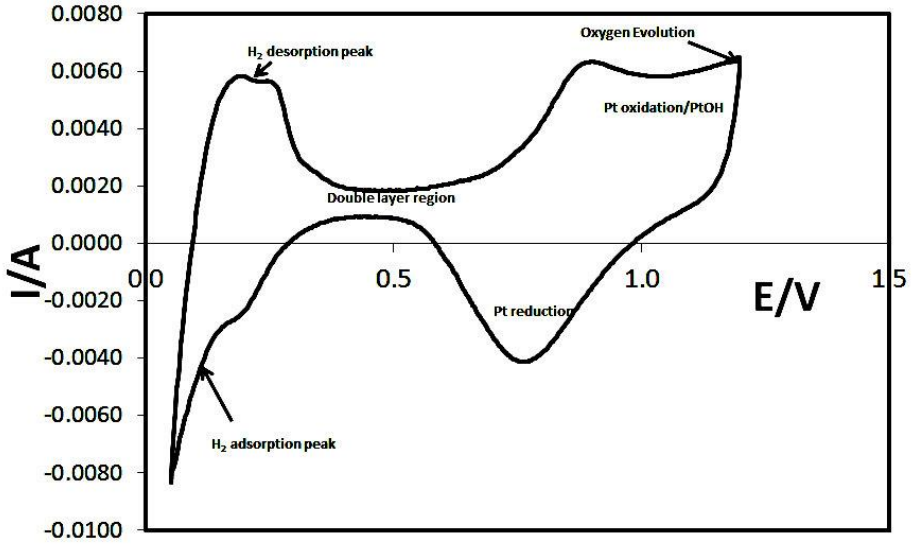

Figure 2-11: Typical cyclic voltammogram obtained for a Pt/C working electrode during test station qualification experiment. CV is obtained for a commercial confidential MEA using a Hydrogenics test station and Solartron Instrument at Waterloo. Test conditions are given in Table 3-2.

Table 2-4: Characteristic peak potentials observed during CV on Pt electrode [127, 128].

Potential (V)	Sweep	Process at Working Electrode	Remarks	No.of Distinct Peaks
0 – 0.4	Anodic	H_2 desorption	The H_2 electrodesorption on Pt (111) and Pt(100) crystal surfaces can be expressed as Pt-H_{ads} $\rightarrow$Pt + H^- +e^- . The ECSA (m^2/g Pt) can be calculated from this peak area .	3
~ 0.4–0.8	Anodic	Double-layer region	Meal surface is free from adsorbed species	
> 0.8	Anodic	Onset of O_2 chemisorption	Oxidation of the Pt surface can be written as Pt + H – O – H$\rightarrow$ Pt – O – H + H^+ + e^- Pt– O – H + H – O – H $\rightarrow$ Pt – $(O – H)_2$ + H^+ + e^- Pt – $(O – H)_2$ $\rightarrow$ Pt – O + H – O – H	–
~ 1.1	Anodic	Formation of platinum hydroxide (PtOH) monolayer	Pt + OH^- $\rightarrow$ PtOH + e^-	–
> 1.1	Anodic	Formation of PtO_x	PtOH+OH $\rightarrow$ PtO+H_2O+e^-	–
~ 1.5	Anodic	O_2 evolution	$2H_2O$ $\rightarrow$ $4H^+$ + O_2 + $4e^-$	1
~ 0.75	Cathodic	PtO_x reduction	Negative shift in potential relative to that of PtO_x formation; irreversible. the reduction of Pt oxide, which can be expressed Pt – O + $2H^+$ + $2e^-$ $\rightarrow$ Pt + H – O – H	1
0 – 0.4	Cathodic	H adsorption	H adsorption on different Pt crystal faces	2
~0	Cathodic	H_2 evolution	The H_2 electroadsorption can be expressed as Pt + H^- +$e^-$$\rightarrow$ Pt-H_{ads}	1

The ECSA (m^2/g Pt) can be calculated according to the equation 2.9. In order to distinguish ECSA from EPSA, equation 2.9 is re-written in the following form.

$$\mathrm{ECSA} = \frac{\mathrm{Q_H}}{\mathrm{L_{pt}} * \mathrm{Q_f}} \tag{2-17}$$

where Q_H is the Coulombic charge with a unit of mC, and the value is usually calculated as the average value between the amounts of charge exchanged during the electroadsorption (Q') and electrodesorption (Q'') of H_2 on Pt sites; L_{Pt} is the Pt loading on the studied electrode, with a unit of g; Q_f is the required Coulombic charge to desorb the hydrogen when a clean Pt surface is covered by a monolayer of hydrogen, and its value is 0.21 mC/cm^2. CV is genrally used for the *in situ* diagnosis of the catalyst layer. Because the catalyst layer is a matrix structure, rather than a smooth electrode surface, not all of the catalyst surface is accessible to the reaction. However, CV is also a useful tool for measurement of the active catalyst area such as the electrochemical Pt surface area (EPSA) which is the active Pt surface area per unit electrode area, cm^2/cm^2). The EPSA can be calculated using the equation below:

$$\mathrm{EPSA} = \frac{\mathrm{Q_H}}{\mathrm{A} * \mathrm{Q_f}} \tag{2-18}$$

where Q_H is the coulombic charge (mC), A is the active electrode area (cm^2) and Q_f has a value of 0.21 mC/cm^2. Pt utilization can be defined as

$$\mathrm{U_{Pt}}\,(\%) = \frac{\mathrm{EPSA}\,(\mathrm{cm^2_{Pt}/cm^2})}{\mathrm{ECSA}\,(\mathrm{cm^2_{Pt}/g_{Pt}})} * L_{pt}(\mathrm{g_{Pt}}/cm^2) \tag{2-19}$$

2.4.4 Linear Sweep Voltammetry

Linear sweep voltammetry (LSV) is similar to cyclic voltammetry in that the potential is varied linearly with time, but it differs in that the scan proceeds in one direction only. LSV has been used to determine the H_2 and O_2 cross-over currents and to identify any short-circuiting in the fuel cell [117]. A plot of a LSV for an MEA in its BOL state is shown in Figure 2-12. Due to the low but finite solubility and diffusivity of H_2 in the membrane, H_2 permeates from the anode compartment of a PEM fuel cell and leaks into the cathode where it can be oxidized electrochemically at the typical cathode potentials (0.5-1.0 V RHE depending on the current density). The resulting parasitic H_2 oxidation robs some of the current that would otherwise be used for O_2 reduction and lowers the net current in an operating fuel cell. This current density is generally referred to as H_2-cross-over current density and can be determined experimentally by polarizing the N_2-purged cathode compartment to 0.4 V above the potential of the H_2-purged anode compartment (this degree of polarization ensures that the resulting H_2 oxidation current density is limited by the H_2 permeation rate). The H_2-cross-over current density rises with increasing H_2 partial pressure and increasing cell temperature. The measured cross-over current can be related to the hydrogen permeability through the membrane. The cross-over of both H_2 and O_2 to the opposite sides lowers the open-circuit of the cell and also affects the cell voltage below 100 mA cm^{-2} [66]. Since oxygen is generally the less permeable of the two, attention is usually focused on hydrogen cross-over.

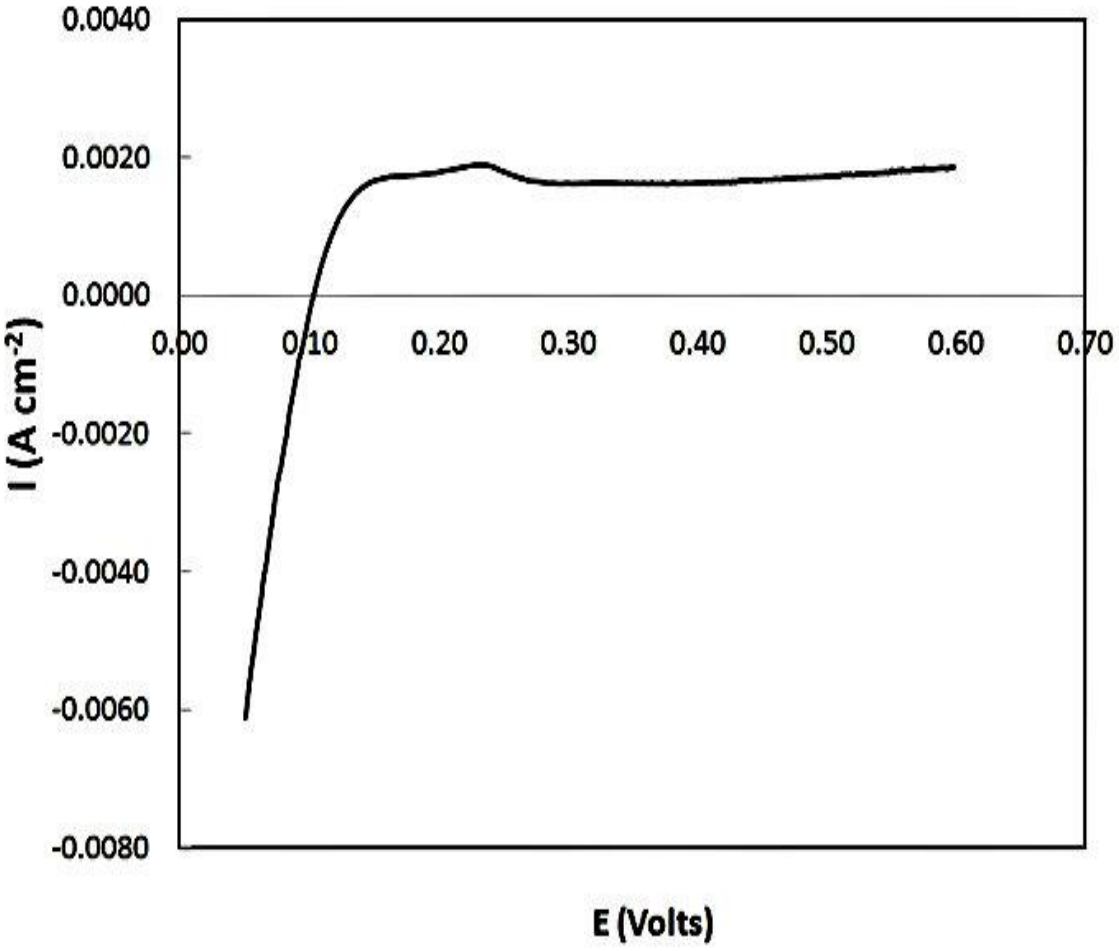

Figure 2-12: Typical LSV obtained for an MEA in its BOL state during test station qualification experiment. LSV is obtained for a commercial confidential MEA using a Hydrogenics test station and Solartron Instrument at Waterloo. Test conditions are given in Table 3-4.

2.4.5 Electrochemical Impedance Spectroscopy (EIS)

EIS can be used to study the cathode behavior during operation to diagnose such phenomena as catalyst layer degradation, cell flooding and drying and determine the electrolyte resistance and double-layer capacitance. EIS is a useful tool to investigate the mass transport behavior of the cathode. Unlike linear sweep and potential step methods where the system is perturbed far from equilibrium, a small-amplitude AC potential or current is applied during EIS so that the system is only slightly perturbed from a stationary condition [122]. The electrode response can be described in terms of an equivalent electric circuit analog made up of elements such as resistors, capacitors and inductors. Complex resistance phenomena occur while AC current flows through a circuit. The resultant amplitude and phase of the electrode response are measured as a function of the frequency of the AC input and typically presented in the form of Bode and Nyquist plots. Figure 2-13 depicts a typical Nyquist spectrum obtained during testing of an MEA in its BOL state while H_2 and air are being fed to the anode and cathode, respectively.

Figure 2-14 shows an impedance spectrum obtained during MEA analysis while H_2 and N_2 are being introduced at the anode and cathode. de Levie reported that impedance measurements obtained while N_2 is fed to the cathode rather than air or O_2 are useful for assessing changes to properties such as porosity [122].

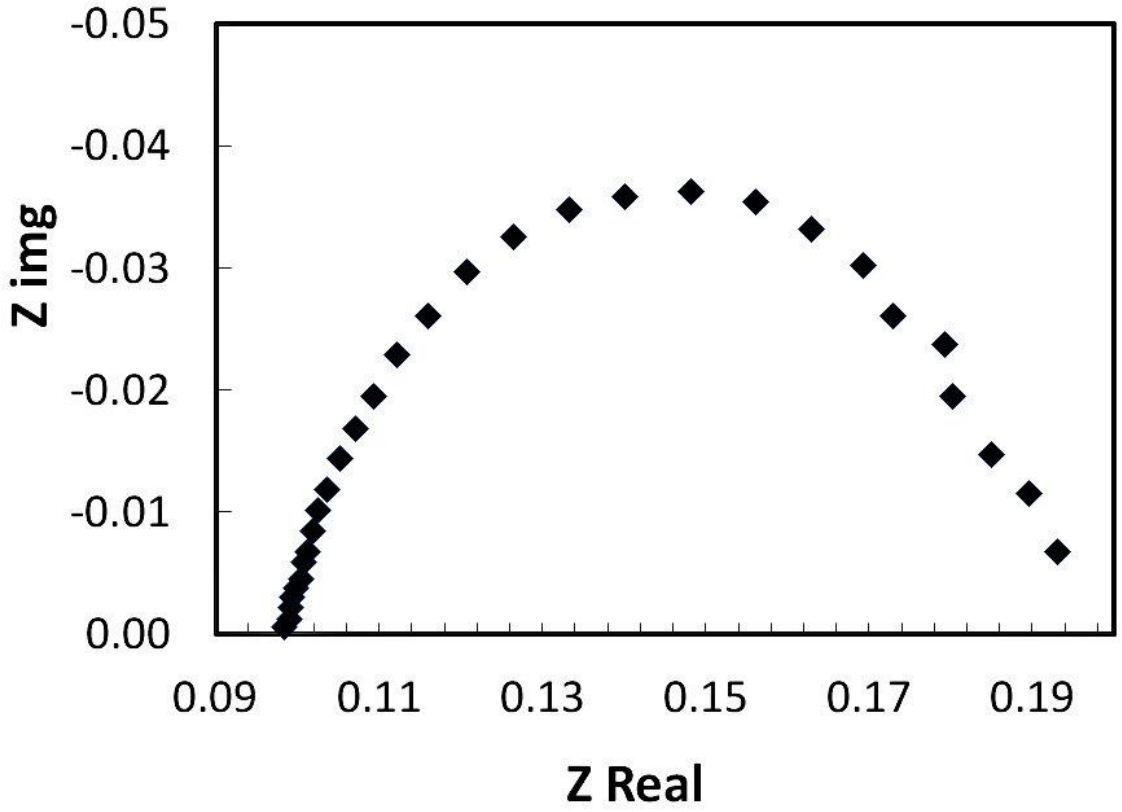

Figure 2-13: Typical Nyquist spectrum obtained for an MEA in its BOL state while H_2 and air are introduced at the anode and cathode, respectively during test station qualification experiment. EIS is obtained for a commercial confidential MEA using a Hydrogenics test station and Solartron Instrument at Waterloo. Test conditions are given in Table 3-2.

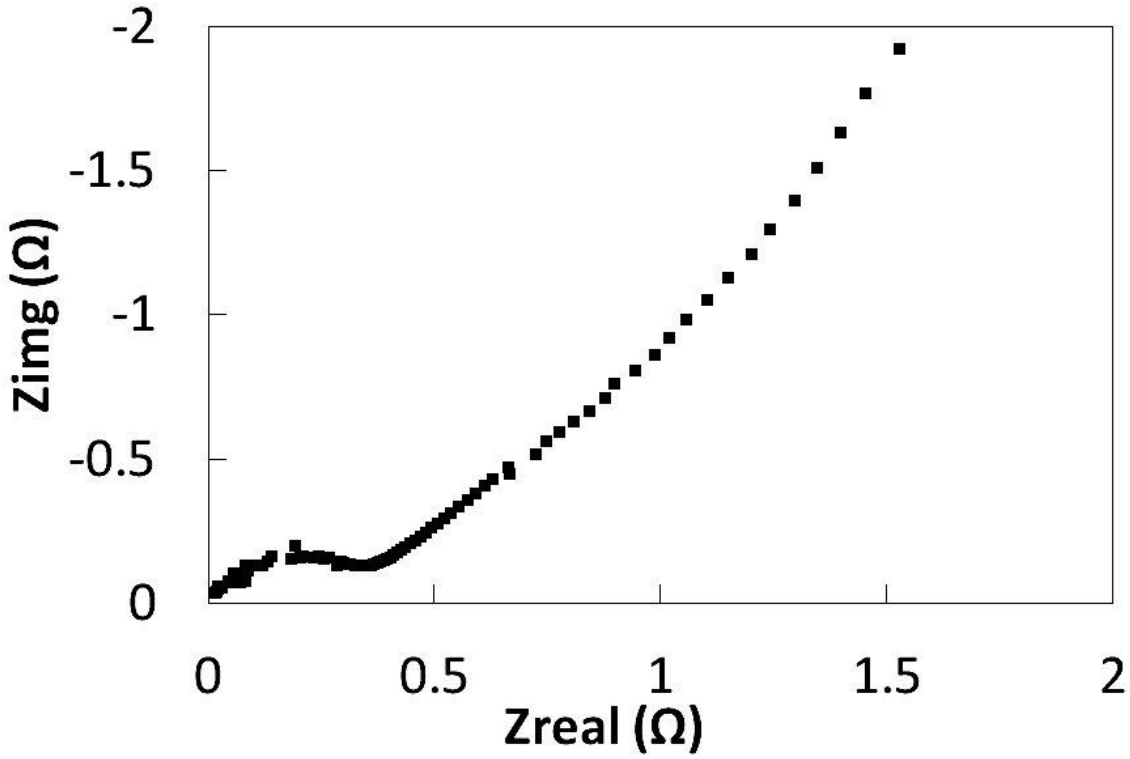

Figure 2-14: Typical Nyquist spectrum obtained for an MEA in its BOL state while H_2 and N_2 are introduced at the anode and cathode, respectively during test station qualification experiment. EIS is obtained for a commercial confidential MEA using a Hydrogenics test station and Solartron Instrument at Waterloo. Test conditions are given in Table 3-4.

The electrode response during EIS measurements is affected by pore size and shape [124, 125]. de Levie simulated the frequency response in a cylindrical single pore using a transmission line model (TLM) based on the assumptions that the electrode pores are purely capacitive, and are completely filled with electrolyte. Keiser et al. extended the TLM presented by de Levie to noncylindrical pores by making use of a recursion method [124, 125]. Figure 2-15 shows impedance spectra for various pore shapes calculated with this method. This model can be used to infer pore size shape from experimental impedance data.

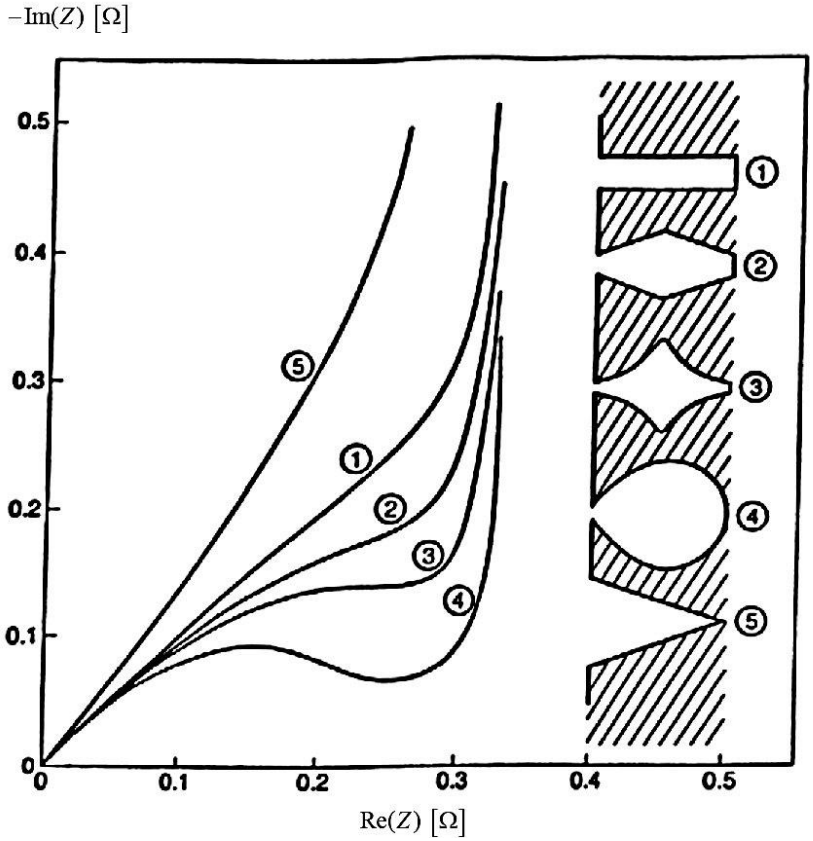

Figure 2-15: Porosity changes in the MEA [123].

2.5 Summary

A literature survey of the background studies on PEMFC durability has been provided to help to identify the areas where further work is warranted to improve the understanding of fuel cell catalyst failure mechanisms. These topics are:

1. An empirical correlation between the voltage loss and the amount of CO_2 produced during operation can be useful for estimating the performance loss at a particular current density during carbon corrosion in fuel cells. A limited number of models correlating the carbon loss to the performance loss during ASTs are available. Moreover, to the best of our knowledge, no model that predicts the contribution of

Pt dissolution alone to MEA performance loss during carbon corrosion ASTs has been reported.

2. A carbon corrosion model of Gallagher and Fuller [95] considered three major sources of current decay when various potentiostatic inputs are applied to the cathode of a MEA catalyst layer. They are the irreversible adsorption of water onto Pt reaction sites, reversible formation of a passivating carbon oxide and the irreversible formation of another surface oxide. This model provides considerable insight into the carbon corrosion processes occurring during ASTs, but is quite complex and involves a large number of reaction steps. It would be desirable to simplify the model of Gallagher and Fuller to make it easier to interpret AST data and develop strategies to mitigate catalyst layer degradation. A sensitivity analysis of the contributions of the various reaction steps to the measured electrode responses can be employed to determine whether simplification of this model can be safely made. In theory, fuel cell performance loss due to carbon corrosion should be correlated to the amount of carbon loss. However, the model of Gallagher and Fuller is unable to predict the performance loss from measurement of the carbon loss. Thus, in order to more closely link the data collected from ASTs to fuel cell performance loss and gain a better understanding of the contributions of the different modes of carbon corrosion to performance loss, it would be very useful to incorporate a correlation between performance loss and carbon loss into the Gallagher and Fuller model (or some simplified version). This would bring improvements to the diagnosis of the causes of performance loss during normal fuel cell operation, design of Pt/C catalysts and the strategies to extend the useful lifetimes of MEAs.

3. Testing protocols and characterization methods for MEA degradation and AST protocols to study catalyst layer degradation that focus primarily on Pt dissolution are not well established. No detailed study has been conducted to examine the role of Pt dissolution on catalyst degradation at different temperatures. Identification of the relationship between EPSA loss and performance loss may shed further light on

the effect of Pt dissolution. Such a study will contribute to the fundamental understanding of Pt dissolution in relation to cathode catalyst layer structure, degradation conditions and operating temperature.

4. Pt dissolution should be enhanced when considerable amounts of water are present in the MEA. Thus, one would expect voltage degradation due to Pt dissolution to be reduced when the RH is maintained at low levels. Unfortunately, such a positive effect is countered by the fact that most membranes must contain sufficient moisture in order to function properly. Thus, a need exists to investigate the effect of RH on Pt dissolution, fuel cell performance and CL structure. However, relatively little data are available on the effect of RH on Pt dissolution and the resulting catalyst reliability. Membrane failure becomes compromised when 'pin-holes' form and the structural integrity is affected, especially during Pt dissolution ASTs. Thus, it would be very useful to investigate the effect of RH on Pt dissolution and fuel cell performance.

2.6 Objectives of the thesis

The overall experimental objectives of the proposed research are as follows:

2.6.1 Development of catalyst layer analysis

Novel accelerated testing techniques are to be developed to estimate the degree of CL degradation, specifically the cell performance loss as a function of time in service. The primary objective of the testing program is to use a mathematical model to investigate the mechanism of the corrosion of carbon supports in the cathode catalyst layer and validate it with experimental results obtained by the application of different carbon corrosion ASTs. Various characterization techniques are employed to evaluate the magnitude of catalyst degradation in the MEA. The novel aspects of this research include the development of (a) carbon corrosion and Pt dissolution diagnostic indicators or 'fingerprints' to predict the performance loss and failure mechanisms in carbon corrosion ASTs, (b) a carbon corrosion kinetic model to predict the performance loss in PEMFC for automotive applications.

2.6.2 Impacts of voltage windows on Pt catalyst failure

The voltage range over which, the cathode catalyst is exposed influences Pt degradation rates. The impact of the different voltage range during ASTs on Pt dissolution at various temperatures and relative humidities is not well known. An important aim of this part of the research is to obtain data with which the kinetic loss contribution during ASTs can be estimated at different cell temperatures. ASTs involving various voltage cycles are applied to each MEA design and the change of catalyst layer properties such as EPSA and platinum utilization are determined over time relative to baseline levels obtained for a stable MEA. The novel aspects of this part of the research are the development of a new Pt dissolution AST protocol and a mathematical model to analyze catalyst layer degradation. Development of ASTs and diagnostic indicators or 'fingerprint' models for degradation of commercial MEAs are two important objectives of this study. ASTs in which Pt dissolution and/or carbon corrosion predominates were applied to study catalyst degradation and failure in commercial membranes.

Chapter 3
Materials and Methods

Experimental aspects of catalyst layer degradation of PEM fuel cell is discussed in this chapter. Fuel cell hardware and one of the test station used in the study is shown in Section 3.1. Detail description of experimental methodologies on

i. MEA prepration techniques
ii. cell conditioning
iii. carbon corrosion and Pt dissolution durability protocols
iv. experimental conditions of durability experiments
v. in-situ techniques such as polarization curve, electrochemical impedance spectroscopy, current interrupt method and CO_2 measurement
vi. ex-situ analysis such as scanning electron microscopy, X-ray diffracation and X-ray photo electron spectroscopy

are presented in this chapter.

3.1 Fuel Cell Hardware and Test Stations

MEA testing was conducted using CAT cell hardware (Figure 3-1) designed by the Automotive Fuel Cell Cooperation (AFCC). The superficial area of the electrodes in the MEA was 48.4 cm^2 [126]. MEA structures were prepared in the electrochemistry laboratory at AFCC and tested in in-house test station at AFCC and also at the University of Waterloo using G50 and Hydrogenics test stations. A photograph and process flowsheet for use of the G50 test station and ancillary equipment are given in Figure 3-2 and Figure 3-3, respectively.

3.2 Preparation of MEAs

The cathode catalyst used in the MEAs was obtained from TKK Corp. In all, four different commercial confidential MEAs were used for the carbon corrosion and Pt dissolution studies – MEAs 1, 2 and 4 which were catalyst coated and membrane-based and MEA 3 which was GDL electrode-based. All MEAs consisted of graphitic carbon-supported platinum (40 wt% platinum) layers and membranes based on perfluorosulfonic acid (PFSA). Schematic diagrams showing the structure of the MEAs are presented in Figure 3-4. The carbon corrosion ASTs to generate the diagnostic fingerprints, kinetic model and carry out the performance loss analysis were done using MEAs 1, 2 and 3 primarily, while the Pt dissolution ASTs were conducted using MEA 4. The Pt loading levels at the cathode were as follows: MEA 1 – 0.4 mg cm^{-2}, MEA 2 – 0.25 mg cm^{-2}, MEA 3 – 0.5 mg cm^{-2}, MEA 4 – 0.4 mg cm^{-2}. The Pt loading in all the anodes of this study was maintained at 0.1 mg cm^{-2}. The anode and cathode GDL electrodes were made from commercially available material with a carbon and Teflon sub-layer or ‘micro-porous layer’ on both electrodes. The catalyst coated membrane and gas diffusion media were cut using a swing beam cutting press, aligned precisely with frames and bonded to make a MEA with active superficial area of 48.4 cm^2.

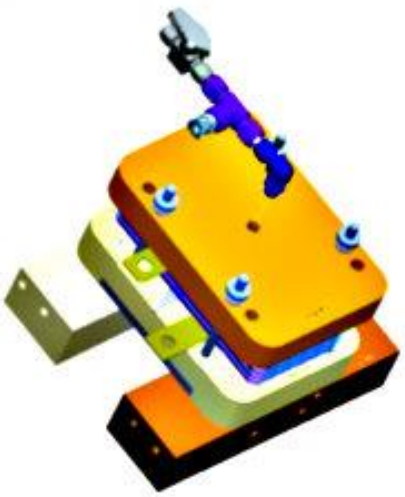

Figure 3-1: Schematic diagrams of the CAT cell [126] used in this study.

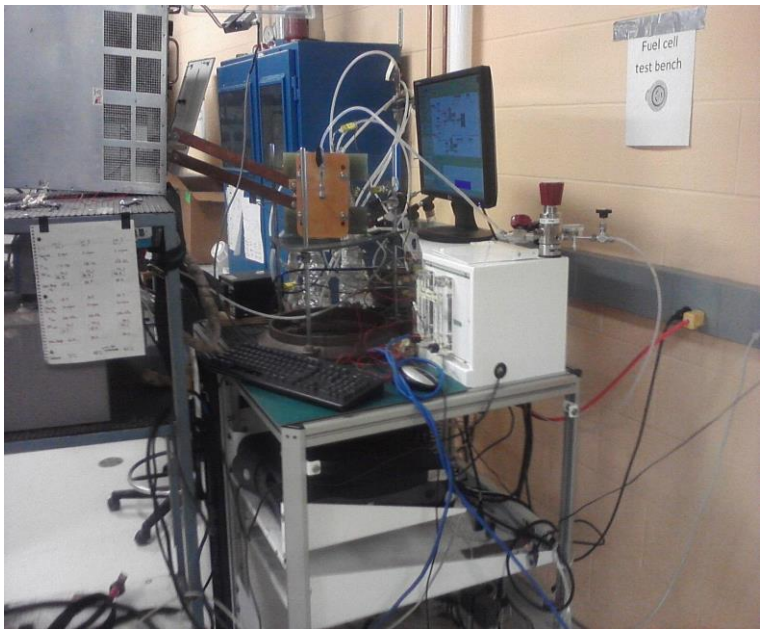

Figure 3-2: Photographic image of G50 Test station.

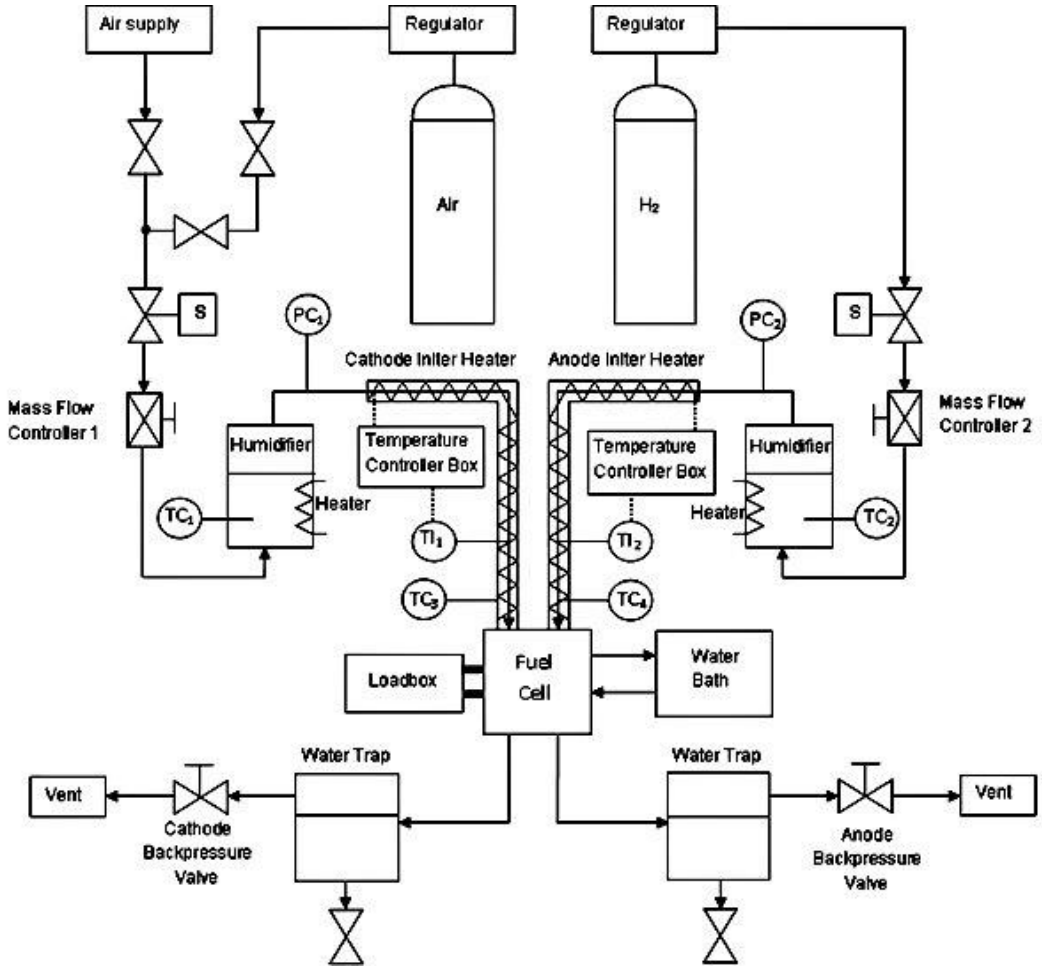

Figure 3-3: Flowsheet of the G50 test station and ancillary equipment.

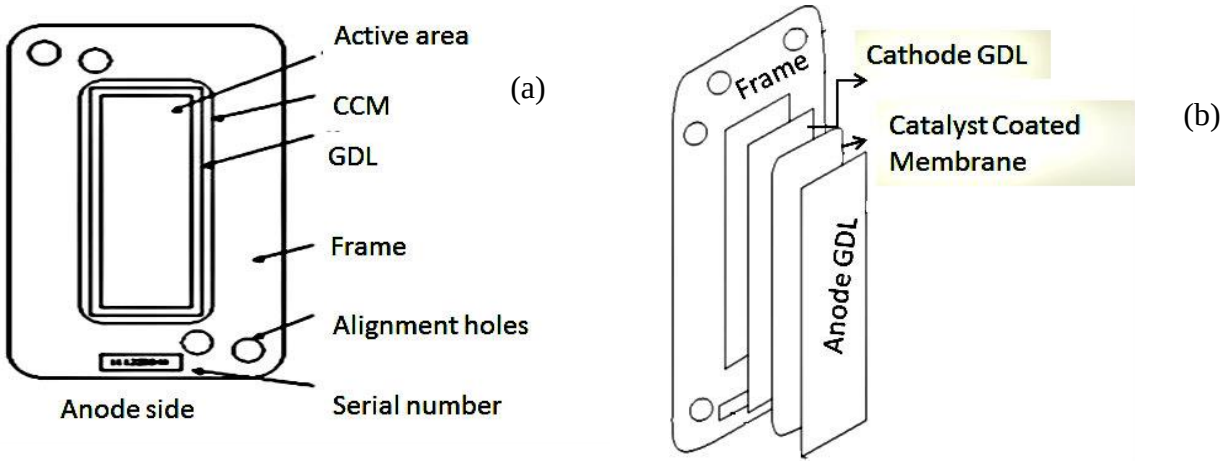

Figure 3-4: Schematic diagrams showing (a) plane and (b) cross-sectional views of the MEAs.

3.3 Fuel cell operating conditions

Some of the details of the accelerated cycling procedures and cell conditions are confidential with our industrial partner and so are not disclosed in this thesis. The sequence of steps followed for each MEA subjected to an AST protocol is as follows: i) conditioning, ii) EPSA measurement, iii) hydrogen cross-over measurement by LSV iv) measurement of a polarization curve, v) measurement of polarization, ohmic and mass transport resistance by EIS, vi) AST protocol, vii) cell recovery and vi) re-measurement of the tests from ii) to vii). A flowsheet showing an example of the testing procedure is displayed in Figure 3-5. The AST experiments chosen based on the objectives defined in Chapter 1 are termed carbon corrosion and Pt dissolution ASTs throughout this thesis. The carbon corrosion ASTs were done at AFCC, while the Pt dissolutions ASTs were carried out at the University of Waterloo.

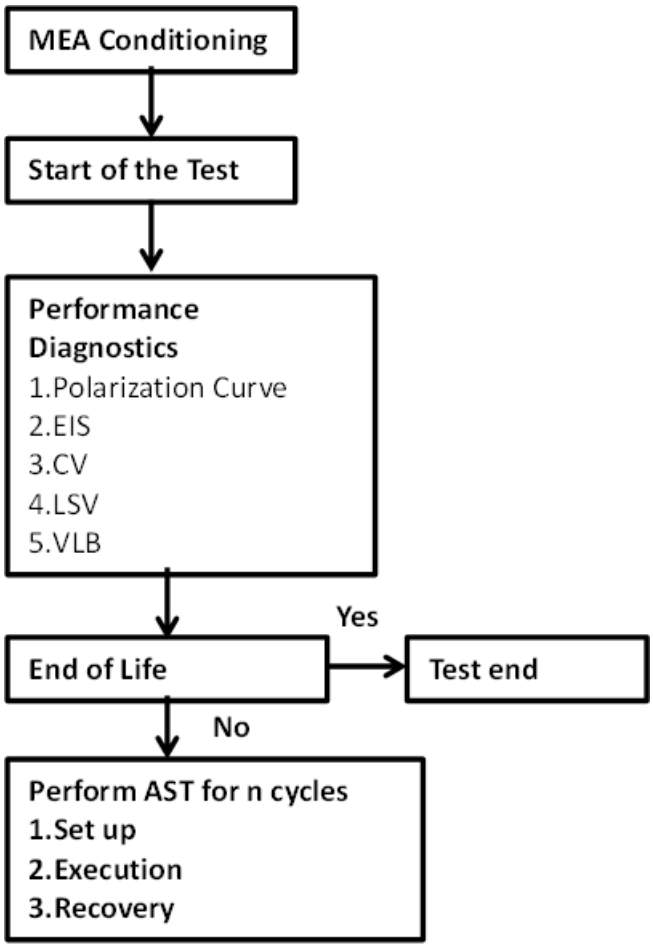

Figure 3-5: Flowsheet showing the general AST protocol for each MEA.

3.3.1 Preliminary Studies

Once an MEA was assembled in the cell hardware, a leak test was done. The details of thise leak test are described in Appendix A1. A pressurized bladder was used to press the MEA against the conducting flow-field plates in order to improve fuel cell performance. The optimal bladder pressure was determined based on the performance of the cell for each assembly. Generally, the bladder pressure was maintained between 60 and 80 psi. After the MEAs were conditioned for 12 hours, polarization curves were obtained to characterize its performance in the BOL state. As stated previously, the MEAs were tested in three

different test stations (G 50 and Hydrogenics at the University of Waterloo and a in-house test station at AFCC, Burnaby). One objective of this study was to examine cell performance using the G 50 station and compare the voltage losses with those obtained using the Hydrogenics and AFCC test station.

3.3.2 Experiments

In order to study carbon corrosion and Pt dissolution in the MEAs causing performance degradation, 25 AST experiments were conducted. Each experiment was repeated three times to confirm the reproducibility of the data. The carbon corrosion ASTs were designed to (a) develop carbon corrosion fingerprint expressions (b) study carbon corrosion kinetics and (c) characterize the breakdown of performance loss. The Pt dissolution AST was aimed at studying Pt dissolution at different temperatures and RH levels. Details of these experiments are provided in the Table 3-1.

3.3.3 Details of Sequence of Steps in ASTs

3.3.3.1 Cell Conditioning

MEAs used in the carbon corrosion AST experiments (MEA 1, 2 and 3) were conditioned for 12 hours at a constant current density of 2.0 A cm^{-2}, 100% RH and 70^0C with the hydrogen and air flow rates maintained at 2 and 8 slpm, respectively. The flow rates of the reactant gases were maintained well above the stoichiometric levels to ensure that neither reactant became depleted within the fuel cell and that the hydrogen and oxygen concentrations would remain uniform and at known levels within the anode and cathode portions of the MEA, respectively. The other conditions during conditioning are listed in Table 3-2. After conditioning, the fuel cell was purged with N_2 for 15 min before beginning the electrochemical experiments to evaluate the BOL performance. MEAs used to

investigate the effects of temperature and RH on Pt dissolution were conditioned at 1.7 A cm^{-2} for 12 hours and at the other conditions listed in Tables 3-3 and 3-4.

3.3.3.2 Cyclic Voltammetry

To assess the changes in the ECSA during ASTs, CVs were obtained at 60^0C using accepted procedures. CO stripping CV analysis was done to measure the ECSA during the carbon corrosion studies at AFCC. The CVs during the carbon corrosion studies were measured using an in-house built set-up assisted by a load bank. Some of the details of this set-up and procedures to characterize CV sensitivity are proprietary and must remain confidential. The conditions used for these CV measurements are given in Table 3-2. Due to safety concerns associated with CO handling, this method was not used to measure the ECSA during the Pt dissolution studies at the University of Waterloo. In this case, ECSA was measured from the H_2 desorption portion of the CVs obtained while N_2 is being fed to the cathode.

The ECSA (cm^2g^{-1}) was determined using the following expression:

$$\mathrm{ECSA} = \frac{Q_{CO}}{[Pt]*0.484} \qquad (3\text{-}1)$$

where [Pt] represents the platinum loading (mg cm^{-2}) at the cathode, Q_H is the charge density for hydrogen desorption (mC cm^{-2}) and 0.484 mC cm^{-2} corresponds to the charge density required to oxidize a monolayer of CO on the Pt surface. The ECSA during the carbon corrosion ASTs was obtained from the CO adsorption peak from voltammograms based on the assumption that one CO atom covers one Pt atom. More specifically, Q_{co} was determined from the area under the CO stripping region of the cyclic voltammogram [127]. The conditions used for these CV experiments are listed in Table 3-2.

Table 3-1: Experiments to assess catalyst durability.

AST experiments	Pt loading on cathode (mg cm^{-2})	MEA
Carbon corrosion fingerprint		
1.0-1.4 V 30s/30s	0.4	MEA 1
0.6-1.4 V 30s/30s	0.4	MEA 1
0.6-1.4 V 27s/3s	0.4	MEA 1
1.0 -1.5 V 5s/5s	0.4	MEA 1
1.0 -1.5 V 5s/5s	0.25	MEA 2
1.0 -1.5 V 5s/5s	0.5	MEA 3
Carbon corrosion kinetics		
1.0-1.4 V 30s/30s	0.4	MEA 4
1.0-1.42 V 5s/5s	0.4	MEA 4
1.0-1.44 V 5s/5s	0.4	MEA 4
1.0-1.468 V 5s/5s	0.4	MEA 4
1.0-1.48 V 5s/5s	0.4	MEA 4
1.0-1.5 V 5s/5s	0.4	MEA 4
1.0 -1.5 V 5s/5s	0.4	MEA 4
1.0 -1.5 V 5s/5s	0.25	MEA 4
1.0 -1.5 V 5s/5s	0.5	MEA 4
Pt dissolution at different temperatures		
0.6-1.0 V 3s/3s at 40^0C	0.4	MEA 5
0.6-1.0 V 3s/3s at 60^0C	0.4	MEA 5
0.6-1.0 V 3s/3s at 80^0C	0.4	MEA 5
Pt dissolution at different RH		
0.6-1.0 V 3s/3s at 0%RH	0.4	MEA 5
0.6-1.0 V 3s/3s at 50%RH	0.4	MEA 5
0.6-1.0 V 3s/3s at 100%RH	0.4	MEA 5

Table 3-2: Operating conditions for experments investigating carbon corrosion.

	Conditioning	Polarization	CV	ASTs	Recovery
Load (A cm^{-2})	2.0	0 − 2.4	0	0	0
Temperature (^{o}C)	70	60	60	70	70
Fuel/oxidant gas	H_2/air	H_2/air	H_2/N_2	H_2/N_2	H_2/N_2
Fuel/oxidant pressure (barg)	1.7/1.5	1.7/1.5	1.5/1.5	1.5/1.5	0.4/0.03
Fuel/oxidant flowrate (slpm)	2/8	2/12	2/12	1/1	1/0
Fuel/oxidant RH (%)	100/100	100/100	100/100	100/100	50/50

Table 3-3: Operating conditions for experiments investigating Pt dissolution at different temperatures.

	Condition-ing	Polariza-tion	EIS	CV	ASTs	Recovery
Load (A cm^{-2})	1.7	0 − 2.4	0	0	0	0
Temperature (^{o}C)	60	60	60	60	AST 1 # 40 AST 2 # 60 AST 3 # 80	60
Fuel/oxidant gas	H_2/air	H_2/air	H_2/air	H_2/N_2	H_2/air	H_2/N_2
Fuel/oxidant pressure (barg)	2.7/2.5	2.7/2.5	2.7/2.5	0/0	1.5/1.5	0.4/0.03
Fuel/oxidant flowrate (slpm)	2/10	2/10	2/10	0.20/ 0.64	2/10	1/0
Fuel/oxidant RH (%)	100/100	100/100	100/100	100/ 100	100/100	50/50

Table 3-4: Operating conditions for experiments investigating Pt dissolution at different RHs.

	Conditio-ning	Polarizat-ion	EIS		CV and LSV	ASTs	Recovery
Load ($A\ cm^{-2}$)	1.7	$0-2.4$	0	0	0	0	0
Temperature (^oC)	60	60	60	60	60	60	60
Fuel/oxidant Gas	H_2/air	H_2/air	H_2/ air	H_2/N_2	H_2/N_2	H_2/air	H_2/N_2
Fuel/oxidant pressure (barg)	2.7/2.5	2.7/2.5	2.7/ 2.5	0/0	0/0	1.5/1.5	0.4/0.03
Fuel/oxidant flowrate (slpm)	2/10	2/10	2/10	0.20/ 0.64	0.20/ 0.64	2/10	1/0
Fuel/oxidant RH (%)	100/100	100/100	100/ 100	100/ 100	100/100	AST 1 100/100 AST 2 50/50 AST 3 0/0	50/50

The CVs conducted during the Pt dissolution studies were conducted using a Solatron model 1287 potentiostat/galvanostat. During these experiments, hydrogen was passed through the anode and the cell voltage was cycled between 0.05 and 1.2 V at a scan rate of 20 mV s^{-1}. As stated above, the Pt dissolution studies were conducted at the University of Waterloo. Due to safety concerns, the ECSA was determined determined from the hydrogen desorption peak in the under-potential region of the CV obtained with the cathode exposed to N_2 and the anode to H_2. During these analysis, the N_2 and H_2 pressures at the working and counter electrodes, respectively, were both controlled to remain constant since their levels have been found to affect the charge measured under the under-potential hydrogen desorption peak which is used to give the area occupied by a monolayer of H atoms. As shown previously, a monolayer charge density of 0.21 mC cm^{-2} on a smooth Pt surface was obtained when both gases are held at 100 kPa [70]. Consequently, both the N_2 and H_2 pressures were maintained at 100 kPa during these experiments for the purpose of estimating the ECSA. Core-view software was used to analyze the cyclic voltammetry data to determine the ECSA during fuel cell testing.

Prior to measuring the ECSA, the cathode was purged using N_2 for 20−30 minutes, which caused the cell voltage to drop. The experimental conditions for ECSA determination during the Pt dissolution experiments are given in Table 3-3 and 3-4. The ECSA of the Pt catalyst expressed in $m^2\ g_{Pt}^{-1}$ was determined from the area under the hydrogen desorption region of the cyclic voltammetry using the following expression [127]:

$$\mathrm{ECSA} = \frac{Q_D}{K\ L_w\ A_g} \qquad (3\text{-}2)$$

where L_w is the cathode loading of the MEA ($g_{Pt}\ m^{-2}$), A_g is the superficial area of the electrode (cm^2) and Q_D is the integrated area (in units of μC) under the hydrogen desorption region of the CV between 0.05 V and 0.4 V_{RHE} corrected for double-layer charging. As discussed in Section 2.5, *K* is taken to be 0.210 mC cm^{-2} for a CV obtained with H_2 and N_2 fed on the anode and cathode sides, respectively [128]. The catalyst loading

was determined from the weight % of platinum added to the carbon powder during preparation of the ink.

The EPSA and the double-layer capacitance C_{dl} were also determined by cyclic voltammetry with a load bank power supply using methods similar to those that are generally accepted [117]. These experiments were conducted using H_2 as the feed gas stream to the anode at a flow rate of two slpm and 100% RH and N_2 containing 1% CO as the feed to the cathode at a flow rate of 12 slpm and 100% RH. The cathode potential was swept between 0.1 and 1.2 V at a scan rate of 20 mV s^{-1}. The double-layer capacitance was measured at 0.45 V [129]. A cathode catalyst loading of 0.4 mg-Pt cm^{-2} was used in this study. Pt utilization (U_{Pt}) of the MEA at the cathode was assumed as 0.8 based on Neyerlin et al [111]. The EPSA was computed using the modified equation (3-3) from the equation (2-18) shown in Section 2.4.3 [96]:

$$EPSA = 10 * U_{Pt} * ECSA * L_{Pt} \qquad (3\text{-}3)$$

3.3.3.3 Linear Sweep Voltammetry (LSV)

LSV was conducted on an MEA in its BOL state and then again after 1000, 10000 and 20000 cycles of the Pt dissolution ASTs to monitor H_2 cross-over. These LSV experiments were conducted under the conditions given in Table 3-4 using a Solartron model 1287. To measure fuel cross-over, a suitable inert gas such as N_2 was used to purge the fuel cell cathode while H_2 passed through the anode. It should be noted that electrochemical cross-over measurements require the use of a potentiostat or other controllable power supply. The potential of the fuel cell cathode was swept to potentials at which any H_2 gas present at the fuel cell cathode would be instantaneously oxidized under mass transfer-limited conditions.

The test cell was equilibrated for about 2 h with humidified H_2 and N_2 at 60°C before the LSV measurements. A potential scan from 0 to 0.6 V at a scan rate of 2 mV s^{-1} was then applied to the cell. Higher voltages were avoided to prevent Pt oxidation and carbon corrosion. Since N_2 gas was the only gas introduced into the cathode side, any current generated in the given potential range could be attributed solely to the electrochemical oxidation of H_2 gas that crossed over from the anode side through the membrane. The cross-over current typically increased with the scan potential and rapidly reached a limiting value when the cell potential reached ~ 300 mV. At this value, all cross-over H_2 should be instantaneously oxidized due to the high overpotential. From the limiting current i_{H_2}, the flux N_{H_2} of H_2 gas across the membrane can be calculated using Faraday's law:

$$N_{H_2} = \frac{i_{H_2}}{2F} \qquad (3\text{-}4)$$

3.3.3.4 Polarization Curves

To characterize the performance losses in this study, polarization curves were obtained at 60^0C under identical conditions at regular intervals during each AST. The conditions used to obtain these polarization curves during the carbon corrosion and Pt dissolution ASTs are given in Tables 3-2 and 3-3. These measurements were made using an electronic load RBL 232 (TDI electronic devices) connected to a fuel cell test bench. The fuel cell was operated with H_2 being fed on the anode side and either air or O_2 on the cathode side during these experiments. Before each polarization curve was determined, the fuel cell was operated at 1.7 A cm^{-2} for 20 minutes to ensure that the system was initially in a stable state. The polarization curve was obtained galvanostatically by varying the cell current density from 2.4 to 0 A cm^{-2} at intervals of 0.1 A cm^{-2} and measuring the resulting cell voltage. The MEA was held at each current density for 15 minutes to ensure that steady-state was reached except when the cell was at open-circuit. The cell was maintained at the OCV for

only 1 minute to avoid OCV-induced degradation. The cell voltage plotted on the I−V curves at each current density represents the average value obtained over the last minute of polarization although data were logged every 10s. The maximum test current density was set based on either the maximum current limit of the instrument load box or the current density at which the cell voltage was less than a minimum set point of 0.1 V. The anode and the cathode gas line temperatures were set at 5°C above the cell temperature in order to avoid water condensation in the inlet gas lines. The fuel used during polarization curve measurements was ultra-high purity hydrogen (99.999% certified) grade.

3.3.3.5 EIS

Electrochemical impedance spectra (EIS) of the MEA is obtained in its BOL state and then again after 1000, 10000 and 20000 cycles to measure the changes in polarization (R_p) and ohmic (R_s) resistances during the Pt dissolution ASTs. The conditions used for this analysis are given in Tables 3-3 and 3-4 for the respective ASTs. A diagram showing the connections between the fuel cell and electrochemical instruments is shown in Figure 3-6. Impedance analysis was carried out only for the Pt dissolution studies using modes with ultra-pure H_2 and compressed air as the inlet gases. A Solatron model 1260 impedance analyzer connected to a Solatron model 1287 potentiostat/galvanostat was used for these measurements. The electrochemical circuit was operated with the counter electrode connected to the reference electrode via a shunt. The EIS spectra were obtained under fully humidified conditions using the potentiostatic mode by applying an AC signal with a 5 mV−amplitude on a 0.85 V DC cell voltage beginning at a frequency of 10 kHz and decreasing down to 10 mHz.

To identify the changes in membrane and ionomer resistance, EIS analysis in H_2-N_2 mode was conducted to prevent any further degradation during the EIS analysis. Impedance analysis was carried out only for RH dependent Pt dissolution studies using ultra-pure H_2 and N_2 as the inlet gases. Electrochemical impedance spectra data were obtained by

applying an AC signal with a 10 mV−amplitude on a 0.45 V DC cell voltage beginning at a frequency of 50 kHz and decreasing down to 0.05 Hz. Z-plot and Z-view software were used to obtain and analyze the electrochemical impedance spectra data to generate Nyquist and Bode plots. The ohmic (R_s) and polarization (R_p) resistances were determined by fitting a basic equivalent circuit model to the electrochemical impedance spectra. The equivalent circuit used to model the impedance response is shown in Figure 3-7.

3.3.3.6 Current Interruption Method

During the course of the carbon corrosion ASTs, the current interruption method was employed to measure the ohmic resistance in the fuel cell while H_2 was being fed to the anode and O_2 to the cathode. When the current density reached 1.7 A cm^{-2} during the polarization experiments, the cell was perturbed for a brief period of time to carry out the current interruption measurement.

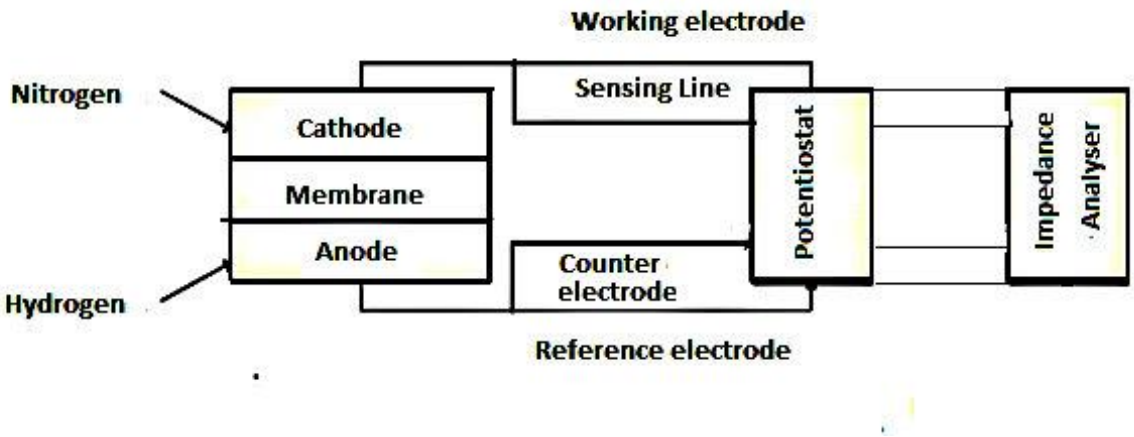

Figure 3-6: Set-up for EIS experiments [118, 130].

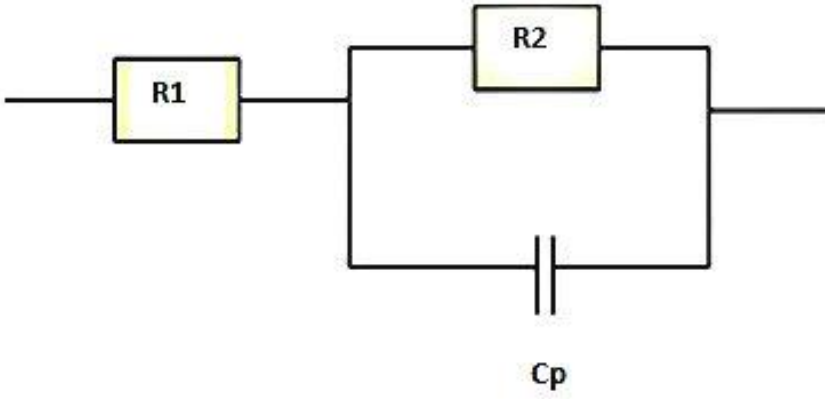

Figure 3-7: Equivalent electrical circuit fitted to EIS spectra of PEM fuel cell.

3.3.3.7 ASTs

ASTs in which the predominant modes of degradation were carbon corrosion alone, Pt dissolution alone and a mixture of carbon corrosion and Pt dissolution were applied in this study. For convenience, these are termed as the carbon corrosion, Pt dissolution and mixed degradation ASTs, respectively, in this thesis. In this section, the experimental details of these ASTs are described.

First, each of the MEAs was subjected to ASTs with the following voltage waveforms to develop the carbon corrosion fingerprint used in deconvoluting the extents of carbon corrosion, mixed degradation and Pt dissolution (Table 3-1): i) square-wave voltage cycles between 1.0 V and 1.4 V with dwell times of 30s and 30s, respectively, ii) square-wave voltage cycles between 1.0 V and 1.5 V with dwell times of 5s and 5s, respectively, iii) constant cell voltage of 1.4 V with durations ranging from 5 hours to 30 hours between each measurement of fuel cell performance (i.e., measurement of polarization curve), iv) square-wave voltage cycles between 0.6 V and 1.4 V with dwell times of 30s and 30s, respectively, and v) square-wave voltage cycles between 0.6 V and 1.4 V with dwell times of 27s and 3s. A schematic diagram showing these waveforms is given in Figure 3-8.

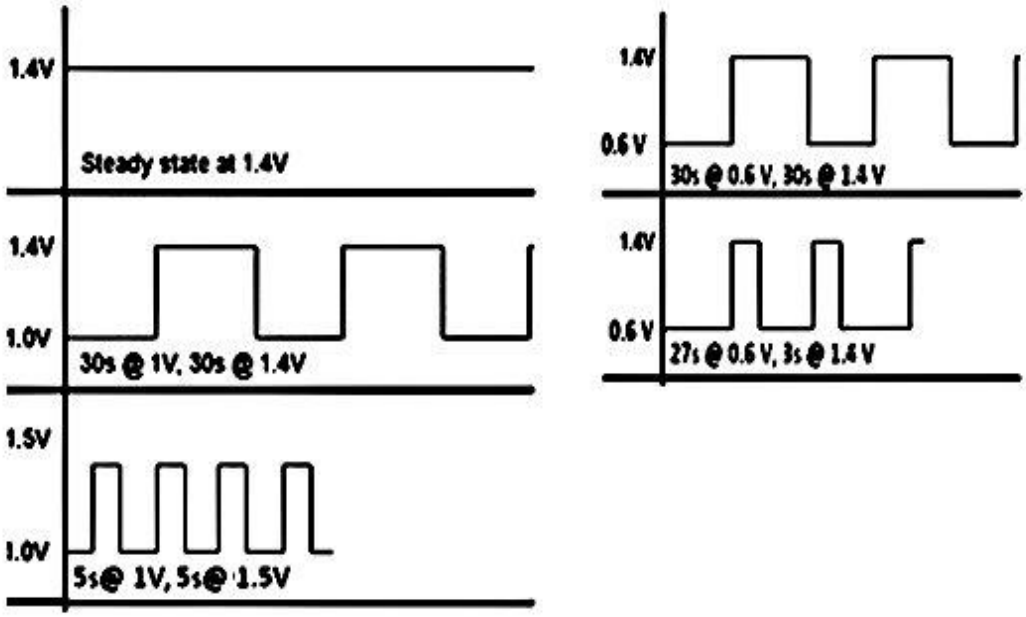

Figure 3-8: AST voltage cycles used to develop fingerprint diagnostic indicator for carbon corrosion.

Carbon corrosion and mixed degradation ASTs were applied to the MEAs to develop a numerical model for carbon corrosion. Carbon corrosion ASTs were conducted by applying square-wave pulses with different upper potential and lower potential limits to the cell operated with H_2 fed on the anode side and N_2 on the cathode side. These include: i) square-wave voltage cycles between 1.0 V and 1.42 V with dwell times of 5s and 5s, respectively, ii) square-wave voltage cycles between 1.0 V and 1.44 V with dwell times of 5s and 5s, respectively, iii) square-wave voltage cycles between 1.0 V and 1.468 V with dwell times of 5s and 5s, respectively, iv) square-wave voltage cycles between 1.0 V and 1.48 V with dwell times of 5s and 5s, respectively, v) square-wave voltage cycles between 1.0 V and 1.5 V with dwell times of 5s and 5s, respectively, and vi) square-wave voltage cycles between 1.0 V and 1.4 V with dwell times of 30s and 30s, respectively. The carbon corrosion rate at the cathode is expected to rise when the upper voltage during ASTs is raised above 1.4 V. However, if the upper limit becomes too high, severe damage to the

cell and its performance can occur. Accordingly, a range of upper limits between 1.4 and 1.5 V was chosen for these ASTs as a compromise to promote carbon corrosion but not cause excessive degradation. All ASTs were applied for 2500 cycles. The effect of cycle profile shape on carbon corrosion variable large potential cycles (lower limit of 1.0 V and upper limit of 1.4-1.5 V) measured in this study in order to identify and analyze the impact of cycle profile. This will help to clarify the mechanism of carbon loss and Pt dissolution during a given cycle. In our study, we study and explore for the first time on the effect of various simplified cycle profiles under normal fuel cell upper voltage ranges (1.4,1.42, 1.44, 1.468 and 1.48 V) measured in MEAs. The results of this work may also provide insight into operation modes of PEMFCs that result in lowered degradation rates. To study mixed Pt dissolution-carbon corrosion, an AST involving square-wave voltage cycles between 0.6 V and 1.4 V with dwell times of 30s and 30s, respectively was chosen. Due to the higher magnitude of degradation in the MEAs, the ASTs between 0.6 and 1.4 V was terminated after 1500 cycles instead of 2500 cycles. The voltage cycle profiles for these ASTs are shown in Figure 3-9.

Fuel cells achieve their highest output voltage at open-circuit (no load) conditions and the voltage drops off with increasing current draw. This is known as polarization. Cell polarization dramatically increases during carbon corrosion ASTs. Severe polarization losses are expected under the conditions where kinetics, ohmic resistance and mass transport become important to carbon corrosion. Consequently, a carbon corrosion AST with square-wave cycles between 1.0 and 1.5 V for dwell times of 5s and 5s was applied to analyze the performance loss in each region and develop a semi-empirical relation describing the breakdown of the total voltage loss into the contributions due to kinetics, ohmic and mass transport effects. In addition, square-wave voltage cycles between 1.0 V and 1.4 V with dwell times of 30 s and 30 s were conducted on catalyst layers with loading levels of 0.25 (MEA 1) and 0.5 mg cm^{-2} (MEA 3) to assess the accuracy of the performance loss breakdown with different MEAs.

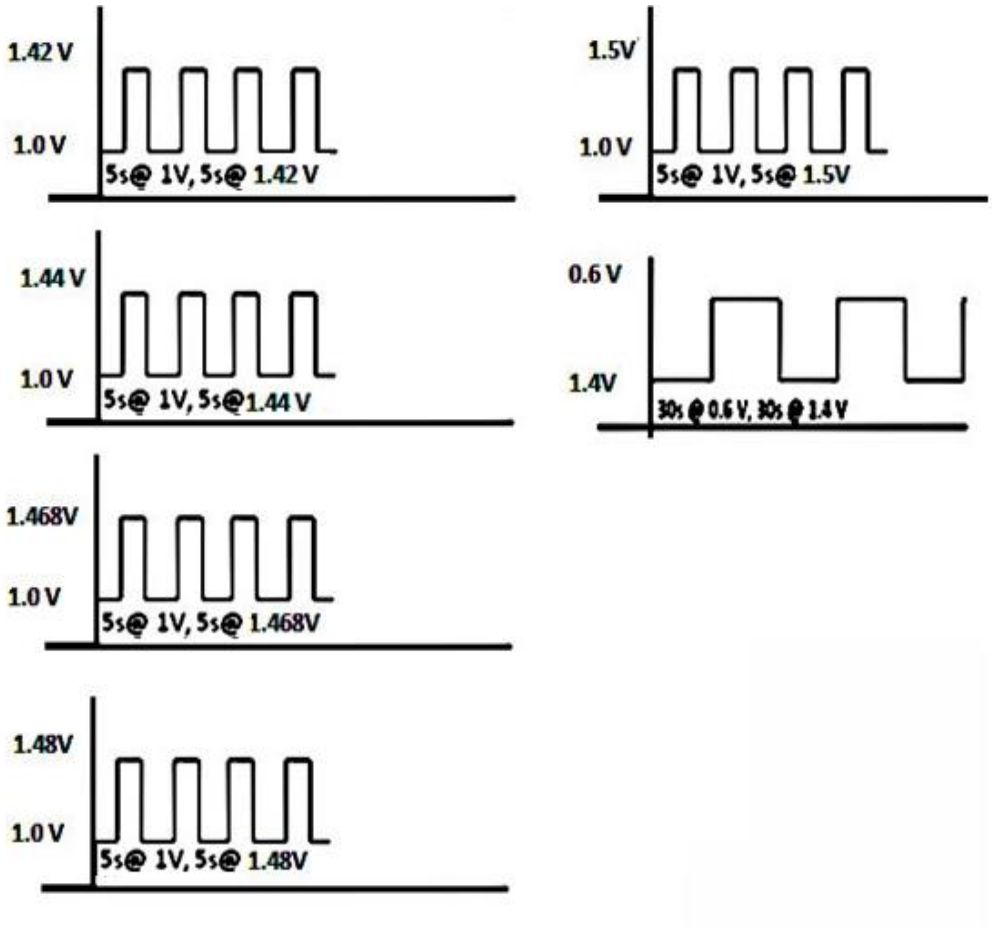

Figure 3-9: AST voltage cycles used to develop and assess carbon corrosion model.

A systematic approach is required to study the modes by which Pt becomes unstable. Common stressors such as increased load cycling tend to exacerbate Pt dissolution. To develop kinetic diagnostic fingerprints for performance loss due to Pt dissolution at different temperatures, the MEAs were subjected to ASTs in which the cell voltage was cycled between 0.6 V and 1.0 V to promote Pt dissolution primarily. An increase in cell operating temperature during voltage cycling has been found to accelerate degradation of the catalyst [70]. Accordingly, the ASTs were conducted at 40, 60 and 80^0C. This waveform was applied for 20000 cycles, which corresponds to the EOL state. In order to simulate real-life vehicle operating conditions, voltage cycling was performed using the H_2/air mode instead of H_2/N_2 mode. Higher performance losses have been reported by cycling with square-wave voltage signals than with triangular waves [100]. Hence, the use of square waves was adopted to induce Pt dissolution in this study. The dwell times of the square waves have also been shown to have important effects on the loss of Pt mass activity [100, 101]. A dwell period of 3 s at both the upper and lower limits of 1.0 V and 0.6 V was selected for the following reasons based on previous findings in the literature [131]. Although these dwell times are short, they are relevant for the operation of fuel cell vehicles. During typical driving conditions, deceleration or braking of the vehicle from peak power to an idle or partial load occurs over a quick period of ~ 3 s. Also, ECSA and mass activity losses are expected to be significant when as many as 20,000 cycles are applied. Thus, losses in both mass activity and ECSA can become excessive when the 0.6-1.0 V AST is applied with dwell times greater than 3 s. Durability measurements were mainly conducted under H_2/air at 100 %RH. Using air and 100% RH for longer dwell times can lead to significant degradation of the carbon support as well. Thus, information gained regarding the degradation occurring when pulses between 0.6 and 1.0 V are applied for a large number of cycles (20000) and small dwell times (3s/3s) should be optimum for investigating Pt dissolution and ultimately useful in improving cathode CL design.

Except when the effect of humidity was investigated, the RH of both reactant streams was maintained at 100% to minimize degradation of other MEA components, mainly the

membrane. The degradation of membrane in the MEA can be severe at lower RHs. By holding the MEA at 100% RH, degradation of Pt can be more effectively isolated from the other modes. The other operating conditions used during the Pt dissolution ASTs are given in Table 3-3. They were performed using H_2/air mode instead of H_2/N_2 mode to mimic the conditions during typical PEM fuel cell operation.

3.3.3.8 Recovery

Voltage cycling may cause a build-up of water at the cathode catalyst and thus reduce cell performance. Since the focus of this study was only on catalyst layer degradation, the following recovery procedure was adopted to remove effects of this water build-up and restore the cell back to its nominal state before the state of the MEA was characterized. After completion of a specified number of cycles during an AST, the load bank was turned off and the cathode was purged with N_2 at a rate of one slpm for 20 minutes. This procedure helped to remove excess water present in the catalyst layer [132]. Then the flow of air to the cathode was resumed and the cell was conditioned for 2 hours before measuring MEA property and performance indicators such as the I-V curves, electrochemical impedance spectra and CV.

3.3.3.9 CO_2 Measurement

Throughout each carbon corrosion AST experiments, the carbon dioxide content in the exhaust gas was measured using a Model 100 Infrared Analyzer (California Analytical Instruments). From this measurement, the amount of carbon lost due to corrosion was calculated.

3.3.3.10 Scanning Electron Microscopy

SEM was used to examine the locations of any Pt deposits or bands within the catalyst layer and membrane and any evidence for thinning or damage to the various MEA layers in BOL samples and EOL samples after being subjected to Pt dissolution ASTs conducted at different temperatures. After the completion of the final electrochemical characterization experiments during these ASTs, a fresh MEA and a degraded MEA were cut along a plane normal to the component layers and cast in epoxy to expose their cross-sections. The cross-sections were examined using a Philips XL30 scanning electron microscope with backscattering detection at 350x magnification and 15 kV. The thicknesses of the membrane and catalyst layer were measured from these cross-sectional images. One of its main purposes was to determine whether Pt bands formed within the membrane layer and if so, their distance from the catalyst layer. Another aim was to characterize the surfaces of the catalyst coated membrane. The backscattering electron imaging mode was preferred for this study. Since the intensity of the backscattering electron image increases with atomic number, Pt-containing particles could be easily distinguished from the lighter PFSA membrane attached to its top surface. During scanning electron microscopy imaging, the holder was tilted until the viewing direction was perpendicular to the cross-Section.

3.3.3.11 X-ray Diffraction

This technique, which provides information on the structure of a crystalline material, is based on the effect of the atomic spacing of this material on an incident X-ray beam. The overlap of the different waves diffracted by successive atomic planes leads to constructive and destructive interferences depending on the (i) spacing d_{hkl} between (hkl) planes within the crystalline network, (ii) wavelength λ of the X-ray radiation and (iii) angle of incidence θ of the radiation on the surface of the solid. These parameters are related by Bragg's law:

$$n\lambda = 2d_{hkl}\sin\theta \qquad (3\text{-}5)$$

When the compound being analyzed is present as a powder, the XRD technique can also be used to estimate the average particle size by using Scherrer's equation to analyze the diffraction peaks.

Diffraction patterns were obtained for both fresh and degraded catalyst samples using a Philips diffractometer (M-PW1710) with a Cu $K_{\alpha 1}$ radiation (λ = 1.54060 Å) source. The catalyst (cathode upwards) was mounted in a quartz block with dimensions 2.5 cm x 2.5 cm x 1 mm. The 2θ Bragg angles were scanned over the range of 0 – 120° at a rate of 0.5° per min. The lattice parameter a was determined from the most intense peak observed in the XRD pattern of each catalyst using the expression:

$$d_{hkl} = \frac{a}{\sqrt{h^2 + k^2 + l^2}} \qquad (3\text{-}6)$$

For Pt, this corresponded to the (111) plane, which appeared at $2\theta \approx 40^{o}$.

The average size of the platinum catalyst particles was estimated from the XRD (111) peak using Scherrer's equation[133]

$$d = \frac{0.94\lambda}{B_{2\theta}\cos\theta} \qquad (3\text{-}7)$$

where d is the average particle diameter and $B_{2\theta}$ is the width (in radians) of the diffraction peak at its half-height. $B_{2\theta}$ is the line broadening at half the maximum intensity (FWHM), after subtracting the instrumental line broadening, in radians by using the Warren formula:

$$B_{2\theta} = B_M^2 - B_s^2 \quad (3\text{-}8)$$

where B_M is the observed width at the peak half-height of the sample and B_S is the corresponding width for a powder made up by mixing the sample with a standard material having a large crystallite size and a diffraction peak near that of the sample. LaB_6 was used as the standard for this purpose. Once the average particle diameter was determined, the catalyst surface area was calculated assuming the particles were spherical in shape. XRD was used to investigate the catalyst layer of the MEA. GDL was removed prior the measurement.

3.3.3.12 X-ray photoelectron spectroscopy

Chemical analysis of MEA surface samples was performed using XPS to identify degradation products and provide clues regarding possible reaction mechanisms. The surface composition of the fresh and degraded samples was analyzed using a Thermo-VG Scientific ESCALab 250 unit with a monochromatic Al KR X-ray source (1486.6 eV). The binding energy (BE) positions, full width-at-half-maxima and area intensities of individual XPS features were determined by using CasaXPS software with the appropriate background correction. Samples from different locations of the samples containing Pt catalyst and Nafion ionomer were analyzed in separate measurements to assess the uniformity of film composition.

The positions and intensities of the various C, O, F and Pt peaks were measured in fresh and degraded samples to determine changes in the oxidation states of these elements and their surface concentrations over the course of the ASTs. X-ray radiation has been shown not to cause a discernible change in the chemical structure of the membrane even after 2 h

of exposure [134]. GDL was removed from the MEA prior the measurement. XPS was used to investigate the catalyst layer at both anode and cathode sides of the sample.

3.3.3.13 Surface Area Analysis

Surface area analysis of the carbon was carried out using Micromeritics® ASAP 2020 accelerated surface area and porosimeter at AFCC.

Chapter 4
Carbon Corrosion ASTs

This chapter presents results obtained from the carbon corrosion ASTs, analysis of these data and the development of a carbon corrosion model. These ASTs have been chosen so that carbon corrosion occurs primarily in the cathode catalyst layer. Carbon corrosion of other PEM fuel cell components such as the GDL, membrane and the flow field have been investigated separately. Due to a confidentiality agreement, these results are not presented in this section. However, carbon loss from these components should be negligible during the ASTs described in this chapter.

Section 4.1 covers the experimental results, a procedure to develop a diagnostic fingerprint expression for the performance loss due to carbon corrosion, development of a method to de-convolute the performance losses due to carbon corrosion and Pt dissolution and a discussion of the failure mechanisms based on the use of this deconvolution method. The derivation of a mechanistic model on carbon corrosion and its application to the ASTs of this study are discussed in Section 4.2. This includes validation of the model predictions by comparison with the experimental results and discussion of the limitations of the model. In Section 4.3, XRD and XPS are used to compare the condition of an MEA in the BOL state to that of another that has undergone an AST involving square-wave pulses between 0.6 and 1.4 V with 5 s/5 s dwell times. The results of an ex-situ analysis of mixed degradation AST is demonstrated in Section 4.3.

4.1 Carbon Corrosion Fingerprint and Deconvolution of Performance Losses

In this Section, a diagnostic indicator or ‘fingerprint’ expression for the performance loss due to degradation of the cathode Pt/C CCL during ASTs is first obtained for each MEA. Fingerpring is an empirical trend that can represent the evidence of MEA failure. Carbon finger print is obtained by plotting the performance loss of the PEM fuel cell against. Carbon loss measured at the fuel cell outlet.This fingerprint is then applied to the performance loss measured during the mixed-mode AST to de-convolute the contribution of carbon corrosion from that of Pt dissolution. Finally, this estimate of the contribution from Pt dissolution is compared to the performance loss measured directly during the AST in which Pt dissolution is the dominant degradation mode. Finally, the effectiveness of this approach is examined and its limitations are discussed. The experimental procedures relevant to these sections are discussed in the following sections of Chapter 3:

1. MEA preparation – Section 3.3;
2. Cell conditioning – Section 3.4.3.1;
3. Cyclic voltammetry – Section 3.4.3.2;
4. Polarization curve measurement – Section 3.4.3.4;
5. Current interruption method – Section 3.4.3.6;
6. ASTs – Section 3.4.3.7;
7. Recovery – Section 3.4.3.8;
8. CO_2 measurement – Section 3.4.3.8;
9. BET surface area analysis – Section 3.4.3.8.

4.1.1 Carbon Corrosion ASTs

Anodic oxidation of carbon in acidic environment occurs by reaction pathways where carbon is oxidized and form surface oxide groups at potentials above 1.2 V [78]. These surface groups are eventually oxidized to CO_2. Active sites for carbon corrosion are associated with carbon atoms at edges, defects, dislocations and single-layer planes (amorphous) [52]. Potentiostatic and galvanostatic protocols induce higher carbon corrosion when the cell voltage is cycled between 1.0 and 1.4 V.

To develop a fingerprint expression for the effect of carbon corrosion on performance loss, three ASTs were applied: constant cell potential of 1.4 V, a square-wave cycle with 30s at 1.0 V and 30s at 1.4 V and a square-wave cycle with 5s at 1.0 V and 5s at 1.5 V. The cell potential was maintained above 1.0 V throughout the three ASTs to accelerate carbon corrosion and to minimize platinum dissolution. The performance loss of MEA 1 obtained from steady-state polarization experiments conducted during the course of the three ASTs is plotted in Figure 4-1. For the purposes of this analysis, the performance loss is obtained by subtracting the cell voltage measured at a current density of 1 A cm^{-2} when the MEA is in its BOL condition from the voltage measured at the same current during a subsequent polarization measurement when the AST is underway. Experiments at each condition were repeated three times and found to yield very reproducible results that differed less than 5%. Each of the performance loss values in Figure 4-1 represents the averages of these three separate measurements. The results indicate that the performance losses over the course of the three ASTs are very similar to each other over the first 20 hours of operation and reach between 200 mV and 215 mV by the end of this period.

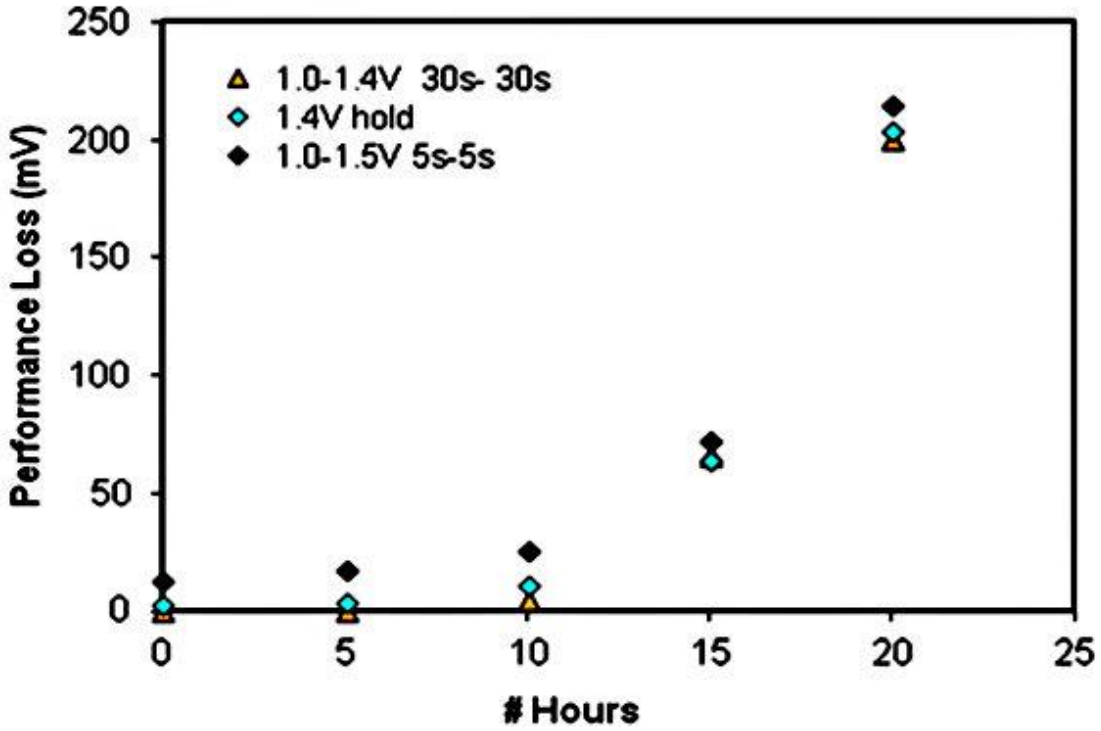

Figure 4-1**:** Evolution of performance loss of MEA 1 with time during carbon corrosion ASTs. Performance loss is taken as the decrease in cell voltage from BOL value measured at a current density of 1 A cm^{-2} during polarization experiment.

4.1.2 Fingerprint for Carbon Corrosion

It is evident from earlier studies that the degree of carbon corrosion and therefore the performance loss are affected by the nature of the accelerated stress test [75]. A fingerprint for carbon corrosion cannot be obtained by relating performance loss only to the number of cycles or hours of operation since the rate of corrosion also depends on other factors such as voltage and temperature. However, the observation of similar performance losses during each of the three ASTs above supports the conclusion that carbon corrosion is the dominant mode of degradation in each case and that the impacts of carbon corrosion on cell performance can be similar although the exact test conditions may differ.

The most direct measurement of carbon corrosion in an operating fuel cell is the amount of carbon dioxide and carbon momoxide produced which allows the total carbon loss to be calculated. However, experiments showed very little evidence of CO being produced during carbon ASTs. In order to explore whether a correlation exists between the amount of carbon corrosion and the performance loss, the voltage loss during the course of the accelerated stress test is plotted against cumulative carbon loss. The performance loss measured at 1.0 A cm^{-2} for MEA 1 during the 1.4 V hold AST is shown in Figure 4-2. Quite remarkably, even when the total carbon loss has reached as high as 6 mg, representing 30% of the initial amount present, fuel cell performance is hardly affected. However, any further corrosion begins to have a dramatic effect and cause an exponential-like rise in performance loss. It is widely accepted that when an MEA is subjected to a constant potential at 1.4 V, the main driver for degradation is carbon corrosion. Based on the assumption that no other significant degradation mechanism operates during this AST, we consider Figure 4-2 to define the performance loss due to carbon corrosion and refer to it as the carbon corrosion fingerprint for MEA 1.

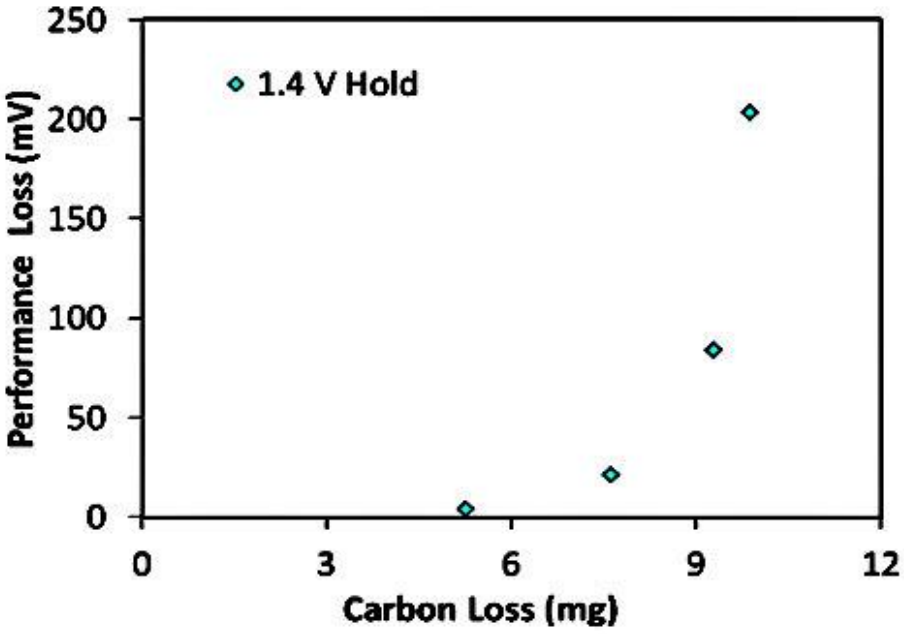

Figure 4-2: Fingerprint relationship between performance loss and cumulative carbon loss for MEA 1 obtained during AST in which cell voltage is held at 1.4 V.

4.1.3 Validation of Carbon Fingerprint with Different Carbon Corrosion ASTs

To validate the carbon corrosion fingerprint shown in Figure 4-2, performance and carbon loss data were obtained for MEA 1 using other ASTs, as discussed in Section 3.4.3.7. The performance losses of MEA 1 measured at 1.0 A cm^{-2} after being subjected to the three ASTs are plotted against carbon loss in Figure 4-3a, while the corresponding losses obtained at 1.7 A cm^{-2} are presented in Figure 4-3b. These results show that the fingerprints obtained using the two square-wave voltage cycles are virtually identical to the one measured during the 1.4 V hold accelerated stress test at both current densities. A repeat experiment was conducted for each experimental condition and found to yield identical results to that shown for each AST in Figure 4-3a. Despite having different upper potentials and cycles, the correlations of carbon loss data to performance loss are the same in all cases. This excellent agreement provides support that the AST in which the potential is held at 1.4 V can be used to determine the amount of carbon corrosion.

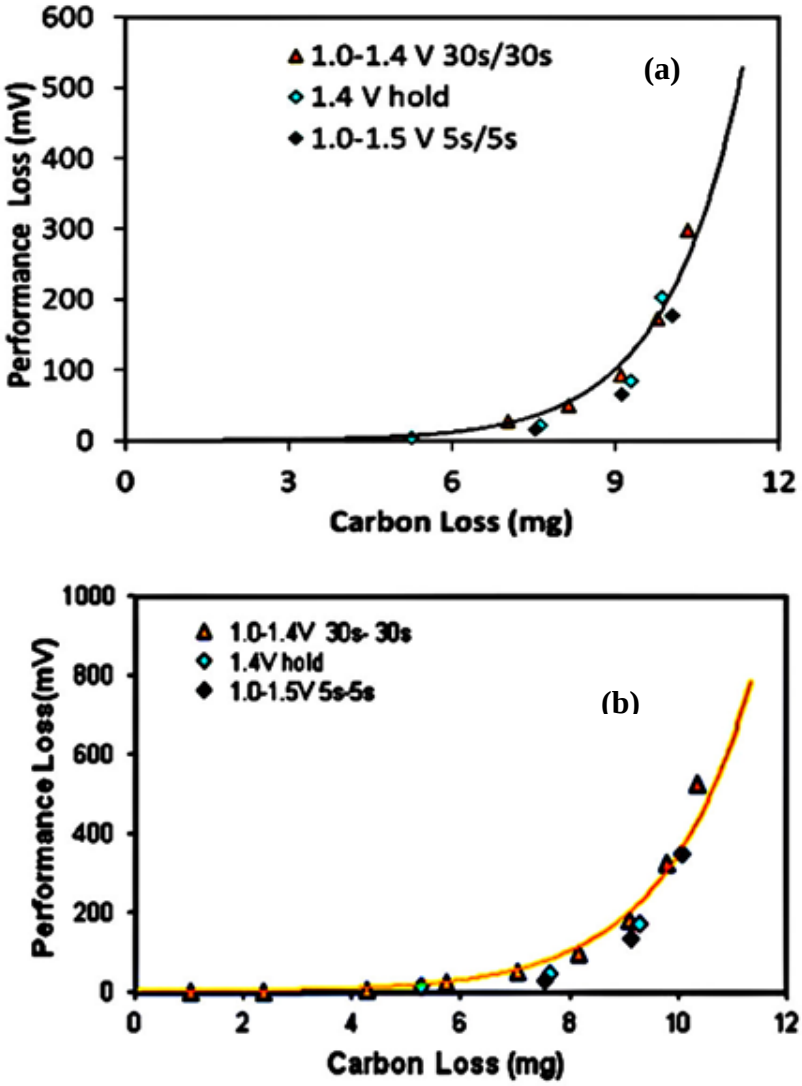

Figure 4-3: Fingerprint relation between performance loss and cumulative carbon loss for MEA 1 obtained during carbon corrosion ASTs. Performance losses are measured at current densities of (a) 1 and (b) 1.7 A cm^{-2} during polarization experiment. Solid lines correspond to empirical fingerprint expressions fitted to experimental data.

In order to use this data to de-convolute the performance loss when mixed modes of degradation are operating, an exponential function relating performance loss Y (in mV) to mass of carbon loss x (in mg) was fit to the data in Figure 4-3a to yield what is termed the 'fingerprint equation' for carbon corrosion. The resulting empirical expression and correlation coefficient (R^2) obtained at 1.0 A cm^{-2} for MEA 1 when subjected to the three carbon corrosion ASTs is presented in Section 3.4.3.7.

4.1.4 Pt Dissolution AST and Mixed Degradation ASTs

An accelerated stress test in which platinum dissolution should be the dominant degradation mode was also applied to MEA 1. This AST consisted of a square-wave cycle with lower and upper voltages of 0.6 and 1.4 V and dwell times of 27s at the lower limit and 3s at the upper limit. Pt dissolution should be the predominant mode of degradation during this test since the cell voltage is maintained at the lower voltage of 0.6 V for 90% of the time during each cycle. An upper limit of 1.4 V was used so that the results obtained could be effectively compared with those obtained after the carbon corrosion ASTs discussed in the previous Section. However, to minimize the amount of carbon corrosion, a short dwell time at the upper potential was selected to ensure that Pt dissolution is the primary mode of degradation [1, 66]. Figure 4.4a presents a comparison between the carbon loss measured during the Pt dissolution AST to that measured during the 1.0-1.4 V, 30s-30s carbon corrosion AST discussed in the previous section. Not surprisingly, the carbon loss increases with the number of cycles during both ASTs. An essentially linear dependence of the carbon loss on the number of cycles is followed over the entire course of the 0.6V-1.4V 27s-3s AST. As would be expected, the carbon loss during the Pt dissolution AST is considerably less than that during the carbon corrosion AST although it should be noted that it is not negligible. However, in view of the results of the previous section that carbon loss does not begin to significantly affect fuel cell performance until it reaches about 30% of the amount initially present, the loss of carbon during the Pt dissolution AST should have minimal impact on the performance loss.

The mixed degradation AST used in this study is favourable for both Pt dissolution and carbon corrosion by allowing long (30 s) dwell times at both the lower limit of 0.6V and upper limit of 1.4V of the square-wave cycles. The variation of the carbon loss during this AST is also included in Figure 4-4a. As would be expected, the application of this accelerated stress test leads to greater carbon loss than during the 1.0-1.4 V, 30s-30s carbon corrosion AST and the 0.6-1.4 V, 27s-3s Pt dissolution AST over the entire course of the cycling procedure. The carbon loss increases linearly over the earlier stages of the mixed degradation accelerated stress test, but begins to slow down after approximately 1000 cycles. Carbon loss during the carbon corrosion (1.0V-1.4V 30s-30s) AST exhibits similar behavior although the linear dependence persists for a longer number of cycles (~ 2000).

Since degradation should occur primarily by Pt dissolution during the 0.6V-1.4V, 27s-3s AST and by carbon corrosion during the 1.0V-1.4V, 30s-30s AST, it is interesting to compare the sum of the carbon losses during these tests to the carbon losses measured during the mixed-mode 0.6V-1.4V, 30s-30s cycles. As shown in Figure 4-4b, this sum (dashed line) is found to lie below the carbon losses during the 0.6V-1.4V, 30s-30s AST. Nevertheless, it should be possible to estimate the portion of the total performance loss due to Pt oxidation/dissolution by the application of an AST such as 0.6V-1.4V, 27s-3s square-wave cycles and the portion due to carbon corrosion by application of an AST such as 1.0V-1.4V, 30s-30s cycles. The carbon losses during the carbon corrosion (1.0V-1.4V, 30s-30s cycles) and mixed-mode degradation (0.6V-1.4V, 30s-30s cycles) ASTs are as much as 4 and 5 times, respectively, larger than that associated with Pt dissolution alone. This observation supports the use of a carbon corrosion fingerprint equation directly to estimate the effect of Pt dissolution from the total performance loss for any mixed degradation ASTs.

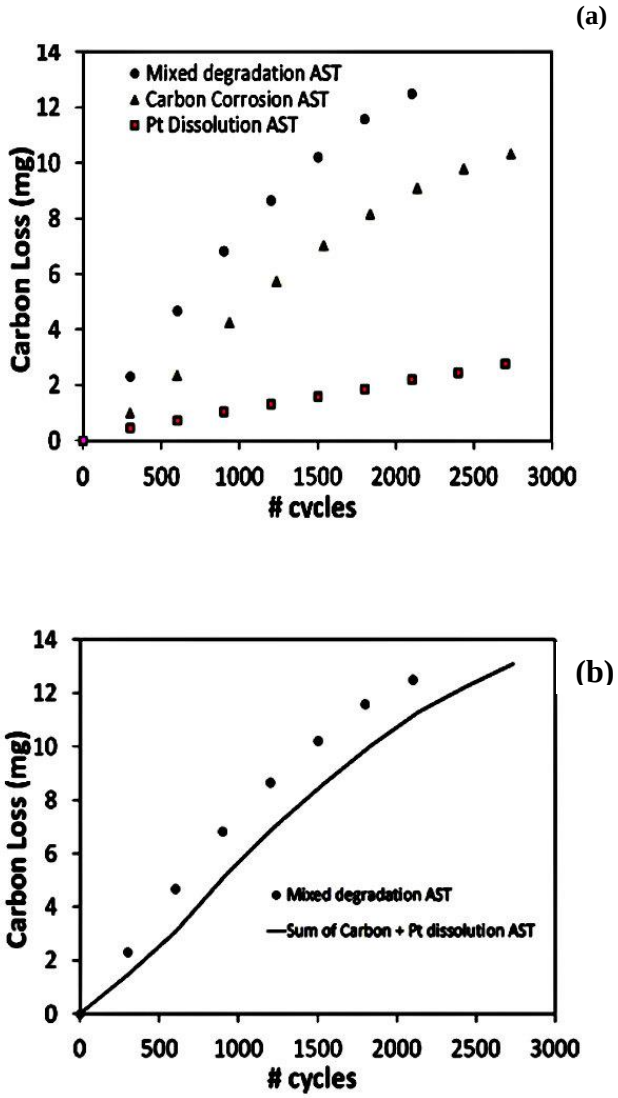

Figure 4-4: (a) Variation of cumulative carbon loss in MEA 1 with number of cycles during carbon corrosion (1.0V-1.4V 30s-30s), Pt dissolution (0.6V-1.4V 27s-3s) and mixed degradation (0.6V-1.4V 30s-30s) ASTs. (b) Comparison of carbon losses during mixed degradation test (symbols) to combined carbon losses during Pt dissolution and carbon corrosion tests (dotted line).

4.1.1 Deconvolution Technique

In this section, a method to de-convolute the contributions to the performance loss arising during a mixed degradation voltage cycle AST (0.6V-1.4V, 30s-30s square-wave cycle) is presented for MEA 1. The resulting breakdown of the performance losses at 1.0 and 1.7 A cm^{-2} using this approach are shown in Figure 4-5a and Figure 4-5b, respectively. The method is summarized as follows. First, the carbon loss from the MEA is estimated from the amount of carbon dioxide present in the exhaust gas at each sampling point during the mixed degradation AST. It is interesting that exponential functions are also found to fit the performance loss-carbon loss data very well at both current densities after this accelerated stress test (solid black curves in Figure 4-5a and Figure 4-5b). Next, the performance loss due to carbon corrosion is calculated using the carbon fingerprint equation described in Sections 4.1.2 and 4.1.3. The calculated performance loss due to carbon corrosion is then subtracted from the total mixed degradation performance loss to yield the carbon corrosion-corrected performance loss, which is attributed to Pt dissolution. Finally, this carbon corrosion-corrected performance loss is compared to the loss measured after the Pt dissolution AST (0.6V-1.4V, 27s-3s square-wave cycle).

Comparison of the experimental data after the 0.6V-1.4V, 27s-3s and 0.6V-1.4V, 30s-30s ASTs indicates that Pt oxidation/dissolution accounts for almost all the performance loss at 1.0 A cm^{-2} until completion of approximately 600 cycles (Figure 4-5a). Beyond this stage, the overall performance loss begins to rise much more sharply, whereas the Pt dissolution-induced performance loss continues to increase only very slightly. This indicates that carbon corrosion does not become significant immediately after the start of the 0.6V-1.4V, 30s-30s AST and only begins to become dominant after about 600 cycles under these conditions. The curves (solid yellow lines) obtained from the difference between the performance losses after the 0.6V-1.4V, 30s-30s and 1.0V-1.4V, 30s-30s ASTs at both current densities are in good agreement with those measured after the 0.6V-1.4V, 27s-3s

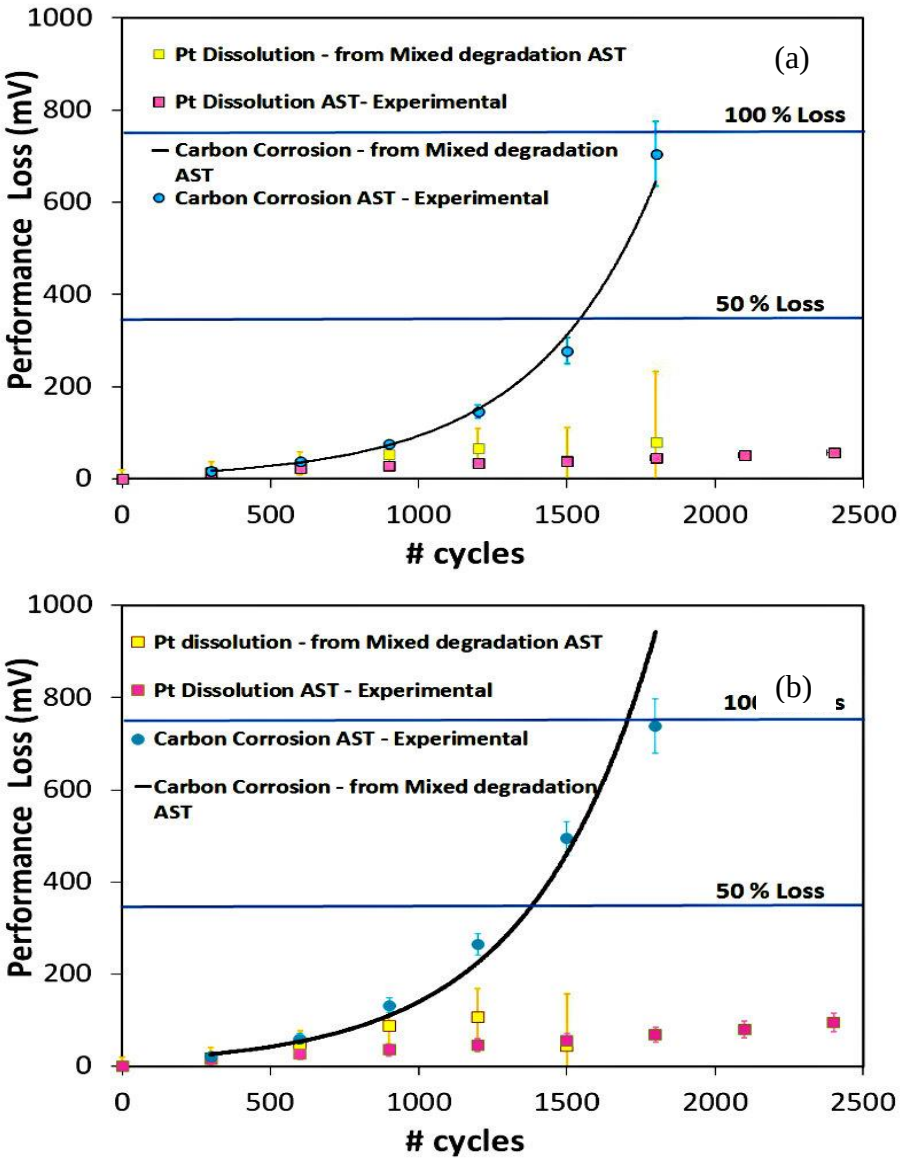

Figure 4-5: Comparison of variation of performance loss of MEA 1 with number of cycles measured during Pt dissolution AST (pink symbols) to that obtained using deconvolution method (solid yellow curve). Performance losses are measured at current densities of (a) 1 and (b) 1.7 A cm^{-2} during polarization experiment. Also included is corresponding behavior during mixed degradation test obtained from measurements (blue symbols) and empirical expressions (solid black curve) fitted to experimental data. Horizontal blue lines correspond to points where performance losses of 50 and 100 % are reached.

accelerated stress test until approximately 1500 cycles have been applied and the performance loss is close to 50%.

In order to assess the reliability of this approach to de-convolute the effects due to both degradation modes, we conducted similar analysis of performance loss at several other current densities between 0.5 and 1.7 A cm^{-2}. The results obtained at 1.7 A cm^{-2} are shown in Figure 4-5b as an example. At all of these current densities, very similar behavior to that at 1.0 A cm^{-2} is observed. Pt oxidation/dissolution contributes to virtually all of the performance loss up to about 500−600 cycles. Again, the error in inferring the contribution of Pt oxidation/dissolution from the difference in the performance losses during the 0.6V-1.4V, 30s-30s and 1.0V-1.4V, 30s-30s ASTs becomes large beyond about 1500 cycles. Thus, a performance loss of about 50% appears to be the upper limit at which the contribution of Pt oxidation/dissolution can be accurately determined on the basis of data obtained from only the 0.6V-1.4V, 30s-30s and 1.0V-1.4V, 30s-30s AST without also applying the 0.6V-1.4V, 27s-3s AST. However, it should be noted that most of the accelerated drive cycle tests used to evaluate PEM fuel cell performance do not usually continue beyond 50% performance loss in the MEA. In this case, the error in estimating the contribution of Pt oxidation/dissolution from the difference in the performance losses after 0.6V-1.4V, 30s-30s and 1.0V-1.4V, 30s-30s ASTs alone appears acceptable.

A factor that may contribute to the error in estimating the contribution of Pt oxidation/dissolution in the later stages of these experiments is that the performance losses measured during the 0.6V-1.4V, 30s-30s and 1.0V-1.4V, 30s/30s ASTs both become large. Since the difference between two large quantities is being used to estimate the much smaller performance loss due to Pt oxidation/dissolution, a significant error in this estimation can arise from the inevitable experimental errors associated with the measurement of the performance losses during the 0.6V-1.4V, 30s-30s and 1.0V-1.4V, 30s/30s ASTs. In this situation, it is preferable to determine the contribution of Pt

oxidation/dissolution directly from an AST such as 0.6V-1.4V, 27s-3s square-wave cycles in which Pt dissolution is the dominant degradation mode.

4.1.2 Application of Deconvolution Method to different MEAs

Repeat experiments with each of the carbon corrosion ASTs for MEA 1 showed good reproducibility in generating the empirical correlations. In order to further assess the value of the fingerprint equations generated, it is important to evaluate their ability to predict the performance loss of other types of MEAs. Consequently, fingerprint curves and expressions for carbon corrosion in MEA 2 and MEA 3 were generated. As with MEA 1, the measurements obtained on these MEAs were found to be very reproducible. Also, very similar trends were observed with these MEAs.

To compare the performance losses obtained during the three MEAs, the loss of voltage in each MEA is normalized with respect to its BOL cell voltage since the degradation of a MEA is affected by its initial state. Thus, the following relation is used:

$$\%\ Performanœ\ loss = \frac{V_{BOL} - V_{n^{th}cycle}}{V_{BOL}}\ x\ 100 \qquad (4\text{-}1)$$

where V_{BOL} is the cell voltage of the BOL sample and $V_{n^{th}cycle}$ is the voltage after the n^{th} cycle. In addition, the carbon losses in a MEA are expressed as percentages of the initial mass present to account for the differences in the amount initially present in the various MEAs. Figure 4-6a presents plots of the percentage performance loss of each MEA versus the percentage carbon loss up to its EOL state obtained from direct experimental measurements at 1.0 A cm^{-2}. The corresponding results obtained at 1.7 A cm^{-2} are shown in Figure 4-6b. Also included are the data obtained for MEA 1 after application of the 1.0-1.4 V, 30s-30s and the constant 1.4 V ASTs. All results shown here were obtained for ASTs, which favour carbon corrosion in order to obtain the fingerprint relations. The 1.0-1.5 V, 5s-5s ASTs were repeated for each MEA to assess the reproducibility of the protocol

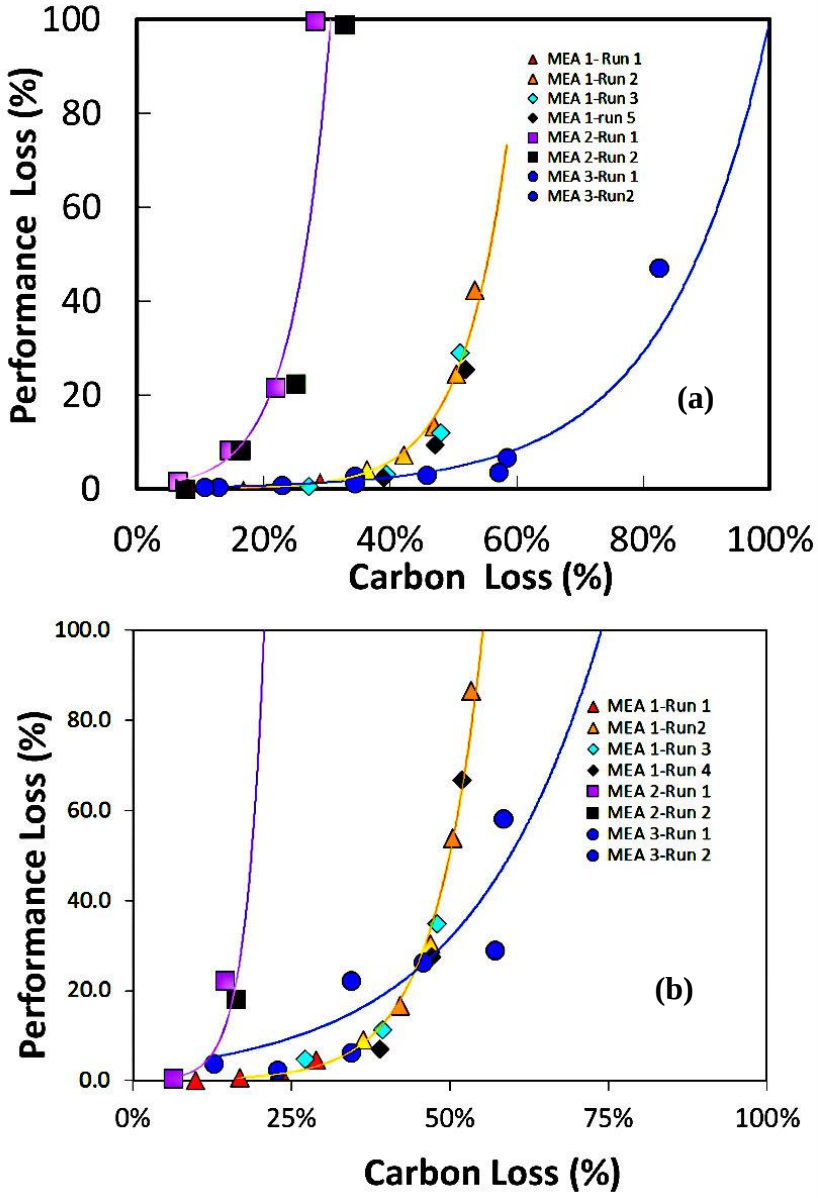

Figure 4-6: Fingerprint relations between percent performance loss and percent carbon loss for MEA 1, MEA 2 and MEA 3 obtained during carbon corrosion ASTs. (a) Performance losses are measured at current densities of (a) 1.0 and (b) 1.7 A cm^{-2} during polarization experiment. Measurements are denoted by symbols, while solid lines (yellow – MEA 1, purple – MEA 2, blue – MEA 3) show behavior corresponding to empirical fingerprint expressions fitted to experimental data.

used. The results from these experiments are also included in Figure 4-6 and show excellent reproducibility in all cases.

Although the plots in Figure 4-6 for the three MEAs are similar to each other in shape and follow exponential behavior, they do not fall along a single universal curve. The behavior for each MEA follows a separate curve, revealing that a separate fingerprint equation is required in each case. Plots of the exponential expressions fitted to the experimental data relating % performance loss to % carbon mass loss in MEA 1 and MEA 2 during the 1.0 − 1.5 V, 5s-5s ASTs are included as the solid curves in Figures 4-6 a and b. The parameters for these expressions are also listed in Table 4-1. As with MEA 1, exponential functions are found to fit the experimental data very well for MEA 2 and MEA 3. The fact that the behavior of each MEA follows a separate curve indicates that the performance loss due to carbon corrosion depends on other factors such as the loading level of cathode Pt/C catalyst and the structure and chemistry of the membrane and GDL. Nevertheless, the results shown in this study hold promise that the approach proposed here of developing fingerprint expressions relating performance loss to carbon loss and deconvoluting the contributions from different degradation modes through combined analysis of specifically chosen ASTs can be extended to a wide variety of MEAs.

Table 4-1: Empirical equations relating performance loss Y measured at 1.0 A cm^{-2} to carbon mass loss x.

	MEA	AST	Fingerprint equations*	R^2
Figure 4-3a	MEA 1	1.0 − 1.5 V, 5s −5s 1.0 − 1.4 V, 30s −30s 1.4 V hold	$Y=0.174\ e^{0.70x}$	0.98
Figure 4-6a	MEA 1	1.0 -1.5 V 5s-5s	$Y = 0.025\ e^{13.695x}$	0.98
	MEA 2	1.0 − 1.5 V, 5s − 5s	$Y = 0.605\ e^{16.69x}$	0.97
	MEA 3	1.0 − 1.5 V, 5s −5s	$Y = 0.211\ e^{6.16x}$	0.98

* In Figure 4-3a, Y denotes performance loss measured in mV and x denotes carbon mass loss expressed in mg. In Fig. Figure 4-6a, Y denotes % voltage loss and x denotes fraction of the initial carbon mass that is lost.

4.2 Kinetic Model for Carbon Corrosion During ASTs

In this section, a model is proposed to describe the mechanism of carbon corrosion in the cathode catalyst layer during carbon corrosion ASTs. The model is assessed by comparing its predictions with experimental results obtained during different carbon corrosion ASTs. Finally, the limitations of the proposed model when applied to a mixed degradation AST are discussed. The experimental procedures relevant to this section are described previously in Chapter 3:

1 MEA preparation – Section 3.3;
2. Cell conditioning – Section 3.4.3.1;
3. Cyclic voltammetry – Section 3.4.3.2;
4. Polarization curve measurement – Section 3.4.3.4;
5. Current interruption method – Section 3.4.3.6;
6. ASTs – Section 3.4.3.7;
7. Recovery – Section 3.4.3.8;
8. CO_2 measurement – Section 3.4.3.8;
9. BET surface area analysis – Section 3.4.3.8.

4.2.1 Mechanistic model development

Kinetic model development requires a comprehensive understanding of the process mechanism and the formulation of elementary steps. Different mechanistic kinetic models based on Gallagher and fuller were simplified to describe the kinetics of electrochemical oxidation of carbon support during PEM fuel operation [44]. In order to study the kinetics of carbon loss, various elementary steps and different mechanistic models reported by Gallagher is investigated and important reaction steps were identified. Scheme of modeling procedure is given in figure below. The detail description of the model is presented in the following sections.

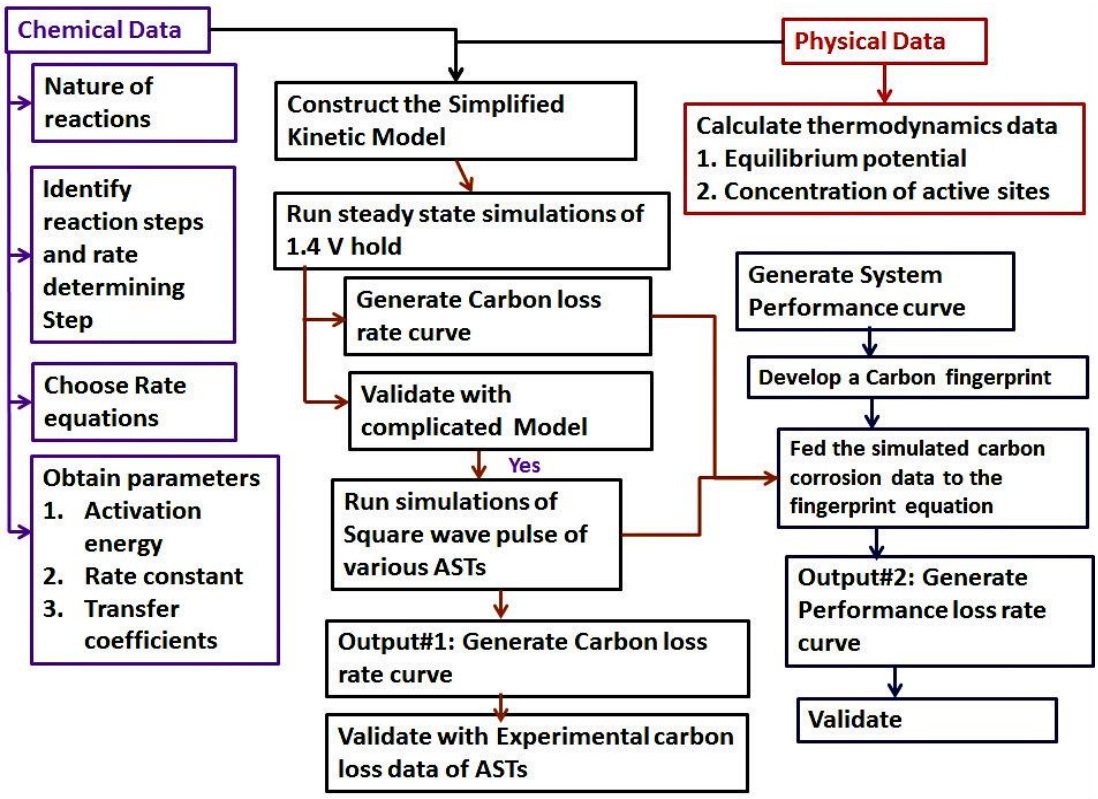

Figure 4.7 Steps required for a mechanistic modeling of the catalyst layer

4.2.2 Carbon Corrosion Model Development

The most comprehensive model to date for the kinetics of carbon corrosion in fuel cell catalyst layers was presented by Gallagher and Fuller [95]. This model describes the electrode response, carbon weight loss and surface oxide growth during the electrochemical oxidation of graphitic carbon as a function of time, temperature and potential. Due to the relevancy of this topic to the subject of this thesis, an important objective here is to apply this model to analyze the experimental data obtained from the various carbon corrosion ASTs of the current study. Despite its success in providing insight into carbon corrosion, the proposed reaction mechanism is quite complicated with many reaction steps, making it somewhat unwieldy particularly for practical design of MEAs and monitoring of their performance during operation. Consequently, before the full Gallagher and Fuller model is applied to the carbon corrosion ASTs, a detailed sensitivity analysis is conducted to determine whether it can be simplified without any adverse effect on its accuracy.

However, it is best to first begin with a brief description of the assumptions and reaction steps involved in the full mechanism. Perhaps its most basic feature is the existence of two types of sites on the carbon support surface. One type of site denoted as # is active for the rate-determining step of CO_2 formation, while the other type denoted as * is involved both in CO_2 formation and the formation of various carbon oxides on the support surface [44, 95]. A key aspect of the mechanism is that the formation of these oxides does not cause any net loss of # sites. The reaction steps included in the mechanism are listed in Table 4-2**.** The number designation for these steps that appears in the left column is that given by Gallagher and Fuller[95]. The formation of CO_2 proceeds via steps 1 and 2. The process begins with the oxidation of # sites to form a $C^{\#}OH$ surface oxide (step 1) and the reversible adsorption of water on other # sites to form $C^{\#}(H_2O)_{ads}$ (step 2a). These two surface species combine together to form a $C^{\#}OC^{\#}OH$ intermediate in step 2b which is the slowest and rate-determining step for CO_2 formation. The $C^{\#}OC^{\#}OH$ intermediate then goes on and begins a sequence of anodic oxidation steps (2c-2e) that yields CO_2. Steps 3-7

make up a competing pathway that leads to the reversible formation of carbon oxide $C_x^{\#}O$ and to the irreversible formation of $C_x^{\#}O_3$, quinone ($C_x^{*}O_2$) and hydroquinone $C_x^{\#}(OH)_2$. These reactions have a deleterious effect on CO_2 formation via step 2 by consuming some of the $C^{\#}OH$ intermediate and passivating the carbon support surfaces. Of course, the most direct effect of this passivation on fuel cell operation is to inhibit oxygen reduction.

Table 4-2: Reactions steps in full Gallagher and Fuller model [95].

No	Reaction	Equation
1	$C^{\#} + H_2O \rightarrow C^{\#}OH + H^+ + e^-$	(4-2)
2a	$C^{\#} + H_2O \leftrightarrow C^{\#}(H_2O)_{ads}$	(4-3)
2b	$C^{\#}(H_2O)_{ads} + C^{\#}OH \rightarrow C^{\#}OC^{\#}OH + 2H^+ + 2e^-$	(4-4)
2c	$2C^{\#}OC^{\#}OH + 3C^{*} + 3H_2O \rightarrow C^{*}O(C^{*}OOH)_2 + 2C^{\#} + 2C^{\#}OH + 4H^+ + 4e^-$	(4-5)
2d	$C^{*}O(C^{*}OOH)_2 \rightarrow C^{*}OOH + C^{*}O + * + CO_2 + H^+ + e^-$	(4-6)
2e	$C^{*}OOH \rightarrow * + CO_2 + 4H^+ + 4e^-$	(4-7)
3	$xC^{\#} + H_2O \leftrightarrow C_x^{\#}O + 2H^+ + 2e^-$	(4-8)
4	$2C^{\#}OH + (x-2)C^{\#} + H_2O \rightarrow C_x^{\#}O_3 + 4H^+ + 4e^-$	(4-9)
5	$C_x^{\#}O + C^{*}O \rightarrow C_x^{*}O_2 + C^{*}$	(4-10)
6	$2C^{\#}OH + (x-2)C^{\#} + H_2O + C_x^{\#}O_2 \rightarrow C^{\#}{}_xO_2 + C^{\#}{}_xO_3 + 4H^+ + 4e^-$	(4-11)
7	$C_x^{\#}(OH)_2 \leftrightarrow C_x^{\#}O_2 + 2H^+ + 2e^-$	(4-12)

The first goal of this section is to investigate whether this model can be simplified for the purposes and experimental conditions of the present study. As shown in the previous section, the analysis revealed a strong correlation between the MEA performance loss and mass of carbon lost from the catalyst layer during the course of the carbon corrosion ASTs. It should also be recalled that the carbon loss during the ASTs is measured from the

amount of CO_2 that is formed. Consequently, the portion of the reaction mechanism proposed by Gallagher and Fuller that is most relevant to the analysis of the ASTs in the present study involves steps 1 and 2. Furthermore, the verification of the presence of the various surface oxides formed via steps 3-7 on the carbon support, let alone determination of the amounts formed, would be a very difficult task, particularly if it is to be done on a routine basis during MEA 4 design and/or monitoring fuel cell operation. For these reasons, it seems reasonable to investigate whether the carbon loss during the ASTs can be satisfactorily predicted by a simplified version of Gallagher and Fuller model involving only steps 1 and 2. Since step 2b is considered to be rate-determining for CO_2 formation, then only steps 1, 2a and 2b would have to be included in this simplified model.

The accuracy of the simplified model is first assessed by comparing its predictions to those of the full Gallagher and Fuller model for conditions described in the original study [95].. The model parameters describing the rates of steps 1, 2a and 2b in the simplified model remain unchanged from those used in the full model. The calculation of the carbon loss is the same in both models and is described as follows. A material balance on the moles of carbon N_c yields the following equation for the instantaneous rate of change of carbon mass [44]:

$$\frac{\partial N_c}{\partial t} = -r_2 \, S \, M \, N_c \qquad (4\text{-}13)$$

where N_c is number of moles of carbon present per unit geometric area (mol cm_{geom}^{-2}), r_2 is the rate of formation of CO_2 (mol cm^{-2} s^{-1}), S is the specific surface area (cm^2 g^{-1}) of the carbon determined from BET measurement and M is the molecular weight of carbon (g-mol^{-1}). A couple of points are worth noting regarding the use of r_2 in Equation (4-13). First, r_2 is the combined rate of steps 2a-e in the full model and represents the rate of generation of CO_2. Secondly, as noted above, the carbon loss during oxidation can only be measured from the amount of CO_2 that is formed. No reliable method exists to measure the amount of oxidized carbon that remains on the surface as oxides that are formed by steps 3-7 of the

full model. Consequently, only r_2 is used in equation (4-13). Material balances for the different oxide species considered in both the full and simplified models are presented in Table 4-3.

Table 4-3: Material Balances used in the model [95].

Gallagher and Fuller	Simplified Model
$[*] = [*]_{vac} + [C*O]$	
$[\#] = [\#]_{vac} + [C^{\#}OH] + x([C^{\#}xO] + [C^{\#}x(OH)_2] + [C^{\#}xO_2] + [C^{\#}xO_3])$	$[\#] = [\#]_{vac} + [C^{\#}OH])$
$\theta_l^s = \left[\frac{l}{s}\right]; \theta_{vac}^* = \left[\frac{[*]_{vac}}{[*]}\right]$	$\theta_l^s = \left[\frac{l}{s}\right];$
$\theta_{cov}^{\#} = 1 - \theta_{vac}^{\#} = \theta_{COH}^{\#} + x(\theta_{C^{\#}xO}^{\#} - \theta_{C^{\#}xO_2}^{\#} - \theta_{C^{\#}xO_3}^{\#})$	$\theta_{cov}^{\#} = 1 - \theta_{vac}^{\#} = \theta_{COH}^{\#}$
$\frac{\partial \theta_{C^{\#}OH}}{\partial t} = \frac{r_1 - 2(r_4 + r_6)}{[\#]}$	$\frac{\partial \theta_{C^{\#}OH}}{\partial t} = \frac{r_1 - r_2}{[\#]}$
$\frac{\partial \theta_{C_xO}^{\#}}{\partial t} = \frac{r_3 + r_5}{[\#]}$	
$\frac{\partial \theta_{CO}^{*}}{\partial t} = \frac{0.5*r_2 + r_5}{[*]}$	
$\frac{\partial \theta_{C_xO_3}^{\#}}{\partial t} = \frac{r_4 + r_6}{[\#]}$	
$\frac{\partial \theta_{C_xO_2}^{\#}}{\partial t} = \frac{r_7 - r_5}{[\#]}$	
$\frac{\partial \theta_{C_x(OH)_2}^{\#}}{\partial t} = \frac{-r_7}{[\#]}$	

The complete set of rate expressions for steps 1-7 in the full model can be found in the paper by Gallagher and Fuller [95]. For the purposes of this analysis, it suffices to present the rate expressions for steps 1 and 2 that comprise the proposed simplified model:

$$r_1 = k_1 \theta_{vac} \exp[\frac{\alpha_1 F}{RT}(V\text{-}U_1)\text{-}g\theta_{cov}] \quad (4\text{-}14)$$

$$r_2 = k_2 \theta_{vac} \theta_{cov} \left(\left[\frac{p_0}{p_o^{ref}}\right]\right) \exp[\frac{\alpha_2 F}{RT}(V - U_2)] \quad (4\text{-}15)$$

$$k_i = k_i^0 \exp[\frac{-E_{a,i}}{RT}) \quad (4\text{-}16)$$

where r_i is the rate (mol cm^{-2} s^{-1}) of reaction *i*, θ_{vac} is the fraction of surface sites that are vacant or free, θ_{cov} is the fraction of sites covered by $C^{\#}OH$, V is the electrode potential (V) on the standard hydrogen scale, p_0 is the partial pressure (kPa) of water vapor and p_o^{ref} is a reference pressure (270 Kpa) for water vapor. The other parameters in these expressions are: equilibrium potential U_i (V) of reaction *i*, transfer coefficient α_i and activation energy $E_{a,i}$ (J mol^{-1}) of reaction *i*, pre-exponential rate constant k_i^0 (mol cm^{-2} s^{-1}) and rate constant k_i (mol cm^{-2} s^{-1}) for reaction *i*, Frumkin factor g, Faraday constant F (96485.3 C mol^{-1}), gas constant R (8.314 J $mol^{-1}K^{-1}$) and temperature T (K). r_2 is equivalent to the rate of step 2b which is rate-determining. Since step 2a is assumed to be much faster than step 2b, it is considered to be at pseudo-equilibrium and the equilibrium constant for step 2a is incorporated within the rate constant k_2 appearing in equation (4-18). The Frumkin factor g was set equal to three by Gallagher and Fuller since this value gave the best fit of their model to the experimental data.

The concentration of the active reaction sites for either the full or partial mechanism or the specific surface area *S* depend on the original carbon black material used and the subsequent heat treatment in an argon atmosphere prior to incorporation into the MEA 4. Both of these quantities can be estimated from knowledge of the temperature of this heat treatment step. To estimate the concentration of total active sites on the carbon support, the following empirical function reported by Gallagher and Fuller is used [95]:

$$[\#] = 70.3 \exp(-0.0075\, T_{(\text{heat trea ted})}) \quad (4\text{-}17)$$

where [#] is given in units of mol m^{-2}. *S* was found by Gallagher and Fuller to vary linearly with the heat treatment temperature and can be obtained from a plot presented in their paper (Fig. 8 in ref. [95]). Since Gallagher and Fuller fitted their model to data collected on

carbon that had been heat treated at 2173°K, [active sites] and *S* are set to 5.88 x 10^{-6} mol m^{-2} and 100 m^2 g^{-1}, respectively, for the purpose of assessing the accuracy of the simplified model. It should be noted that the carbon supports used in the present study were heat treated at 2200°C. Thus, different values of [active sites] and *S* are used when the carbon corrosion model is applied to the experimental data obtained during the ASTs of the present study. S is obtained using BET analysis.

The equilibrium potential U_2 of step 2 depends on temperature according to the following expression used by Gallagher and Fuller [95]:

$$U_2 = -0.00023T + 0.2326 \quad (4\text{-}18)$$

All the electrochemical parameter values used in the simplified carbon model are the same as those obtained by Gallagher and Fuller [95]. They are given in Table 4-3.

Table 4-4: Parameters used in fitting the simplified model to experimental data.

Parameters	Symbol	Value	Units
Transfer coefficient of step 1	α_1	0.35	no units
Transfer coefficient of step 2	α_2	0.65	no units
Activation energy for step 1	$E_{a,1}$	10	kJ mol^{-1}
Activation energy for step 2	$E_{a,2}$	110	kJ mol^{-1}
Rate constant for step 1	k_1	2.35 x 10^{-16}	mol cm^{-2} s^{-1}
Rate constant for step 2	k_2	9.50 x 10^{-3}	mol cm^{-2} s^{-1}
Equilibrium potential of step 1	U_1	1	V
Equilibrium potential of step 2	U_2	0.15	V

$C^{\#}OH$ formation is calculated using equation (4-17) and the reaction rate for CO_2 formation is calculated with equation (4-14). Carbon loss is calculated using equation (4-13) once equation (4-15) is used for r_2. The values obtained from equations (4-17) and (4-18) are

used to obtain U and [#], respectively. The carbon surface is assumed to be completely unoxidized at the outset of each AST before cycling.

4.2.3 Accuracy of the Simplified Model

To assess the accuracy of the simplified model, comparisons were made between the simulations of the electrode response to various ASTs using this model to that obtained using the full model. Figure 4-7 shows the predictions of the two models on the evolution of the carbon mass loss over the course of an AST in which the cell voltage is held fixed at 1.4 V. Model simulation was done for 18 h of operation by keeping the cell potential constant at 1.4 V hold at 60^0C for H_2 and N_2 conditions. Although the curve obtained using the simplified model does not perfectly overlay that of the full model, the difference is very small even after 18 h. Comparisons of predictions by the two versions of the model for other conditions showed similar excellent agreement. Based on these comparisons, one can conclude that the simplified model is accurate enough for use in analyzing the carbon corrosion ASTs of the current study.

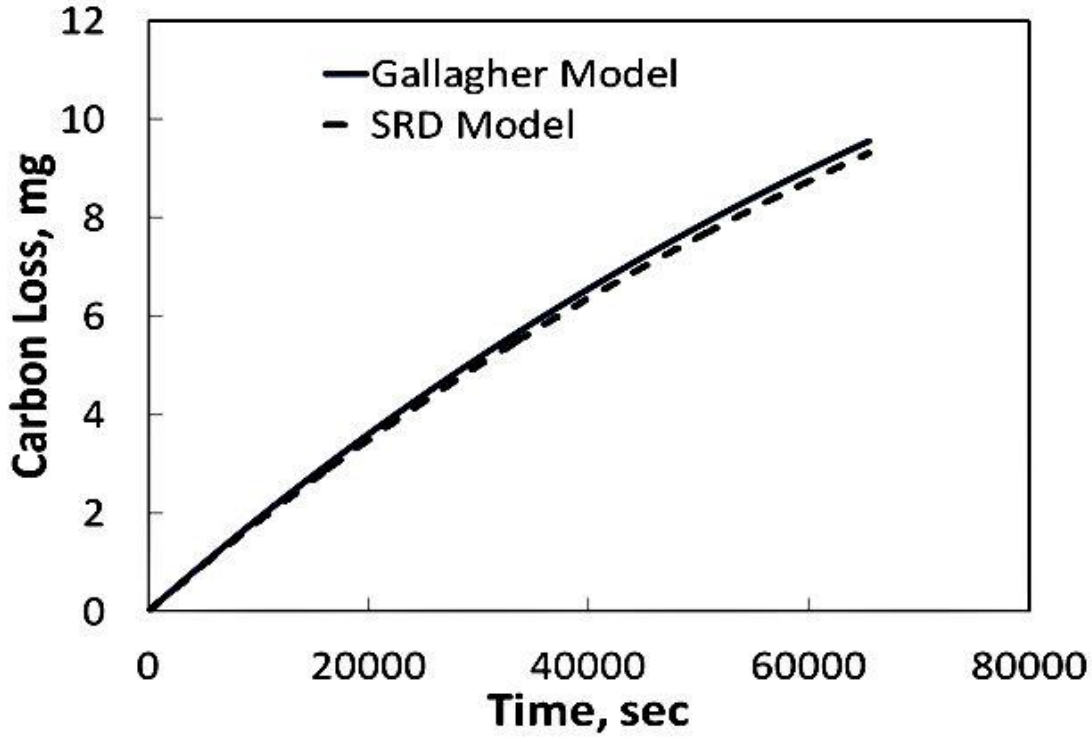

Figure 4-8: Comparison of the evolution of carbon loss during an AST in which the cell voltage is held constant at 1.4 V computed using the full Gallagher and Fuller model [95] and the simplified model presented in this study.

4.2.3.1 COH Coverage

Figure 4-8 shows a comparison between θ_{cov} over the course of the constant voltage-AST at 1.4 V predicted by the simplified and complete models. Once again, good agreement between the two versions of the model is obtained. The rate of carbon loss is beginning to tail off near the end of the 1.4 V hold AST (Figure 4-7), whereas the coverage of active sites is accelerating at the end. This growth in θ_{cov} shows that the rate at which, it is being consumed is falling behind its rate of production.

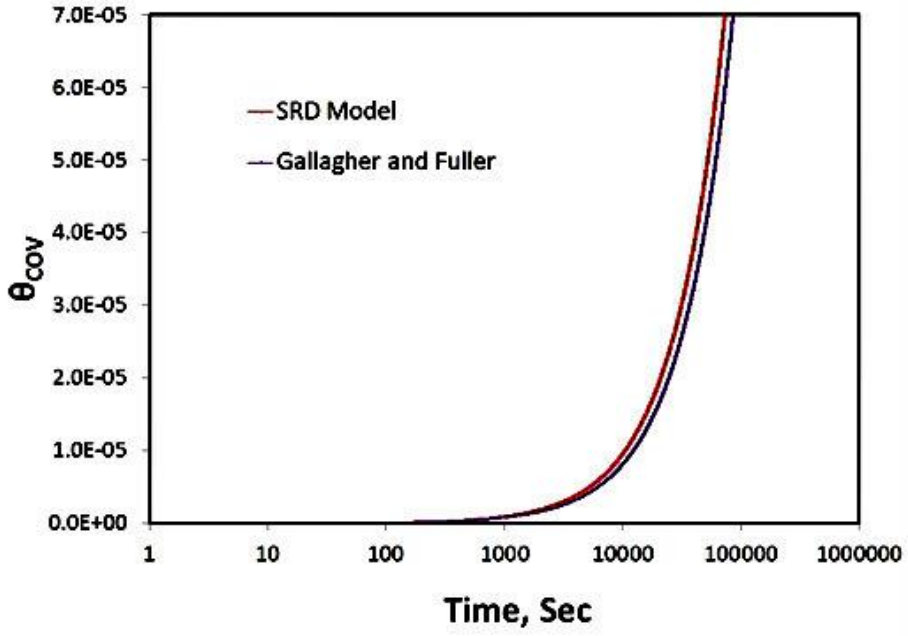

Figure 4-9: Variation in COH sites during AST of 1.4 V hold as computed by the simplified carbon corrosion model presented in this study.

4.2.4 Validation of Carbon Loss Measurement for Different ASTs

In order to validate the simplified model against experimental data, the carbon loss measured during an AST involving square-wave cycles between 1.0 and 1.5 V with 5s/5s dwell times is plotted in Figure 4-10a along with the curve calculated using the model for the identical conditions. The results show excellent agreement between the experimental and computed curves. It is important to emphasize that all model parameter values are identical to those reported by Gallagher and Fuller [95] or are adjusted in the case of [#] and *S* using the relations given by Gallagher and Fuller to account for the fact that the heat treatment step used to prepare the carbon support in the current study was carried out at 2200°C. Thus, the computed curve is obtained without any fitting of the simplified model to the experimental data and so represents a true prediction of the model. A closer examination of Figure 4-9a reveals that the model overpredicts the carbon loss slightly during the first 1000 cycles of the AST, but comes into excellent agreement thereafter.

Carbon loss observed during the first 1000 cycles amounts to less than 6% of the total carbon loss measured.

Also included in the plot are the experimental results obtained during four other related ASTs. The lower limit (1.0 V) and dwell times (5 s/5 s) of the square-wave voltage cycle input signal are identical for these five ASTs. They differ only with regard to the upper limit, which varies over the narrow range from 1.42 to 1.5 V. The results of these ASTs with their experimental comparision are provided in Appendix C. The carbon loss observed throughout the AST when the voltage is increased up to 1.5 V is significantly higher than during the other carbon corrosion ASTs. The effect of the upper limit on carbon loss is particularly striking. A relatively small increase from 1.42 V to 1.5 V more than doubles the carbon loss at comparable points throughout the AST. Repeated cycling of the potential of the fuel cell cathode above 1.0 V promotes the corrosion of the carbon support. In such cases, it has previously been shown that non-catalyzed oxidation of a significant portion of the carbon on the catalyst layer surface likely occurs during the ASTs and the remaining carbon tends to agglomerate and shrink [41, 44, 74, 95, 135]. Although carbon corrosion is the predominant mode of MEA 4 degradation during these ASTs, a small amount of dissolution of the Pt catalyst will still occur when the potential is cycled above 1.0 V [92, 136]. Such degradation of the catalyst layer leads to losses in conductivity within the MEA 4 and cell voltage and ultimately to catastrophic MEA failure in extreme cases.

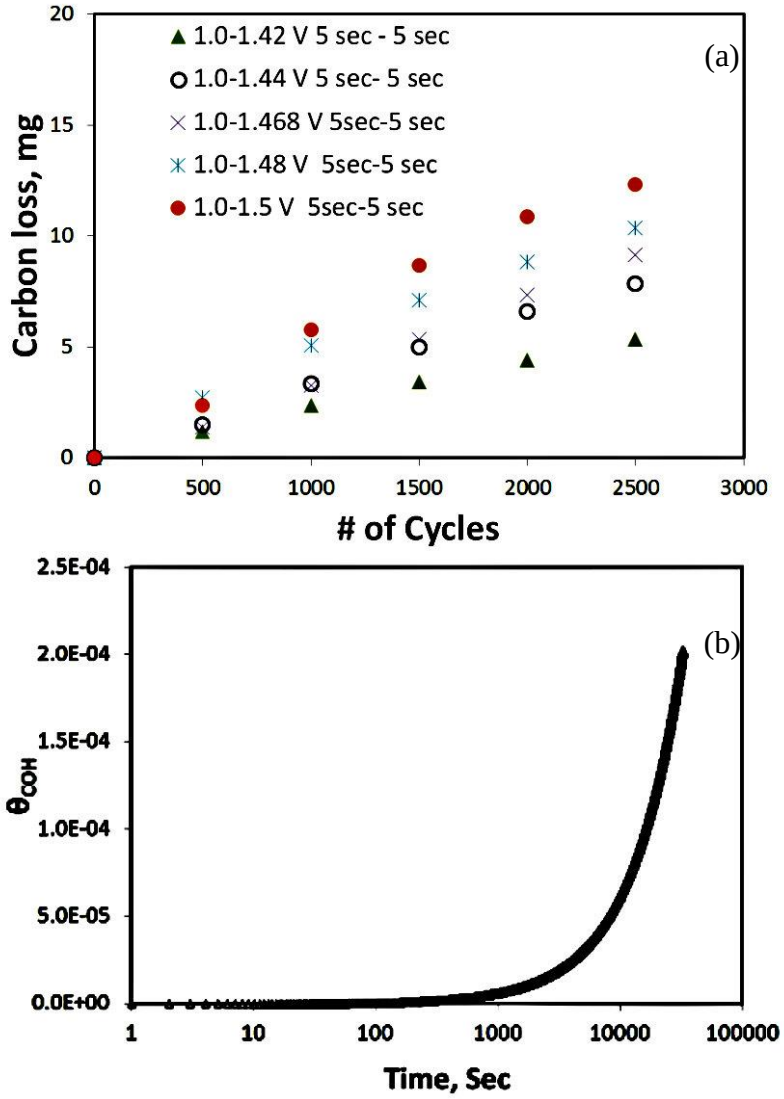

Figure 4-10: (a) Experimental and computed carbon loss measured during various carbon corrosion ASTs having lower limits of 1.0 V, dwell times of 5 s/5 s and upper limits varying between 1.4 and 1.5 V. The operating conditions during these ASTs are listed in Table 3.2. (b). Variation in COH sites over the course of 1.0 -1.5 5s/5s V AST as simulated using the simplified carbon corrosion model.

The validity of the simplified model can be further assessed by applying a t-test and analysis of variance (ANOVA) to the experimental and model data for carbon loss collected from these ASTs to determine whether the differences between the two are statistically significant. The results of these analyzes for the various ASTs are presented in Table 4-5. A p-value obtained from a t-test that is greater than 0.05 indicates that the mean differences between model predictions and experimental data are not statistically significant. The statistical analyzes show that the threshold for the p-value is easily met in all of the ASTs of this study, indicating that the differences between the experimental and model data are not statistically significant in any of these cases. In fact, with the exception of the AST involving square-wave cycles between 0.6 V and 1.4 V with 30 s/30 s dwell times, the p-value of 0.46 in t-test. The lower p-values obtained for this AST are expected since Pt dissolution as well as carbon corrosion should occur during these cycles, unlike the other cases listed in Table 4-5 where carbon corrosion is predominant. Since the simplified model only accounts for carbon corrosion, a very high p-value for the 0.6 - 1.4 V AST would in fact be worrisome. In summary, these statistical results provide further evidence of the suitability of the simplified carbon corrosion model to predict the carbon loss measured during the carbon corrosion ASTs.

Testing the efficacy of the simplified model to predict carbon loss or performance loss by conducting individual t−tests on each of the parameters may not be sufficient enough to accept or reject the model prediction. Even if we conduct each test at $\alpha = 0.05$ level, the overall probability of incorrectly rejecting H_0 (the probability of a Type I error) can be larger than 0.05. Hence, the larger the number of predictors in the model, the higher is the probability that at least one of the hypothesis tests will give an incorrect conclusion. Instead, we use ANOVA, which encompasses both model-predicted and experimental data sets and test hypotheses. F_{obs} are obtained by calculating the ratio between variance between groups (MSB) and the variance within the gropus MSW for each AST from the ANOVA table. The critical F-value is decided using an F table for $\alpha = 0.05$.

Table 4-5: Results of ANOVA, t-test and F-test analyzes of the simplified carbon corrosion model.

ANOVA test					t-Test: Two-Sample assuming unequal variances			
Carbon Corrosion Model								
Cycle	F_{obs}	$F_{critical}$ α =0.05	p-value	Hypothesis	p va ue	$t_{critical}$ α =0.05	$t_{statistic}$	Hypothesis
1.0 -1.4 V 30s/30s	88.47	9.55	0.002	$F_{obs} > F_{critical}$ – Reject H_0	0.96	2.3	0.04	$t_{statistic} < t_{critica}$ Accept H_0
1.0 -1.42 V 5s/5s	49.31	9.55	0.01	$F_{obs} > F_{critical}$ - Reject H_0	0.68	2.3	0.42	$t_{statistic} < t_{critica}$ Accept H_0
1.0 -1.44 V 5s/5s	51.74	9.55	0.01	$F_{obs} > F_{critical}$ - Reject H_0	0.97	2.3	0.02	$t_{statistic} < t_{critica}$ Accept H_0
1.0 -1.468 V 5s/5s	57.70	9.55	0.004	$F_{obs} > F_{critical}$ - Reject H_0	0.88	2.3	-0.15	$t_{statistic} < t_{critica}$ Accept H_0
1.0 -1.48 V 5s/5s	49.23	9.55	0.005	$F_{obs} > F_{critical}$ - Reject H_0	0.82	2.3	-0.23	$t_{statistic} < t_{critica}$ Accept H_0
1.0 -1.5 V 5s/5s	100.96	9.55	0.001	$F_{obs} > F_{critical}$ - Reject H_0	0.90	2.3	-0.13	$t_{statistic} < t_{critica}$ Accept H_0
0.6 -1.4 V 30s/30s	9.23	9.55	0.05	$F_{obs} < F_{critical}$ – Fail to Reject H_0	0.19	2.3	2.3	$t_{statistic} < t_{critica}$ Accept H_0 but case is very weak
Performance Loss Model fit								
Cycle	F_{obs}	$F_{critical}$	p-value	Hypothesis	p-value	$t_{critical}$ α =0.05	$t_{statistic}$	Hypothesis
1.0 -1.4 30s/30s	191.68	9.55	0.001	$F_{obs} > F_{critical}$ – Reject H_0	0.90	2.3	-0.11	$t_{statistic} < t_{critica}$ Accept H_0
1.0 -1.42 V 5s/5s	15.25	9.55	0.02	$F_{obs} > F_{critical}$ - Reject H_0	0.97	2.3	0.03	$t_{statistic} < t_{critica}$ Accept H_0
1.0 -1.44 V 5s/5s	43.54	9.55	0.06	$F_{obs} > F_{critical}$ - Reject H_0	0.90	2.3	0.11	$t_{statistic} < t_{critica}$ Accept H_0
1.0 -1.468 V 5s/5s	50.09	9.55	0.004	$F_{obs} > F_{critical}$ - Reject H_0	0.97	2.3	-0.02	$t_{statistic} < t_{critica}$ Accept H_0
1.0 -1.48 V 5s/5s	50.13	9.55	0.004	$F_{obs} > F_{critical}$ - Reject H_0	0.86	2.3	0.17	$t_{statistic} < t_{critica}$ Accept H_0
1.0 -1.5 V 5s/5s	71.38	9.55	0.002	$F_{obs} > F_{critical}$ - Reject H_0	0.90	2.3	0.13	$t_{statistic} < t_{critica}$ Accept H_0
0.6 -1.4 V 30s/30s	5.09	9.55	0.1	$F_{obs} < F_{critical}$ – Fail to Reject H_0	0.32	2.3	0.46	$t_{statistic} < t_{critica}$ Accept H_0 but case is very weak

ANOVA/ F distribution hypotheses: $H_0 : \mu_1 = \mu_2 = \cdots = \mu_k$; H_a : at least one of the μi 's is different. The null hypothesis specifies a global relationship between the means and the result of the test is significant if p-value ≤ α; Null distribution of the statistic F_{obs}=MSB/MSW. Reject H_0 if Fobs ≥ $F_{\alpha;k-1,N-k;}$ Fail to reject H_0 if $F_{obs} < F_{\alpha;k-1,N-k}$

T-test procedure: μ_1 and μ_2 means of the experimental and model-predicted populations of interest, the null hypothesis for comparing the two means is H_0: $\mu_1 = \mu_2$. If two means are same accept the hypothesis. The alternative hypothesis can be any one of H_1: $\mu_1 \neq \mu_2$; H_1: $\mu_1 > \mu_2$ or H_1: $\mu_1 < \mu_2$.

* Samples were treated with single-factor ANOVA

**p-values of t-test obtained from 'two-sample assuming unequal variance' method

Null hypothesis can be rejected if $F_{obs} \geq F_{\alpha;k-1,N-k;}$ $F_{\alpha;k-1,N-k;is}$ is also known as $F_{critical}$. F-values obtained for carbon corrosion model is much higher than $F_{critical}$ for the carbon corrosion ASTs (Table 4-5). The cumulative carbon loss during the various ASTs obtained from experiments and the carbon corrosion model are plotted versus their respective upper potential limits in Figure 4-11. As shown previously, very good agreement between the measurements and model predictions is observed in all cases. CO_2 concentration measured increased from 2.72 x 10^6 ppm at 1.4 V to more than 6.17 x 10^6 ppm with increasing the upper potential, the contribution of non-catalyzed carbon corrosion is expected to increase. Linse et al observed that electrodes with the same carbon, Pt and ionomer loading experienced non-catalyzed carbon corrosion when subjected to ASTs with lower potential of 1.0 V and upper potentials from 1.2, 1.3, 1.4 and 1.5 V [5]. We observed similar magnitudes of carbon loss in our ASTs, which could be primarily be occurred by non-catalyzed carbon corrosion.

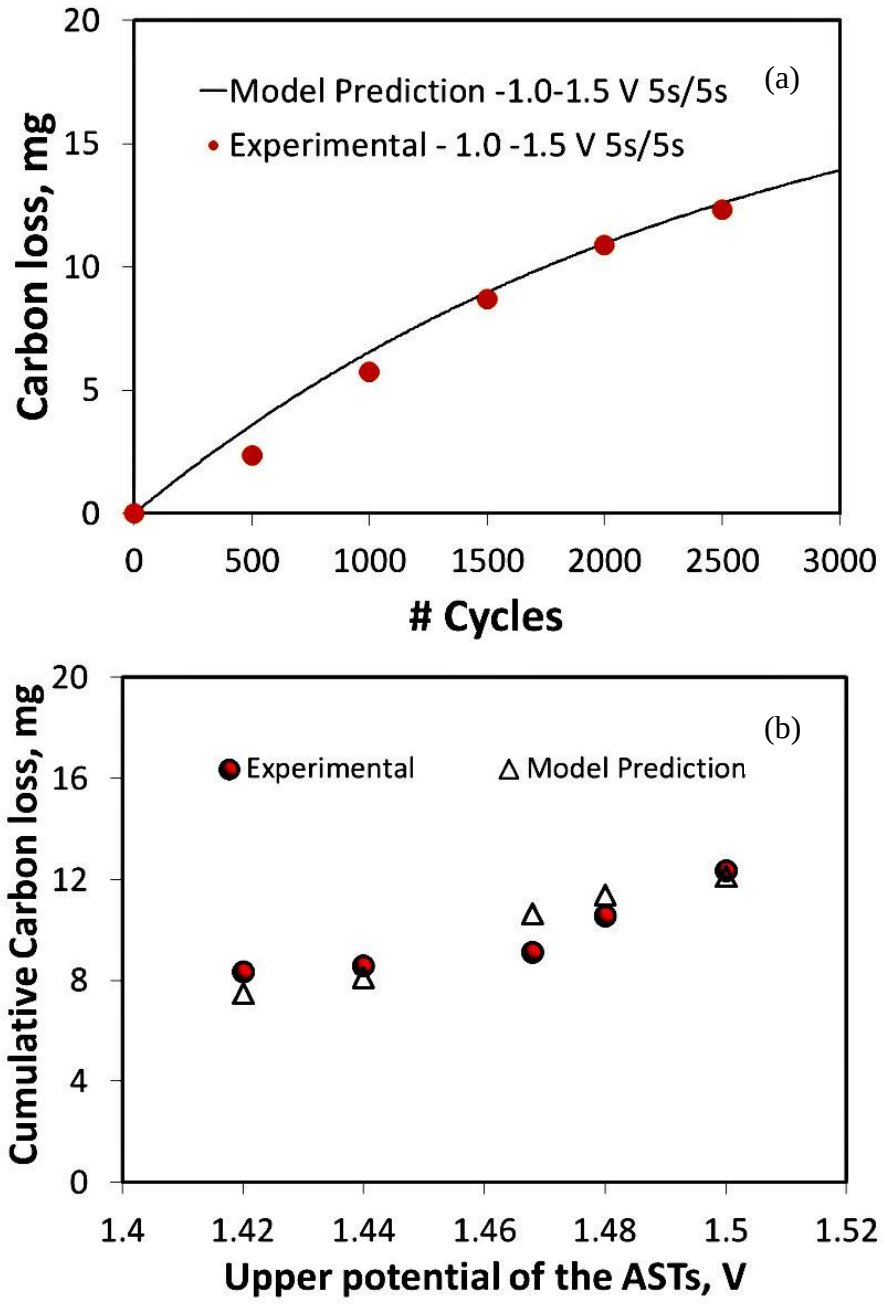

Figure 4-11: Variation of the (a) Carbon loss during 1.0-1.5 V 5s/5s AST (b) Total carbon loss with the upper potential limit of the ASTs as determined from experiments and the carbon corrosion model of this study.

4.2.5 Performance Loss during the Carbon Corrosion ASTs

The maximum current density obtained during the carbon corrosion ASTs was found to be ~2.0 A cm^{-2}. The voltage loss at a current density of 1.5 A cm^{-2} on the polarization curve has been chosen as the condition to characterize the performance loss of the MEA 4 during the ASTs. This current density has been chosen since this puts the system in a condition where activation, ionic, electronic and contact resistances play a role in determining cell performance, whereas mass transport effects are still unimportant.

The evolution of the performance loss during the various ASTs is plotted against number of cycles in Figure 4-12 in order to understand the impact of the different carbon corrosion cycling on the MEA 4. As in the case of carbon loss, the upper potential limit during the ASTs strongly affects the performance loss. The degradation in performance remains relatively modest (less than 60 mV) over the entire AST of 2500 cycles as long as the upper limit remains below ~1.47 V. However, with any further increase in the upper limit, the losses begin to grow dramatically, particularly after 2000 cycles. The decay in potential reaches 150 mV after 2500 cycles when the upper limit is raised to 1.48 V and as much as 625 mV with a further increase in the upper limit to 1.5 V. This last case is quite striking since a performance loss of 625 mV represents 82 % of the initial BOL cell voltage BOL cell voltage observed at 1.5 A cm^{-2}. As shown in Section 4.1, the loss of carbon does not significantly affect the performance loss during the initial stages of these carbon corrosion ASTs. However, as the number of cycles increases beyond 1500, the impact on the performance loss becomes much larger, as shown below.

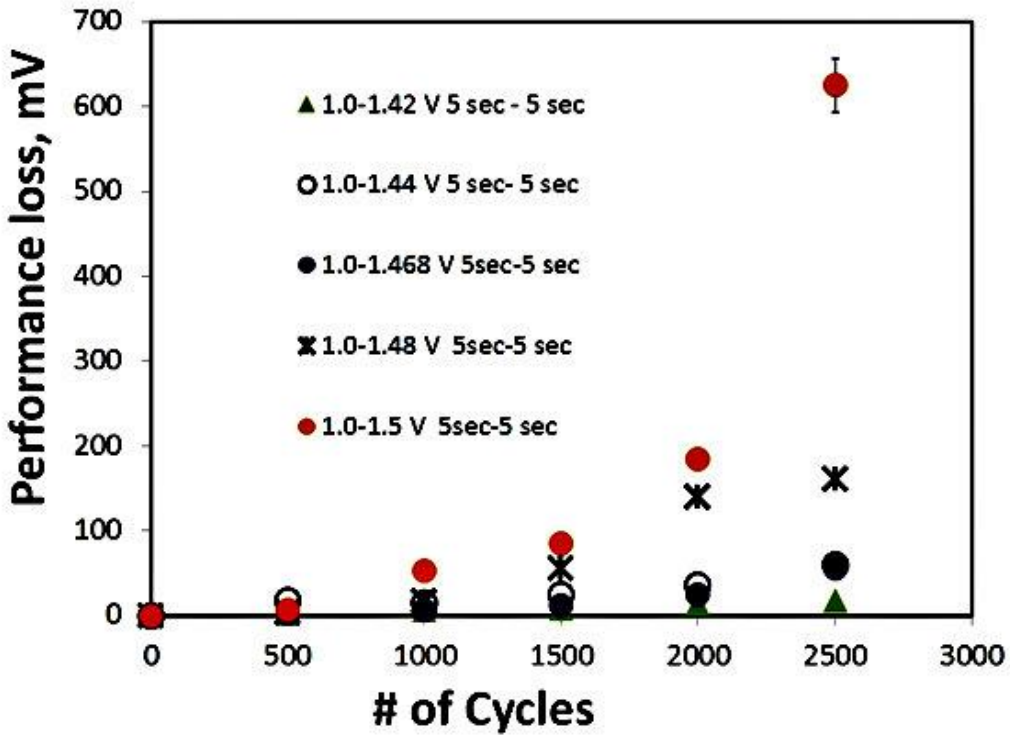

Figure 4-12: Performance loss measured during the course of the carbon corrosion ASTs. Operating conditions during these ASTs are given in Table 3-2.

4.2.6 Use of Carbon Corrosion Fingerprint in the Simplified Model

Performance loss is generally caused by both Pt dissolution and carbon corrosion [44, 92, 137, 138]. However, oxidation of the carbon support is expected to be the major contributor to performance loss during the carbon corrosion ASTs of this study. In Section 4.1, an empirical correlation or 'fingerprint' relating performance loss to the carbon loss was developed for the carbon corrosion ASTs [139]. An exponential function relating the performance loss obtained from a polarization curve to the measured carbon loss at a specific current density was found to fit the data for each AST very well. This expression termed the fingerprint for carbon corrosion during a particular AST can be used to predict the performance loss from knowledge of the carbon loss. Although useful, this approach

has some disadvantages. It requires the simultaneous and independent measurements of both the amount of CO_2 generated and a polarization curve. The CO_2 measurement requires that the cell be connected to an infrared instrument for continuous in-situ analysis, which is not always convenient or possible, particularly for routine monitoring of fuel cell performance during typical operation. However, it should be possible to eliminate the need for such a measurement by replacing it with the carbon corrosion model presented in this section that is able to determine the carbon loss as a function of time or the number of cycles during the ASTs. In this way, only a polarization measurement, which is electrochemically based and so, can be easily conducted in-situ during ASTs or fuel cell operation is required.

The following procedure is adopted to carry this out:

a. Based on the experimental results presented previously, the simplified model computes the carbon loss as a function of time or number of cycles. Since the performance loss is measured independently at a known time or number of cycles, we can associate the model-predicted carbon loss at a given time with the performance loss measured at the same point in time and plot them as a point in figure 4-12.
b. To determine whether a general correlation exists between the amount of carbon corrosion and the performance loss measured at 1.5 A cm^{-2} for MEA 4, the data for all ASTs obtained using the approach described in point a are shown in figure 4-12.
c. Despite having different upper potentials for the ASTs, the data appear to fall along a single curve. The rationale for this could be (a) different MEA used in this study (b) closer range upper potential variation in the ASTs (c) same dwelling time used between UPL and LPL
d. An empirical fingerprint equation relating the performance loss at 1.5 A cm^{-2} to carbon loss applicable to all ASTs was developed for the MEA 4 used in this study. The curve for the fingerprint is shown as the solid line in figure 4-12 and the corresponding expression is given in the figure legend.

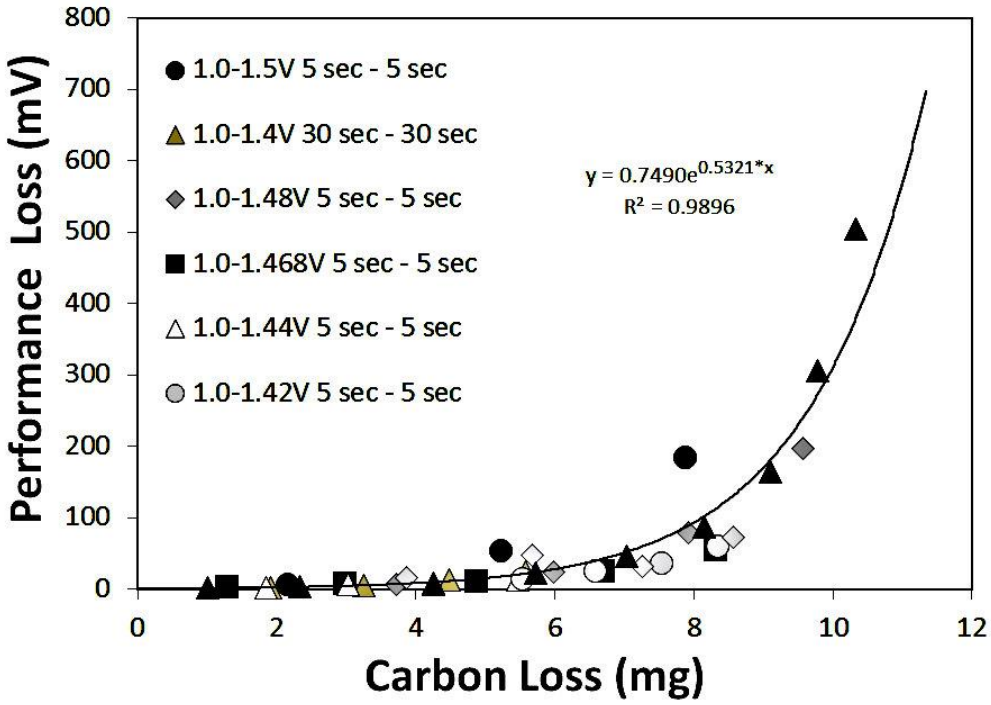

Figure 4-13: Relation between performance loss and cumulative carbon loss measured at 1.5 A cm^{-2} during carbon corrosion ASTs as determined directly from experiments (symbols) and by using the fingerprint equation (solid line) based on estimation of the carbon loss by the carbon corrosion model. Operating conditions during the ASTs are given in Table 3-2.

Although the fingerprint equation is able to predict the performance loss for all ASTs, we look more closely at the results obtained for the 1.0 – 1.5 V, 5s/5s AST as an example. A comparison of variation of the measured and predicted performance loss with cycle number during this AST is presented in Figure 4-14a. Again, good agreement is obtained. Statistical analysis of the measured and computed performance loss data yields an acceptable p-value of 0.90 from a t-test. Based on this p-value, we may conclude that the difference between the model predictions and experimental data are not statistically significant. The fitted performance loss at the end of the AST deviates from the experimental data by 8%. The deviation of the fitted results during the early stages of the potential cycling is similar to that of the carbon loss predicted by the proposed kinetic model, as noted earlier. An F distribution was obtained from a single-factor ANOVA to compare the variances for all of the carbon corrosion ASTs. Acceptable p-values from both a t-test and ANOVA for the experimental and fitted performance loss data are obtained for all ASTs.

In addition, the observed and fitted performance losses during the various carbon corrosion ASTs are plotted versus the corresponding upper potential limits in Figure 4-14b. Again, good agreement between the experimental and fitted data is obtained. The results of t and F –tests of each AST suggest that the difference in variance between the two sets of data is not statistically significant. Hence, our approach can be used to estimate the performance loss of the model.

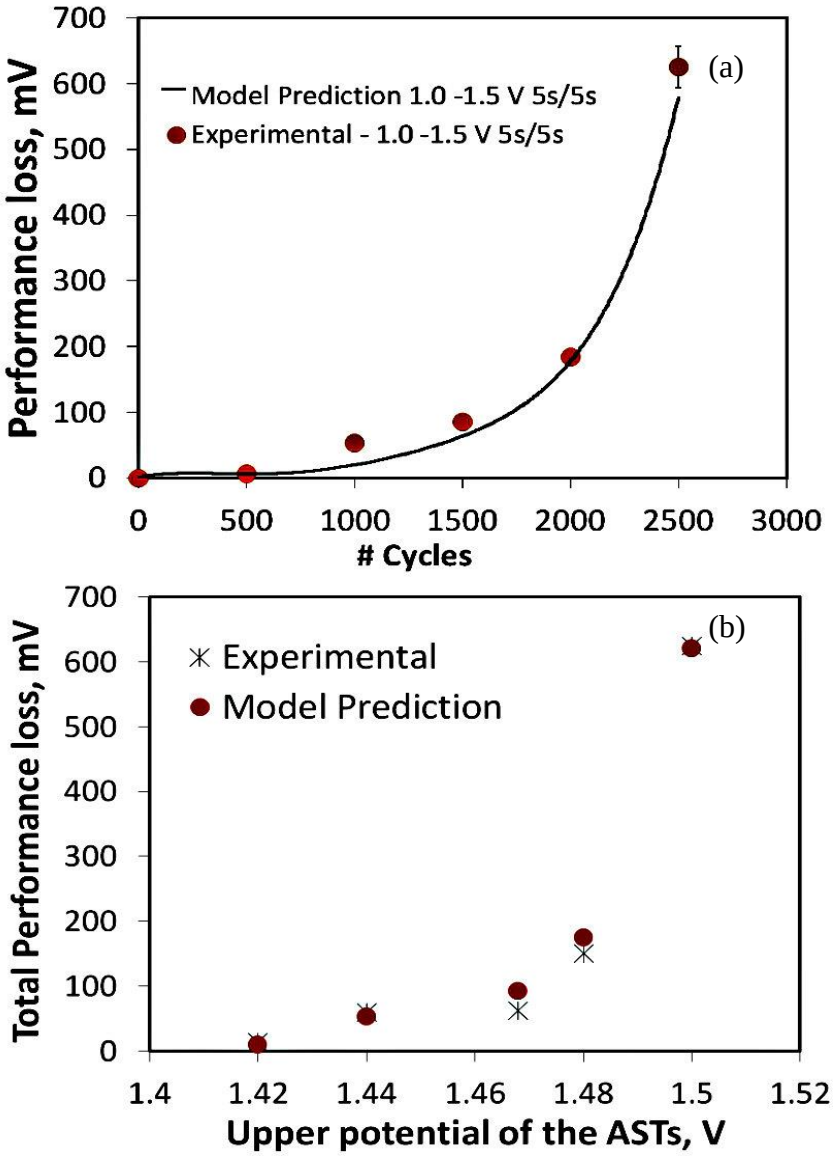

Figure 4-14: (a) Comparsion of the kinetic model results with carbon loss data for 1.0-1.5 V AST; and (b) Experimentally observed and predicted total performance for different upper potentials of the carbon corrosion ASTs obtained at 1.5 A cm^{-2}.

Young et al postulated the following reasons for the performance loss due to carbon loss from the membrane electrode assemblies [140]. Complete or partial oxidation of carbon to CO_2 due to the ASTs affects the catalyst layer structure and presumably the porosity of the CL. Hence, higher performance loss could be caused by problems related to oxygen transport especially when catalyst porosity value decreases. On the whole, the novel approach of using a mechanistic carbon corrosion model to compute the carbon loss for use in the fingerprint equation developed in Section 4.1 [139] rather than having to measure the carbon loss directly during the ASTs appears to be successful.

4.2.7 Applicability of the Model to Mixed degradation ASTs

In this section, the carbon corrosion model and fingerprint equation developed previously are applied to a mixed-mode degradation AST during which both Pt dissolution and carbon corrosion operate in order to test their limitation. This AST consists of square-wave voltages cycles between 0.6 and 1.4 V with 30s dwell times at each potential. The application of these cycles leads to much higher carbon losses than do the carbon corrosion ASTs in Figure 4-10 (with the exception of the AST between 1.0 and 1.5 V) despite the fact that the upper limit of 1.4 V is lower than the others and only 1500 cycles have been applied. Figure 4-15a shows a comparison of the measured carbon loss to that predicted by the carbon corrosion model over the course of the mixed-mode degradation AST. It should be noted that the model parameters have been left unchanged from those used to analyze the carbon corrosion ASTs and no attempts have been made to fit the model to the experimental data. The comparison in Figure 4-14a shows that the model underestimates the amount of carbon lost and that the deviation grows over the course of the AST. This result is understandable given that the model accounts for only CO_2 formation during carbon oxidation and ignores catalyst-induced effects [74]. The higher carbon loss observed during the 0.6 – 1.4 V, 30s/30s AST may be due to a complex interplay of different surface oxides of carbon and platinum that exist during the potential cycling. As with the carbon loss, the performance loss is underestimated by the fingerprint equation

(Figure 4-14b). The p-value from a t-test is found to be 0.19, indicating that the difference in the experimental and predicted performance losses are not statistically significant. The value of F_{obs} from the ANOVA table suggests that statistical treatment between the experimental and model-predicted values are failed to reject H_0.In general, carbon corrosion during the mixed-mode degradation AST may follow two different pathways. Firstly, the formation of quinone/hydroquinone species during potential cycling may modify the carbon surface and promote carbon corrosion [41, 44, 75, 92, 95]. However, this pathway may not be that critical given that the model is able to accurately predict the carbon loss during the carbon corrosion ASTs which have the same or a higher upper voltage limit than that of the mixed-mode degradation AST. Secondly, Pt likely has a stronger effect on carbon corrosion during cycles from 0.6 V to 1.4 V than it does during cycles from 1 V to 1.4 V. Maass et al observed increased carbon corrosion due to changes in the catalytic activity of platinum in the potential range of 0.6 - 1.0 V [75]. Linse et al suggested that the oxidation state of platinum can strongly influence carbon corrosion [74]. Takeuchi et al. investigated carbon corrosion under dynamic potential conditions and also showed that the presence of Pt affects on inhibiting carbon oxidation when at potentials below 1 V [141]. The underestimation of both the carbon loss and performance loss during the 0.6 V–1.4 V 30s/30s AST by the fingerprint equation is likely due to the fact that the carbon corrosion model on which it is based does not consider these effects of Pt.

Information on the effect that the state of Pt has on carbon corrosion can be gained by measuring the loss of EPSA during the carbon corrosion and mixed-mode degradation ASTs. Figure 4-16a shows the relation between % carbon loss and % EPSA loss during the various ASTs. Several expected trends are observed. A strong correlation exists between these two quantities and both increase together during any given AST. Furthermore, the correlation between % carbon loss and % EPSA loss is almost perfectly linear in all cases. A linear dependence of % carbon loss on % EPSA loss during the carbon corrosion ASTs would be expected assuming that the Pt catalyst is uniformly distributed over the carbon support. Furthermore, if the Pt catalyst were to become detached as the carbon is oxidized

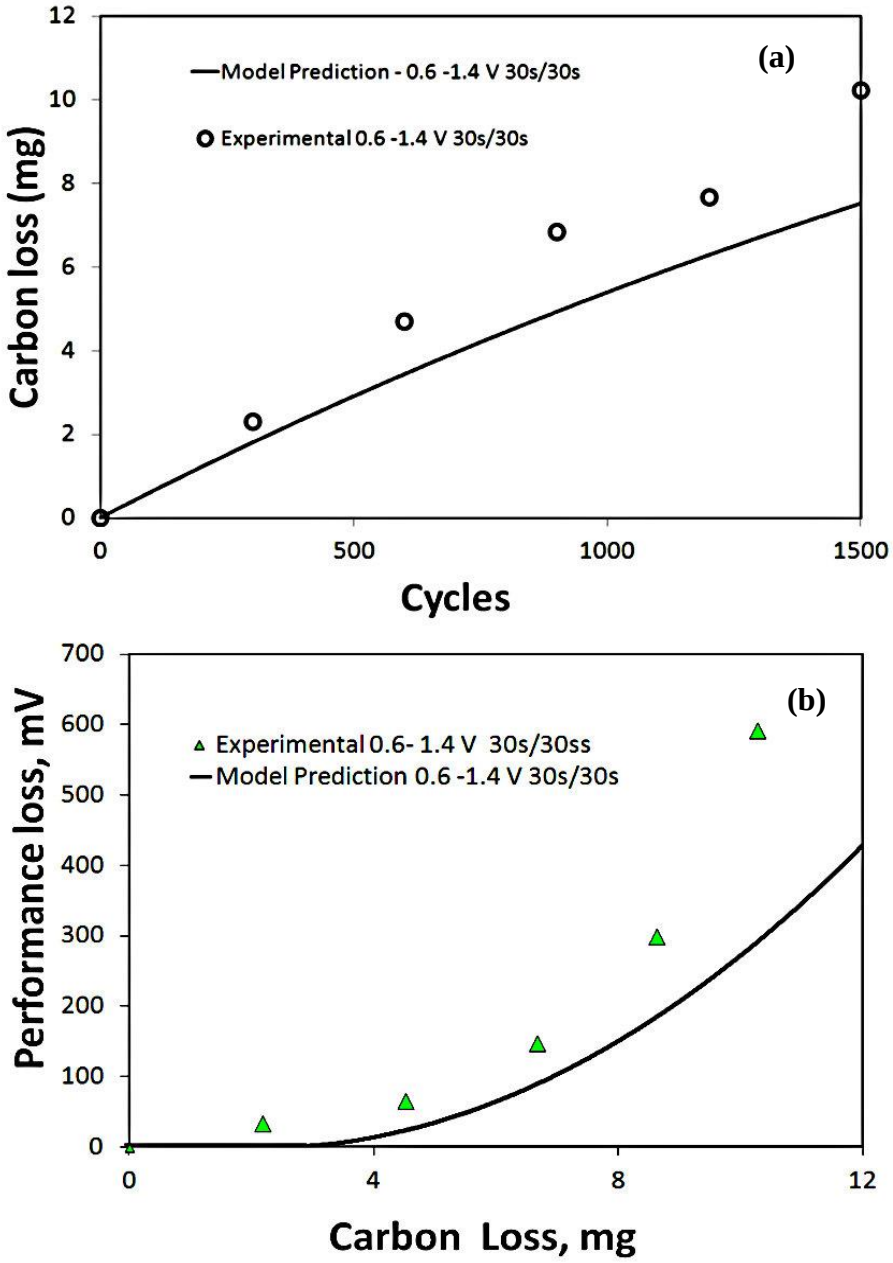

Figure 4-15: (a) Variation of the measured and model-predicted carbon loss with number of cycles and (b) variation of the measured and model-fitted performance loss with carbon loss during the mixed-mode degradation AST 0.6 -1.4 30s/30s AST.

to CO_2, one would expect this line to lie close to the 45° diagonal. The data obtained during most of the carbon corrosion ASTs lie above the diagonal line, suggesting that when carbon is oxidized to CO_2 some of the catalyst attached to it remains in electrochemical contact. An exception to this trend is observed in the case of the 1.0 V–1.4 V 30s/30s AST where the data fall somewhat below the diagonal, suggesting that some direct attack of the catalyst may be occurring. It is also observed that a change in the upper voltage limit during the carbon corrosion ASTs has a significant effect on the amount of carbon that is oxidized, but much less influence on the loss of % EPSA. The curve for the mixed-mode degradation AST lies well below the diagonal, reflecting that a considerable amount of the attack occurs directly on the catalyst without oxidizing the support.

An interesting comparison can be made between the % carbon loss and % EPSA loss during the mixed-mode degradation AST with that during the carbon corrosion AST. Care must be taken in comparing the trends observed during the mixed-mode degradation AST to those during most of the carbon corrosion ASTs in Figure 4-15a since the dwell times differ. However, a clear comparison can be made with the results obtained during the 1.0 V–1.4 V 30s/30s AST where the dwell times are the same. Overall, both the % EPSA loss and % carbon loss vary over much wider ranges and reach much higher levels when the MEA is subjected to the mixed degradation AST than to the 1.0 V–1.4 V 30s/30s AST. The much higher % EPSA loss during the mixed-mode degradation AST than during the carbon corrosion AST is not surprising although the observation that it grows to a level above 80% is worth noting. Somewhat more surprising is the observation that the corresponding % carbon losses during the mixed-mode degradation ASTs are also much higher than those during the carbon corrosion AST. While the % carbon loss by the end of the 1.0 V–1.4 V 30s/30s AST of 2500 cycles reaches 22%, as much as 45% of the carbon is lost by the end of the 0.6 V–1.4 V 30s/30s AST which is carried out for only 1500 cycles. Obviously, these effects can be attributed to processes occurring at potentials below 1.0 V.

Particularly interesting are the trends observed when comparisons are made over the course of the two ASTs. Measurements in the earlier stages of both ASTs reveal similar carbon loss levels of approximately 10%. However, the corresponding EPSA loss of 40% during the 0.6 V–1.4 V 30s/30s AST is more than double the level reached during the 1.0 V–1.4 V 30s/30s AST. This, of course, reflects the particular attack on the Pt catalyst during this stage of the mixed-mode degradation AST. However, it is interesting to note that this does not appear to have a spill-over effect on the carbon loss over that occurring during the carbon corrosion AST at this stage of the cycling. As the 0.6 V–1.4 V 30s/30s AST proceeds, the degradation of the catalyst continues, but so does that of the carbon support. The carbon loss of ~20% reached when the EPSA loss rises to ~60% matches the maximum level reached during the 1.0 V–1.4 V 30s/30s AST. Thereafter, both the Pt catalyst and carbon support continue to degrade until the AST is terminated. The fact that the carbon loss is significantly higher than that observed during the carbon corrosion AST by the end of the cycling suggests that the attack on Pt also tends to enhance carbon corrosion either directly or indirectly. Examination of the results in figure 4-15a also indicates that the reverse is true, but to a lesser extent. As much as 30% loss in EPSA is observed by the end of the carbon corrosion ASTs.

The % performance loss corresponding to the % carbon loss shown in figure 4-15a is plotted versus % EPSA loss in Figure 4-15b. Some of the trends observed are similar to those in the case of the carbon loss. The performance losses reached during the later stages of the 0.6 V–1.4 V 30s/30s AST are much greater than those during the carbon corrosion ASTs. On the other hand, some differences in the effect of degradation on the cell performance are evident. The % performance loss tends to lag behind the % EPSA loss and % carbon loss throughout the carbon corrosion and mixed-mode degradation ASTs. In fact, perhaps the most significant observation regarding the carbon corrosion ASTs is the loss in performance always remains small (10% or less) even when the carbon loss and EPSA loss become substantial. This trend is even more remarkable during the earlier stages of the mixed-mode degradation AST. For example, even when 60% of the EPSA and 25% of the

carbon have been lost, the performance is only diminished by 10%. However, thereafter the situation changes and the performance begin to deteriorate much more rapidly with further degradation of the support and catalyst.

4.2.8 Summary

The use of carbon corrosion ASTs with different upper potential limits and cycling periods was studied. A simplified kinetic model was proposed to predict the carbon loss during different carbon corrosion ASTs. The model successfully predicted the carbon loss, proving to be a useful tool for characterizing carbon loss behavior. Furthermore, a carbon fingerprint equation was combined with the kinetic model to estimate the cell performance loss. The performance loss obtained using this method showed good agreement with the experimental data for all carbon corrosion ASTs considered. Limitations of this approach were assessed by using it to analyze the results obtained when a mixed-mode degradation AST was applied.

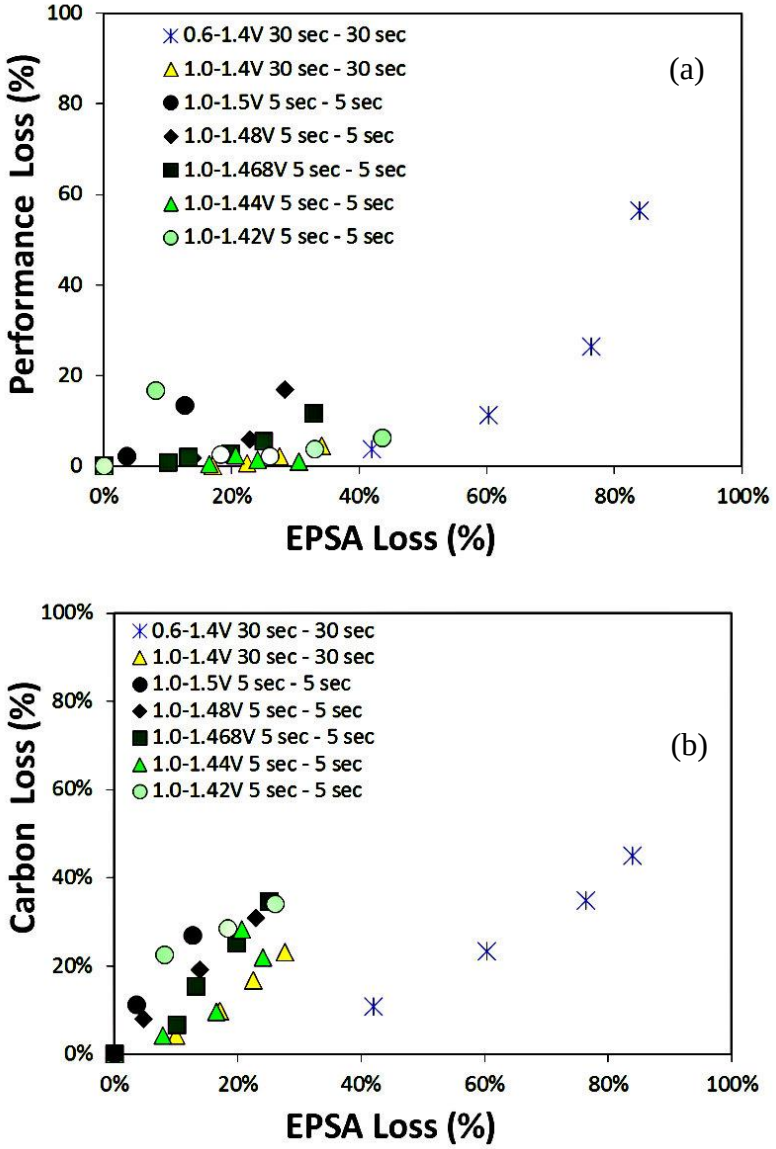

Figure 4-16: Correlation between (a) % carbon loss and % EPSA loss and (b) % performance loss and % EPSA loss measured during carbon corrosion and mixed degradation ASTs. Operating conditions during these ASTs are given in Table 3-2.

4.3 Diagnosis of degradation of the MEA through XRD and XPS analysis

The results of ex-situ XRD and XPS analyzes of MEAs subjected to a mixed-mode degradation 0.6-1.4 V 30s/30s AST are described in this section to examine the nature of the surface products formed in the cathode catalyst layer due to carbon corrosion and Pt oxidation/dissolution. These effects are assessed by comparing catalyst layers in their EOL and BOL states. The experimental procedures relevant to this section are described in Chapter 3:

1 XRD analysis – Section 3.4.3.11
2. XPS analysis – Section 3.4.3.12

The detailed BOL structure and composition of the MEAs used for this analysis are confidential. XRD analysis is used to examine the changes in the crystallinity of compounds due to degradation of the membrane and catalyst layer [142]. XPS analysis can reveal evidence of membrane decomposition and oxidation of the Pt catalyst [134]. MEA samples for both XRD and XPS analyzes were prepared by first cutting small pieces from MEAs before (fresh) and after fuel cell operation (degraded) and then stripping off their GDLs [134, 142, 143]. XRD patterns were recorded using a Brucker AXS D8 unit at a scanning speed of 0.02 °/s and an accelerating voltage of 40 kV. XPS spectra were collected by an ESCALAB Mk II spectrophotometer using Mg K_{α} incident radiation (1253.6 eV) operating at 20 kV and 20 mA as the excitation source. The binding energies of the XPS peaks were referenced to the 1s peak for graphitic carbon located at 284.5 eV. Peak deconvolution was carried out assuming the peaks can be described as mixed Gaussian/Lorentzian curves after applying Shirley-background subtraction.

4.3.1 XRD Analysis

The XRD patterns obtained for fresh and degraded MEAs obtained from the cathode are shown in figures 4.16 a and b. It is important to note that XRD analysis is intended only as a qualitive tool to understand the effect of mixed degradation AST on the CL structure. The characteristic peak at 37° in both patterns arises due to diffraction of the incident beam by the aluminum stub sample holder. It has been reported that PFSA membranes possess a semi-crystalline structure [142]. A peak at 18.3° diffraction angle observed in the fresh sample (Figure 4.16a) is characteristic of all PFSA membranes [142]. This peak shifts to a slightly lower diffraction angle and its intensity has increased somewhat in the degraded sample (Figure 4.16b). The characteristic peaks observed in both samples at 26° and 40^{o} correspond to the C(002) and Pt(111) planes, respectively. Similarly, other peaks observed in the fresh sample such as those corresponding to Pt (220), Pt(222), Pt(400) have changed in the degraded sample. The peaks corresponding to Pt(222) and Pt(400) have largely disappeared while Pt(220) and Pt(200) peak intensities have decreased in the degraded sample. The mean particle size and lattice parameters of the catalyst before and after operation can be estimated from the Pt(111) peak at 40^{0} in the XRD patterns by using JADE software to yield the results listed in Table 4-6. The results indicate that degradation has caused the catalyst particle size and lattice parameter to increase significantly. Further analysis of the XRD patterns reveals that the specific surface area S_{XRD} of the degraded sample has decreased by 10.2 % from that of the fresh sample.

Table 4-6: XRD parameters obtained from Pt (111) peak in fresh and degraded MEAs.

	Fresh MEA	Degraded MEA
$d_{XRD\ (nm)}$	7.2	9.2
Relative change of d_{XRD} (%)	27.7%	
$S_{XRD\ (nm)}$	41.2	36.2
Relative change of S_{XRD} (%)	10.2%	

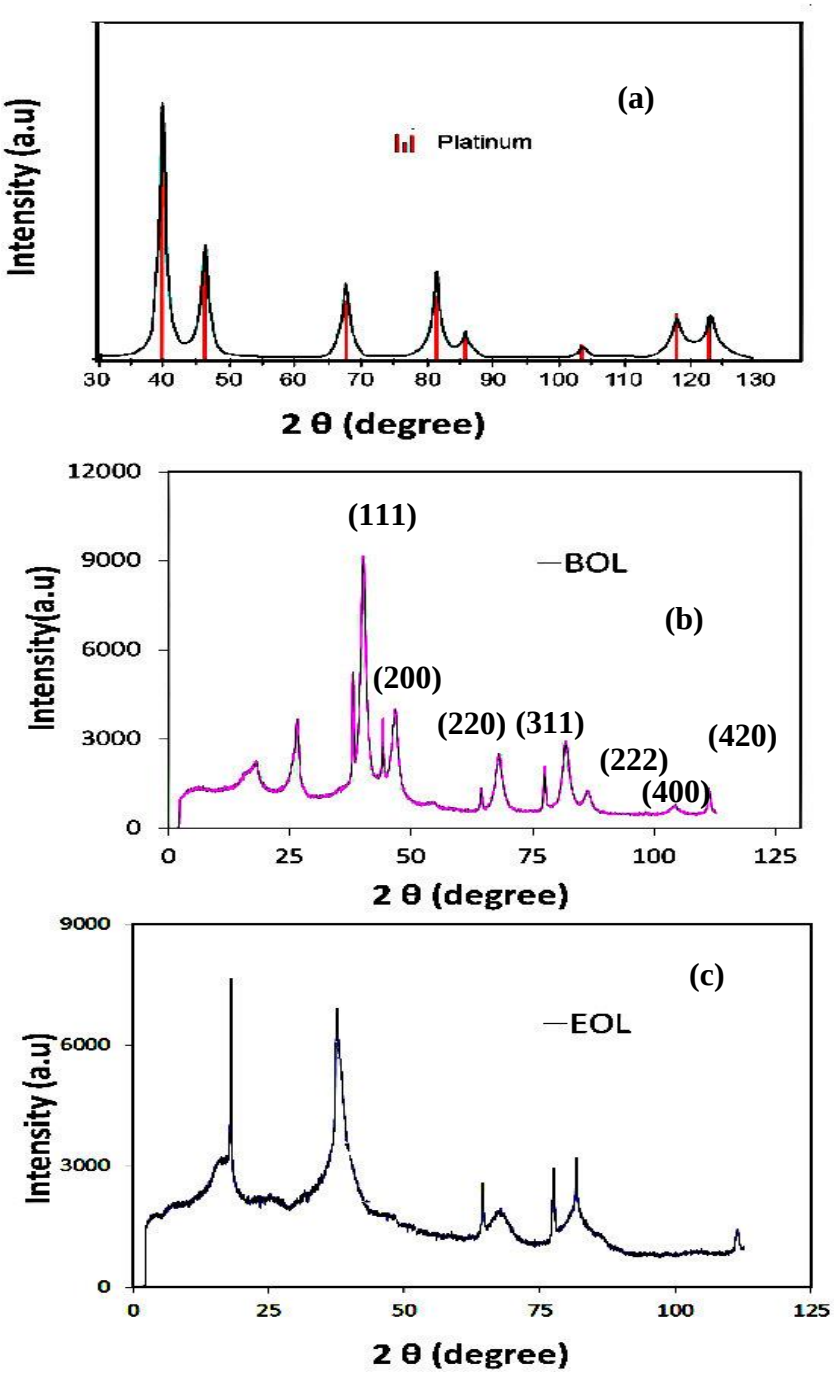

Figure 4-17: XRD patterns of (a) reference Pt [142] (b) BOL and (c) EOL CL

4.3.2 XPS Analysis

The degraded and fresh MEA samples of the catalyst layer were examined by XPS to identify chemical differences of surface species present. XPS data are plotted in the form of intensity versus binding energy. Intensity is measured in counts per unit time. Often, intensity is reported as arbitrary units (arb. units) since only relative intensities provide relevant information. Comparison of the areas under the peaks gives relative percentages of the elements detected on the sample surface. Initially, a wide scan survey XP spectrum is obtained to identify all of the detectable elements present in the sample. XPS survey scans show the presence of fluorine, carbon, sulfur, oxygen and platinum on the surfaces of both MEA samples (Figure 4-17). The elemental compositions of fresh and used catalyst layers based on analysis of the higher resolution spectra are summarized in Table 4-7. Based on this analysis, the surface concentrations of fluorine, sulfur, platinum and oxygen decreased from 30.8% to 24.5%, 1.2% to 0.9%, 3.6% to 2.1% and 4.6% to 1.5%, respectively, while the carbon content decreased from 71% to 59.0%.

Table 4-7: Surface compositions obtained from XPS scans of cathode catalyst layers BOL and EOL

Name	Fresh MEA		Degraded MEA	
	Peak Position (eV)	Atomic %	Peak Position (eV)	Atomic %
O 1s	531.5	4.6	532.5	1.5
C 1s	284.5	71.0	284.5	59.0
F 1s	688	30.8	681	24.5
S 2p	168.5	1.2	169	0.9
Pt 4f	71.5	3.6	71	2.1

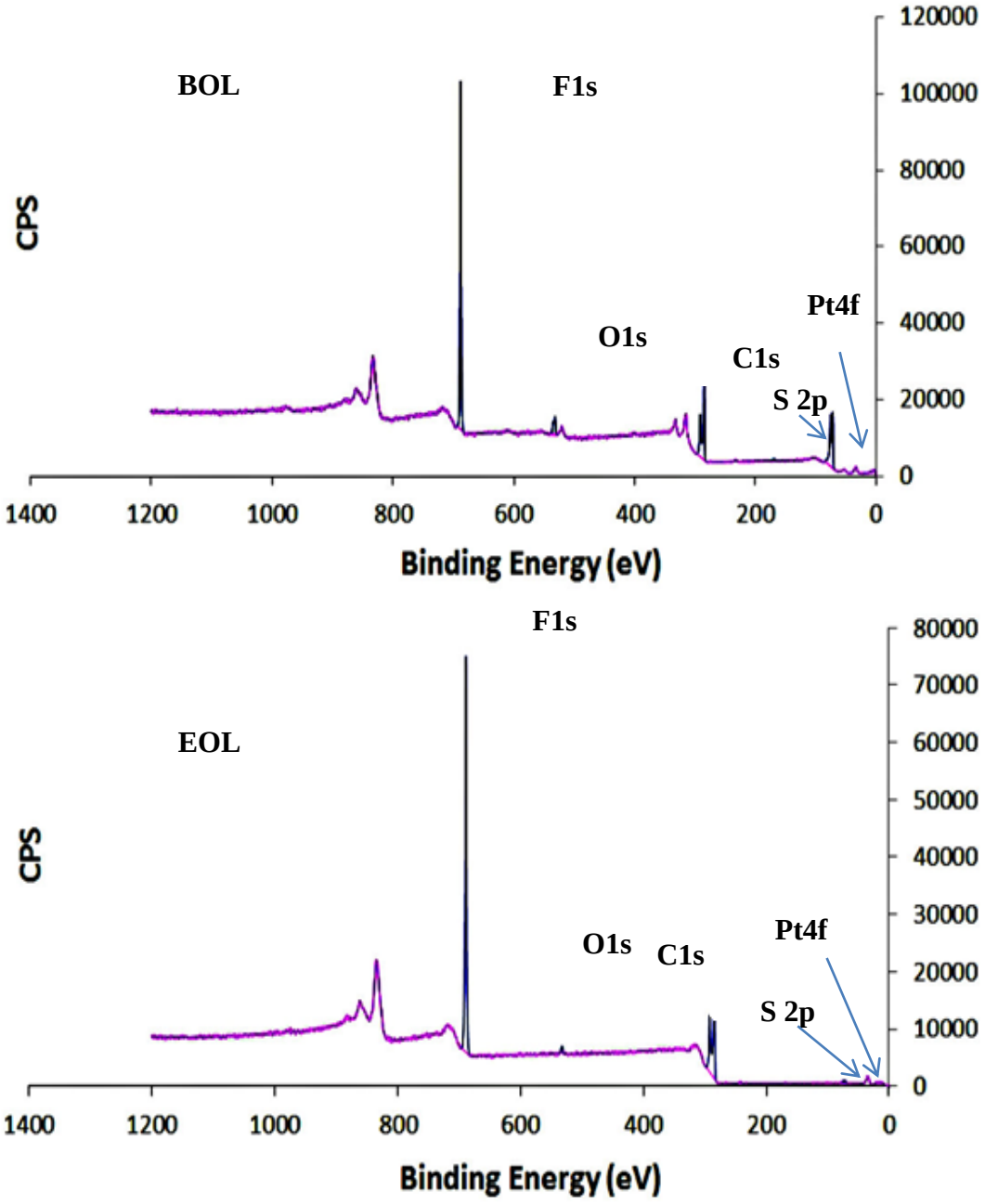

Figure 4-18: XPS survey scan of the catalyst layer before and after fuel cell operation.

Table 4-8: Peak assignments and binding energies in the XPS spectrum

Signal	Binding energy, E_b (ev)		Remarks
	Fresh sample	Degraded sample	
C 1s	284.4	284.3	-C-C
	285.6	284.7	-C-O
	-	286.5	-C=O
	288.7	-	-CF
	290.9	290.5	$-CF_2$
	292.2	291.8	$-CF_3$
F 1s	688.1	689	-OCF
	689.9	691.1	$-(CF_2)_n$
	686.4	686.9	-Pt-F
O 1s	531.7	-	Oxidized form of C and Pt
	-	532.5	Oxidized form of C
	534.3	-	-S=O
Pt 4f	71.4	71.2	Pt (0) (4f7/2)
	74.7	74.6	Pt (0) (4f5/2)
	72.6	72.9	Pt (II) (4f7/2)
	75.9	76.0	Pt (II) (4f5/2)
	74.7	75.5	Pt (IV) (4f7/2)
	77.9	78.5	Pt (IV) (4f5/2)

Table 4-8 summarizes the binding energies and assignments of the peaks observed in the high resolution XPS scans of the fresh and degraded samples. The scans over the C 1s region of the fresh and degraded samples are shown in Figure 4-18. Based on previous research reported in the literature, the C 1s region in the scans of MEAs can be decomposed into five peaks associated with the following carbon bonds: 1) –C-C, 2) –C-O, 3) –C=O, 4) $–CF_2$, CF-O and 5) $–CF_3$ [134, 144]. The peak C=O appears in only in the EOL samples. In both cases, graphitic carbon is the dominant form at 284.4 eV in fresh MEA and 284.3 eV in degraded MEA. Comparison of the spectra shows some changes in the chemical states of carbon in the fresh and degraded MEA samples. The peak for the -CF form of fluorinated carbon present at 288.7 eV in the fresh sample is absent in the degraded sample. On the other hand, a peak for –C=O appears only in the degraded sample, while the peak for $–CF_2$ has broadened significantly in the used sample. These trends are consistent with those of previous studies that have reported an increase in the surface concentration of oxidized forms of carbon and decrease in the relative amount of ionomer-type carbon (CF, CF_2 and CF_3 species) on catalyst layer surfaces after fuel cell operation [142, 144].

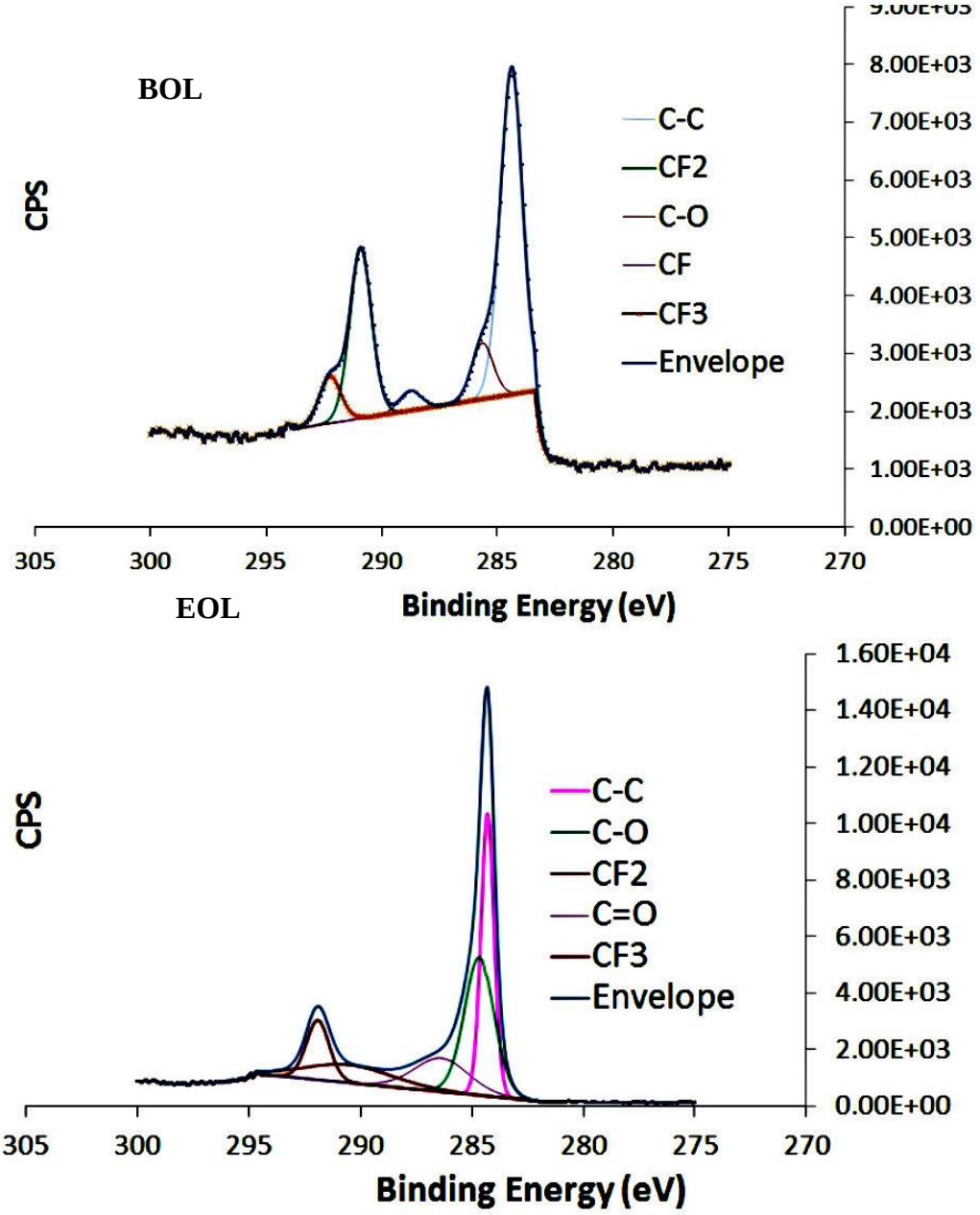

Figure 4-19: XPS scans in C1s region.

The F 1s spectra for both degraded MEA and fresh MEA samples are presented in figure 4-19 and the assignements of the significant fluorine-containing species are listed in Table 4-8. The F 1s region for fresh MEA sample can be decomposed into three components: i) a peak at a high binding energy at 689.8 eV attributed to $(CF_2)_n$, the hydrophobic part of the PFSA polymer, ii) a peak at 688.1 eV assigned to -OCF, the hydrophilic part of the membrane and iii) a peak at 686.4 eV due to Pt–F[142]. Unlike that observed for the C 1s region, the F 1s scans of the fresh and used samples are very similar to each other. The total surface concentration of fluorine is found to decrease from 30.8 % in the fresh sample to 24.5% after degradation, as shown in Table 4-7. The catalyst layer surface is generally expected to become less hydrophobic due to the decomposition of $(CF_2)_n$ groups and increase in oxidized forms of carbon, as observed in previous research [134, 144, 145]. In view of the small differences between the fluorine spectra in the fresh and degraded MEA samples, it would be useful to collect water from the cathode region during ASTs to confirm whether fluorine is being lost from the MEA. However, water analysis is not done during this study. Literature reports suggest a higher percentage of fluorine loss occurs during potential cycling compared to start-up/shut-down [134, 142, 144, 145].

Figure 4-20 Figure 4-21: shows the O 1s spectra in the fresh and degraded MEAs. Oxygen in PFSA membranes have two different binding states. One of the three oxygen atoms in PFSA is bound to a sulphonic acid group and has a binding energy at 534.2 eV (higher binding energy peak) in the fresh sample. Two of the oxygen atoms in the polymer chain are in ether groups with a lower binding energy at 531.7 eV due to their association with oxidized states of carbon and platinum [144]. The broad peak at ~ 520 eV in the fresh sample can be attributed to the presence of Pt 4p. After fuel cell operation, the signal at the higher binding energy for oxygen bound to sulphonic acid has all but disappeared, whereas a broad peak at lower binding energy (532.5 eV) remains.

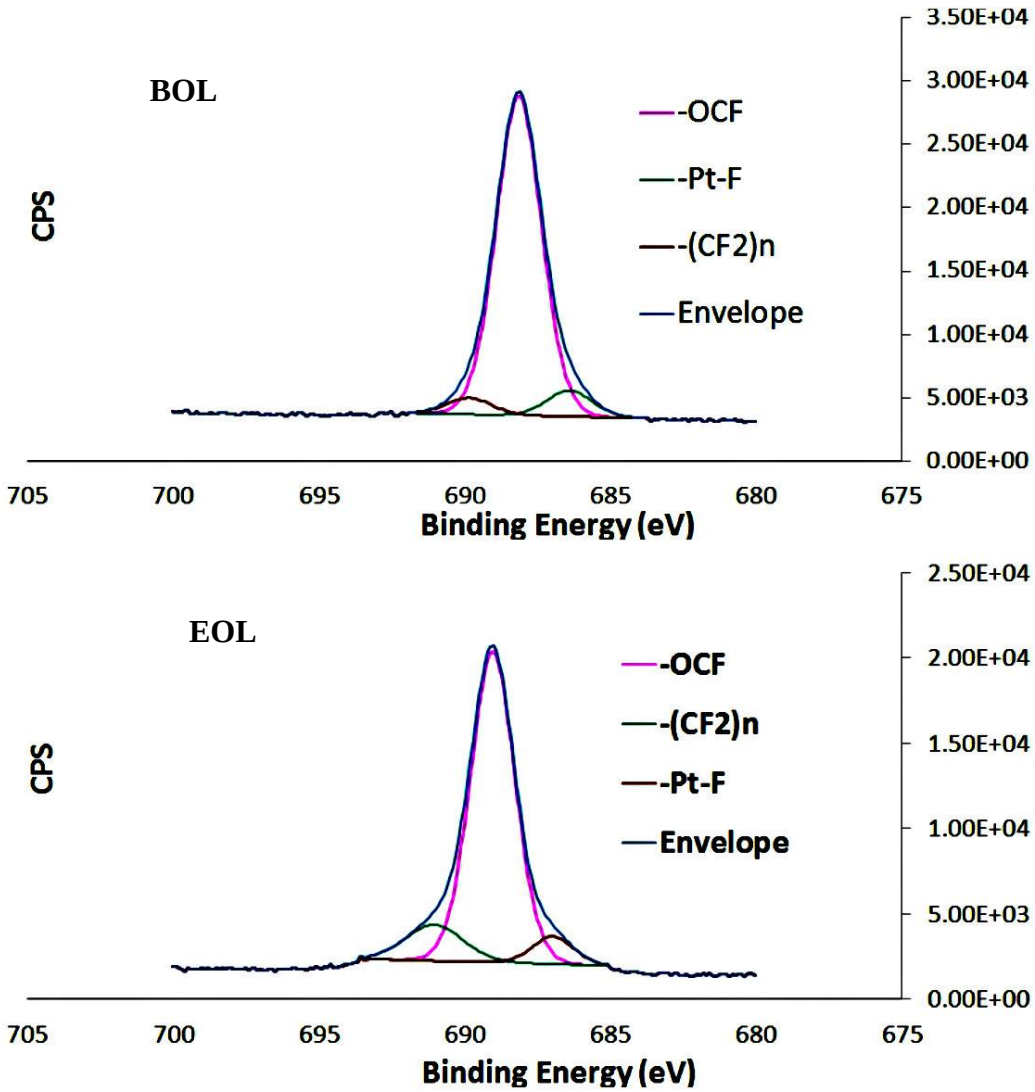

Figure 4-20: XPS scans in F 1s region.

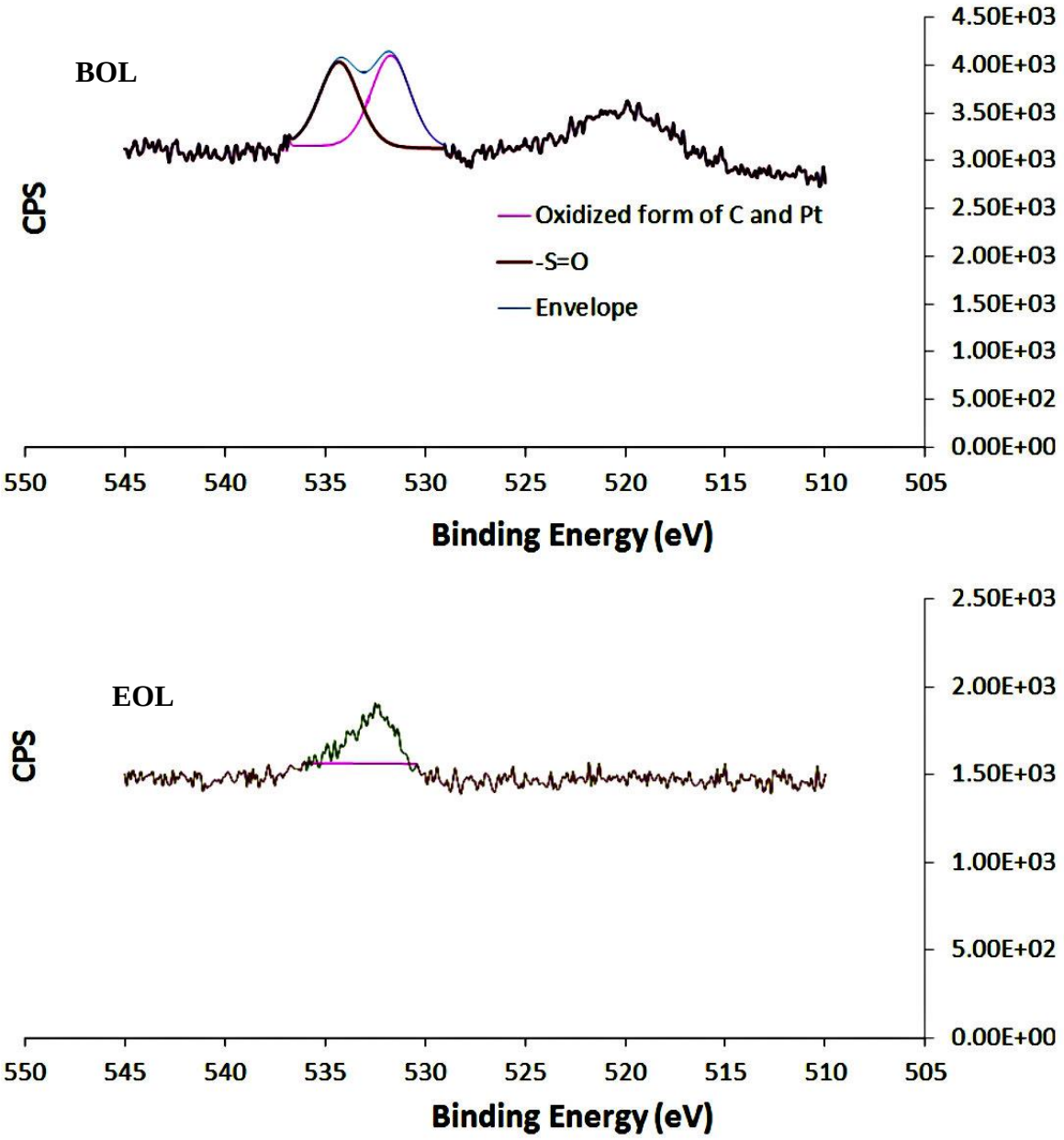

Figure 4-21: XPS scans in O 1s region.

It was not possible to corroborate any change associated with the sulphonic acid groups from the S 2p spectra since the signal-to-noise ratios in the fresh and used samples were found to be so low that it was not possible to draw any definite conclusions. The XPS survey scan finds the oxygen and sulfur concentrations in the fresh polymer to be 4.6 % and 1.2 %, respectively, but only 1.5 % and 0.9 %, respectively, in the degraded sample. Taken together, these results suggest that most of the oxygen loss occurred predominantly by removal of $–SO_3H$ groups, in agreement with some previous studies [134, 144, 145].

The Pt 4f spectra of the fresh and degraded MEAs are shown in Figure 4-21. The presence of Pt in XPS is indicated by photoelectrons for fresh and degraded samples originating in the 4f orbital, which appears as doublets due to spin-orbit coupling into 4f7/2 and 4f5/2 states. Three sets of doublet peaks appear in both samples, indicating three oxidation states: Pt(0), Pt(II) and Pt(IV)). The binding energies and assignments provided in Table 4-8 give evidence for the presence of three oxidation states for Pt in both fresh and degraded MEA samples. The three oxidation states are observed at the following doublets: 1) 71.4 and 74. 7 eV attributed to Pt(0), 2) 72.6 eV and 75.9 eV attributed to either PtO or $Pt(OH)_2$ formation [142] and 3) 74.7 eV and 77.9 eV corresponding to compounds such as PtO_2[142, 144]. The presence of these three oxidation states is also observed in the degraded MEA. Although not apparent from the spectra in figure 4-21, the proportion of Pt present in the elemental state is generally expected to decrease while the oxidized Pt is expected to increase as a result of fuel cell operation. This would occur concurrently with a reduction in the total amount of platinum in the surface, as indicated from the survey scan in Figure 4-17 and previous studies [144, 145]. Platinum oxidation is presumably driven by oxygen reduction that takes place on the cathode side of the catalyst layer [60, 146, 147].

4.3.3 Summary

Comparision of BOL and EOL samples is investigated using XRD and XPS analysis respectively. The analysis showed the degradation of MEA through the mixed degradation AST

1. increase the catalyst particle size
2. formed new oxides species
3. Corroded the carbon support, fluorine in the ionomer, Pt content in the catalyst layer

An increase in the relative proportion of oxidized forms of carbon and evidence of the breakdown of acid groups from the catalyst layer surface could have caused kinetic, ohmic and mass transported related losses when the MEA was subjected to mixed-mode degradation AST. The presence of different surface oxide groups helped to verify the various mechanistic steps involved in the development of the predictive model described in the previous section.

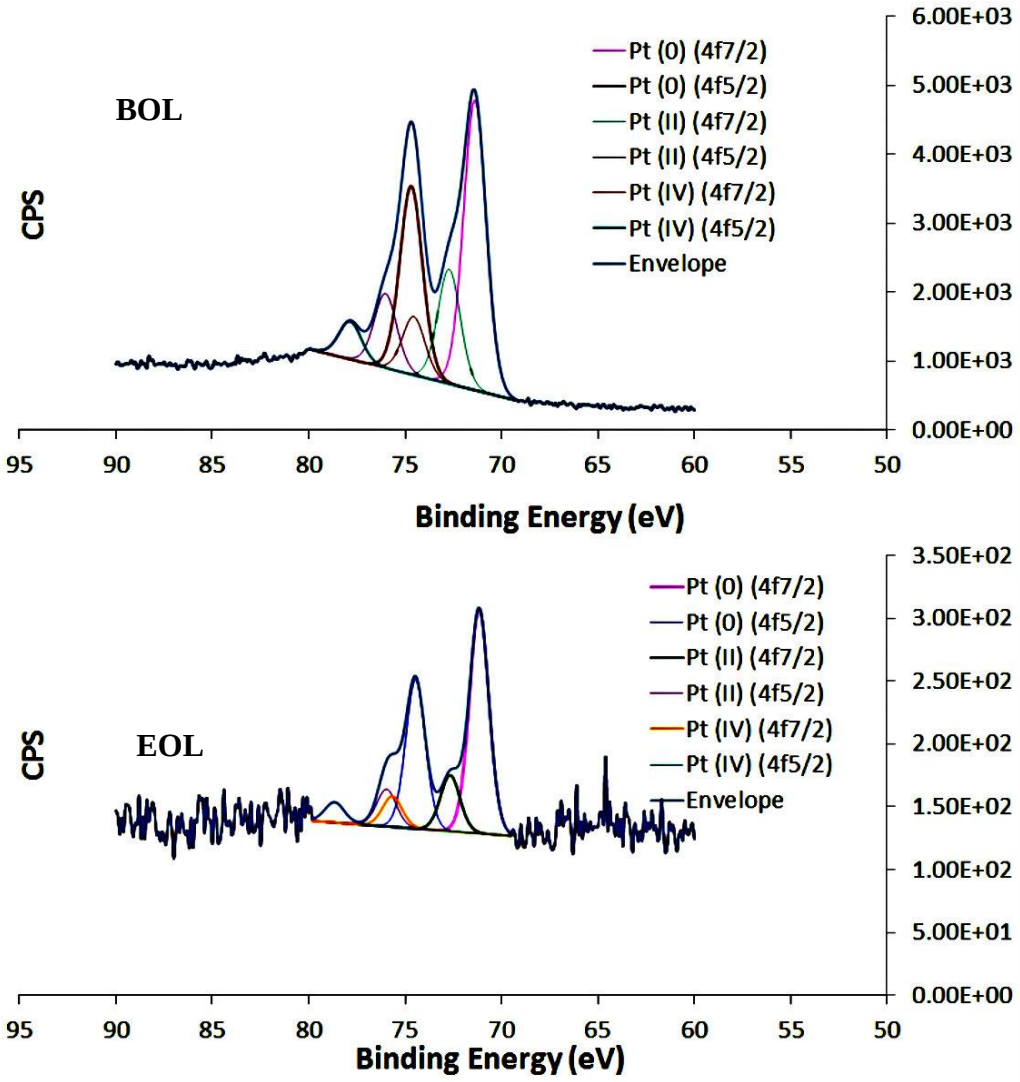

Figure 4-22: XPS scans in Pt 4f region.

Chapter 5
Platinum Dissolution ASTs

To understand the failure mechanism of Pt dissolution the experimental findings of the newly developed AST protocol is provided in Section 5.1. Included are details of the effect of Pt dissolution protocol at different temperature, impedance analysis, electrochemical activity of the MEA during the testing and the effect of kinetic performance loss. The derivation involved with the fingerprint development to analyze kinetic performance loss is given in the Section 5.1.1. A Kinetic fingerprint is developed to study the effect of the temperature during Pt dissolution AST based on the derivation. Kinetic finger print is a plot of fuel cell performance loss against effective Pt surface area loss (EPSA) obtained from CV analysis. The results of proposed plan on the effect of Pt dissolution protocol at different RH is outlined in Section 5.2, which includes pertinent information on performance analysis such as polarization curve, EIS and CV on the given MEA.

5.1 Pt Dissolution Protocol Fingerprint at Different Temperatures

In this Section, the results of Pt dissolution AST protocol involving the application of a potentiostatic square-wave with 3s at 0.6 V followed by 3s at 1.0 V was developed to test fuel cell MEAs is discussed. The effect of the Pt dissolution protocol is discussed at three different temperatures (40°C, 60°C and 80°C) for the same MEA 5 composition. Experimental procedures relevant to this Section are discussed in the Chapter 3 as follows:

1. MEA preparation – Section 3.3;
2. Cell conditioning – Section 3.4.3.1;
3. Cyclic voltammetry – Section 3.4.3.2;
4. Polarization curve measurement – Section 3.4.3.4;
5. EIS– Section 3.4.3.5;

5. Current interruption method – Section 3.4.3.6;
6. ASTs – Section 3.4.3.7;
7. Recovery – Section 3.4.3.8;
8. SEM – Section 3.4.3.10.

5.1.1 Pt Dissolution Kinetic Fingerprint Model Formulation

The contributions of the overpotential associated with the HOR are small under fully humidified conditions. Thus, the iR-corrected cell voltage $E_{IR\text{-}corrected}$ for a PEMFC in the absence of oxygen diffusion losses can be written as [127, 148]:

$$E_{IR-corrected} = E_{cell} + iR_{\Omega} = E_{cell} - \eta_{\mathrm{ORR}} \qquad (5\text{-}1)$$

where E_{cell} is the observed cell voltage (V), i is the current density in A cm^{-2}, R_{Ω} is the sum of the membrane, contact and bulk electronic resistances (ohm-cm^2) and η_{ORR} is the cathode overpotential (V). Assuming simple Tafel kinetics i.e., a single Tafel slope during the entire cathode potential range, the overpotential and current density for the ORR are related as in Equation (5-2) [149]:

$$\eta_{ORR} = \frac{2.303RT}{n\alpha_c F}\log\left[\frac{i + i_x}{10\, U_{Pt}\, ECSA\, L_W\, i_{o,s}\left(\frac{p_{O_2}}{p_{O_2}^*}\right)^{\gamma}\exp\left[\left(\frac{E_c}{R}\right)\left(1-\frac{T}{T^*}\right)\right]}\right] \qquad (5\text{-}2)$$

where i is the measured cell current density in A cm^{-2}, i_x is current density associated with H_2 cross-over in A cm^{-2}, $i_{o,s}$ is the catalyst specific exchange current density normalized to the reference oxygen partial pressure in A cm_{Pt}^{-2}, U_{Pt} is the catalyst utilization in %, ECSA is the electrochemical surface area in cm_{Pt}^2 $mg^{-1}_{Pt,}$ L_w is the cathode loading of the MEA 5 (g_{Pt} m^{-2}), E_c is the activation energy in kJ mol^{-1}, F is the Faraday constant in C mol^{-1}, R is the gas constant (8.314 J mol^{-1} K^{-1}), n is the number of electrons being transferred, α_c is the cathodic transfer coefficient, $p_{O_2}^*$ is the reference partial pressure of 101.3 kPa for O_2

p_{O_2} is the partial pressure of O_2 in kPa under the fuel cell operating conditions. γ is the kinetic reaction order for the ORR, while T and T* are the operating and reference temperatures in K. Pt utilization U_{Pt} of the MEA 5 is assumed to be 0.8 and the EPSA can be related to ECSA using Equation (5-3)

$$EPSA = 10\, U_{Pt}\, ECSA\, L_W \tag{5-3}$$

Equation (5-2) can be simplified based on Equation (5-3) to yield:

$$\eta_{ORR} = \frac{2.303RT}{n\alpha_c F}\log\left[\frac{i + i_x}{EPSA\, i_{o,s}\left(\frac{p_{O_2}}{p_{O_2}*}\right)^{\gamma}\exp\left[\left(\frac{E_c}{R}\right)\left(1-\frac{T}{T*}\right)\right]}\right] \tag{5-4}$$

The iR-corrected voltage is plotted against log (iγ) to obtain $i_{o,s}$ and Tafel slope b; γ is taken to be 0.75 based on the literature[148]. Since low current measurements are not considered in this analysis, the current density in the data set is much larger than the calculated cross-over current in this analysis,. Thus, for the data included in this analysis, $i >> i + i_x$ and so equation (5-4) can be further simplified to Equation (5-5):

$$\eta_{ORR} = b\log\left[\frac{i}{EPSA\; i_{o,s}\left(\frac{p_{O_2}}{p_{O_2}*}\right)^{\gamma}\exp\left[\left(\frac{E_c}{R}\right)\left(1-\frac{T}{T*}\right)\right]}\right] \tag{5-5}$$

During the *in-situ* experiments to obtain the polarization curves and EIS spectra, temperature and partial pressure of O_2 are kept constant. Thus, the denominator in equation (5-5) can be written as $EPSA\; i_{o,s}|_{T,P_{O_2}}$ where $i_{o,s}|_{T,P_{O_2}}$ is the exchange current density corresponding to the operating temperature and pressure. For convenience, this is written as i_o and Equation (5-5) becomes:

$$\eta_{ORR} = b\log\left[\frac{i}{EPSA * i_o)}\right] \quad (5\text{-}6)$$

During the life testing of catalyst in PEMFC, the Tafel slope b and the exchange current density i_o remain constant. Using EPSA values measured after 0, 1000, 10000 and 20000 cycles, the kinetic overpotential MEA can be estimated using Equation (5-6) without the need for polarization curve data. The overpotential of MEA in its BOL and after 'n' number of cycle measured at a current density i can therefore be expressed as Equations (5-7) and (5-8):

$$\eta_0 = b\log\left[\frac{i}{EPSA\,(0) * i_o)}\right] \quad (5\text{-}7)$$

$$\eta_n = b\log\left[\frac{i}{EPSA\,(N) * i_o)}\right] \quad (5\text{-}8)$$

Finally, to correct for sample-to-sample differences in the membrane electrode assemblies, the change in this overpotential is then obtained by subtracting Equation (5-8) from equation (5-7) and then normalized with respect to the BOL cell voltage $E(0)$ of the particular MEA to yield:

$$\frac{\Delta\eta_{kin}}{E(0)} = b\frac{\log\left(1-\frac{\Delta EPSA(N)}{EPSA(0)}\right)}{E(0)} \quad (5\text{-}9)$$

where $\Delta\eta_{kin} = \eta_0 - \eta_n$ and $\Delta EPSA(N) = EPSA(0) - EPSA\,(N)$.

All EPSA values obtained during the Pt dissolution ASTs were used in Equation (5-9) in order to compute the theoretical polarization curve similar to that presented previously

(33). This theoretical curve was validated using experimental data from the ASTs conducted at 40, 60 and 80 °C using the following procedure:

1. Plot iR corrected voltage against log(iγ) from polarization curve obtained at H_2-O_2 mode.
2. Find the Tafel slope b and exchange current density (i_0)
3. Assume a constant 'b' values and choose arbitory values of EPSA and then calculate $b.\log\left(1-\frac{\Delta EPSA(N)}{EPSA(0)}\right)$
4. The calculated value is equal to kinetic overpotential of cell ($\Delta\eta_{kin}$)
5. Divide the calculated kinetic overpotential to BOL of the MEA obtained from the polarization curve at H_2-air mode
6. To obtain kinetic overpotential fingerprint, plot $\frac{\Delta\eta_{kin}}{E(0)}$ vs $b.\log\left(1-\frac{\Delta EPSA(N)}{EPSA(0)}\right)$
7. Compare the fingerprint with experimental data obtained from three ASTs
    a. Find kinetic overpotential of each ASTs during BOL to EOL performance check points
    b. Obtain $\frac{\Delta\eta_{kin}}{E(0)}$
    c. Find EPSA using equation 3-3 from CV spectra
    d. Calculate $b.\log\left(1-\frac{\Delta EPSA(N)}{EPSA(0)}\right)$
    e. Finally, plot the experimentally obtained ratios $\frac{\Delta\eta_{kin}}{E(0)}$ vs. $\log\left(1-\frac{\Delta EPSA(N)}{EPSA(0)}\right)$

Comparison of the theoretical curve based on Equation (5-9) with that obtained experimentally should help in determining the portion of the performance loss due to Pt dissolution.

5.1.2 Polarization Curve

The BOL and EOL polarization curves measured during the ASTs conducted at 40, 60 and 80^0C are shown in Figure 5-1. Although the ASTs were conducted at these different temperatures, the measurement of all the polarization curves were carried out at a standard temperature and pressure of 60^0C and 270/250 barg, respectively, to be able to make fair comparisons. The performance degrades at all cell voltages for all three AST testings compared to BOL performance. Comparison of the EOL curves with BOL demonstrates that degradation during the ASTs occurred in the low current density region between 0 and 0.2 A cm^{-2} at all three temperatures. During performance evaluation of these ASTs, the OCV dropped at a slower rate of 0.08, 0.1 and 0.217 µV/cycle at 40, 60 and 80^oC, respectively, suggesting that very little hydrogen cross-over was occurring during the ASTs. Similar observations were reported for the MEAs (MEA 5) cycles at 80^oC than 60^o C ASTs during constant OCV hold [150]. The decrease in cell voltage measured at the current density of 1.7 A cm^{-2} in the MEAs tested at 40, 60 and 80^0 C ASTs were approximately 30, 50 and 90 mV, respectively, reflecting that the polarization losses increase as the temperature is raised. The results of EOL polarization plots suggest that only a relatively small loss in cell performance occurred at 40°C, but that considerably more degradation is observed at 80°C. The performance losses that occur in the low current region where kinetic factors tend to be dominant likely arise due to changes in catalyst activity, catalyst area and polarization resistance. At 80°C, some additional degradation is observed at intermediate and higher currents.

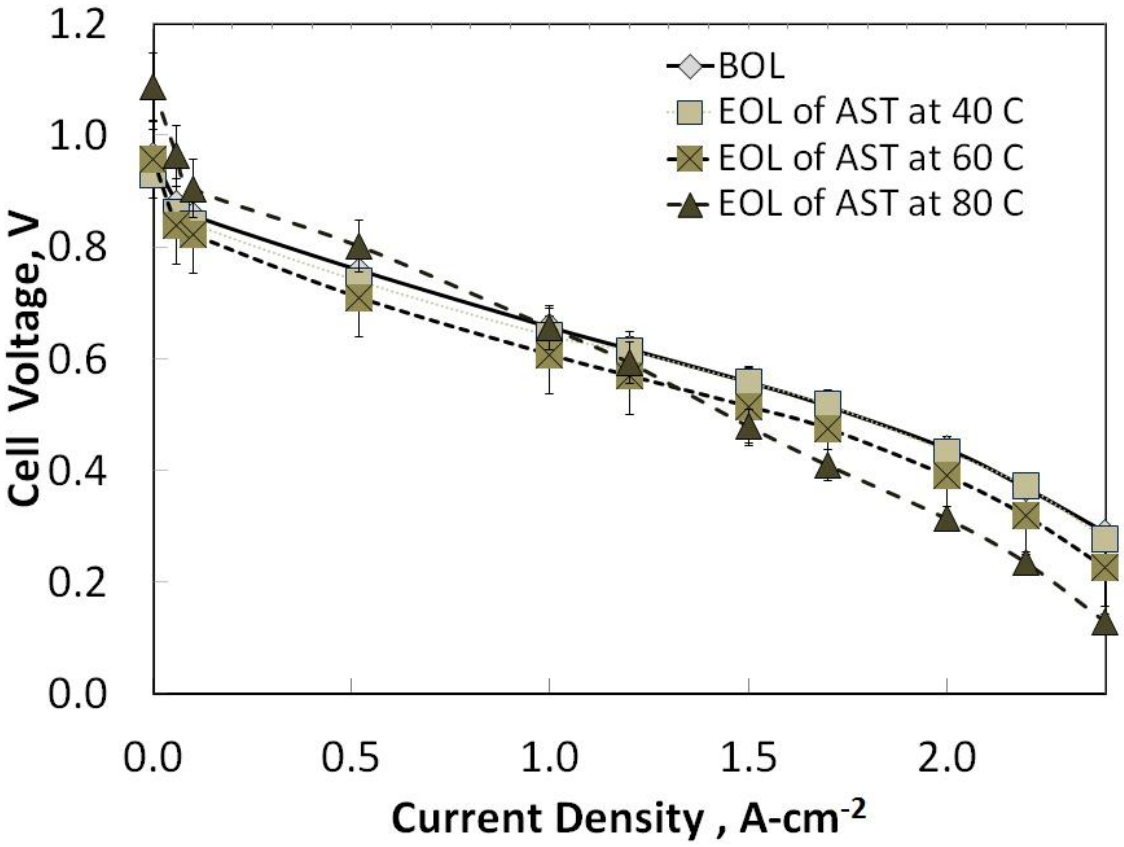

Figure 5-1: Polarization curves obtained during Pt dissolution AST. Conditions during AST and polarization measurements are given in Table 3-3.

5.1.3 Cell Voltage and ECSA

Figure 5-2a shows the variation in the loss of cell potential with the number of cycles at the three temperatures when a current density of 0.1 A cm^{-2} is applied, while Figure 5-2b presents the corresponding curves for a current density of 1.7 A cm^{-2}. The plots indicate the performance loss decays more rapidly as both temperature and current density rises.

Voltage decay rates were determined from the slope of the polarization curve (Figure 5-1) using Equation (5-10), i.e.,

$$Voltage\ decay\ rate = \frac{E_{\ BOL\ measured\ at\ 0.1Acm^{-2}} - E_{\ After\ n\ cycles\ measured\ at\ 0.1Acm^{-2}}}{\#of\ \ Cycles} \qquad (5\text{-}10)$$

Voltage loss rates of 0.96, 1.8 and 4.5 µV/cycle at 0.1 A cm^{-2} were obtained for 40, 60 and 80^{o}C, respectively. At 1.7 A cm^{-2}, the measured potential decay rates were 1.75, 2.5 and 5 µV/cycle for 40, 60 and 80^{o}C ASTs, respectively. In previous studies, higher cell potential loss rates of 30 and 20 µV/cycle at 0.1 A cm^{-2} during the square-wave potential cycling have been reported [42, 151]. However, the conditions during these studies differ considerably from those of the current study in many regards: cell temperature, cathode catalyst composition and design, method of material preparation, MEA 5 hardware, upper and lower potentials during cycling and dwell time at the upper and lower potential limits. At 80°C and 0.1 A cm^{-2}, the drop in cell potential was steep at the outset of cycling, but then quickly leveled off until about 10000 cycles had been applied whereupon it increased again. The decay rate measured during recovery period between cycles was observed to be about three times higher during the last 10000 cycles than during the first 10000 cycles at this current. Increases in the number of potential cycles and cell operating temperature accelerate cell degradation and irreversible performance decay. Cell temperature during cycling plays a role in degradation of the membrane in addition to Pt dissolution.

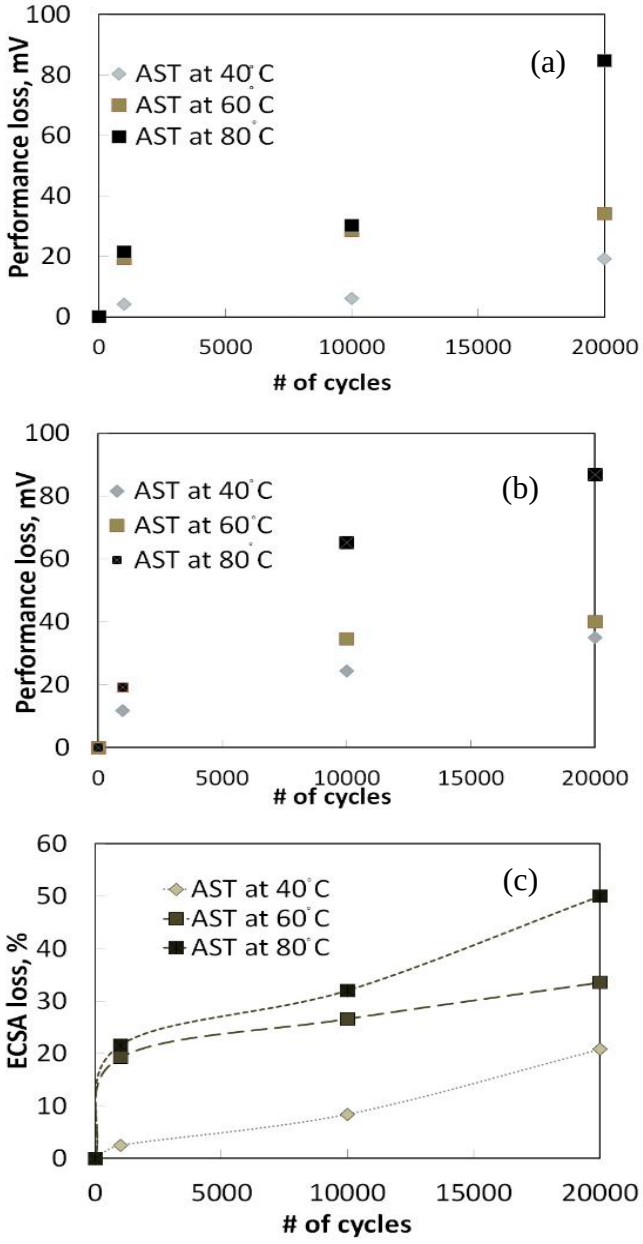

Figure 5-2: Performance loss measured for MEAs during Pt dissolution ASTs from polarization curve at (a) 0.1 A/cm^2; (b) 1.7 A/cm^2 (c) % ECSA loss obtained during ASTs. Conditions of the analysis are given in Table 3-3.

As described in Chapter 3, six consecutive cyclic voltammetry cycles between 0.6 and 1.2 V were performed periodically during the ASTs at the three temperatures to determine the influence of potential cycling on the ECSA. ECSA for all the MEA 5s were calculated using equation 3-2. The effect of cycle number on % loss of ECSA at the three temperatures is shown in Figure 5-2c. The ECSA values for the three MEAs in their BOL state were found to be very close to each other, showing only a slight variation with a mean value of 80 ± 1.0 m^2 g^{-1}. To account for this slight variation, the ECSA data at each temperature are presented as the percentage loss from the respective BOL value of the respective MEA to normalize for the sample-to-sample differences. Overall, the loss in ECSA increases as the temperature rises. At 40°C, the ECSA decreases from 80 to 63.4 m^2 g^{-1} (corresponding to a 21 % loss) over the course of the AST until the EOL state is reached. This decrease is gradual with a slight increase in rate after 10000 cycles have been applied. The decrease in ECSA at 60°C from 81 to 54 m^2 g^{-1} as the MEA 5 changes from the BOL state to EOL state corresponds to a 33 % loss. However, this loss is not uniform and is steep during the first 1000 cycles of the AST before leveling off and rising linearly and more slowly thereafter. The behavior observed at 80°C is qualitatively similar to that at 60°C, with the ECSA dropping from 81 to 40 m^2 g^{-1} (50.6 % loss) over the course of the AST.

5.1.1 EIS Spectra

The Nyquist plots obtained from the EIS experiments during the Pt dissolution ASTs at the three temperatures are shown in Figure 5-3a-c. Each spectrum exhibits a semi-circle with a high frequency intercept equal to the ohmic resistance of the membrane and a low frequency intercept equal to the sum of the ohmic resistance of the membrane and the charge transfer resistance of the catalyst layer [152]. In order to focus on the kinetics of the cathodic reaction, impedance was measured at low overpotential with pure hydrogen at the anode and high air flow rate at the cathode in order to minimize possible mass transport effects at the cathode and anode. Several trends are evident from the spectra. The MEAs in

their BOL state generally exhibit lower impedance, particularly at lower frequencies, than those that have been subjected to the ASTs at all temperatures. The diameter of the semi-circular arc in the Nyquist plots increased during degradation tests of all three cases (Figure 5-3). This is due to a rise in polarization resistance as the MEAs age from their BOL states to EOL states. This effect is particularly strong at 80°C, as shown in Figure 5-3.c.

The variation of the charge transfer (R_p) and ohmic (R_s) resistances during the AST obtained from the fitting of equivalent circuit models (Figure 3.7) to the EIS spectra are presented in Figure 5-4 a and b, respectively. During the AST at 40°C, the R_p of the cell increases at a very low average rate of 1 $\mu\Omega\text{-cm}^2$/cycle from 0.0949 to 0.1157 $\Omega\text{-cm}^2$ (Figure 5-4a). When the operating temperature is raised to 60°C, R_p increases at a faster average rate of 2 $\mu\Omega\text{-cm}^2$/cycle from 0.101 to 0.137 $\Omega\text{-cm}^2$. This trend continues with a further rise in temperature to 80°C as the resistance increases from 0.110 to 0.161 $\Omega\text{-cm}^2$ at an average rate of 2.5 $\mu\Omega\text{-cm}^2$/cycle. This increase is likely caused by the higher rate of Pt dissolution at 80^oC than at 40 ^oC, which leads to a significantly higher cell impedance in the EOL state. It should be noted that the increase in the R_p with respect to cycle number is not linear. At all three temperatures, it increases at a much higher rate of approximately 6 $\mu\Omega\text{-cm}^2$/cycle during the first 1000 cycles than it does later during the AST. R_s can be considered to be a combination of electronic and ionic resistances within the membrane phase in the catalyst layer [152]. Since the humidity in both the cathode and anode of the cell was kept at 100 % at all three temperatures, one would not expect significant changes in the initial R_s in the three cases, as is confirmed in Figure 5-4b. Furthermore, the R_s values remain virtually unchanged as the MEAs are aged at 40°C and 60°C. However, at 80°C, the time course of the R_s changes from the others after approximately 10000 cycles have been applied whereupon it rises to 0.1292 $\Omega\text{-cm}^2$ at the rate of 2 $\mu\Omega\text{-cm}^2$/cycle. This behavior suggests that the carbon support and/or the recast ionomer at the electrolyte–catalyst interface may have begun to degrade [71]. Importantly, temperature has a stronger effect on the chemical and morphological stability of the catalyst layer and the Pt dissolution rate at 80°C than at 40 or 60°C. Thus, one must exercise caution in

extrapolating the behavior observed at lower temperatures to accurately predict the behavior at 80°C which is the typical operating temperature of PEMFCs.

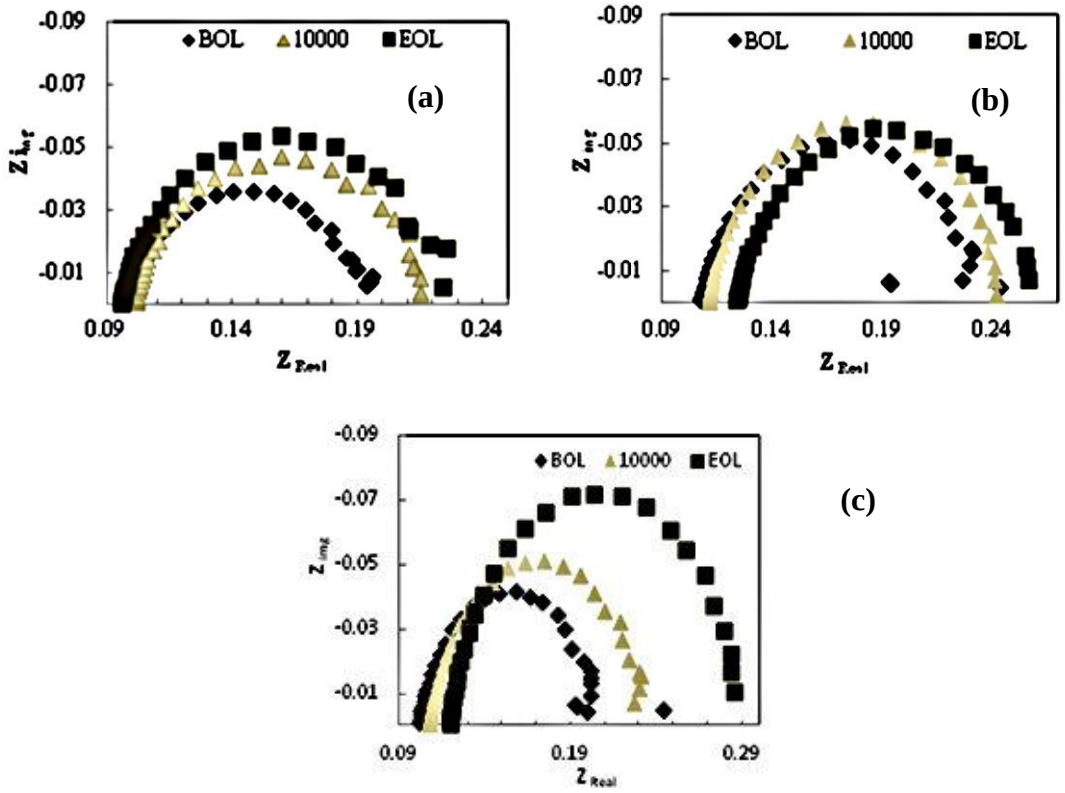

Figure 5-3: Nyquist plots of MEAs during the AST testing at (a) 40°C, (b) 60 °C and (c) 80 °C. Conditions during the AST and EIS measurements are given in Table 3.3.

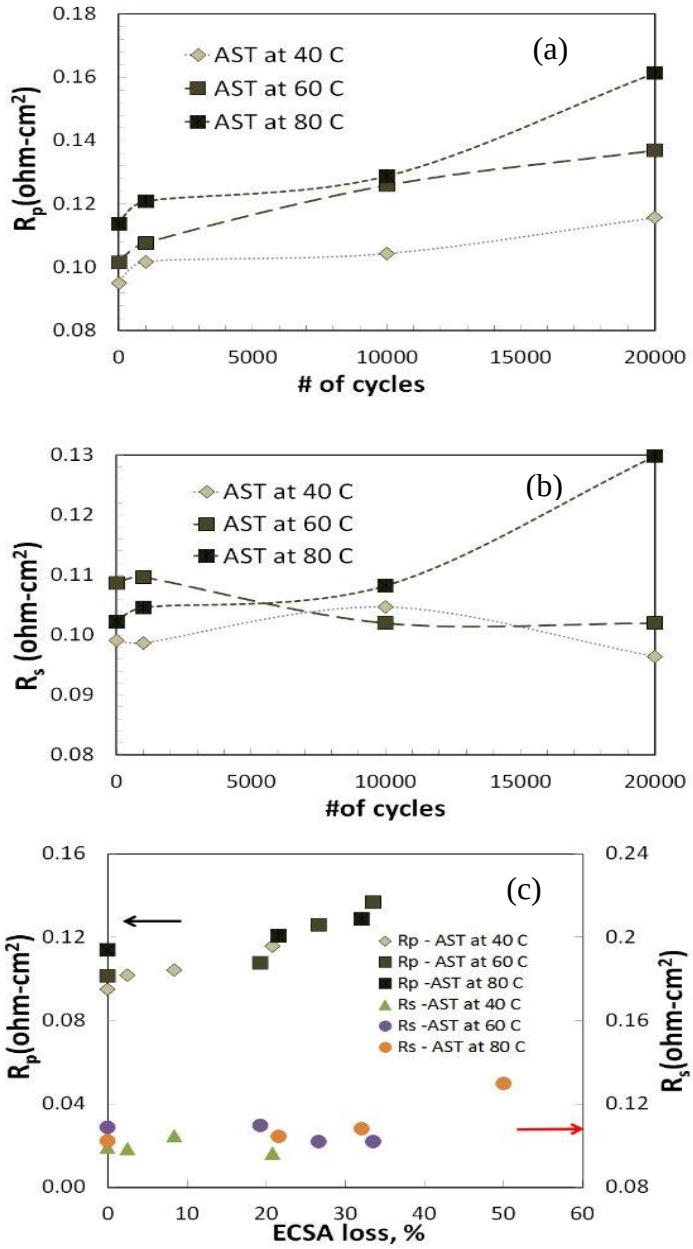

Figure 5-4: Variation in (a) polarization resistance R_p, (b) ohmic resistance R_s with cycle number during AST at 40, 60 and 80°C. (c) Correlation of R_p and R_s to % ECSA loss measured from CV analysis and the polarization at 40, 60 and 80°C. Conditions during the AST and EIS measurements are given in Table 3.3.

Plots of R_s and R_p versus the ECSA loss at the three temperatures are shown in Figure 5-4c. A near linear dependence of R_p on ECSA loss is observed at all three temperatures. Since ECSA gives a measure of the amount of electrocatalyst that is electrochemically accessible during the ASTs, this suggests that the loss of active electrocatalyst contributes significantly to the loss in cell voltage observed from the polarization experiments (Figure 5-1 and Figure 5-2 a and b). On the other hand, the results in Figure 5-4c reveal that temperature has very little effect on R_s. This is important since it validates the experimental procedure adopted during this study. Recall that fuel cell performance during the ASTs was always characterized at 60°C regardless of the temperature during the AST potential cycling so that temperature effects during the characterization of cell performance would not be confounded with temperature effects on Pt degradation during potential cycling. In addition, R_s should not be strongly affected by Pt dissolution. Given that the applied AST in this case was aimed at promoting Pt dissolution and not carbon corrosion, the observation that R_s remains largely constant regardless of the degree of degradation and temperature is expected (Figure 5-4c). Again, this validates the experimental protocol used whereby the humidity of both the cathode and anode of the cell was kept at 100 % at all three temperatures to ensure that the ohmic resistance would not change significantly.

5.1.2 Changes in the Morphology of the MEA due to ASTs

SEM images of a BOL and EOL MEAs after being subjected to ASTs at 40, 60 and 80°C are shown to better understand the changes in the catalyst layer such as dissolution and migration of Pt catalyst in Figure 5-5 a-d. These images confirm that some Pt in the catalyst layer dissolved and formed Pt bands at all three temperatures when EOL is reached. The only apparent difference between the BOL and EOL MEA samples studied at 40°C is the presence of a thin platinum band in the membrane near the CCL. The Pt bands in the images of the MEAs at 60 and 80°C appear more intense than the one appearing at 40°C, mirroring the differences in Pt concentration in the respective MEA samples. Bands are formed when Pt dissolved from the catalyst layer diffuses into the membrane and is reduced chemically by hydrogen permeating from the anode [60].

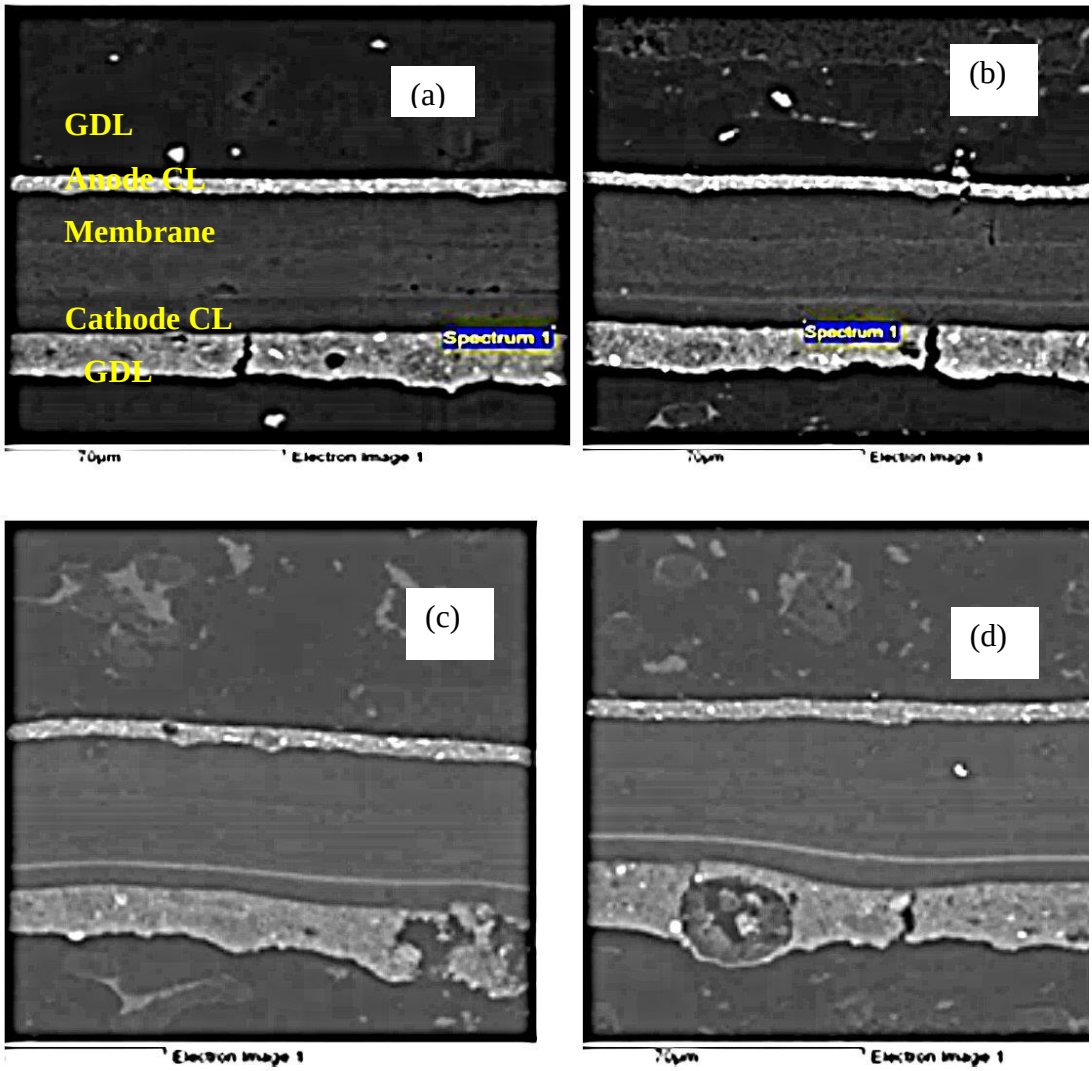

Figure 5-5: SEM images of (a) BOL sample; (b) EOL of 40^{o}C AST MEA; (c) EOL of 60^{o}C AST MEA; and (d) EOL of 80^{o}C AST MEA.

The Pt (II) and Pt (IV) species, which are highly mobile in the membrane, tend to increase upon ageing. Band formation is dependent on the partial pressures of H_2 and O_2, permeability of reactants through the membrane, size distribution of Pt (II), diffusion properties and humidity [19, 60]. As shown in Figure 5-5 b-d, the Pt band near the CCL is thicker for 80, 60^{o}C AST MEAS to 40^{o}C AST MEA, similar to that reported by Bi et al [65, 103], presumably due to the accelerated rates of repeated oxidation and reduction reactions. Based on a model proposed by Kundu et al. [19], a Pt band should appear at the location where cross-over hydrogen and oxygen are consumed and their concentrations reach zero. This leads to the following expression for the location of a Pt band:

$$\frac{1}{x} = 1 + \frac{\alpha_{H_2/O_2}}{2}\frac{p_{H_2}}{p_{O_2}} \qquad (5\text{-}11)$$

where p is the gas partial pressure and x is the dimensionless distance in the membrane defined with x = 0 being the cathode membrane/catalyst layer interface and x = 1 being the anode membrane/catalyst interface. An ionomer membrane selectivity α_{H_2/O_2} taken to be 0.38 from literature values is used to calculate the location of the Pt band [62, 65]. Based on these calculations, a Pt band is predicted to form at distances 3.2, 4.6 and 5.2 μm from the cathode for the three MEAs tested at 40, 60 and 80^{0}C, respectively. These are in excellent agreement with the band locations of 3.1, 4.8, and 5.1 μm estimated from the SEM images. As expected, the Pt bands appear farther from the CCL as the cell temperature is increased. Faster dissolution of Pt should enable it to have diffused farther from the cathode/membrane interface when it contacts hydrogen and is reduced to its elemental form [100].

5.1.3 Diagnostics of Cell Performance and EPSA Loss

The computation of the EPSA requires the estimation of U_{Pt} and ECSA values. The values of ECSA were calculated using Equation 3-2, respectively. Computed values of BOL ECSA and U_{Pt} are 80 $m_{Pt}^2 g_{Pt}^{-1}$ and 0.80, respectively. The EPSA of the MEA in its BOL

state determined by equation equation 3-3 is 224 $cm^2_{(Pt)}.cm^{-2}_{(geom)}$. Important parameters that provide measures of catalyst activity loss during the Pt dissolution AST are the current density determined at a given overpotential and the exchange current density. The current density at which the effect of EPSA loss was studied was kept relatively low where interferences from hydrogen cross-over and mass transfer effects would be minimized [153]. Consequently, on the basis of the polarization curves, the performance loss was measured at 0.1 A cm^{-2} at the three temperatures. This current density occurred at overpotentials in the range of 10 to 100 mV where kinetic effects dominate MEA performance.

The performance degradation expressed in terms of the drop in cell voltage obtained at 0.1 A cm^{-2} relative to that measured in the BOL state is plotted versus the normalized EPSA loss obtained after 1000, 10000 and 20000 AST cycles at 40, 60 and 80°C in Figure 5-6. Not surprisingly, a strong correlation between performance loss and EPSA loss resulting from the Pt dissolution ASTs is observed. After 20000 AST cycles, the EPSA loss of 33% at 60°C is higher than the 20% measured at 40°C at the EOL presumably due to the greater EPSA degradation at the higher temperature. The corresponding performance losses at 60 and 40°C are 34 and 20 mV, respectively, at this current when the EOL state is reached. The EPSA and performance losses at 80°C are even higher, reaching 50% and 84 mV, respectively, by the end of 20000 cycles. In addition to Pt degradation, other factors such as membrane drying, proton conductivity and polarization resistance limit the electrochemical reactions and may contribute to these losses. The relation between performance loss and % EPSA loss becomes less linear at 80°C and, in fact, may be qualitatively different than at the lower temperatures since it appears to be accelerating as the AST proceeds. Another reason for the deviation could be that dissolved platinum ions have subsequently migrated into the membrane during the AST which has been shown to occur more readily at higher temperatures [99]. The SEM image in Figure 5-4 (d) confirms that Pt migration and band formation have occurred. Direct comparison of the EPSA and performance loss shows that a single universal curve can be drawn through all the data obtained at the three

temperatures (Figure 5-6). Nevertheless, in-situ characterization (CV and polarization curve) of the cell was carried out at common conditions for all AST experiments. Different amounts of EPSA loss obtained after a given number of cycles in each AST clearly revealed that the amount of EPSA loss affects the performance loss. Detailed analysis of the relation between EPSA loss and ORR kinetics may be required to sort out the contribution of EPSA loss to the total performance loss from that due to membrane or GDL degradation during high temperature Pt dissolution ASTs.

The experimental observations presented in Figure 5-6 confirm a strong correlation between EPSA and the performance loss of the MEA during ASTs. One would also expect the loss of EPSA to directly affect the overpotential associated with the kinetics of the ORR. This hypothesis can be assessed by examining whether a correlation exists between these two quantities. This approach will also provide a breakdown of the contribution of electrode kinetics to the overall performance loss during the ASTs at different temperatures and enable in-situ real-time and non-destructive diagnostic analysis of performance degradation. Consequently, we have derived a relationship between the EPSA and the overpotential for ORR kinetics based on Tafel behavior and applied it to the experimental data of this study.

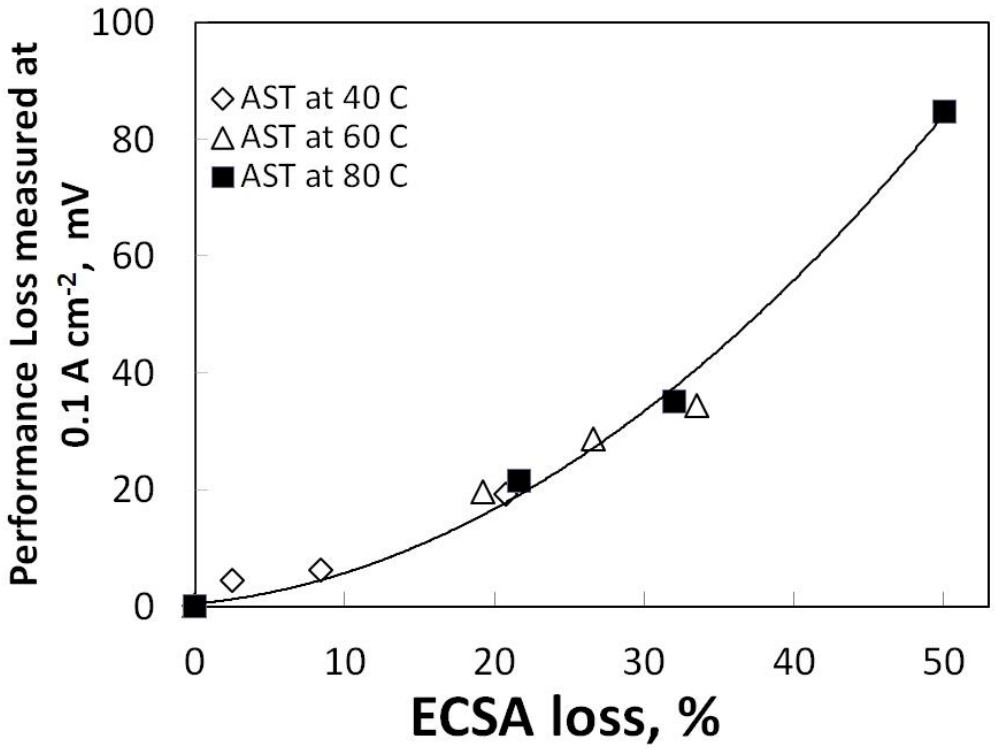

Figure 5-6: Correlation between performance loss, as measured from polarization at 0.1 A cm^{-2} and % ECSA loss at 40, 60 and 80°C.

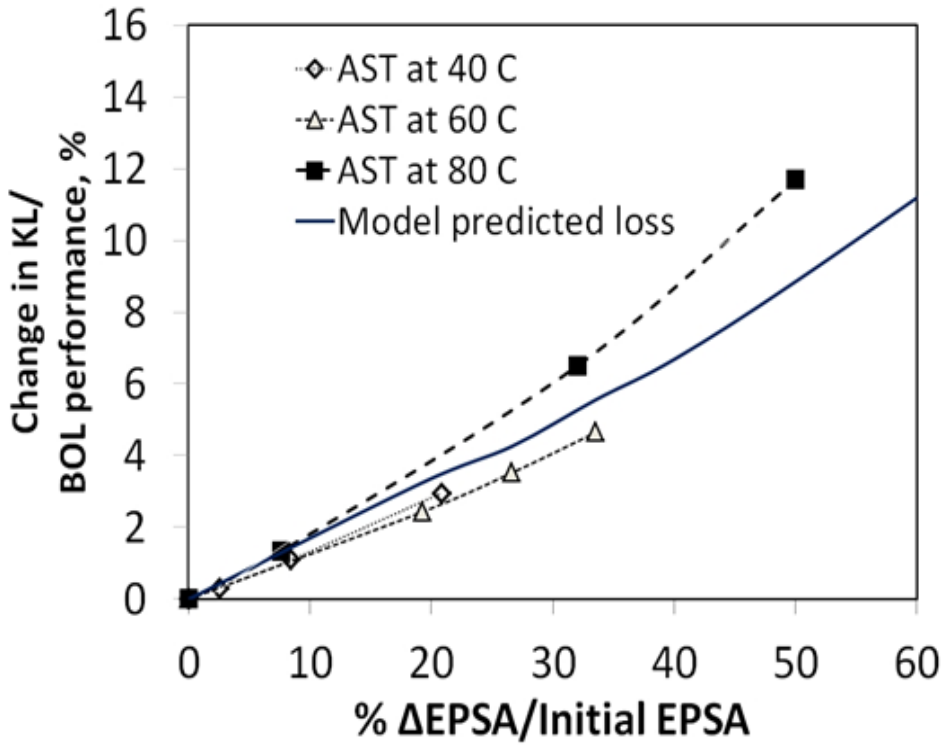

Figure 5-7: Degradation fingerprints for each AST of a cell subjected to Pt dissolution testing at 0.1 A cm^{-2}.

The details of the derivation were presented in section 5.1.1 and led to Equation (5-9):

$$\frac{\Delta\eta_{kinetic}}{E(0)}\% = b\,\frac{\log\left[\frac{\Delta EPSA}{EPSA(0)}\right]}{E(0)} \times 100 \qquad (5\text{-}9)$$

where $\Delta EPSA$ is the difference between EPSA(0) and EPSA(N). EPSA values obtained after conditioning, 1000, 5000, 10000 and 20000 cycles of the ASTs conducted at three different temperatures were used to predict the theoretical value of kinetic loss using Equation
(5-9).

A plot of $\frac{\Delta\eta_{kinetic}}{E(0)}$ versus $\left[\frac{\Delta EPSA}{EPSA(0)}\right]$ is shown in Fig. 5.7. The experimental $\frac{\Delta\eta_{kinetic}}{E(0)}$ at the three temperatures agreed well with the theoretical estimates until a normalized EPSA loss of about 20% was reached. The experimental $\frac{\Delta\eta_{kinetic}}{E(0)}$ of the membrane electrode assemblies subjected to accelerated stress testing at 40 and 60^{o}C were in good general agreement with the computed losses based on Equation (5-9). Hence, based on this comparison, it may be concluded that the kinetic loss is associated mainly with the EPSA loss during the AST at 40 and 60°C. The experimental curve obtained at 80°C show less agreement, particularly when the EPSA loss becomes large. Unlike the situation at the lower temperatures, the theoretical expression underestimates the experimentally observed overpotential loss. This may in part be the consequence of other confounding degradation modes or because the ionomer resistance has increased at the catalyst/membrane interface due to drying or variation of humidity within the cathode layer [154]. Also, the exchange current density, which was assumed to be constant in the derivation shown in section 5.1.1, may actually decrease over time. In addition, the catalyst particle size may be increasing via Pt dissolution/re-precipitation.

5.2 Effect of RH on Pt Dissolution ASTs

The use of a Pt dissolution AST protocol involving the application of a potentiostatic square-wave with 3s at 0.6 V followed by 3s at 1.0 V is investigated at three different relative humidities (100 %, 50 % and 0% RH) for the same MEA composition. The results of impedance, CV, polarization analysis and ECSA were discussed. Experimental procedures relevant to this sSection are discussed in the Chapter 3 as follows:

1. MEA preparation – Section 3.3;
2. Cell conditioning – Section 3.4.3.1;
3. Cyclic voltammetry – Section 3.4.3.2;
4. Polarization curve measurement – Section 3.4.3.4;
5. EIS– Section 3.4.3.5;
5. Current interruption method – Section 3.4.3.6;
6. ASTs – Section 3.4.3.7;
7. Recovery – Section 3.4.3.8.

5.2.1 Cell Performance and Durability

Polarization curves were measured after 1000, 10000 and 20000 cycles of each AST to yield the results shown in Figure 5-8. Although the ASTs were conducted at different RH, the polarization curves were obtained under identical conditions as given in Table 3-2 to be able to make fair comparisons. In all cases, cell performance continually declined as the AST proceeded through the number of cycles. Typically polarization curves can be divided in to regions where kinetic (0 to ~0.1 A cm^{-2}), ohmic (~0.1 to ~1.7 A cm^{-2}) and mass transport (~1.7 to ~2.4 A cm^{-2}) effects begin to be significant. At 100% RH, the major effects on the polarization curves obtained as the MEA 5 is aged from its BOL to EOL state occur at very low current densities close to 0.1 A cm^{-2} (Figure 5-8a). Thereafter, degradation does not have much influence over the remainder of the polarization curves. Similar trends are observed at 50 and 0% RH (Figure 5-8 b-c). Following are the likely factors contributing to the effect at low currents:

1. Some inhibition of the ORR and HOR at the cathode and anode catalyst interfaces, respectively, may have occurred [109, 155].
2. A slight decrease in OCV is observed over the course of each of the ASTs. One notable exception to this trend is observed in the case of the MEA maintained at 0% RH, which showed a significant drop in OCV compared to its BOL state once it had reached its EOL state. Fuel cross-over has been previously identified as one of the major contributors to an OCV drop during potential cycling [46]. Degradation of the electrocatalyst rather than the membrane could also cause a lower OCV.

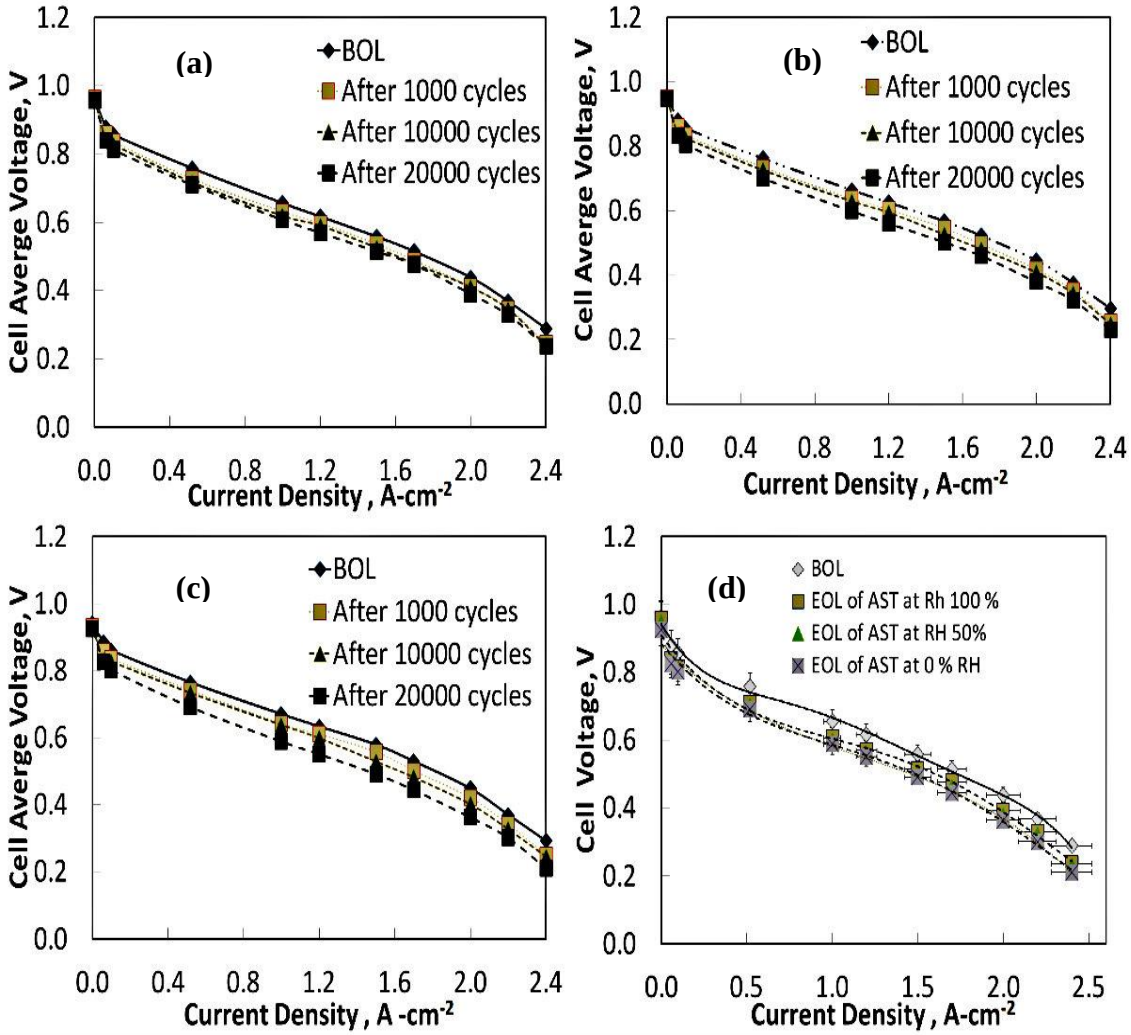

Figure 5-8: Polarization curves of Pt dissolution AST at (a) RH 100% (b) RH 50% and (c) RH 0% condition (d) Comparison of BOL (average) and EOL of each cases. Polarization curves were obtained using conditions given in Table 3-4.

During durability testings under different operation conditions, utilization of the catalyst in the MEA changes with respect to the current density of the cell. Our repeated polarization analysis on the MEA showed higher catalyst and fuel utilization at 0.1 A cm^{-2} [156]. In addition to this, a Tafel slope of ~70 mV/decade is obtained for current densities in the range from 0.01 to 2.0 A cm^{-2}. This finding suggests that cell performance is controlled by ORR kinetics at a current density of 0.1 A cm^{-2} [125]. Hence, this is an appropriate current density to use to evaluate the kinetic performance of the cell during ASTs. However, such a low current density is not feasible for commercial applications and a much higher level is required. Fuel cell operating design is decided based on the cost, size of the system and efficiency. Operation of a cell at 1.7 A cm^{-2} or above will help to reduce its cost, size and weight required for commercial application, although its efficiency tends to drop [157]. Automotive vehicle applications require higher current densities in this range, whereas stationary power sources can operate in the lower part of this range [117, 158]. A current density of 1.7 A cm^{-2} (corresponding cell voltage of 0.6 V) puts the system in a condition where ohmic effects are important, but mass transfer effects are not yet important. At 1.7 A cm^{-2}, the current density has reached its maximum level and it is likely that the flow of ions in the membrane and resistance to the flow of electrons through the electrode are in steady-state [117]. Hence, 1.7 A cm^{-2} is also another useful current density at which the degree of degradation can be assessed during ASTs. Thus, the effect of RH on cell performance loss is examined more closely by plotting the degradation in cell voltage at current densities of 0.1 and 1.7 A cm^{-2} (Figure 5-9). At 0.1 A cm^{-2}, the cell voltage decreases by approximately 43, 52 and 59 mV from the beginning to the end of the AST at % RH levels of 100, 50 and 0 %, respectively (Figure 5.9a). Figure 5-9b presents the corresponding data for a current density of 1.7 A cm^{-2}. The plot shows that the cell potential dropped by 39, 63 and 86 mV of its BOL level at 100%, 50 % and 0% RH, respectively. The most notable difference from the results obtained at the lower current density is the larger effect that RH has on the performance loss at the higher current. In particular, the much larger voltage drop at 1.7 A cm^{-2} when the cell is operated under dry

conditions presumably reflects the contribution from degradation of the membrane and catalyst ionomer [109].

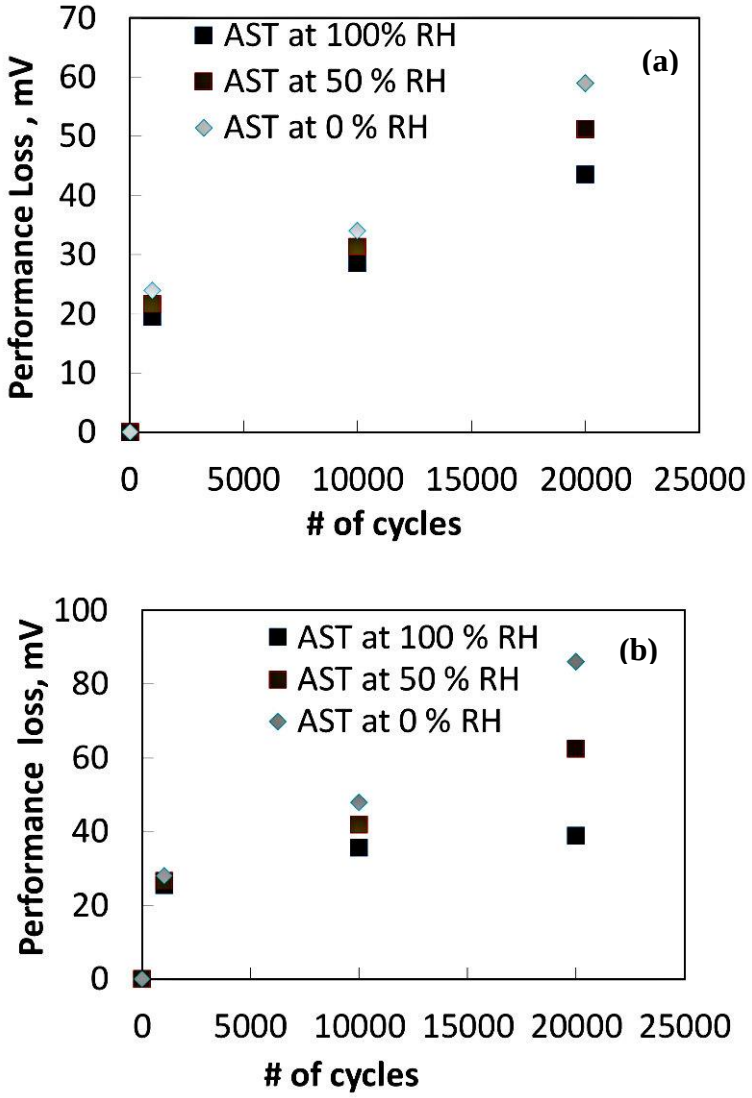

Figure 5-9: (a) Performance loss measured from polarization curve for MEAs during ASTs at 0.1 A-cm^{-2} (b) at 1.7 A cm^{-2}.

5.2.2 Electrochemical Surface Area and Cell Performance

Electrochemical analyzes were carried out to further examine the degradation behavior of the cells during the Pt dissolution ASTs at the different RHs. The ECSA of the Pt catalyst in its BOL state and again after 1000, 10000 and 20000 AST cycles was obtained using the following procedure. Repeated CV scans were conducted until identical electrode responses were obtained on consecutive cycles. Experience revealed that this was always achieved by the end of five cycles. Consequently, the standard procedure adopted was to base the ECSA measurement on the electrode response during the 5^{th} cycle. The characteristic and well-defined region corresponding to the adsorption and desorption of hydrogen on Pt appeared in the voltage range between 0.05 and 1.2 V. The coulombic charge Q was determined from the integrated area under the hydrogen desorption (anodic) portion of the scan. Charge contributed by the double-layer region was subtracted from this area before determining the ECSA of the cathode Pt catalyst. The ECSA values of the BOL state for MEAs used in the three ASTs showed similar values, exhibiting only a small variation with a mean value of 81 ± 1.0 $m^2\ g^{-1}$. To account for differences in the BOL ECSA values from sample-to-sample, the ECSA data obtained during each AST were expressed in terms of the percentage difference from the respective BOL value of the particular MEA. The variation of % ECSA with the number of AST cycles obtained at the three humidities is given in Figure 5-10a. The overall trend observed at the three RH levels is similar, exhibiting a large rise in % ECSA over the first 1000 cycles and a much slower and essentially linear increase thereafter. The ECSA loss over the first 1000 cycles was found to increase as the RH level rises. At 100% RH, the ECSA decreases from 82 to 55 $m^2\ g^{-1}$ (corresponding to a 33% loss) over the course of the AST until the EOL state is reached. The decrease in ECSA at 50% RH from 81 to 58.32 m2 g^{-1} as the MEA changes from the BOL state to EOL state corresponds to a 28.5% loss. The loss observed at 0% RH condition AST is lowest with the ECSA dropping from 80 to 60 $m^2\ g^{-1}$ over the course of the AST (corresponding to a 26% loss). It is evident that ECSA losses increase during the

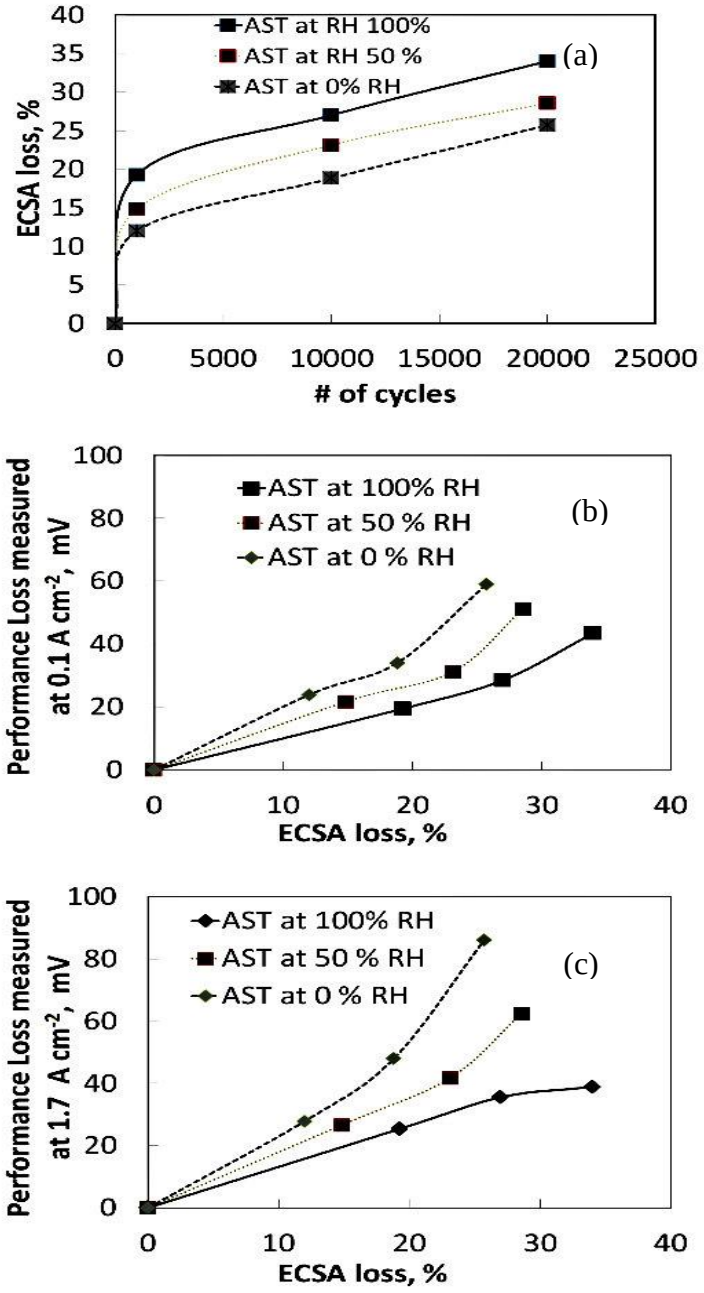

Figure 5-10: (a) Variation in % ECSA loss with cycle number during ASTs. Correlation between performance loss vs. % ECSA loss at (b) 0.1 and (c) 1.7 A cm^{-2}.

final 10000 cycles, unlike the behaviour reported in the literature[125]. This difference could be due to the shorter dwell times (3s/3s) and higher number of cycles (20000 cycles) used in the ASTs of the current study.

The loss in ECSA over the course of the potential cycles is likely caused by Pt particle coarsening, agglomeration and dissolution [103]. It would be interesting to examine the correlation between ECSA and the performance loss at the three RH levels. Accordingly, the performance degradation of the MEA 5 during these ASTs characterized in terms of the decrease in the cell voltage from that measured in its BOL state at 0.1 A cm^{-2} is plotted against the % ECSA loss in Figure 5-10b. The performance loss obtained at 0.1 A cm^{-2} where ohmic and mass transport resistances are negligible [127]. A different correlation between performance loss and EPSA loss is observed at each RH level. After 20000 AST cycles of operation, an ECSA loss of 34% under fully humidified conditions is observed, which is higher than the 28% loss measured at 50% RH and 26% under dry conditions. The corresponding performance losses at 100 % and 0% RH condition ASTs are 44 and 59 mV, respectively, at a current density of 0.1 A cm^{-2} at the EOL. Figure 5-10b shows that the ECSA loss after a given number of AST cycles rises, whereas the corresponding performance loss decreases, as the RH increases. The fact that the cell voltage loss is highest, while the % ECSA loss is lowest, at 0% RH might indicate that the conductivity loss in the catalyst layer contributes more to performance loss than does catalyst activity loss (Figure 5-9a) [109]. However, at this low current density, conductivity should not be an important factor. This suggests that other factors such as membrane drying which can limit the kinetics of the electrochemical reactions may be significant [155, 159]. Similar trends are observed at 1.7 A cm^{-2} at the three RH levels. At this current density, conductivity losses in the catalyst layer presumably contribute significantly to the performance loss. As expected, this is most striking at 0% RH where ionic conductivity would be most limited. It is interesting to note the different trend observed at 100 % RH in figure 5-10c. Unlike the other two cases, the performance loss begins to level off in the later stages of the AST although the ECSA loss continues to rise. Presumably, factors

leading to improvement in the conductivity are able to offset the loss in active catalyst at this point of the AST.

5.2.3 Linear sweep voltammetry (LSV)

Figure 5-11 a-c shows the electrode responses obtained during LSVs conducted on each MEA to monitor hydrogen cross-over and the occurrence of electrical shorts. Hydrogen gas was passed into the anode side of the cell, while nitrogen was flowed into the cathode. The anode was shunted to the reference electrode so that the potential applied to the working electrode was the same as the cell potential. The analysis was carried out by scanning the cell potential from 0.05 to 0.6 V. The scan was not allowed to proceed to any more positive potential to avoid oxidation of Pt in the cathode catalyst. Hydrogen that crosses over from the anode and across the membrane onto the cathode side is oxidized at the cathode (working electrode) when voltage is increased above ~0.1 V. The oxidation rate quickly becomes limited by the permeation rate of hydrogen permeates across the membrane and the current levels off to a plateau. Thus, the measured current along this plateau gives a good measure of the hydrogen permeation or cross-over rate. For our purposes here, the leakage or fuel cross-over current density was determined from the amount that flows at a voltage above 0.4 V [160]. RH has only a very small effect on hydrogen leakage rate and degradation during the ASTs of 100% and 50 %. However an increase in the hydrogen leakage rate is found during 0% RH ASTs.

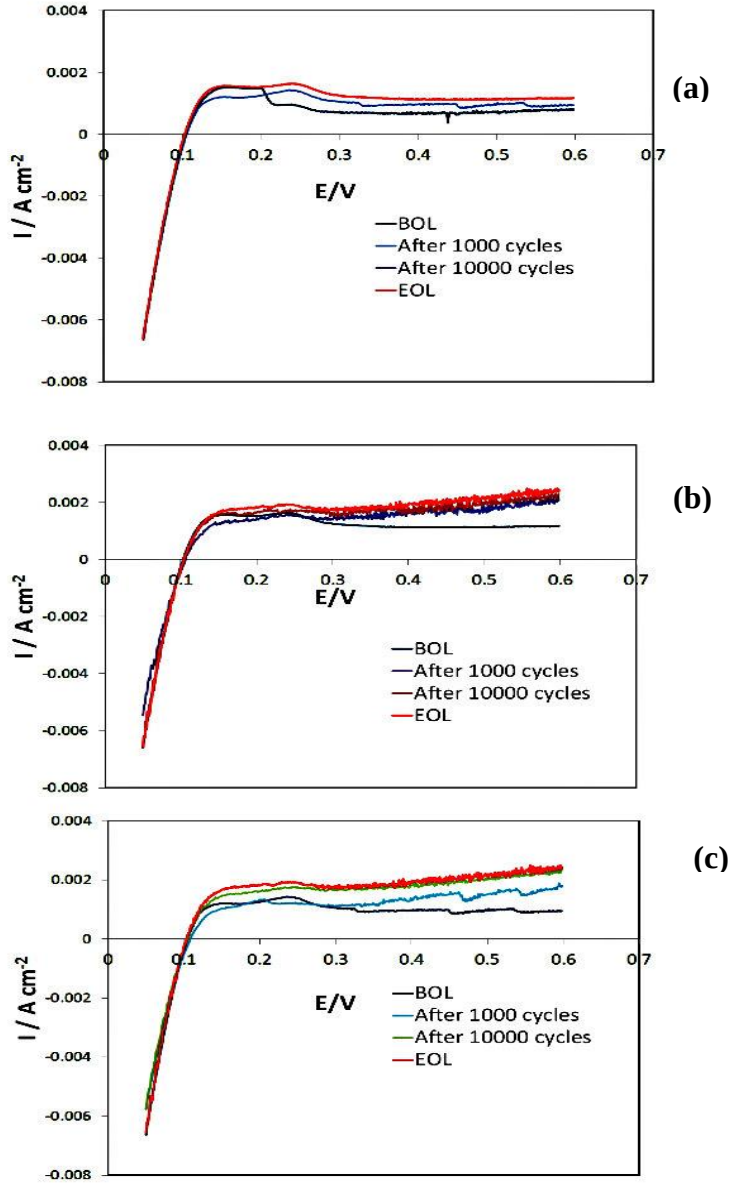

Figure 5-11: LSV of MEAs during (a) 100% RH AST (b) 50 % RH AST (c) 0% RH Conditions of the analysis is given in Table 3-4.

5.2.3 Impedance Analysis

Information on electrode kinetics, transport processes and membrane hydration during ASTs can be obtained using AC impedance analysis. Nyquist plots for the MEAs undergoing the ASTs at 100, 50 and 0 % RH are presented in Figure 5-12 a-c. The EIS experiments were conducted potentiostatically at a base potential of 0.85 V and sinusoidal wave amplitude of 5 mV. The other experimental conditions used during these measurements are given in Table 3-4. Regardless of the RH level, the MEAs in their BOL state generally exhibit lower impedance than after they have been aged, particularly at lower frequencies. As expected, the diameter of the semi-circular arc in the Nyquist plots which gives a measure of the charge transfer resistance increased during the course of the ASTs in all three cases (Figure 5-12). At the same time, the intercept at the high frequency end of the loop, this corresponds to the ohmic resistance shifts in the positive direction as the MEAs are aged. This shift suggests that some structural change to the MEA occurs during the course of the AST and tends to increase the ohmic resistance across the cell. The variation of the charge transfer (R_p) and ohmic (R_s) resistances over the course of the AST obtained by fitting an equivalent circuit model (Figure 3.7) to the EIS spectra are presented in Figure 5-13 a -b. During the AST at 50% RH, R_p increases at an average rate of 2.92 $\mu\Omega$-cm^2/cycle from 0.1071 to 0.1655 Ω-cm^2. At 0 % RH, the rise is larger from 0.1158 to 0.2312 Ω-cm^2 at an average rate of 6 $\mu\Omega$-cm^2/cycle. Such changes in R_p during ASTs have been correlated with morphological changes in the catalytic layer in previous studies [161].

Since the base potential for the EIS measurements was close to the OCV, R_p or low frequency resistance can be approximated as follows:

$$R_p = \frac{RT}{nFi_0} \qquad (5\text{-}12)$$

where R is the gas constant, T is the temperature (K), n is the number of electrons transferred, F is the Faraday constant and i_0 is the apparent exchange current density (A cm^{-2}). This expression relates R_p directly to i_0. Factors that affect the exchange current

density include the ORR, catalyst type, temperature and electrolyte (membrane). Of these, membrane and catalyst are likely the two major factors accounting for the difference in R_p observed during the ASTs.

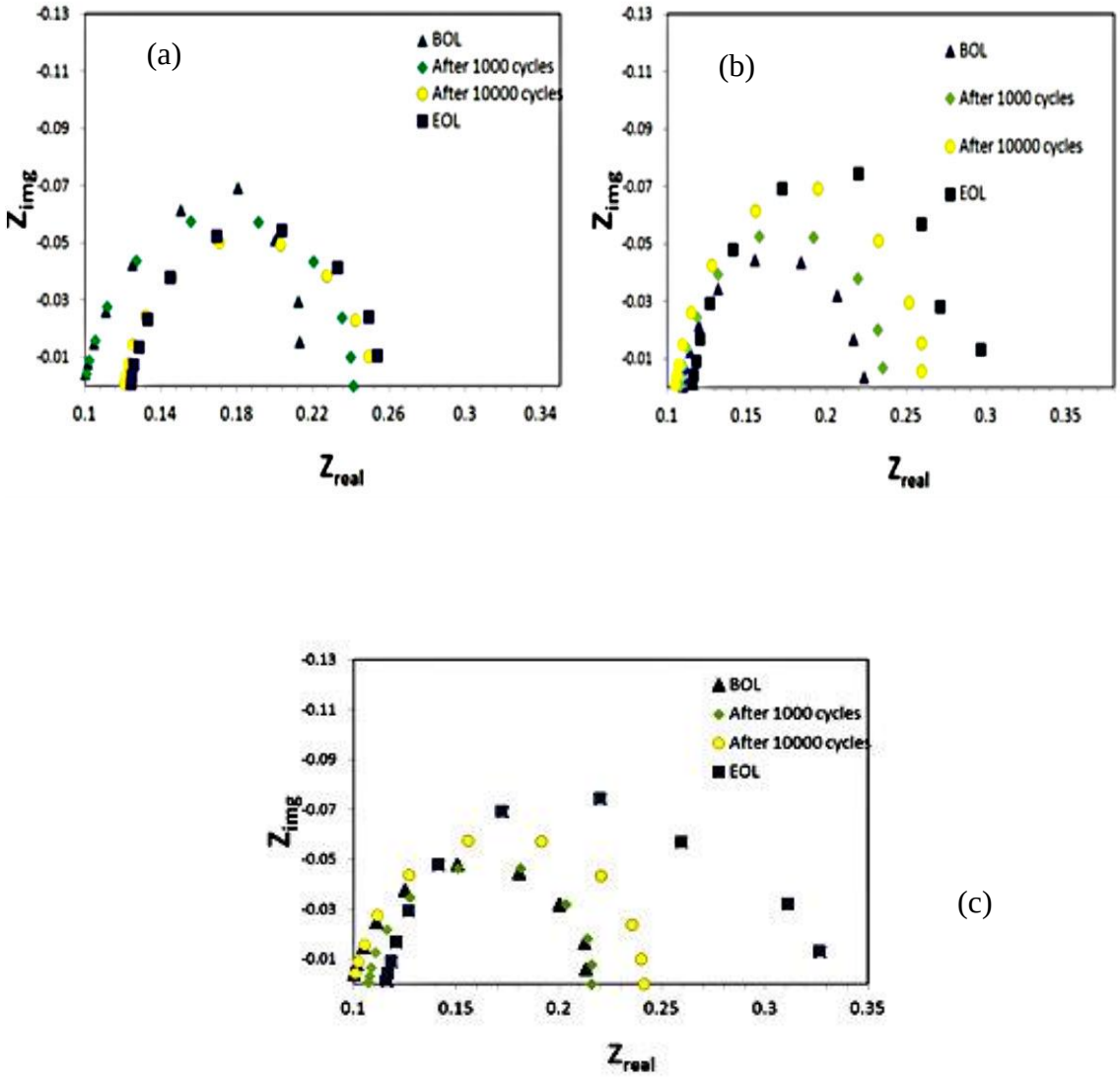

Figure 5-12: Nyquist plot of MEAs during (a) 100% RH AST (b) 50 % RH AST (c) 0 % RH AST Conditions of the analysis is given in Table 3-4.

As shown in Figure 5-13a, R_p increases with the number of AST cycles at 0 and 50% RH, but remains virtually unchanged when the cell is operated at 100% RH. Since a higher R_p signifies a reduction in i_0, these results suggest that some inhibition in ORR kinetics has occurred over the course of the ASTs at 50 and 0% RH, but not at 100% RH. Some of the contributing factors to the reduction in i_0 are catalyst sintering, loss of the carbon support, degradation of the catalyst layer structure and hydrogen cross-over. Also, any reaction between cross-over hydrogen and air at the cathode/membrane interface during the later stages of ASTs could have damaged the cathode morphology due to exothermicity. Such an effect has been reported by Bi et al during potential cycling ASTs [65].

The values of R_s also obtained from fitting the equivalent circuit model (Figure 3.7) to the EIS spectra demonstrate the changes in ohmic resistance over the course of ageing. Since the humidity at both the cathode and anode of the cell are varied during these AST, significant changes to R_s would be expected, as is confirmed in Figure 5-13 b. As expected, operation at higher humidity leads to lower Rs at any point during the AST. Furthermore, R_s rises more steeply during the AST as the humidity decreases, particularly over the first 1000 cycles. The higher R_s and faster rise in R_s during the AST as RH is reduced may be caused by the reduced wettability at the reaction zones within CL [161] and dehydration of the ionomer. A similar observation was reported by Zhang et al during RH cycling experiments [159].

The impedance spectra obtained with N_2 flowing into the cathode rather than air is given in Figure 5-14 in order to further investigate ageing effects on ionic conductivity and the physicochemical state of the MEA. This plot represents Nyquist plot for an MEA in its BOL state and then in its EOL state after being subjected to the AST at 100%, 50 % and 0% RH. Two distinct regions are apparent in all of the EIS spectra – a very small semi-circle at high frequencies and a sharply rising portion at lower frequencies. Structural changes affecting the electrode geometry and conductivity have been associated with the appearance of the small semi-circle at high frequencies [152].

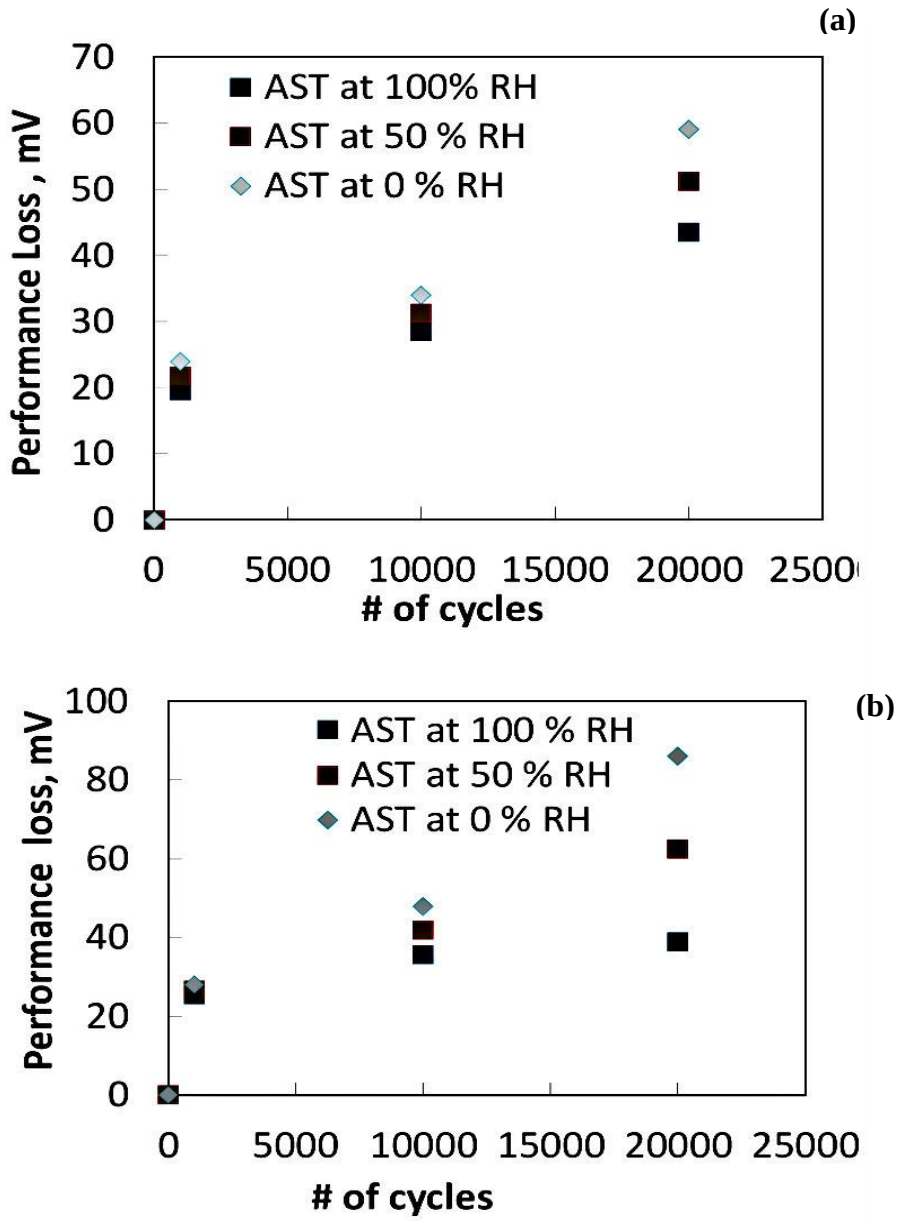

Figure 5-13: Variation in (a) R_p and (b) R_s over the course of the AST conducted at 100, 50 and 0 % RH. Experimental conditions during the analysis are given in Table 3-4

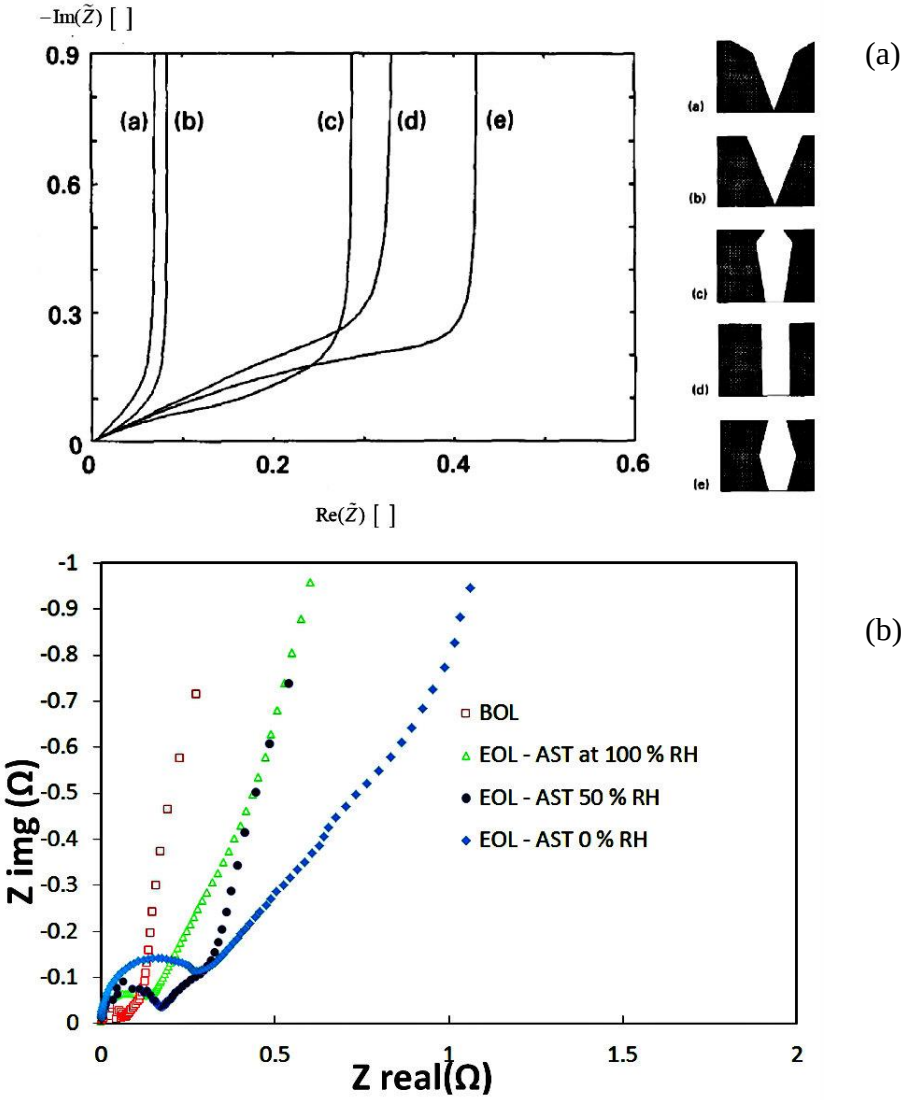

(a)

(b)

Figure 5-14: (a)Theoretical impedance spectra computed for various pore shapes (adapted from ref. [162]).(b) EIS spectra measured obtained at 60 °C, 100%RH, 1bar N_2/H_2, 0.45V bias, H_2-N_2 - flowrates 2-7 slpm, H_2-N_2 RH - 100% - 100%

Examination of Figure 5-14 shows that the semi-circle of the BOL state is very small compared to those of the EOL states after all ASTs. The sloping line at lower frequencies is less steep for MEAs in their EOL state than in their BOL state. This sloping line is be steeper for the MEAs operated at higher relative humidity. With increasing relative humidity, the Nafion conductivity inside the pores of the catalyst layer increases and the system tends to exhibit more capacitive behavior. The sloping line does not reach an ideal vertical line even when the MEA is in its BOL state ane exposed to 100% relative humidity. This phenomenon is called frequency dispersion and is mainly associated with the porous structure/geometric factors in the case of highly porous electrodes. It is evident that the MEAs in their EOL states showed changes at both low and high frequencies and that the MEA maintained at 0% RH could possibly experience larger changes in porous structure than other two MEAs. The sloping lines at low frequency are usually associated with transport control.

It can be shown theoretically that diffusion control leads to a line with a 45° slope. The impedance in this portion of the spectra increases as the MEA ages, suggesting that transport of reactants is becoming more difficult. Keiser et al. reported that the shape of impedance curves is affected by pore geometry (Figure 5-14 b) [123]. This would be expected if the porosity of the CL increases during ageing. Comparing the figures 5-14 a and b of the EOL and BOL state of 0 % RH AST suggest that that the pore shapes in the catalyst layers could be different. However, it is difficult to conclude about pore shape changes only based on EIS results as one may have sample variability.

The equivalent circuit used for analysis of the EIS spectra in figure 5-15a is presented in Figure 5-15a [123]. The circuit consists of an inductor (L), ohmic resistor (R_c), shorting resistor (R_{sh}) and Warburg impedance ($W_{De\text{-}Levie}$). L and R_{sh} are included to account for system artifacts such as inductance in the wire used to connect the fuel cell and impedance analyzer. and electrical shorts across the membrane, respectively. The R_c represents the ionic resistance of the membrane and the electrical resistance of the cell. The Warburg element represents the effect of the porous CL and is determined by the CL ionic resistance

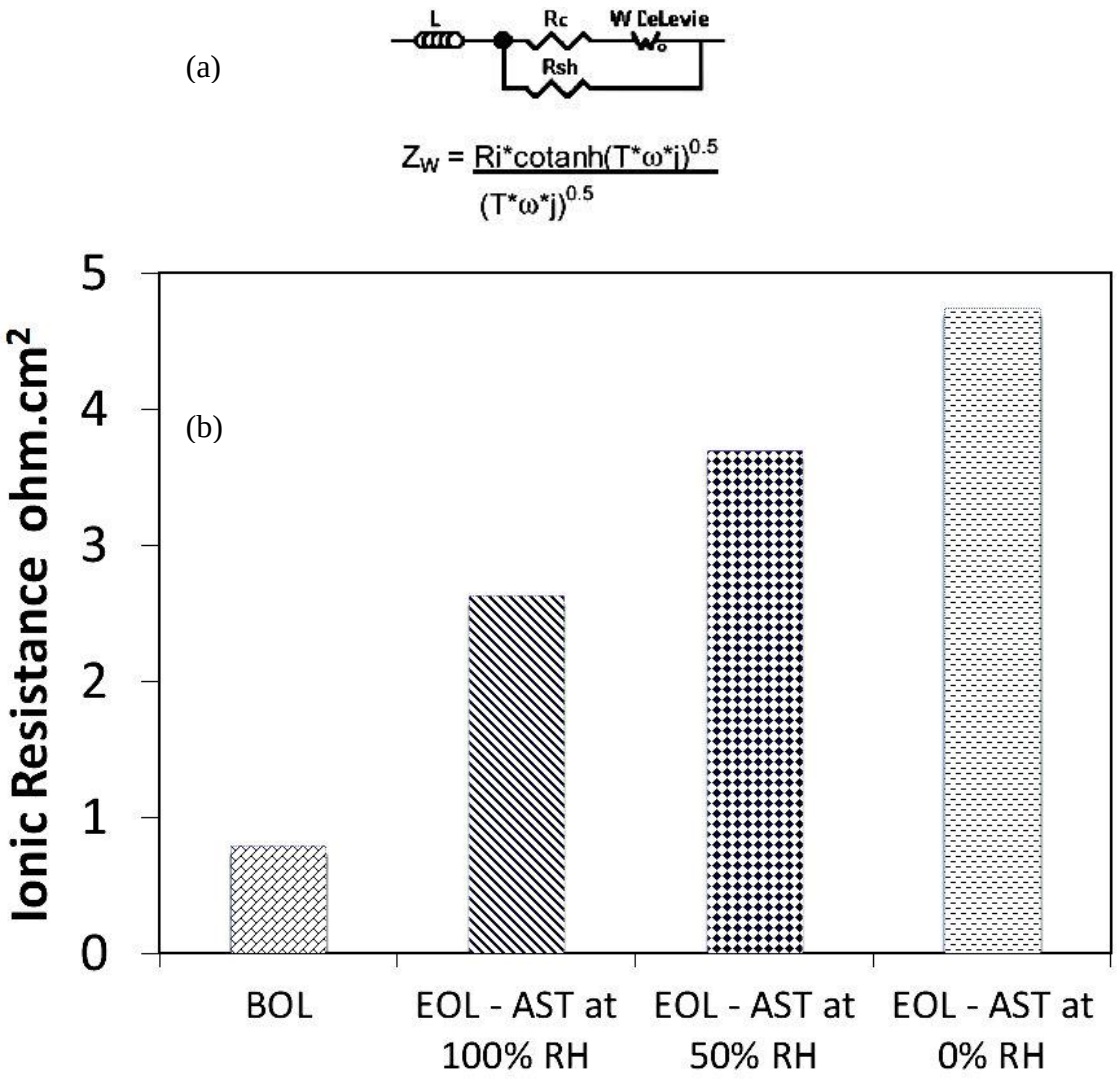

Figure 5-15: (a) Equivalent circuit for a porous catalyst used to fit the EIS spectra and (b) ionomer resistance of MEAs in their BOL and EOL states obtained by fitting equivalent circuits to spectra in Figure 5-14a [163].

(R_i) and double-layer capacitance C_{dl}. The impedance of the Warburg parameter (Z_w) is defined by the cotanh function given in figure 5-15a, where T is the time constant (R_i x C_{dl}) and ω is the frequency. Ionomer resistance is obtained from the Warburg parameter. The values of R_i obtained by fitting the equivalent circuit to the spectra in figure 5-15a for each RH level are presented in figure 5-15 b. The analysis reveals that ageing due to the AST leads to a sunstantial increase in the ionomer resistance by the end of the AST and that this effect is magnified as the RH decreases. Hence, it appears that the interplay between the effects of RH and the voltage cycling during the Pt dissolution AST leads to degradation of ionomer and catalyst in the MEAs.

Examination of the MEAs by SEM reveals that the thickness of the cathode catalyst layer evaluated at 100% RH is reduced by about 30 % from that in its BOL state by the end of the AST. Surface oxidation of the carbon support at the cathode could have occurred especially at 100 % RH. Similar observations have been reported by Borup et al on the impact of carbon corrosion at lower RH and higher potential [52]. SEM images of a BOL and EOL MEAs after being subjected to the AST at 100, 50 and 0 % RH were also obtained to examine whether phenomena such as dissolution and migration of Pt catalyst in the catalyst layer had occurred. These images presented in figure 5-16 a-d confirm that some Pt in the catalyst layer dissolved and formed Pt bands by the end of the ASTs at all three RH levels. Another apparent difference between the BOL sample and the EOL sample subjected to the AST at 100 % RH is the thinning of the CCL.

In summary, accelerated stress testing at 0% RH leads to higher polarization, membrane and ionomer resistances compared to that of its BOL state. Catalyst layer thinning is also observed at the cathode catalyst/membrane interface. The combination of all these effects results in higher performance loss as measured at both 0.1 and 1.7 A cm^{-2} when the MEA is subjected to an Pt dissolution AST at 0 % RH than at 50 and 100% RH.

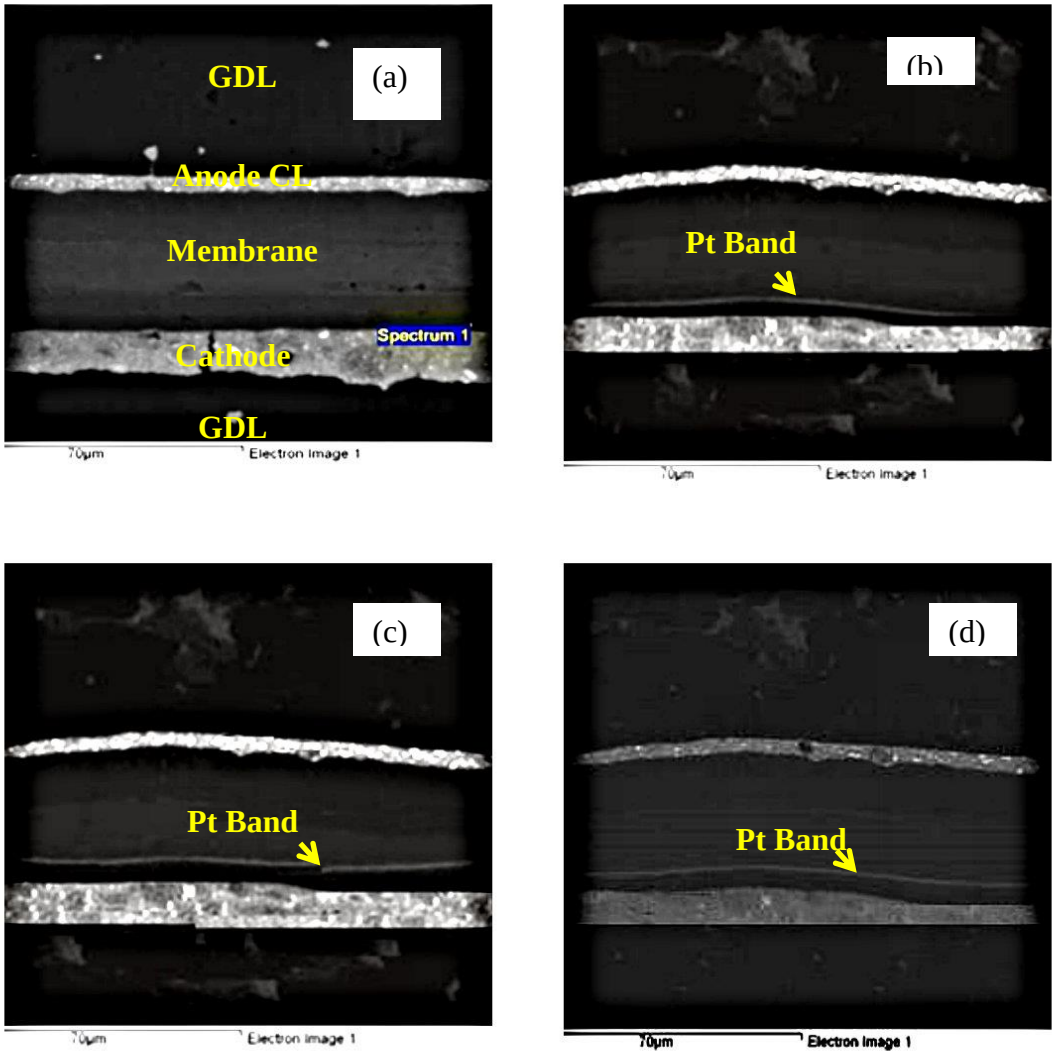

Figure 5-16: SEM images of (a) BOL sample and EOL samples tested at (b) 100 %, (c) 50 % and (d) 0 % RH.

Chapter 6
Conclusions and Recommendations

6.1 Conclusions

The current research has addressed the degradation associated with the cathode catalyst layer in PEMFC MEAs. Analyzes have been conducted to identify the causes, modes and effects of degradation and failure. Causes for the degradation considered in this study are associated with MEA properties, catalyst design and the influence of fuel cell operating conditions such as potential, RH and temperature. Specifically, carbon oxidation and Pt dissolution are identified as important degradation modes of fuel cell catalyst failure. The corrosion of the catalyst support and evolution of CO_2 may affect the electrode structure of the catalyst causing severe cell performance losses. Pt oxidation/dissolution from the catalyst layer involves chemical and electrochemical reactions. Furthermore, this degradation of the catalyst increases at higher temperatures and lower relative humidity during ASTs, causing electrode thinning, increased cross-over especially at lower RH and higher performance losses.

One of the main results of this work has been the development and application of diagnostic indicators or 'fingerprints' for carbon corrosion and Pt dissolution for use during durability testing of MEAs. These fingerprints are based on a combination of empirical and mechanistic models of carbon corrosion and have been validated on ASTs conducted on in-house built MEAs. Additional preliminary experiments involving the cycling of the potential to higher values were designed to study the impact of carbon oxidation and evaluate how carbon loss changes with degradation. Not surprisingly, degradation, as measured by carbon loss rate, was found to worsen as the upper potential during the cycles increased. This work formed the basis for development of the carbon fingerprint characterizing the performance loss during ASTs.

A MEA with 0.4 mg cm^{-2} Pt loading (MEA 1) was tested using different carbon corrosion AST protocols in a CAT cell to determine the performance fingerprints. A deconvolution method was presented and found to successfully estimate the performance loss contributions due to Pt dissolution and carbon oxidation during a mixed-mode degradation test. The information gathered from the ASTs on MEA 1 was used to distinguish the contributions that Pt oxidation/dissolution and carbon corrosion have on the overall performance loss, as measured at various current densities between 0.5 and 1.7 A cm^{-2}. Empirical expressions correlating the performance loss to the carbon loss based on the number of AST cycles have been developed. These should prove useful as tools to predict performance loss in drive cycle models for vehicle fuel cell stacks.The diagnostic fingerprint obtained from different carbon corrosion ASTs was found to provide an excellent fit between carbon loss and performance loss although a separate correlation was required for each MEA tested. As such, this method can be used to de-convolute the performance loss into components due to Pt oxidation/dissolution and carbon corrosion which will aid in the development of new catalyst structures.

Carbon corrosion ASTs for PEMFC was studied with ASTs involving different upper potentials and cycling periods to degrade the catalyst layer. Initial results showed that higher performance loss, as indicated by loss of the EPSA at 1.7 A cm^{-2}, is observed during the 1.0-1.5 V 5s/5s carbon corrosion ASTs. A kinetic model for carbon corrosion modified from a more comprehensive one reported in the literature has been found to predict the carbon loss measured during the carbon corrosion ASTs very well. This model is based on a reaction mechanism for CO_2 evolution during catalyst degradation in which oxidation of a carbon oxide intermediate is the rate-determining step. Furthermore, an empirical equation relating performance loss to carbon loss was combined with this kinetic model and found to be in good agreement with the experimental data for all carbon corrosion ASTs.

An AST protocol was developed to study Pt oxidation/dissolution in a MEA as a function of temperature. ECSA measurement and SEM observation of Pt band formation showed

that that an increase in temperature affected the electrocatalytic activity and the rates of ECSA loss. The performance loss due to Pt dissolution of the MEA is modeled and validated with experimental results. The model is used as a diagnostic tool to study the Pt dissolution failure mechanism. A potential cycling AST has been applied to study Pt dissolution at different RH conditions. The results suggest that Pt dissolution, ionomer dehydration, fuel cross-over are some factors influencing degradation. Intrepretation of LSV, CV and EIS analysis have confirmed the presence of Pt dissolution and membrane degradation.

6.2 Contributions

Comprehensive experimental studies, empirical and numerical models have been conducted to investigate chemical and physical processes associated with carbon oxidation and Pt dissolution in PEMFC catalyst layers. An empirical model has been shown to accurately predict the performance loss and carbon loss during a variety of ASTs.

A mechanistic model for carbon corrosion in the catalyst layer which determines the evolution of the carbon loss over the course of ASTs and validated with experimental data obtained under conditions related to those in automotive drive cycles. Identification of carbon corrosion indicators and development of experimental procedures to determine the performance loss due to carbon loss represents an important step in understanding the durability of the fuel cell for automotive applications. This effort should help reduce carbon corrosion related degradation of the catalyst layer.

The research also focused on a detailed investigation of the role of Pt oxidation/dissolution in catalyst layer degradation. Pt dissolution test protocols developed in this work assessed the durability of the catalyst layer under transient load conditions. The durability cycles employed in this study will help to isolate effects and failure modes associated with the Pt catalyst from those related to the membrane or carbon support. The study on role of the

temperature and humidity during cycling is intended for automotive applications where rapid changes in voltage, temperature, humidity and gas composition are anticipated.

The research work presented here is original and unique as it provides an important basis for studies on catalyst degradation in PEMFC, focuses on understanding Pt dissolution and carbon corrosion failure mechanisms and highlights the use of mathematical models in analyzing durability of catalyst design and fuel cell stack applications.

6.3 Suggestions for Future Work

1. More work on carbon corrosion ASTs is needed to extend the carbon fingerprint approach presented here to different MEA designs and a wider range of RH and temperature operating conditions. Durability protocols involving potential cycling at RH levels above 100 % are expected to accelerate carbon corrosion. Such studies will provide more insight into the carbon corrosion mechanism and hopefully design of improved catalyst supports for PEMFCs.
2. Further experiments on ASTs involving both carbon corrosion and Pt dissolution are needed to extend the mechanistic model and fingerprint expressions to mixed-mode degradation ASTs. This study will help to improve the model and its applicability for the automotive sector.
3. Experiments should be conducted to investigate other possible membrane and GDL degradation mechanisms beyond Pt oxidation/dissolution and carbon corrosion, specifically those operating at high current densities and after % carbon loss becomes high. Fuel cell operation at high current densities leads to the generation of larger amounts of water and to more severe carbon corrosion. It would be interesting to validate and analyze experimental data obtained during ASTs at higher current densities with the carbon corrosion model presented in this thesis. The operation of fuel cells at current densities above 2.6 A cm^{-2} is expected to cause severe support corrosion. However, this condition has not been well explored in the literature. Most

MEAs are not capable of producing current densities above 2.4 A cm^{-2}. However, recently developed Generation 5 MEAs have this capability. The study of MEA durability at these higher current densities is necessary for next generation fuel cell vehicles.

4. Further investigation of the carbon corrosion kinetic model by conducting additional experiments examining the effect of varying partial gas pressure and the irreversible and reversible formation of carbon oxides should be performed. In its present form, our model does not account for variation in gas pressure duringth course of an AST. However, during fuel cell operation under realistic conditions, the partial pressures of the gases tend to vary depending on the driving profile. During normal cell operation, the performance of the cell increases with the increase in the back-pressure of the reactants. Increasing the cathode and anode back-pressure will also increase the partial pressure of the reactants at the catalyst surface and the rates of the ORR and HOR. However, the effect of pressure on oxide formation in the Pt catalyst during ASTs is not well understood. No studies reported in the literature provide information on these questions. A better understanding of the relation between oxide formation and partial pressure will also be very useful in the design of new and improved catalysts.
5. Carbon corrosion ASTs should be conducted to assess the durability of MEAs fabricated with alternative carbon support designs such as multiwalled carbon nanotubes (MWNT) and compare it with that of more conventional MEAs considered in this study. In addition, these studies should include investigations into the degradation mechanisms and the development of fingerprint expressions describing the contribution of carbon corrosion to performance loss of these MEAs.
6. Investigation of the relationship between EPSA loss and performance loss presented in this work should be extended to MEAs that make use of catalysts of Pt alloyed to transition metals such as Co or Ni and non-precious metals.

References

[1] R. Borup, J. Meyers, B. Pivovar, Y.S. Kim, R. Mukundan, N. Garland, D. Myers, M. Wilson, F. Garzon, D. Wood, P. Zelenay, K. More, K. Stroh, T. Zawodzinski, J. Boncella, J.E. McGrath, M. Inaba, K. Miyatake, M. Hori, K. Ota, Z. Ogumi, S. Miyata, A. Nishikata, Z. Siroma, Y. Uchimoto, K. Yasuda, K.-i. Kimijima, N. Iwashita, Scientific Aspects of Polymer Electrolyte Fuel Cell Durability and Degradation, Chemical Reviews, 107 (2007) 3904-3951.

[2] H.A. Gasteiger, S.S. Kocha, B. Sompalli, F.T. Wagner, Activity benchmarks and requirements for Pt, Pt-alloy, and non-Pt oxygen reduction catalysts for PEMFCs, Applied Catalysis B: Environmental, 56 (2005) 9-35.

[3] S. Ball, S. Hudson, D. Thompsett, B. Theobald, An investigation into factors affecting the stability of carbons and carbon-supported platinum and platinum/cobalt alloy catalysts during 1.2 V potentiostatic hold regimes at a range of temperatures, Journal of Power Sources, 171 (2007) 18-25.

[4] S.R. Dhanushkodi, N. Mahinpey, A. Srinivasan, M. Wilson, Life cycle analysis of fuel cell technology, Journal of Environmental Informatics, 11 (2008) 36-44.

[5] L. Hughes, N. Chaudhry, The challenge of meeting Canada's greenhouse gas reduction targets, Energy Policy, 39 (2011) 1352-1362.

[6] F.D.R. Maillard, M. Eikerling, O. Cherstiouk, S. Schreier, E. Savinova, U. Stimming, Size effects on reactivity of Pt nanoparticles in CO monolayer oxidation: The role of surface mobility, Faraday Discuss., 125 (2003) 357-377.

[7] Q. Li, R. He, J.-A. Gao, J.O. Jensen, N.J. Bjerrum, The CO poisoning effect in PEMFCs operational at temperatures up to 200 C, Journal of The Electrochemical Society, 150 (2003) A1599-A1605.

[8] G. Hoogers, Fuel cell technology handbook CRC publication, NY, 2003.

[9] M. Eikerling, A. Kornyshev, Modelling the performance of the cathode catalyst layer of polymer electrolyte fuel cells, Journal of Electroanalytical Chemistry, 453 (1998) 89-106.
[10] L. Schlapbach, A. Züttel, Hydrogen-storage materials for mobile applications, Nature, 414, (2001), 353-358.

[11] N.H. Association, Energy evolution: an analysis of alternative vehicles and fuels to 2100, in, 2009.

[12] F. Syed, M. Fowler, D. Wan, Y. Maniyali, An energy demand model for a fleet of plug-in fuel cell vehicles and commercial building interfaced with a clean energy hub, International Journal of Hydrogen Energy, 35 5154-5163.

[13] M.F. Mathias, R. Makharia, H.A. Gasteiger, J.J. Conley, T.J. Fuller, C.J. Gittleman, S.S. Kocha, D.P. Miller, C.K. Mittelsteadt, T. Xie, Two fuel cell cars in every garage?, Interface-Electrochemical Society, 14 (2005) 24-36.

[14] S.A. Sherif, F. Barbir, T.N. Veziroglu, Wind energy and the hydrogen economy—review of the technology., Solar Energy, 78, (2005), 647–660.

[15] F.A.d. Bruijn, V.A.T. Dam, G.J.M. Janssen, Review: Durability and Degradation Issues of PEM Fuel Cell Components, Fuel Cells, 8, (2008), 3-22.

[16] D. Stevens, J. Dahn, Thermal degradation of the support in carbon-supported platinum electro-catalysts for PEM fuel cells, Carbon, 43, (2005), 179-188.

[17] W. Dai, H. Wang, X.-Z. Yuan, J.J. Martin, D. Yang, J. Qiao, J. Ma, A review on water balance in the membrane electrode assembly of proton exchange membrane fuel cells, International Journal of Hydrogen Energy, 34 (2009), 9461-9478.

[18] F.D.R. Maillard, S. Schreier, M. Hanzlik, E.R. Savinova, S. Weinkauf, U. Stimming, Influence of particle agglomeration on the catalytic activity of carbon-supported Pt nanoparticles in CO monolayer oxidation, Physical Chemistry Chemical Physics, 7, (2005), 385-393.

[19] S. Kundu, M. Cimenti, S. Lee, D. Bessarabov, Fingerprint of automotive fuel cell cathode catalyst degradation: Pt band in PEMs, Membrane Technology, 2009, 7-10.

[20] P.J. Ferreira, G.J. la O, Y. Shao-Horn, D. Morgan, R. Makharia, S. Kocha, H.A. Gasteiger, Instability of Pt/C Electro-catalysts in Proton Exchange Membrane Fuel Cells, Journal of The Electrochemical Society, 152, 2005, A2256-A2271.

[21] J. Xie, D.L. Wood, Iii, K.L. More, P. Atanassov, R.L. Borup, Microstructural Changes of Membrane Electrode Assemblies during PEFC Durability Testing at High Humidity Conditions, Journal of The Electrochemical Society, 152, (2005) A1011-A1020.

[22] E. Guilminot, A. Corcella, F. Charlot, F. Maillard, M. Chatenet, Detection of Pt[sup z+] Ions and Pt Nanoparticles Inside the Membrane of a Used PEMFC, Journal of The Electrochemical Society, 154, (2007), B96-B105.

[23] Y. Shao-Horn, W. Sheng, S. Chen, P. Ferreira, E. Holby, D. Morgan, Instability of Supported Platinum Nanoparticles in Low Temperature Fuel Cells, Topics in Catalysis, 46, (2007), 285-305.

[24] K. Kinoshita, Carbon: Electrochemical and Physicochemical Properties, Willey, NY, 1988.

[25] K.H. Kangasniemi, D.A. Condit, T.D. Jarvi, Characterization of Vulcan Electrochemically Oxidized under Simulated PEM Fuel Cell Conditions, Journal of the Electrochemical Society, 151, (2004), E125-E132.

[26] L.M. Roen, C.H. Paik, T.D. Jarvi, Electrocatalytic Corrosion of Carbon Support in PEMFC Cathodes, Electrochemical and Solid-State Letters, 7, (2004), A19-A22.

[27] Z. Siroma, K. Ishii, K. Yasuda, Y. Miyazaki, M. Inaba, A. Tasaka, Imaging of highly oriented pyrolytic graphite corrosion accelerated by Pt particles, Electrochemistry Communications, 7, (2005), 1153-1156.

[28] D.A. Stevens, J.R. Dahn, Thermal degradation of the support in carbon-supported platinum electro-catalysts for PEM fuel cells, Carbon, 43, (2005), 179-188.

[29] P.W. Voorhees, The theory of Ostwald ripening, Journal of Statistical Physics, 38, (1985), 231-252.

[30] A. Honji, T. Mori, K. Tamura, Y. Hishinuma, Agglomeration of Platinum Particles Supported on Carbon in Phosphoric Acid, Journal of The Electrochemical Society, 135, (1988), 355-359.

[31] E. Antolini, R.R. Passos, E.A. Ticianelli, Effects of the carbon powder characteristics in the cathode GDL on the performance of polymer electrolyte fuel cells, Journal of Power Sources, 109, (2002), 477-482.

[32] A.C.C. Tseung, S.C. Dhara, Loss of surface area by platinum and supported platinum black electrocatalyst, Electrochimica Acta, 20, (1975), 681-683.

[33] K. Sasaki, M. Shao, R. Adzic, Dissolution and Stabilization of Platinum in Oxygen Cathodes, in: Polymer Electrolyte Fuel Cell Durability, 2009, pp. 7-27.

[34] D. Stevens, J. Dahn, Electrochemical characterization of the active surface in carbon-supported platinum electro-catalysts for PEM fuel cells, Journal of the Electrochemical Society, 150, (2003), A770-A775.

[35] Y. Shao, G. Yin, Y. Gao, Understanding and approaches for the durability issues of Pt-based catalysts for PEM fuel cell, Journal of Power Sources, 171 (2007) 558-566.

[36] Z. Liu, X.Y. Ling, X. Su, J.Y. Lee, Carbon-supported Pt and PtRu nanoparticles as catalysts for a direct methanol fuel cell, The Journal of Physical Chemistry B, 108, (2004) 8234-8240.

[37] H. Yu, C. Ziegler, M. Oszcipok, M. Zobel, C. Hebling, Hydrophilicity and hydrophobicity study of catalyst layers in proton exchange membrane fuel cells, Electrochimica Acta, 51, (2006), 1199-1207.

[38] W. Dai, H. Wang, X.Z. Yuan, J.J. Martin, D. Yang, J. Qiao, J. Ma, A review on water balance in the membrane electrode assembly of proton exchange membrane fuel cells, International Journal of Hydrogen Energy, 34, (2009), 9461-9478.

[39] T. Ralph, M. Hogarth, Catalysis for low temperature fuel cells, Platinum Metals Review, 46, (2002), 117-135.

[40] T. Ralph, G. Hards, J. Keating, S. Campbell, D. Wilkinson, M. Davis, J. St-Pierre, M. Johnson, Low Cost Electrodes for Proton Exchange Membrane Fuel Cells Performance in Single Cells and Ballard Stacks, Journal of the Electrochemical Society, 144, (1997), 3845-3857.

[41] N. Linse, G.G. Scherer, A. Wokaun, L. Gubler, Quantitative analysis of carbon corrosion during fuel cell start-up and shut-down by anode purging, Journal of Power Sources, (2012).

[42] W. Bi, T.F. Fuller, Temperature Effects on PEM Fuel Cells Pt/C Catalyst Degradation, Journal of The Electrochemical Society, 155 (2008) B215-B221.

[43] A. Young, V. Colbow, D. Harvey, E. Rogers, S. Wessel, A Semi-Empirical Two Step Carbon Corrosion Reaction Model in PEM Fuel Cells, Journal of The Electrochemical Society, 160 F381-F388.

[44] K. Gallagher, R. Darling, T. Fuller, Carbon support corrosion mechanisms and models, Handbook of Fuel Cells, (2010).

[45] V.A. Sethuraman, S. Khan, J.S. Jur, A.T. Haug, J.W. Weidner, Measuring oxygen, carbon monoxide and hydrogen sulfide diffusion coefficient and solubility in Nafion membranes, Electrochimica Acta, 54 (2009) 6850-6860.

[46] F. De Bruijn, V. Dam, G. Janssen, Review: Durability and degradation issues of PEM fuel cell components, Fuel Cells, 8 (2008) 3-22.

[47] S. Ball, S. Hudson, B. Theobald, D. Thompsett, The effect of dynamic and steady-state voltage excursions on the stability of carbon-supported Pt and Pt-Co catalysts, in, 2006, pp. 595-605.

[48] M.S. Wilson, F.H. Garzon, K.E. Sickafus, S. Gottesfeld, Surface Area Loss of Supported Platinum in Polymer Electrolyte Fuel Cells, Journal of The Electrochemical Society, 140 (1993) 2872-2877.

[49] J. Aragane, T. Murahashi, T. Odaka, Change of Pt distribution in the active components of phosphoric acid fuel cell, Journal of the Electrochemical Society, 135 (1988) 844-850.

[50] K.F. Blurton, H.R. Kunz, D.R. Rutt, Surface area loss of platinum supported on graphite, Electrochimica Acta, 23 (1978) 183-190.

[51] P. Ascarelli, V. Contini, R. Giorgi, Formation process of nanocrystalline materials from x-ray diffraction profile analysis: Application to platinum catalysts, Journal of Applied Physics, 91 (2002) 4556-4561.

[52] R.L. Borup, J.R. Davey, F.H. Garzon, D.L. Wood, M.A. Inbody, PEM fuel cell electrocatalyst durability measurements, Journal of Power Sources, 163 (2006) 76-81.

[53] T. Patterson, Fuel Cell Technology Oportunities and Challenges in: AIChE Spring National Meeting, New Orleans, LO, 2002, pp. pp. 313–318.

[54] T.W. Patterson, R.M. Darling, Damage to the cathode catalyst of a PEM fuel cell caused by localized fuel starvation, Electrochemical and Solid-State Letters, 9 (2006) A183-A185.

[55] E. Guilminot, A. Corcella, M. Chatenet, F. Maillard, F. Charlot, G. Berthome, C. Iojoiu, J.Y. Sanchez, E. Rossinot, E. Claude, Membrane and Active Layer Degradation upon PEMFC Steady-State Operation, Journal of The Electrochemical Society, 154 (2007) B1106-B1114.

[56] E. Antolini, J.R.C. Salgado, E.R. Gonzalez, The stability of Pt-M (M = first row transition metal) alloy catalysts and its effect on the activity in low temperature fuel cells: A literature review and tests on a Pt-Co catalyst, Journal of Power Sources, 160 (2006) 957-968.

[57] P.J. Ferreira, Y. Shao-Horn, Formation Mechanism of Pt Single-Crystal Nanoparticles in Proton Exchange Membrane Fuel Cells, Electrochemical and Solid-State Letters, 10 (2007) B60-B63.

[58] A.T. Yasuda, Tomoki Akita, Tsutomu Ioroi and Zyun Siroma Platinum dissolution and deposition in the polymer electrolyte membrane of a PEM fuel cell as studied by potential cycling Phys. Chem. Chem. Phys, 8 (2006) 746-752.

[59] K. Yasuda, A. Taniguchi, T. Akita, T. Ioroi, Z. Siroma, Characteristics of a Platinum Black Catalyst Layer with Regard to Platinum Dissolution Phenomena in a Membrane Electrode Assembly, Journal of The Electrochemical Society, 153 (2006) A1599-A1603.

[60] W. Bi, G.E. Gray, T.F. Fuller, PEM Fuel Cell Pt/C Dissolution and Deposition in Nafion Electrolyte, Electrochemical and Solid-State Letters, 10 (2007) B101-B104.

[61] J. Zhang, B.A. Litteer, W. Gu, H. Liu, H.A. Gasteiger, Effect of Hydrogen and Oxygen Partial Pressure on Pt Precipitation within the Membrane of PEMFCs, Journal of The Electrochemical Society, 154 (2007) B1006-B1011.

[62] D. Bessarabov, P. Kozak, Measurement of gas permeability in SPE membranes for use in fuel cells, Membrane Technology, 2007 (2007) 6-9.

[63] Fowler.M.W., Degradation and Reliability Modelling of PEM Fuel Cells, in: Royal Military College of Canada, Queens University, Kingston, 2003.

[64] R. Borup, J. Meyers, B. Pivovar, Y.S. Kim, R. Mukundan, N. Garland, D. Myers, M. Wilson, F. Garzon, D. Wood, Scientific aspects of polymer electrolyte fuel cell durability and degradation, Chemical Reviews-Columbus, 107 (2007) 3904-3951.

[65] W. Bi, G.E. Gray, T.F. Fuller, PEM Fuel Cell Pt/ C Dissolution and Deposition in Nafion Electrolyte, Electrochemical and solid-state letters, 10 (2007) B101-B104.

[66] J. Wu, X.Z. Yuan, J.J. Martin, H. Wang, J. Zhang, J. Shen, S. Wu, W. Merida, A review of PEM fuel cell durability: Degradation mechanisms and mitigation strategies, Journal of Power Sources, 184 (2008) 104-119.

[67] J. Kim, S.M. Lee, S. Srinivasan, C.E. Chamberlin, Modeling of proton exchange membrane fuel cell performance with an empirical equation, Journal of the Electrochemical Society, 142 (1995) 2670-2674.

[68] S.M. Andersen, M. Borghei, P. Lund, Y.-R. Elina, A. Pasanen, E. Kauppinen, V. Ruiz, P. Kauranen, E.M. Skou, Durability of carbon nanofiber (CNF) & carbon nanotube (CNT) as catalyst support for Proton Exchange Membrane Fuel Cells, Solid-State Ionics, 231 (2013) 94-101.

[69] W.R. Baumgartner, E. Wallnöfer, T. Schaffer, V. Hacker, V. Peinecke, P. Prenninger, Electrocatalytic Corrosion of Carbon Support in PEMFC at Fuel Starvation, ECS Transactions, 3 (2006) 811-825.

[70] M.K. Debe, A.K. Schmoeckel, G.D. Vernstrom, R. Atanasoski, High voltage stability of nanostructured thin film catalysts for PEM fuel cells, Journal of Power Sources, 161 (2006) 1002-1011.

[71] S. Zhang, X.Z. Yuan, J.N.C. Hin, H. Wang, K.A. Friedrich, M. Schulze, A review of platinum-based catalyst layer degradation in proton exchange membrane fuel cells, Journal of power sources, 194 (2009) 588-600.

[72] W. Schmittinger, A. Vahidi, A review of the main parameters influencing long-term performance and durability of PEM fuel cells, Journal of Power Sources, 180 (2008) 1-14.

[73] W.R. Baumgartner, E. Wallnöfer, T. Schaffer, J.O. Besenhard, V. Hacker, V. Peinecke, P. Prenninger, Electrocatalytic corrosion of carbon support in PEMFC at fuel starvation, in, 2006, pp. 811-825.

[74] N. Linse, L. Gubler, G.G. Scherer, A. Wokaun, The effect of platinum on carbon corrosion behavior in polymer electrolyte fuel cells, Electrochimica Acta, 56 (2011) 7541-7549.

[75] S. Maass, F. Finsterwalder, G. Frank, R. Hartmann, C. Merten, Carbon support oxidation in PEM fuel cell cathodes, Journal of Power Sources, 176 (2008) 444-451.

[76] Y. Shao, J. Wang, R. Kou, M. Engelhard, J. Liu, Y. Wang, Y. Lin, The corrosion of PEM fuel cell catalyst supports and its implications for developing durable catalysts, Electrochimica Acta, 54 (2009) 3109-3114.

[77] H. Schulenburg, B. Schwanitz, N. Linse, G.n.G. Scherer, A. Wokaun, J. Krbanjevic, R. Grothausmann, I. Manke, 3D Imageing of Catalyst Support Corrosion in Polymer Electrolyte Fuel Cells, The Journal of Physical Chemistry C, 115 (2011) 14236-14243.

[78] H. Zhong, H. Zhang, G. Liu, Y. Liang, J. Hu, B. Yi, A novel non-noble electrocatalyst for PEM fuel cell based on molybdenum nitride, Electrochemistry Communications, 8 (2006) 707-712.

[79] M.F. Mathias, R. Makharia, H.A. Gasteiger, J.J. Conley, T.J. Fuller, C.J. Gittleman, S.S. Kocha, D.P. Miller, C.K. Mittelsteadt, T. Xie, S.G. Van, P.T. Yu, Two fuel cell cars in every garage?, Electrochemical Society Interface, 14 (2005) 24-35.

[80] S.D. Knights, K.M. Colbow, J. St-Pierre, D.P. Wilkinson, Aging mechanisms and lifetime of PEFC and DMFC, Journal of Power Sources, 127 (2004) 127-134.

[81] C.A. Reiser, L. Bregoli, T.W. Patterson, J.S. Yi, J.D. Yang, M.L. Perry, T.D. Jarvi, A reverse-current decay mechanism for fuel cells, Electrochemical and Solid-State Letters, 8 (2005) A273-A276.

[82] S. Mitsushima, S. Kawahara, K.-i. Ota, N. Kamiya, Consumption Rate of Pt under-Potential Cycling, Journal of the Electrochemical Society, 154, (2007), B153-B158.

[83] S.C. Ball, S.L. Hudson, J.H. Leung, A.E. Russell, D. Thompsett, B.R.C. Theobald, Mechanisms of activity loss in Pt-Co alloy systems, in, 2007, pp. 1247-1257.

[84] Z. Luo, D. Li, H. Tang, M. Pan, R. Ruan, Degradation behavior of membrane electrode assembly materials in 10-cell PEMFC stack, International Journal of Hydrogen Energy, 31 (2006) 1831-1837.

[85] S. Zhang, X.-Z. Yuan, J.N.C. Hin, H. Wang, K.A. Friedrich, M. Schulze, A review of platinum-based catalyst layer degradation in proton exchange membrane fuel cells, Journal of Power Sources, 194 (2009) 588-600.

[86] X. Wang, R. Kumar, D.J. Myers, Effect of voltage on platinum dissolution relevance to polymer electrolyte fuel cells, Electrochemical and Solid-State Letters, 9 (2006) A225-A227.

[87] M. Cai, M.S. Ruthkosky, B. Merzougui, S. Swathirajan, M.P. Balogh, S.H. Oh, Investigation of thermal and electrochemical degradation of fuel cell catalysts, Journal of Power Sources, 160 (2006) 977-986.

[88] T. Yoda, H. Uchida, M. Watanabe, Effects of operating potential and temperature on degradation of electrocatalyst layer for PEFCs, Electrochimica Acta, 52 (2007) 5997-6005.

[89] H. Xu, R. Kunz, J.M. Fenton, Investigation of platinum oxidation in PEM fuel cells at various relative humidities, Electrochemical and Solid-State Letters, 10 (2007) B1-B5.

[90] K.H. Kangasniemi, D. Condit, T. Jarvi, Characterization of vulcan electrochemically oxidized under simulated PEM fuel cell conditions, Journal of The Electrochemical Society, 151 (2004) E125-E132.

[91] L. Roen, C. Paik, T. Jarvi, Electrocatalytic corrosion of carbon support in PEMFC cathodes, Electrochemical and solid-state letters, 7, (2004), A19-A22.

[92] J.P. Meyers, R.M. Darling, Model of carbon corrosion in PEM fuel cells, Journal of The Electrochemical Society, 153 (2006) A1432-A1442.

[93] J.P. Meyers, Modeling of Catalyst Structure Degradation in PEM Fuel Cells, Modeling and Numerical Simulations, (2009) 249-271.

[94] A.A. Franco, M. Gerard, Multiscale model of carbon corrosion in a PEFC: coupling with electrocatalysis and impact on performance degradation, Journal of The Electrochemical Society, 155 (2008) B367-B384.

[95] K.G. Gallagher, T.F. Fuller, Kinetic model of the electrochemical oxidation of graphitic carbon in acidic environments, Phys. Chem. Chem. Phys., 11 (2009) 11557-11567.

[96] R. Makharia, S. Kocha, P. Yu, M.A. Sweikart, W. Gu, F. Wagner, H.A. Gasteiger, Durable PEM fuel cell electrode materials: requirements and benchmarking methodologies, ECS Transactions, 1 (2006) 3-18.

[97] C.He, S.Desai, G.Brown, S.Bollepalli, PEM Fuel Cell Catalysts: Cost, Performance, and durability,The Electrochemical Society interface, 14 (2005) 41 - 44.

[98] F.A. de Bruijn, V.A.T. Dam, G.J.M. Janssen, Review: Durability and Degradation Issues of PEM Fuel Cell Components, Fuel Cells, 8 (2008) 3-22.

[99] K. Yasuda, A. Taniguchi, T. Akita, T. Ioroi, Z. Siroma, Platinum dissolution and deposition in the polymer electrolyte membrane of a PEM fuel cell as studied by potential cycling, Physical Chemistry Chemical Physics, 8 (2006) 746-752.

[100] M. Uchimura, S.S. Kocha, The Impact of Cycle Profile on PEMFC Durability, ECS Transactions, 11 (2007) 1215-1226.

[101] M. Uchimura, S. Sugawara, Y. Suzuki, J. Zhang, S.S. Kocha, Electrocatalyst Durability under Simulated Automotive Drive Cycles, ECS Transactions, 16 (2008) 225-234.

[102] S.C. Zignani, E. Antolini, E.R. Gonzalez, Evaluation of the stability and durability of Pt and Pt–Co/C catalysts for polymer electrolyte membrane fuel cells, Journal of Power Sources, 182 (2008) 83-90.

[103] W. Bi, T.F. Fuller, Temperature Effects on PEM Fuel Cells Pt/C Catalyst Degradation, Journal of the Electrochemical Society, 155 (2008) B215-B221.

[104] J. Stumper, R. Rahmani, F. Fuss, In-situ Diagnostics for Cell Performance and Degradation, ECS Transactions, 25, (2009), 1605-1615.

[105] J. Zhang, Y. Tang, C. Song, X. Cheng, J. Zhang, H. Wang, PEM fuel cells operated at 0% relative humidity in the temperature range of 23 & 1200;Â°C, Electrochimica acta, 52 (2007) 5095-5101.

[106] K. Neyerlin, H.A. Gasteiger, C.K. Mittelsteadt, J. Jorne, W. Gu, Effect of relative humidity on oxygen reduction kinetics in a PEMFC, Journal of The Electrochemical Society, 152 (2005) A1073-A1080.

[107] T. Gierke, Ionic clustering in Nafion perfluorosulfonic acid membranes and its relationship to hydroxyl rejection and chlor-alkali current efficiency, J. Electrochem. Soc, 124, (1977), 319.

[108] W.Y. Hsu and T.D. Gierke, Elastic theory for ionic clustering in perfluorinated ionomers, Macromolecules, 15, (1982), 101-105.

[109] W. Bi, Q. Sun, Y. Deng, T.F. Fuller, The effect of humidity and oxygen partial pressure on degradation of Pt/C catalyst in PEM fuel cell, Electrochimica Acta, 54 (2009) 1826-1833.

[110] E. Endoh, S. Terazono, H. Widjaja, Y. Takimoto, Degradation study of MEA for PEMFCs under low humidity conditions, Electrochemical and Solid-State Letters, 7 (2004) A209-A211.

[111] V. Ramani, H. Kunz, J. Fenton, Investigation of Nafion/HPA composite membranes for high temperature/low relative humidity PEMFC operation, Journal of membrane science, 232 (2004) 31-44.

[112]Z. Nagy, H. You, Applications of surface X-ray scattering to electrochemistry problems, Electrochimica Acta, 47, (2002) 3037-3055.

[113] J.L.a.A. Dicks, Fuel cell systems explained, New York 2003.

[114] T.G. Benjamin, E.H. Camara, L.G. Marianowski, Handbook of fuel cell performance, in, Institute of Gas Technology, Chicago, IL (USA), 1980.

[115] J. Durst, A. Lamibrac, L. Dubau, F. Maillard, M. Chatenet, J. Dillet, G. Maranzana, O. Lottin, Relation between Local Loss of Performances in a Segmented PEMFC and Local Degradations of the Pt/C Cathode Catalyst, in: Meeting Abstracts, The Electrochemical Society, 2012, pp. 1345-1345.

[116] L. You, H. Liu, A two-phase flow and transport model for the cathode of PEM fuel cells, International Journal of Heat and Mass Transfer, 45 (2002) 2277-2287.

[117] J. Wu, X.Z. Yuan, H. Wang, M. Blanco, J.J. Martin, J. Zhang, Diagnostic tools in PEM fuel cell research: Part I Electrochemical techniques, International Journal of Hydrogen Energy, 33 (2008) 1735-1746.

[118] F. Barbir, PEM Fuel Cells, in: Fuel Cell Technology, 2006, pp. 27-51.

[119] R. O'Hayre, S.-J. Lee, S.-W. Cha, F.B. Prinz, A sharp peak in the performance of sputtered platinum fuel cells at ultra-low platinum loading, Journal of Power Sources, 109 (2002) 483-493.

[120] S. Lee, D. Bessarabov, R. Vohra, Degradation of a Cathode Catalyst Layer in PEM MEAs Subjected to Automotive-Specific Test Conditions, International Journal of Green Energy, 6 (2009) 594 - 606.

[121] S.W.C. R. O'Hayre, W. Colella and F.B. Brinz,, Fuel cell fundamentals, New York 2006.

[122] X. Yuan, H. Wang, J. Colin Sun, J. Zhang, AC impedance technique in PEM fuel cell diagnosis—A review, International Journal of Hydrogen Energy, 32 (2007) 4365-4380.

[124] H. Keiser, K. Beccu, M. Gutjahr, Evaluation of the Pore Structure of Porous Electrodes From Impedance Measurements, Electrochimica Acta, 21 (1976) 539-543.

[125] K. Eloot, F. Debuyck, M. Moors, A. P. Van Peteghem – Calculation of the impedance of noncylindrical pores Part II: Experimental verification on pores drilled into stainless steel. Journal of Applied Electrochemistry, 25 (1995) 334

[126] E. Hillstrom, Design and Validation of a Subscale PEMFC Test Hardware, Proceedings Hydrogen + Fuel cells International Conference 2011, (2011).

[127] H. Gasteiger, W. Gu, R. Makharia, M. Mathias, B. Sompalli, BOL MEA performance—efficiency loss contributions, Wiley Online Library, 2003.

[128] S.B. Brummer, J.I. Ford, M.J. Turner, The Adsorption and Oxidation of Hydrocarbons on Noble Metal Electrodes. I. Propane Adsorption on Smooth Platinum Electrodes, The Journal of Physical Chemistry, 69 (1965) 3424-3433.

[129] K.-S. Lee, B.-S. Lee, S.J. Yoo, S.-K. Kim, S.J. Hwang, H.-J. Kim, E. Cho, D. Henkensmeier, J.W. Yun, S.W. Nam, T.-H. Lim, J.H. Jang, Development of a

galvanostatic analysis technique as an in-situ diagnostic tool for PEMFC single cells and stacks, International Journal of Hydrogen Energy, 37 (2012) 5891-5900.

[130] X. Yuan, J.C. Sun, M. Blanco, H. Wang, J. Zhang, D.P. Wilkinson, AC impedance diagnosis of a 500 W PEM fuel cell stack: Part I: Stack impedance, Journal of Power Sources, 161 (2006) 920-928.

[131] M. Uchimura, S. Kocha, The impact of cycle profile on PEMFC durability, 2007, pp. 1215-1226.

[132] X. Cheng, Z. Shi, N. Glass, L. Zhang, J. Zhang, D. Song, Z.S. Liu, H. Wang, J. Shen, A review of PEM hydrogen fuel cell contamination: Impacts, mechanisms, and mitigation, Journal of Power Sources, 165 (2007) 739-756.

[133] A. Taylor, H. Sinclair, Proc. Phys. Soc., 57 (1945) 108.

[134] C. Chen, G. Levitin, D.W. Hess, T.F. Fuller, XPS investigation of Nafion® membrane degradation, Journal of Power Sources, 169 (2007) 288-295.

[135] K.G. Gallagher, D.T. Wong, T.F. Fuller, The effect of transient potential exposure on the electrochemical oxidation of carbon black in low temperature fuel cells, Journal of The Electrochemical Society, 155 (2008) B488-B493.

[136] N. Takeuchi, T.F. Fuller, Modeling and investigation of design factors and their impact on carbon corrosion of PEMFC electrodes, Journal of The Electrochemical Society, 155 (2008) B770-B775.

[137] J.D. Fairweather, B. Li, R. Mukundan, J. Fenton, R.L. Borup, In-situ and ex-situ characterization of carbon corrosion in PEMFCs, ECS Transactions, 33 (2010) 433-446.

[138] M. Wesselmark, C. Lagegren, G. Lindbergh, Degradation studies of PEMFC cathodes based on different types of carbon, ECS Transactions, 25 (2009) 1241-1250.

[139] S.R. Dhanushkodi, M. Tam, S. Kundu, M.W. Fowler, M.D. Pritzker, Carbon Corrosion Fingerprint Development and Deconvolution of Performance Loss According to Degradation Mechanism in PEM Fuel Cells - In press, Journal of Power Sources, (2013).

[140] A. Young, J. Stumper, E. Gyenge, Characterizing the structural degradation in a PEMFC cathode catalyst layer: carbon corrosion, Journal of the Electrochemical Society, 156 (2009) B913-B922.

[141] E.N.J. N. Takeuchi, and T.F Fuller., Investigation and modeling of carbon oxidation of Pt/C under dynamic potential condition., ECS Transactions, (2009) 25 (21) 1045-1054.

[142] C. Huang, K. Seng Tan, J. Lin, K. Lee Tan, XRD and XPS analysis of the degradation of the polymer electrolyte in H2-O2 fuel cell, Chemical Physics Letters, 371 (2003) 80-85.

[143] M. Schulze, N. Wagner, T. Kaz, K.A. Friedrich, Combined electrochemical and surface analysis investigation of degradation processes in polymer electrolyte membrane fuel cells, Electrochimica Acta, 52 (2007) 2328-2336.

[144] F.-Y. Zhang, S.G. Advani, A.K. Prasad, M.E. Boggs, S.P. Sullivan, T.P. Beebe Jr, Quantitative characterization of catalyst layer degradation in PEM fuel cells by X-ray photoelectron spectroscopy, Electrochimica Acta, 54 (2009) 4025-4030.

[145] M. Huang, A. Adnot, S. Suppiah, S. Kaliaguine, XPS observation of surface interaction between H2 and CO2 on platinum foil, Journal of Molecular Catalysis A: Chemical, 104 (1995) L131-L137.

[146] H.A. Gasteiger, S.S. Kocha, B. Sompalli, F.T. Wagner, Activity benchmarks and requirements for Pt, Pt-alloy, and non-Pt oxygen reduction catalysts for PEMFCs, Applied Catalysis B: Environmental, 56 (2005) 9-35.

[147] J. Zhang, K. Sasaki, E. Sutter, R.R. Adzic, Stabilization of Platinum Oxygen Reduction Electro-catalysts Using Gold Clusters, Science, 315 (2007) 220-222.

[148] K. Neyerlin, W. Gu, J. Jorne, H.A. Gasteiger, Determination of catalyst unique parameters for the oxygen reduction reaction in a PEMFC, Journal of the Electrochemical Society, 153 (2006) A1955-A1963.

[149] H. Gasteiger, W. Gu, R. Makharia, M. Mathias, B. Sompalli, Beginning of • life MEA performance efficiency loss contributions, Wiley Online Library, 2003.

[150] M. Inaba, T. Kinumoto, M. Kiriake, R. Umebayashi, A. Tasaka, Z. Ogumi, Gas cross-over and membrane degradation in polymer electrolyte fuel cells, Electrochimica Acta, 51 (2006) 5746-5753.

[151] S. Qing, W. Huang, D. Yan, Synthesis and characterization of thermally stable sulfonated polybenzimidazoles, European Polymer Journal, 41 (2005) 1589-1595.

[152] X. Yuan, H. Wang, J. Colin Sun, J. Zhang, AC impedance technique in PEM fuel cell diagnosis - A review, International Journal of Hydrogen Energy, 32 (2007) 4365-4380.

[153] H.A. Gasteiger, S.S. Kocha, B. Sompalli, F.T. Wagner, Activity benchmarks and requirements for Pt, Pt-alloy, and non-Pt oxygen reduction catalysts for PEMFCs, Applied Catalysis B: Environmental, 56 (2005) 9-35.

[154] J. Zhang, Z. Xie, J. Zhang, Y. Tang, C. Song, T. Navessin, Z. Shi, D. Song, H. Wang, D.P. Wilkinson, Z.-S. Liu, S. Holdcroft, High temperature PEM fuel cells, Journal of Power Sources, 160 (2006) 872-891.

[155] J. Zhang, Y. Tang, C. Song, X. Cheng, H. Wang, PEM fuel cells operated at 0% relative humidity in the temperature range of 23 -120 C, Electrochimica Acta, 52 (2007) 5095-5101.

[156] J. Zhang, Y. Tang, C. Song, Z. Xia, H. Li, H. Wang, J. Zhang, PEM fuel cell relative humidity (RH) and its effect on performance at high temperatures, Electrochimica Acta, 53 (2008) 5315-5321.

[157] J. Zhang, J. Wu, H. Zhang, PEM Fuel Cell Testing and Diagnosis, Elsevier, 2013.

[158] F. Barbir, PEM fuel cells: theory and practice, Academic Press, 2012.

[159] J. Hirschenhofer, D. Stauffer, R. Engleman, M. Klett, Fuel cell handbook, (1998).

[160] S.S. Kocha, Polymer Electrolyte Membrane Fuel Cells, Automotive Applications, in: Fuel Cells, Springer, 2013, pp. 473-518.

[161] B.-T. Huang, Y. Chatillon, C. Bonnet, F. Lapicque, S. Leclerc, M. Hinaje, S. Raël, Experimental Investigation of Air Relative Humidity (RH) Cycling Tests on MEA/Cell Ageing in PEMFC Part II: Study of Low RH Cycling Test with Air RH at 62%/0%, Fuel Cells, 12 (2012) 347-355.

[162] K. Eloot, F. Debuyck, M. Moors, A. Van Peteghem, Calculation of the impedance of noncylindrical pores Part I: Introduction of a matrix calculation method, Journal of applied electrochemistry, 25 (1995) 326-333.

[163] A. Young, J. Stumper, S. Knights, E. Gyenge, Ionomer degradation in polymer electrolyte membrane fuel cells, Journal of the Electrochemical Society, 157 (2010) B425-B436.

[164] L. Petzold, W. Zhu, Model reduction for chemical kinetics: An optimization approach, AIChE Journal, 45 (1999) 869-886.

[165] J. Zhu, R. Dittmeyer, H. Hofmann, Application of sensitivity analysis to the reduction of a complex kinetic model for the homogeneous oxidative coupling of methane, Chemical Engineering and Processing: Process Intensification, 32 (1993) 167-176.

Appendix A
Leak Test

A.1 Introduction

This document outlines the recommended AFCC PEM fuel cell leak test procedure as adapted from other single cells. A leak test of a cell is recommended prior to operation or testing. A fuel cell that leaks, especially at fuel ports, may present a safety hazard and should not be operated. During the leak test, any flammable or hazardous gas should not be used. In this particular procedure, air will be used at 20 psi for the leak test. A photograph and schematic diagram of the fuel cell are shown in Figures A-1 and A-2. The fuel cell has a total of 12 ports: coolant inlet, fuel inlet, oxidant inlet, coolant outlet, fuel outlet, oxidant outlet and connections for 6 thermocouples (T1, T2, T3, C1, C2 and C3). However, in Pt dissolution and carbon corrosion AST experiments, they are unnecessary and thus plugged to ensure a closed system in the fuel cell. Figure A-2 preesents a rough overview of the location of each port in the fuel cell to facilitate this description of the leak test procedure

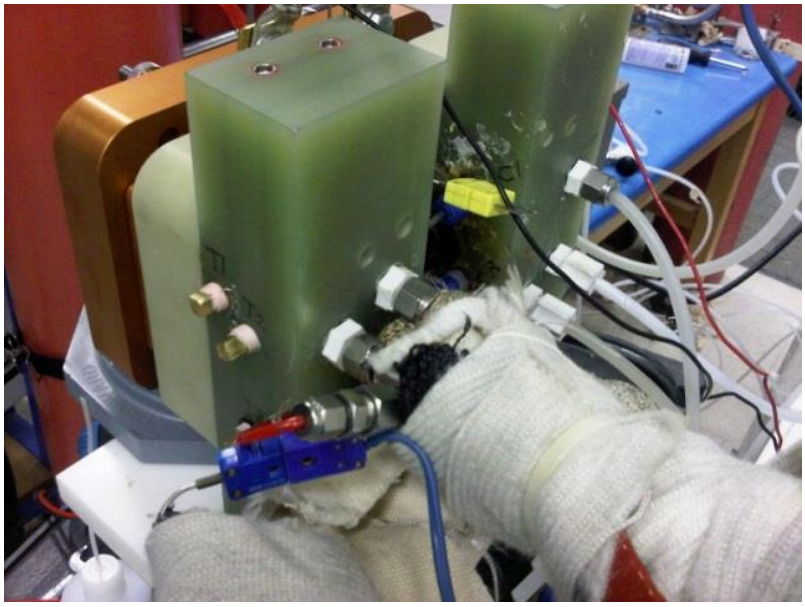

Figure A-1: AFCC fuel cell during operation

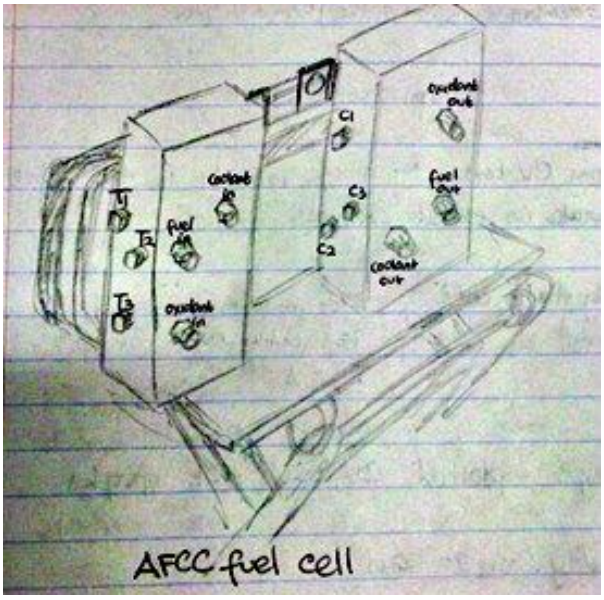

Figure A-2: Sketch of AFCC PEM fuel cell showing all 12 ports

A.2 Basic Circuit Leak Test

This leak test is repeated three times for each coolant, fuel and oxidant port. It is recommended to start by testing the coolant port. The basic circuit leak test measures the total gas leak rate from all sources, including hydrogen cross-over. This is an important test due to the use of hydrogen during fuel cell operation. A schematic diagram showing the set-up for the coolant circuit leak test is given in Figure A-3. The same set-up and procedure is used to test for leaks at the fuel and oxidant ports. It involves first slowly pressurizing the fuel cell using air until it is locked automatically. An air source is then connected to the coolant inlet and the coolant outlet is sealed, while the fuel and oxidant ports are left open to the atmosphere. The thermocouple ports T1, T2, T3, C1, C2, and C3 are properly plugged throughout the test.

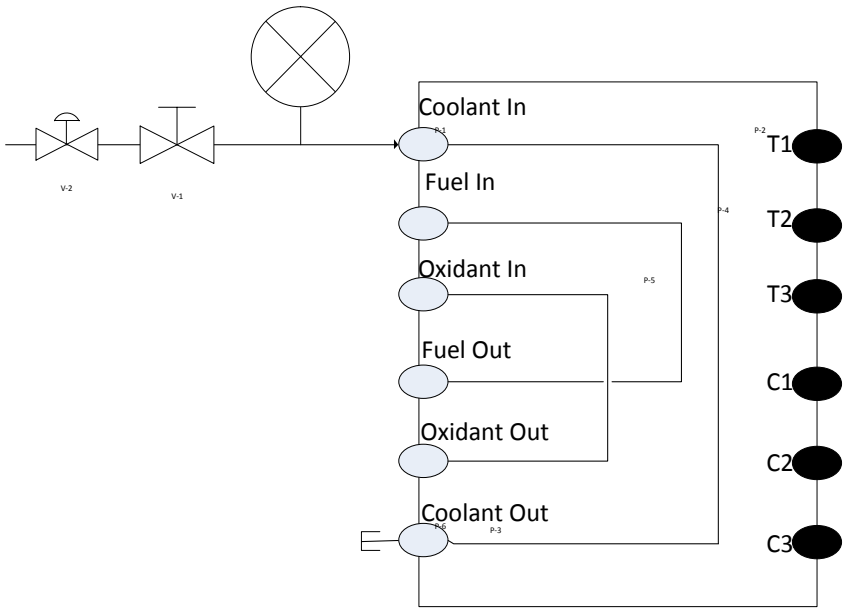

Figure A-3: Basic circuit leak test set-up

The air source to the coolant inlet is set to 20 psi and the pressure is monitored. A 1 psi drop within 5 minutes is tolerable. However, a larger pressure drop signifies a leak

somewhere in the cell. The leak can be located by applying a soap solution to each port (including T1, T2, T3, C1, C2, C3) and watching for bubbles to appear.

A.3 External Leak Test

A schematic diagram showing the set-up to test for external leaks is given in Figure A-4. Again, the fuel cell is slowly pressurized using air until it locks automatically. The air source is then connected to the coolant inlet and a plastic tube is used to connect the coolant outlet to the fuel inlet. Then, another plastic tube is used to connect the fuel outlet to the oxidant inlet and the oxidant outlet is kept closed. The pressure of the air source connected to the coolant inlet is then set to 20 psi and the pressure is monitored. A 1 psi drop within 5 minutes is tolerable. Any larger pressure drop signifies a leak. A soap solution is then sprayed on each of the ports (including T1, T2, T3, C1, C2, C3) to locate the leak. The appearance of bubbles indicates a gas leak, which must then be addressed. The soap solution is also sprayed on the bipolar plates due to the possibility of a leak in the gaps between the plates.

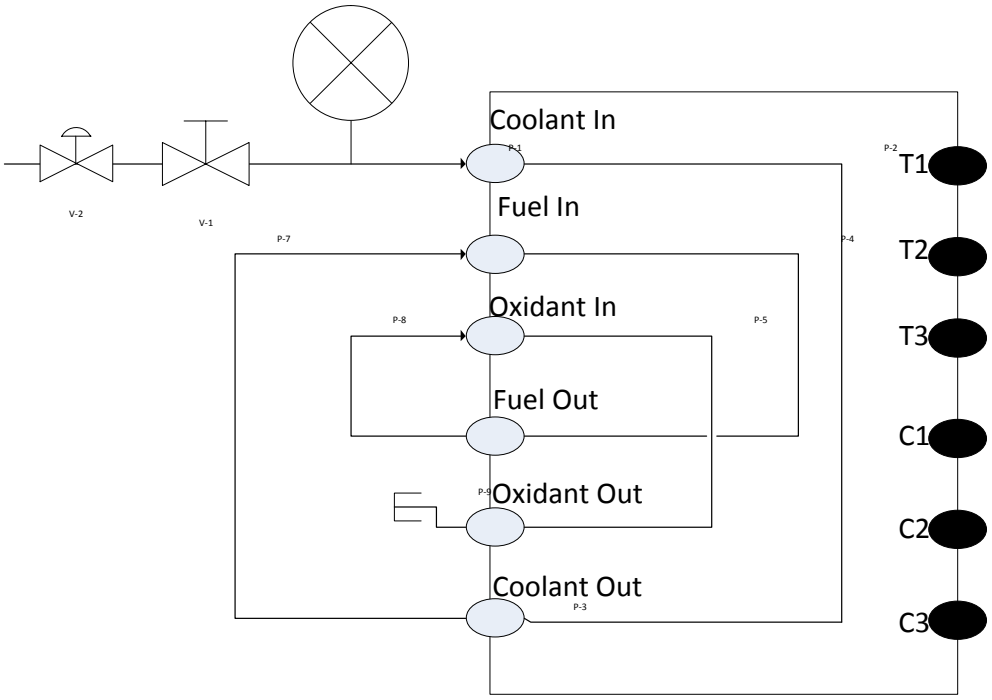

Figure A-4: External leak test set-up

A.4 Coolant-to-Oxidant Leak Test

After performing the basic circuit leak and external leak tests, all external leak and seal integrity problems are addressed before progressing to the transfer check test. This test provides information about possible leaks from the coolant circuit to the oxidant circuit. Figure A-5 shows a schematic of the set-up for this test. The fuel cell is slowly pressurized using air until it locks automatically. The air source is connected to the coolant inlet and the coolant outlet is sealed. Tubing is connected to the oxidant inlet and submerged in a beaker of water. Then the oxidant outlet is sealed, while the fuel inlet and outlet are left to vent to the atmosphere. Any leakage between the coolant and oxidant circuits is identified by bubbles leaving the submerged tube.

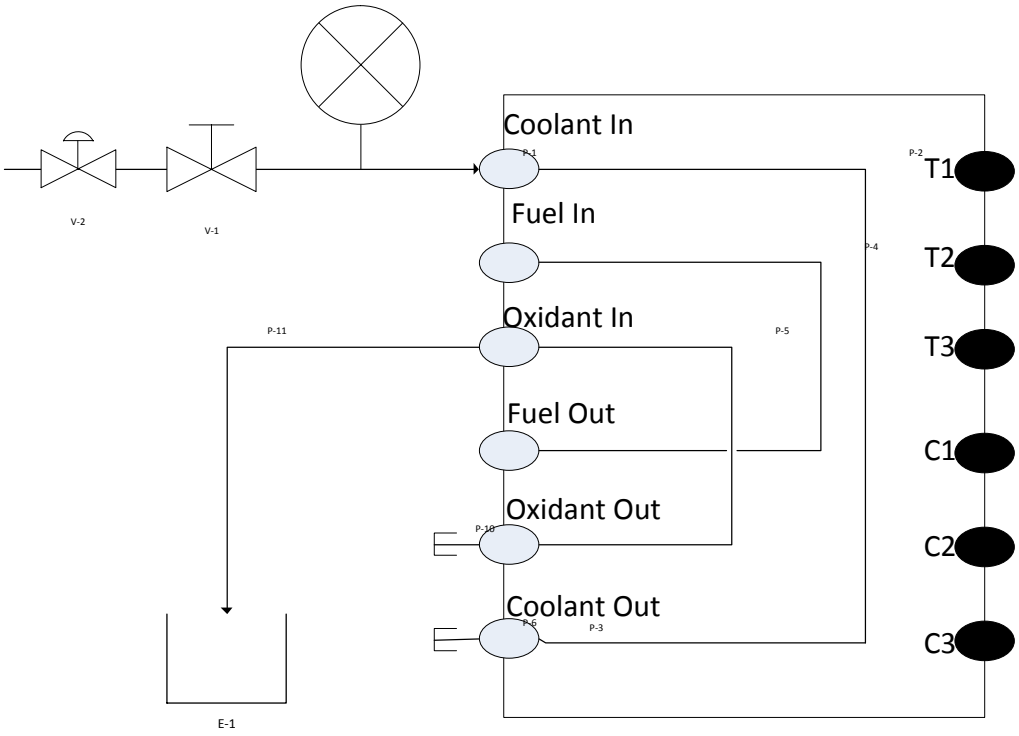

Figure A-5: Coolant-to-oxidant leak test set-up

A.5 Fuel-to-Oxidant Leak Test

This test provides information about possible leaks from the fuel circuit to the oxidant circuit. The set-up for this test is shown in Figure A-6. The fuel cell is slowly pressurized using air until it locks automatically. The air source is connected to the fuel inlet and the fuel outlet is closed. Tubing is connected to the oxidant inlet and then submerged in a beaker of water. The oxidant outlet is sealed, while the coolant inlet and outlet are left to vent to atmosphere. Leakage between the fuel and oxidant circuits is located by bubbles leaving the submerged tube.

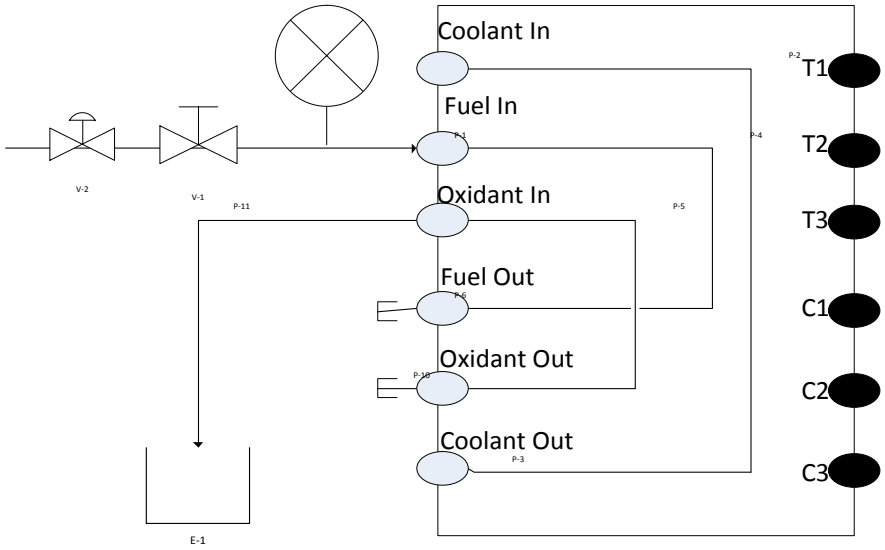

Figure A-6: Fuel-to-oxidant leak test set-up

A.6 Coolant-to- Fuel Leak Test

Figure A-7 shows the set-up to test for leaks from the coolant circuit to the fuel circuit. The fuel cell is slowly pressurized using air until it locks automatically. The air source is connected to the coolant inlet, while the coolant outlet is closed. Tubing is connected to the fuel inlet and submerged in a beaker of water. The fuel outlet is then sealed, while the oxidant inlet and outlet are left to vent to atmosphere. Leaks between the coolant and fuel circuits are identified by bubbles leaving the submerged tube.

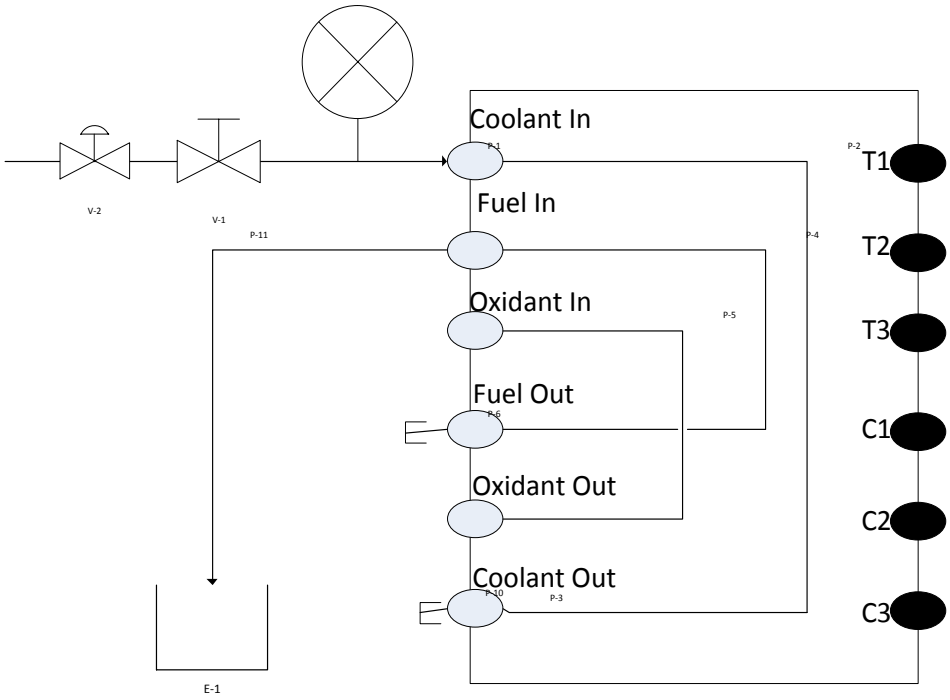

Figure A-7: Coolant-to-fuel leak test set-up

Appendix B

Carbon Model Sensitivity Analysis

B.1. Alternate Simplification Procedure for the Carbon Model

To determine whether the full Gallagher and Fuller model can be satisfactorily simplified as discussed in the carbon model development, a sensitivity analysis of the model was conducted using the parameters reported by Gallagher and Fuller [87]. In this section, several reaction steps involved in the Gallagher and Fuller model is simplified based on the values of the sensitivity coefficient analysis. To assess the accuracy of the simplified model, we determined its incident matrix.

B.2. Sensitivity Coefficient Method

This analysis was used to identify any reaction steps that do not contribute to carbon loss in any significant way. A method proposed by Zhu et al is used to calculate overall normalized sensitivity coefficients and do the sensitivity analysis [164, 165]. Generally, most of the kinetic studies of carbon corrosion in metal or fuel cell environments that have been proposed in the literature make use of different models with a large number of elementary steps. However, for most practical applications, many of the details of these models and intermediate steps are ignored during the design or process optimization of fuel cell catalysts. Instead, it would be beneficial to make use of much simpler schemes. Thus, it is important to identify the most important reactions and their impacts during fuel cell operation. The reduction of a complex kinetic model can be achieved by means of sensitivity analysis, which can be carried out by making use of normalized linear sensitivity coefficients calculated according to the following equation:

$$S_{i,j} = \frac{k_j}{m_i}\left(\frac{\partial m_i}{\partial k_j}\right) = \left(\frac{\partial \ln m_i}{\partial \ln k_j}\right) \qquad \text{A-1}$$

where k_j is the model parameter being considered, m_i is the carbon mass loss predicted by the model and $S_{i,j}$ is the overall sensitivity coefficient for the mass loss m_i with respect to the model parameter k_j. The use of equation A -1 eliminates artificial variations owing to the magnitudes of m_i and k_j so that only relative changes in m_i due to relative changes in k_j are compared with each other. The simplification of a kinetic model with the help of sensitivity analysis can be done based on the criterion

$$|S_{i,l}| > |S_{i,n}| \qquad \text{A-2}$$

When this conditions is met, it signifies that reaction l has a stronger effect on the carbon loss change in species i than does reaction n. This implies that reaction n is less important with respect to changes in carbon loss of the species i than is reaction l. If the magnitude of the sensitivity coefficient of a particular reaction is very small for all species participating in a reaction, then this reaction can be removed from the model without significantly affecting the model predictions. In our work, a kinetic model of carbon corrosion in PEMFC consisting of seven elementary reactions and many species, originally proposed by Gallagher and Fuller [95], was simplified with the help of a modified sensitivity analysis. Mass loss of carbon species and linear sensitivity coeffcients $\frac{\partial m_i}{\partial k_j}$ for all the species are calculated for the respective reactions as a function of the time. The following steps are used in the analysis

1. For an arbitrarily chosen set of operating conditions Table 4-4, a sensitivity analysis was done.
2. Global sensitivity coefficient B_j was defined by summing the squared normalized sensitivity coefficients $S_{i,j}$ of any species at q = 7 reaction times equally spaced between t = 0 and t = τ. B_j can be defined as

$$B_j = \sum_{t=1}^{q} \sum_{i=1}^{N} \left[\left[\frac{\partial \ln m_i}{\partial \ln k_j} \right]^2 \right] \qquad \textbf{(A-3)}$$

3. According to the above definition, a maximum value of B_j = 17.69 was calculated. However, only two reactions, representing about two-thirds of the total number of reactions contained in the original model, reached a magnitude of B_j larger than 0.1. In our analysis, the sensitivity of the predicted carbon mass loss was assessed with respect to each rate constant in the full model, while keeping all other parameters fixed at the values used by Gallagher and Fuller. Model simulations were carried out three times to determine the sensitivity of the computed surface coverage θ_{cov} of $C^{\#}OH$ sites and carbon mass loss to each rate constant – each time using three arbitrary rate constants. Rate constants reported in Gallagher and Fuller used as reference values for this analysis.

4. To simplify the kinetic model, initially all reactions with were considered. Then B_j values were calculated. To simplify the kinetic model, the rate equations, which yield $B_j \geq 0.5$ are considered. This assumption is based on the simulation results of the models which yield $B_j \geq 0.5$ showed that no carbon corrosion reaction took place. Evaluation of the full Gallagher and Fuller model yields an O_j value of 17.69. Zhu et al also used similar threshold to remove reactions from a complex model [165]. Maximum value of B_j = 15.61 is calculated for rate equation for the reaction given by equation (4-3). Only two reactions, given by equations (4-3) and (4-4), yielded a value of $b_j \geq 0.5$ (1.22 and 15.61, respectively). Negligibly small values of b_j were obtained for the remaining five rate equations in the model. Based on the results of the sensitivity analysis and subsequent simulations based on active site reductions, the reactions of 4-5 to 4-12 are excluded from the Gallagher model.

5. In addition to this, model simulations were run for the entire model to identify any notable change in the predicted amount of carbon loss due to the reduction of # sites, so that those reactions were considered to be significant. If no change was observed in carbon loss, the reaction was ignored. Only equations (4-3) and (4-4) given in

Table 4-2 were found to be important in the full model proposed by Gallagher and Fuller. The rate expressions corresponding to equations (4-3) and (4-4) are used to predict the carbon loss for the simulated ASTs

B.3. Sensibleness of the Simplified Model Based on Incidence Matrix

Sensibleness of the simplified model is tested based on the incidence matrix given in Table B-1**.** The equation numbers of the simplified reaction steps are given in the first row of Table B-1 and the species involved in these reactions are shown in the first column. A species produced by a reaction is given a value +1, while a species that is consumed is denoted with a value of −1. If the species is not involved in a reaction, the corresponding column is left as blank. The Boolean sum of each species was calculated. If there is no net change in the moles of a species in the entire mechanism, then the Boolean sum for that species is zero. If the sum is positive, then the mechanism leads to a net generation of the corresponding species; if it is negative, the species is being consumed overall. The sum is zero for the intermediate species $C^{\#}OH$, $C^{\#}(H_2O)_{ads}$, $C^{\#}OC^{\#}OH$, $C^{\#}O(C^{\#}OOH)_2$, $C^{\#}O(C^{\#}OOH)_2$ and $C^{\#}OOH$. In contrast, the value for CO_2 is positive since it is an overall product. The incidence matrix further indicates that no initiating reaction is included in the simplified mechanism because no column contains a negative sum for any species.

Table B-1: Sensibleness of the simplified model based on incidence matrix.

	1	2a	2b	2c	2d	2e	Boolean Sum
$C^{\#}OH$	1		-1	1			0
$C^{\#}(H_2O)_{ads}$		1	-1				0
$C^{\#}OC^{\#}OH$			1	-1			0
$C^{*}O(C^{*}OOH)_2$				1	-1		0
$C^{*}OOH$					1	-1	0
CO_2					1	1	1

Appendix C

Carbon Model and Performance fitting of other ASTs

(a)

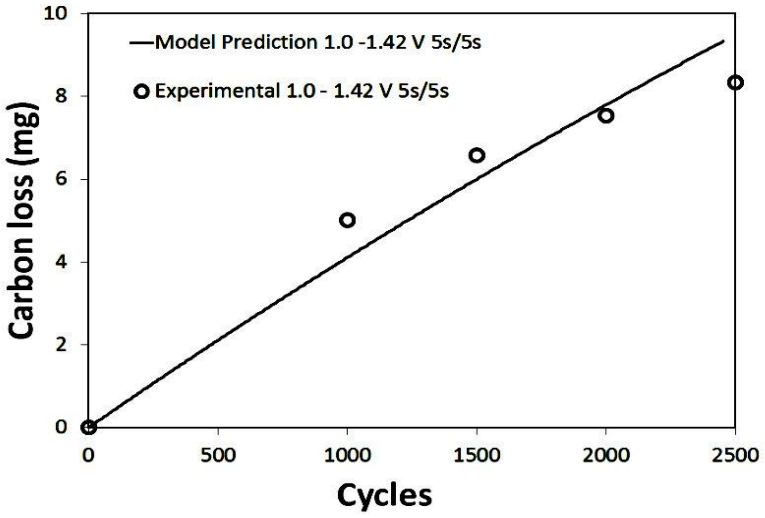

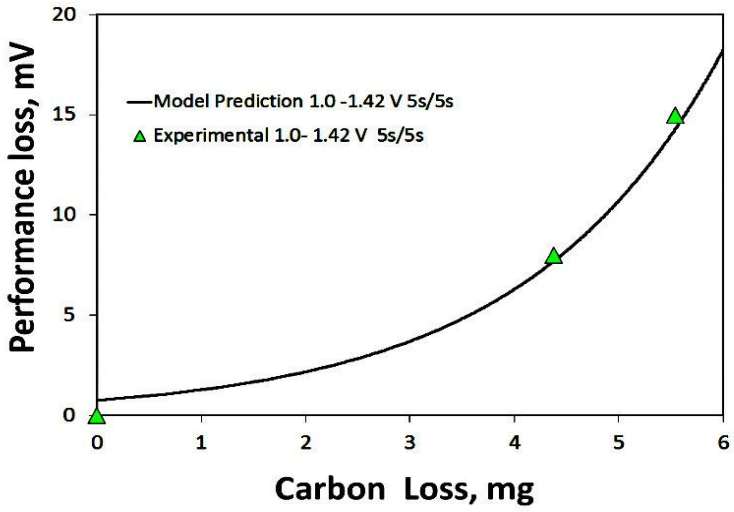

(b)

Figure C-1: (a) Validation of the carbon corrosion kinetic model with different voltage cycles at 70°C, 1.5 barg/1.5 barg, H_2-Air flow rates 1-1 slpm, 100 % gas humidity and N_2-H_2 atmosphere at the cathode and anode for ASTs for 1.0 -1.42 5s/5s square-wave AST (b) Model fitting of carbon loss and performance loss obtained using the model with the experimental results of ASTs for 1.0 -1.42V 5s/5s square-wave AST.

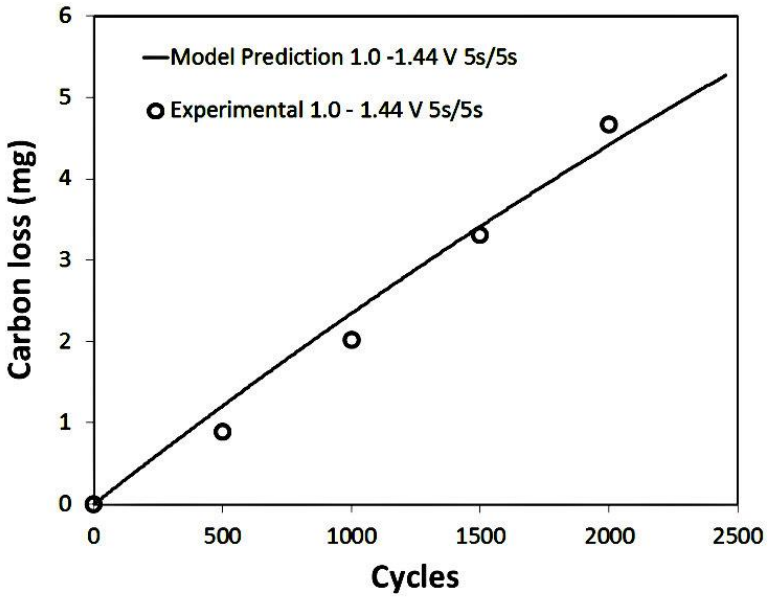

(a)

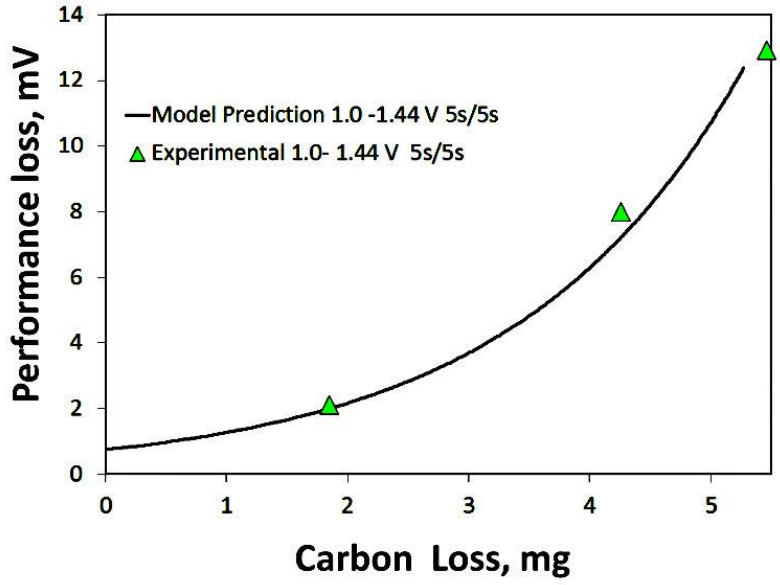

(b)

Figure C-2 (a) Validation of the carbon corrosion kinetic model with different voltage cycles at 70°C, 1.5 barg/1.5 barg, H_2-Air flow rates 1-1 slpm, 100 % gas humidity and N_2-H_2 atmosphere at the cathode and anode for ASTs for 1.0 -1.44 5s/5s square-wave AST (b) Model fitting of carbon loss and performance loss obtained using the model with the experimental results of ASTs for 1.0 -1.44V 5s/5s square-wave AST.

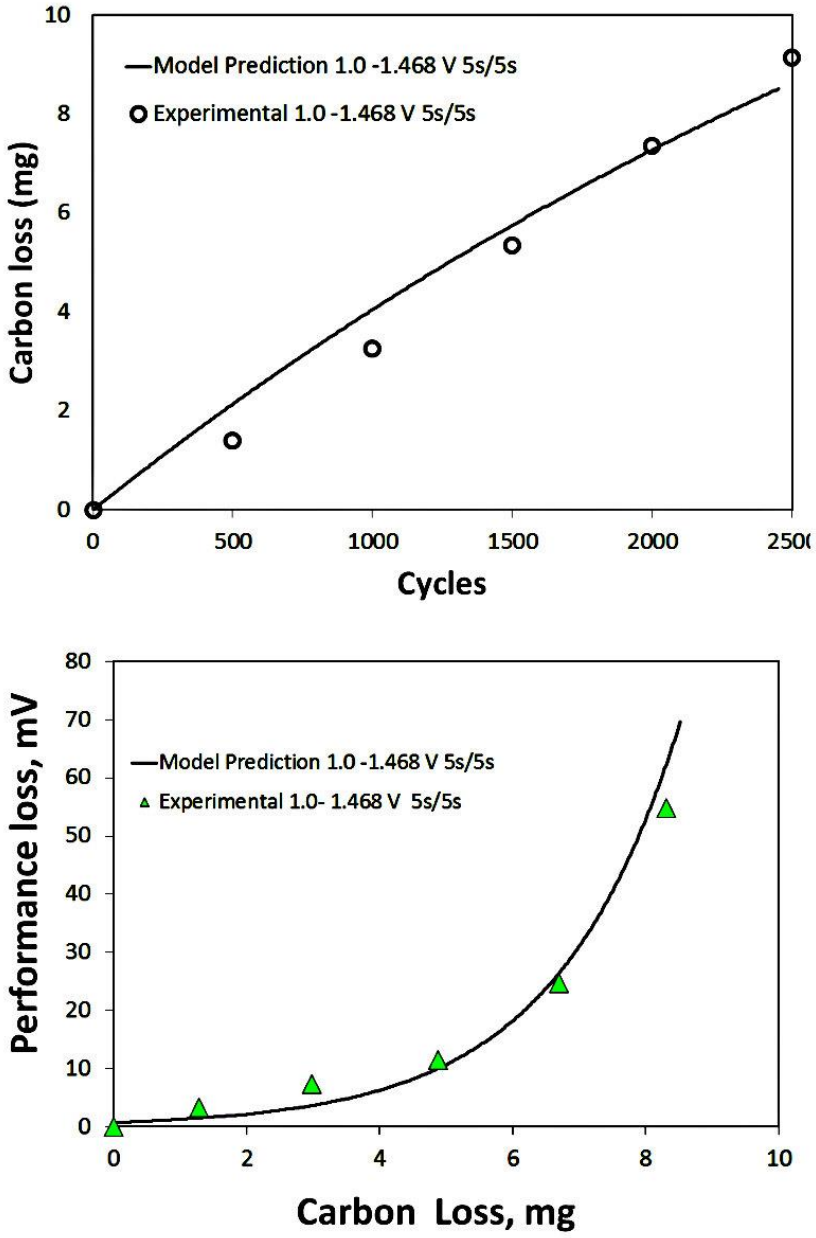

Figure C-3 (a) Validation of the carbon corrosion kinetic model with different voltage cycles at 70°C, 1.5 barg/1.5 barg, H_2-Air flow rates 1-1 slpm, 100 % gas humidity and N_2-H_2 atmosphere at the cathode and anode for ASTs for 1.0 -1.468 5s/5s square-wave AST (b) Model fitting of carbon loss and performance loss obtained using the model with the experimental results of ASTs for 1.0 -1.468 V 5s/5s square-wave AST.

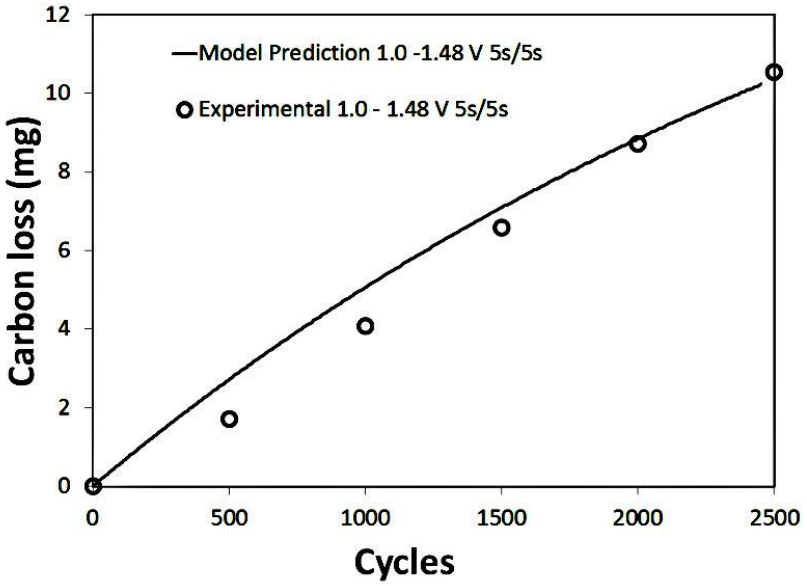

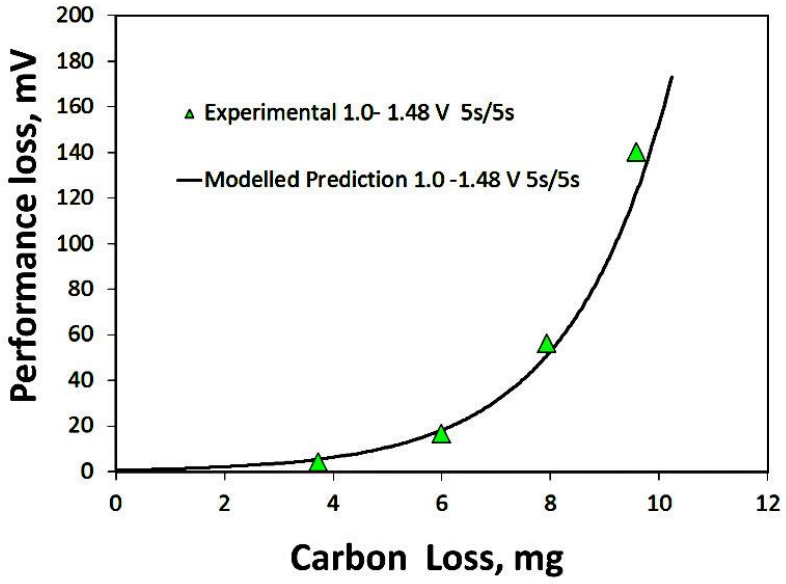

Figure C-4 (a) Validation of the carbon corrosion kinetic model with different voltage cycles at 70°C, 1.5 barg/1.5 barg, H_2-Air flow rates 1-1 slpm, 100 % gas humidity and N_2-H_2 atmosphere at the cathode and anode for ASTs for 1.0 -1.48 5s/5s square-wave AST (b) Model fitting of carbon loss and performance loss obtained using the model with the experimental results of ASTs for 1.0 -1.48V 5s/5s square-wave AST.

Appendix D

Related Publications

Journal Articles

1. Dhanushkodi, S.R, Kundu, S., Fowler, M.W, Pritzker, M.D, 2013 (submitted). Study of the Effect of temperature during Platinum dissolution ASTs. Journal of Power Sources.
2. Dhanushkodi, S.R, Tam, M., Kundu, S., Fowler, M.W, Pritzker, M.D, 2012. Carbon Corrosion Fingerprint Development and De-convolution of Performance Loss According to Degradation Mechanism in PEM Fuel Cells. Journal of Power Sources, Vol 240, Pages 114–121.
3. Dhanushkodi, S.R, Mahinpey, N., Srinivasan, A., Wilson, M., 2008. Life Cycle Analysis of Fuel Cell Technology. Journal of Environmental Informatics, 11, 36-44. (3 Citations)

Book Chapter

1. Dhanushkodi, S.R, Fowler, M.W, Mazza, A., Pritzker, M.D, 2010. Membrane Electrode Assembly Contamination. (2 Citations)

Conferences

1. Dhanushkodi, S.R., Fowler, M.W., Pritzker, M.D., 2010. Characterization of Porous Gas Diffusion Media for Polymeric Electrolyte Membrane Fuel Cell using Novel Technique (Oral Presentation). Graduate Student Research Conference, University of Waterloo, Waterloo, ON.

2. Dhanushkodi, S.R., Fowler, M.W., Pritzker, M.D., Yuan, X.Z., Wang, H., 2010. Degradation and Diagnostic Analysis of Gas Diffusion Layers under Humidity Cycling. ECS Meeting, The Electrochemical Society, Vancouver, pp. 349-349. (1 Citation)
3. Arzutug, M., Fowler, M.W., Singaram, V., Dhanushkodi, S.R, 2010. Influence of Gradient PTFE Coating in Cathode Gas Diffusion Layer on the Performance of PEMFCs. ECS Meeting, The Electrochemical Society, pp. 277-277.
4. Dhanushkodi, S.R., Fowler, M.W., Pritzker, M.D., Kundu, S., 2010. Role of Pt banding in PEMFC Performance Loss during Start up / Shut down Cycling (Poster Presentation). OFCRIN Technical Review Day, Queens University, Kingston, ON.
5. Dhanushkodi, S.R., Fowler, M.W., Pritzker, M.D., Gostick, J.T., Yuan, X.Z., Wang, H., 2009. Comparison Study of Gas Diffusion Layer Degradation between RH cycling and Near Open-circuit Conditions (Poster Presentation). OFCRIN Technical Review Day, Poster Presentation,, University of Waterloo, Waterloo, ON.